Radio and Millimeter Observations of the Environments of Young Stars Undergoing Accretion Bursts

Zsófia Marianna Szabó

A thesis submitted for the degree of Doctor of Philosophy (PhD)

at the University of St Andrews

Dissertation

zur Erlangung des Doktorgrades (Dr. rer. nat.)

der Mathematisch-Naturwissenschaftlichen Fakultät

der Rheinischen Friedrich-Wilhelms-Universität Bonn

UNIVERSITÄT BONN

University of St Andrews

Angefertigt mit Genehmigung der Mathematisch-Naturwissenschaftlichen Fakultät der Rheinischen Friedrich-Wilhelms-Universität Bonn

Betreuer (Max-Planck-Institut für Radioastronomie): Prof. Dr. Karl M. Menten

Betreuer (University of St Andrews): Dr. Claudia Jane Cyganowski

Betreuer (University of Bonn): Prof. Dr. Pavel Kroupa

Gutachter: Dr. Aleksander Scholz

Gutachter: Prof. Dr. Sebastián Pérez Márquez

Tag der Promotion: 14.05.2025

Erscheinungsjahr: 2026

Declaration

Candidate's declaration

I, Zsófia Marianna Szabó, do hereby certify that this thesis, submitted for the degree of PhD, which is approximately, 35,000 words in length, has been written by me, and that it is the record of work carried out by me, or principally by myself in collaboration with others as acknowledged, and that it has not been submitted in any previous application for any degree. I confirm that any appendices included in my thesis contain only material permitted by the 'Assessment of Postgraduate Research Students' policy.

I was admitted as a research student at the University of St Andrews in late August 2021.

I received funding from an organisation or institution and have acknowledged the funder(s) in the full text of my thesis.

Date Signature of candidate

Supervisor's declaration

I hereby certify that the candidate has fulfilled the conditions of the Resolution and Regulations appropriate for the degree of PhD in the University of St Andrews and that the candidate is qualified to submit this thesis in application for that degree. I confirm that any appendices included in the thesis contain only material permitted by the 'Assessment of Postgraduate Research Students' policy.

Date Signature of supervisor

Permission for publication

In submitting this thesis to the University of St Andrews we understand that we are giving permission for it to be made available for use in accordance with the regulations of the University Library for the time being in force, subject to any copyright vested in the work not being affected thereby. We also understand, unless exempt by an award of an embargo as requested below, that the title and the abstract will be published, and that a copy of the work may be made and supplied to any bona fide library or research worker, that this thesis will be electronically accessible for personal or research use and that the library has the right to migrate this thesis into new electronic forms as required to ensure continued access to the thesis.

I, Zsófia Marianna Szabó, confirm that my thesis does not contain any third-party material that requires copyright clearance.

The following is an agreed request by candidate and supervisor regarding the publication of this thesis:

Printed copy

No embargo on print copy.

Electronic copy

No embargo on electronic copy.

Date Signature of candidate

Date Signature of supervisor

Underpinning Research Data or Digital Outputs

Candidate's declaration

I, Zsófia Marianna Szabó, understand that by declaring that I have original research data or digital outputs, I should make every effort in meeting the University's and research funders' requirements on the deposit and sharing of research data or research digital outputs.

Date Signature of candidate

Permission for publication of underpinning research data or digital outputs

We understand that for any original research data or digital outputs which are deposited, we are giving permission for them to be made available for use in accordance with the requirements of the University and research funders, for the time being in force.

We also understand that the title and the description will be published, and that the underpinning research data or digital outputs will be electronically accessible for use in accordance with the license specified at the point of deposit, unless exempt by award of an embargo as requested below.

The following is an agreed request by candidate and supervisor regarding the publication of underpinning research data or digital outputs: No embargo on underpinning research data or digital outputs.

Date Signature of candidate

Date Signature of supervisor

Abstract

Studying the formation and evolution of Sun-like stars is crucial for understanding the origins of the Solar System. Young stellar objects (YSOs) undergo episodic outbursts that may impact disk chemistry and planet formation. The FU Orionis- and EX Lupi-type objects (FUors and EXors) experience dramatic brightness increases due to enhanced accretion, and while these outbursts may have lasting effects on the disk chemistry and surrounding environments, their impact remains poorly explored, especially in the radio and millimeter wavelengths.

In this PhD thesis, I conducted the first dedicated radio surveys of FUors and EXors, using ammonia (NH_3) with the Effelsberg 100-m telescope to trace their dense cores and water (H_2O) maser emission as an accretion burst indicator. Additionally, I performed the first wideband millimeter line survey of the evolved FUor V1057 Cyg with the IRAM 30-m telescope, complemented with additional data from the APEX 12-m telescope.

The NH_3 survey detected (1,1) emission in over half of the sampled objects (28/51), revealing cold regions (below 25 K) with column densities similar to those found in infrared dark clouds. Archival *Herschel* SPIRE data provided H_2 column densities and dust temperatures, identifying dense material in at least seven sources. The detection of the (2,2) emission suggests some FUors and EXors may be younger than previously classified.

The 22.2 GHz H_2O maser survey detected emission in three sources (6%), including two FUors and one EXor. Notably, masers were observed in the FUor HH 354 IRS for the very first time, and multiple flares were identified in archival data for other sources, suggesting episodic variability.

The millimeter survey of V1057 Cyg identified over 35 molecular species, including complex organic molecules. Position-velocity diagrams of ^{12}CO suggest past episodic outbursts, with a dynamical timescale of the outflow on the orders of tens of thousands of years, indicating that it cannot represent the ongoing outburst alone. This work demonstrates the potential of molecular line studies to refine the classification and chemical characterization of eruptive stars.

Dedication

"A hídon akkor kell átkelni, amikor odaér az ember."

This thesis is dedicated to the memory of my dear Grandmother, whose love, wisdom, and unwavering belief in me shaped my journey in ways words cannot fully capture. Though you are no longer with me, your spirit has been my guiding light.

To my family, whose boundless encouragement, patience, and faith in me have made this accomplishment possible. Your love has been a constant source of strength and inspiration, and I am forever grateful for your presence in my life. I am immensely proud of the women in my family who have broken generational cycles, which have allowed me to become the first women in our family to pursue higher education and not even stopping until a PhD!

To my precious little niece: always remember that you can be anything your heart desires when you grow up, and I hope you'll always have the coolest auntie by your side to cheer you on!

And to my beloved partner, Niki, whose support and understanding have been my anchor. Your extreme patience, love, and companionship have sustained me through the toughest moments. Thank you for always believing in me, especially when I doubted myself, and for never letting me give up on this dream (especially when I was ready to leave). Your love has been the greatest gift I could ever receive.

Acknowledgments

"We do these things not because they are easy, but because they are hard." – John F. Kennedy

Funding

My PhD was supported by the St Leonard's Global PhD Scholarship, by the Max-Planck-Institute for Radio Astronomy, the University of Bonn, and the International Max Planck Research School (IMPRS).

General acknowledgments

My journey from a small town in Hungary to study science, to become an astronomer, and to embark on this journey for a co-tutelle PhD and navigating all its various hardships were anything but easy. However, along the way, I met incredible people, whose view on science, collaboration, and life allowed me to become who I am today, and I am utterly grateful for all of them.

First and foremost, I would like to express my deepest gratitude to my supervisors. To Claudia Cyganowski, thank you for your unwavering guidance, insightful feedback, and encouragement, which have been crucial to the completion of this thesis. I am deeply grateful for the opportunity to work under your mentorship, and I am thankful for the many valuable lessons I have learned along the way. I would like to express my deepest gratitude to my other supervisor, Karl Menten, whose guidance, support, and encouragement were invaluable throughout my research. Karl was not just a mentor but a source of inspiration, and I am profoundly grateful for the time and knowledge he shared with me. When writing this, I have still not come to terms about the fact that he is no longer with us. The lessons I learnt under his mentorship continue to shape my work and my approach to research, and I hope that those fractions of knowledge I gathered during this PhD can live through my work.

I would also like to thank my collaborators in Bonn, whose support and for providing me with the freedom to explore new ideas, as well as their practical advice and constructive criticism. Their contributions have greatly enhanced my work and the quality of my thesis. To Yan Gong and Wenjin Yang, thank you for helping me prepare my first proposals for radio and millimeter observations, for teaching me how to conduct those, the data reduction, and many more. You have been wonderful teachers to me, and I cherish the memories of our brain-storming sessions and random discussions about our results. To Yan, thank you for working closely with me on deriving

H_2 column densities from Herschel data, that I have used throughout my work. To Arnaud Belloche, thank you for offering to become my unofficial second supervisor. Your patience, guidance, insightful feedbacks has guided me on this journey. The millimeter line survey that we worked on together fostered my interest in astrochemistry, and I truly look forward to extend my expertise in this field in the future. Thank you for always taking time to discuss and teach me the difficult steps of handling such large data sets, and ultimately teaching me everything I know now. I am deeply grateful for everything!

I am utterly grateful to my collaborators, especially Ágnes Kóspál and Péter Ábrahám, who have given me an opportunity as a BSc student at Konkoly Observatory in Hungary to be involved in research. I will be forever grateful. Thank you for your shared expertise, fruitful discussions, and contributions to the projects that formed this Thesis.

I would like to extend my thanks to the various institutions and facilities that made this research possible, particularly the staff and operators at the Effelsberg 100-m telescope for providing access and additional time to gather more data for my surveys. I am extremely thankful for the staff at the APEX 12-m telescope. I had the immense privilege to conduct a two week observing shift in 2022 November, where I have learnt so much first hand experience from the wonderful staff. I am very thankful for all the administration staff and the help I received at MPIfR and IMPRS, and at the School of Physics and Astronomy in St Andrews.

On a personal note, I wish to thank my family for their love, patience, and understanding throughout this long process. To my parents Gabi, Gyula, and my brother Andris, your constant belief in me has been a source of strength and motivation. No words can express my gratitude that you have supported me on this journey, not knowing anything about the topic or subjects I wanted to learn, but you still kept being my biggest cheerleaders. To my partner, Niki, your love, support, and encouragement have kept me grounded and inspired. I am incredibly fortunate to have such a supportive family by my side.

I would also like to express my gratitude to friends, colleagues, office mates, and flatmates from Hungary to Germany, to the UK. Thank you all for your support for creating an intellectually stimulating and supportive environment. You may not know, but you all contributed to this Thesis! I would also like to give a special thanks to the best flatmate to date, Petra, whose dedication to napping, occasional "helpful" pawing at my chair with a little toy, has been an endless source of comfort and amusement, the most purrfect little buddy!

Finally, I would like to thank all those who have been part of this journey, whether through direct academic or personal support, or simply by being there when I needed you. While not all names can be listed here, I am grateful to each and every one of you.

Research Data/Digital Outputs access statement

Research data underpinning this thesis are available at the following: Chapter 2 is available at DOI, Chapter 3 at DOI, and Chapter 4 at DOI.

Contents

Declaration i

Abstract v

Dedication vii

Acknowledgments ix

1 Introduction 1

1.1 The Formation of Sun-like Stars 2

1.2 Observing the Circumstellar Structure around Young Stars 6

1.3 Variations in Light and Accretion 7

1.4 The FU Orionis-type Objects 10

1.5 The EX Lupi-type Objects 13

1.6 Intermediate or Hybrid Eruptive Stars 16

1.7 Chemical Tracers 17

1.7.1 Ammonia as a Tracer of Dense Cores around Young Stars 17

1.7.2 Water Masers as Indicators of Star Formation 19

1.8 Telescopes and Instruments Utilised in This Thesis 21

1.8.1 Introduction to Single-Dish Radio Astronomy 22

1.8.2 Radio Telescopes Utilised for My Research 24

1.9 Thesis Overview 29

2 Host environments of FU Orionis- and EX Lupi-type objects traced by NH_3 33

2.1 Introduction 34

2.2 Observations and data reduction 35

2.2.1 Sources with non-detections 37

2.3 Results and analysis 37

2.3.1 Molecular excitation . . . 40
2.3.2 Beam filling factor . . . 42
2.3.3 LSR velocities . . . 44
2.3.4 Classification and $v_{\rm LSR}$ . . . 45
2.3.5 Line widths . . . 45
2.3.6 Spectral Energy Distributions (SEDs) . . . 49
2.3.7 Ammonia abundance . . . 56
2.4 Discussion . . . 56
2.4.1 Ammonia in the neighbourhood of outbursting systems . . . 56
2.4.2 Is the standard classification scheme reliable for outbursting systems? . . 59
2.5 Conclusions . . . 62

3 H_2O maser observations of FU Orionis and EX Lupi objects 65
3.1 Introduction . . . 65
3.2 Observations . . . 66
3.3 Results . . . 68
3.3.1 Non-detections in the survey . . . 69
3.3.2 FUors . . . 71
3.3.3 EXors – V512 Per (SVS 13A) . . . 74
3.3.4 Serendipitous detections towards Class 0 protostars . . . 75
3.4 Discussion . . . 79
3.4.1 Long-term time variation . . . 79
3.4.2 Scarcity of water masers in selected eruptive systems . . . 80
3.5 Conclusions . . . 82

4 Molecular inventory of the host environment of V1057 Cyg 85
4.1 Introduction . . . 85
4.2 Observations and data reduction . . . 87
4.3 Results and analysis . . . 90
4.3.1 Line detection and identification . . . 90
4.3.2 Line profiles, LSR velocities, and line widths . . . 94
4.3.3 Line mapping . . . 95
4.3.4 Radiative transfer modelling . . . 99

4.3.5 Population diagrams and abundances 104
4.4 Discussion 107
4.4.1 Large- and small-scale structures in the environment of V1057 Cyg . . . 107
4.4.2 Temporal variations in the molecular outflow 108
4.4.3 Brief comparison to other FUors 110
4.4.4 Chemical signatures of outbursts and outlook 114
4.5 Conclusions 116

5 Summary and Future Work **119**
5.1 Summary 119
5.2 Future Work 122

A Appendix of Chapter 3 **125**
A.1 W75N 126

B Appendix of Chapter 4 **127**
B.1 Line detection 128

Bibliography **159**

List of Figures

1.1 Spitzer Space Telescope image of star formation in the Rho Ophiuchi cloud. . . . 2

1.2 Sketch of the star-formation process on various scales. 4

1.3 Schematic diagram of the structure and spatial scales of the disk around a young star. 7

1.4 Diagram depicting the time evolution of accretion rates based on model calculations and the observed phenomena in low-mass stars. 9

1.5 Optical light curves of the first outbursting FU Orionis objects. 11

1.6 Schematic diagram of an FUor system. 12

1.7 Optical colour images of HBC 722, a FUor that went into outburst in the 2010s. . 14

1.8 The historic light curve of EX Lupi, the prototype object of the EXors class. . . . 15

1.9 The structure of an ammonia molecule. 18

1.10 Schematic graph of the stimulated emission process in a maser. 21

1.11 A schematic illustration of the atmospheric window. 23

1.12 The anatomy of a single-dish radio telescope. 25

1.13 Aerial view of the valley showing the Effelsberg 100-meter radio telescope. . . . 26

1.14 The IRAM 30-meter telescope. 28

1.15 The APEX 12-meter telescope. 30

2.1 Examples of the detected ammonia transitions towards young eruptive stars. . . . 38

2.2 H_2 column density and dust temperature maps of RNO 1B/1C and AR 6A/6B . . 47

2.3 H_2 column density and dust temperature maps of FUors/EXors. 51

2.3 Figure 2.3 continued. 52

2.3 Figure 2.3 continued. 53

2.3 Figure 2.3 continued. 54

2.3 Figure 2.3 continued. 55

3.1 Spectrum of the water maser emission detected towards Z CMa. 73

3.2 Spectra of the water maser emission observed in HH 354 IRS. 73
3.3 Water maser spectra toward V512 Per. 75
3.4 Water maser spectra of V512 Per and H_2O(B). 76
3.5 Channel maps of the water maser distribution in H_2O(B) and V512 Per. 77
3.6 Water maser spectra observed in IRAS 00338+6312. 78
3.7 Long-term variations in flux density of detected water masers. 81

4.1 The complete spectrum of V1057 Cyg obtained with the IRAM 30-m telescope. . 92
4.2 Selection of lines detected with the IRAM 30-m telescope. 93
4.3 Integrated intensity maps of molecular lines obtained with the IRAM 30-m telescope. 97
4.3 Figure 4.3 continued. 98
4.3 Figure 4.3 continued. 99
4.4 Integrated intensity maps of ^{12}CO and its isotopologues obtained with APEX. . . 100
4.5 Integrated intensity map of ^{12}CO (3–2) with outflow contours. 101
4.6 Position-velocity diagram of the ^{12}CO (3–2) emission. 102
4.7 Population diagrams of several molecular species. 106

A.1 Spectrum of the water maser emission toward W75N. 126

B.1 Spectra of lines detected towards V1057 Cyg with the 30-m telescope in the 73 GHz tuning. 134
B.1 Figure B.1 continued. 135
B.1 Figure B.1 continued. 136
B.2 Same as Figure B.1 but for the tuning at 80 GHz. 137
B.2 Figure B.2 continued. 138
B.3 Same as Figure B.1 but for the tuning at 90 GHz in the otf mode at the source position. 139
B.3 Figure B.3 continued. 140
B.4 Same as Figure B.1 but for the tuning at 94 GHz. 141
B.4 Figure B.4 continued. 142
B.4 Figure B.4 continued. 143
B.5 Same as Figure B.1 but for the tuning at 133 GHz. 144
B.5 Figure B.5 continued. 145
B.6 Same as Figure B.1 but for the tuning at 141 GHz. 146

B.6 Figure B.6 continued. 147
B.7 Same as Figure B.1 but for the tuning at 202 GHz. 148
B.7 Figure B.7 continued. 149
B.8 Same as Figure B.1 but for the tuning at 210 GHz. 150
B.8 Figure B.8 continued. 151
B.9 Same as Figure B.1 but for the tuning at 242 GHz. 152
B.10 Spectra of lines detected towards V1057 Cyg with the APEX 12-m telescope with nFLASH. 153
B.11 Same as Figure B.10 but for the 227 GHz tuning. 154
B.11 Figure B.11 continued. 155
B.12 Spectra of lines detected towards V1057 Cyg with the APEX 12-m telescope with LAsMA. 155
B.13 Spectra of lines detected towards V1057 Cyg with the APEX 12-m telescope with SEPIA. 155

List of Tables

2.1 Non-detection of ammonia in FUors/EXors. 37

2.2 NH_3 (1,1) line parameters for the FU Orionis-type objects. 39

2.3 NH_3 (1,1) line parameters for the EX Lupi-type objects. 39

2.4 NH_3 (2,2) and (3,3) line parameters for the FU Orionis-type objects. 40

2.5 NH_3 (2,2) and (3,3) line parameters for the EX Lupi-type objects. 43

2.6 Derived parameters for FU Orionis-type objects detected in NH_3 emission. 43

2.7 Derived parameters for EX Lupi-type objects detected in NH_3 emission. 44

2.8 Reference classification of FUors/EXors in the ammonia survey. 46

3.1 Basic information of sources with water maser detection. 69

3.2 Properties of observed water maser features. 70

3.3 List of sources of water maser non-detections. 72

4.1 Information on the IRAM 30-m observations. 88

4.2 Information on the APEX 12-m observations. 90

4.3 Overview of molecules and isotopic species detected towards V1057 Cyg. 94

4.4 Parameters of the best-fit LTE model and population diagram fit of several molecular species. 105

4.5 Properties of each lobe of the outflow of V1057 Cyg determined from the APEX ^{12}CO 3–2 observations. 110

4.6 Overview of molecular species reported in relevant outbursting FUors. 112

A.1 Water maser velocity components of W75N. 126

B.1 Lines detected toward V1057 Cyg with the IRAM 30-m telescope 128

B.1 Table B.1 continued. 129

B.1 Table B.1 continued. 130

B.1 Table B.1 continued. 131

B.1 Table B.1 continued. 132
B.2 Lines detected toward V1057 Cyg with the APEX 12-m telescope. 132
B.2 Table B.2 continued. 133

1

Introduction

" The lives and deaths of the stars seem impossibly remote from human experience. Yet, we are related in the most intimate way to their life cycles. The very matter that makes us up was generated long ago and far away in red giant stars. "
— Carl Sagan – Cosmos: The Shores of the Cosmic Ocean

In this chapter, the main focus is not to give an exhaustive description of the physics of star formation, but to give a main knowledge necessary for understanding the scientific results to be discussed in my Thesis. The reader is encouraged to find further information in the referenced articles and books.

1.1 The Formation of Sun-like Stars

Today, our understanding of the formation of Sun-like stars has expanded significantly, primarily due to the ability to observe nearby star-forming regions. These regions, including Taurus, Orion, Chameleon, Serpens, Aquila, Lupus, and Ophiuchus, are part of the Gould Belt (Herschel, 1847; Gould, 1879), a vast ring of dense molecular clouds and young stars. The Gould Belt spans approximately 1000 pc in diameter and is located at a distance of about 100 to 450 pc. With the advances of large missions such as *Gaia* (Gaia Collaboration et al., 2016) and other surveys, our understanding of the Gould Belt has evolved. The structure is a part of the Radcliffe Wave, a large-scale filament structure of gas and star-forming regions extending over 9000 light-years (e.g., Alves et al., 2020; Inutsuka et al., 2023, and references therein). As an example, Figure1.1 shows Rho Ophiuchi's main cloud called Lynds 1688 imaged by the IRAC instrument on the *Spitzer Space Telescope* (Fazio et al., 2004). In this image, blue represents the 3.6 μm light, green corresponds to 4.5 μm, orange indicates 5.8 μm, and red is 8.0 μm. The colours in this image convey additional information about the evolutionary stages of the stars. The youngest stars, still surrounded by their gaseous and dusty disks (some even with compact nebulae), appear yellowish-red (some prominent example are seen at the centre of this image). In contrast, more evolved stars, which have already dispersed their natal material, are represented as blue-white.

Figure 1.1: Spitzer Space Telescope image of star formation in the Rho Ophiuchi cloud, a nearby star-forming region. The youngest stars, still embedded within and surrounded by their dusty disks, appear as yellowish-red dots, while the more evolved stars, which have cleared their surrounding material, are seen as blueish-white dots. Image credit: NASA/JPL-Caltech/Harvard-Smithsonian CfA (available here).

Molecular clouds (MCs) eventually begin to form stars, however, these clouds are not homogenous or uniform structures: they often contain complex clumps of material and filaments. Initially, these molecular clouds are in equilibrium, though this balance can easily be disrupted. Certain regions of a molecular cloud may start to collapse spontaneously, while others might be influenced by external forces such as cloud collision, shock waves following a supernova explosion, or the strong stellar winds of nearby high-mass stars (see e.g., Stahler & Palla, 2004, and references therein). In these situations, gravity can overcome the resisting forces (which are thermal gas pressure, magnetic fields, and turbulent motions) leading to the formation of contracting *cloud cores* (see Figure 1.2). These cores typically have densities of 10^3–10^4 cm^{-3}, sizes of a few 0.1 pc, and masses of a few solar masses (see e.g., Stahler & Palla, 2004, and references therein). Current theories suggest that many solar-type low-mass stars (less than $2\,M_\odot$) form within these cloud cores. In the following, I will focus on, and summarise the key aspects of low-mass star formation, building upon the foundational works of Shu et al. (1987); Andre et al. (1993); Stahler & Palla (2004); Schulz (2005).

Initially, cloud cores are starless and do not contain any stars. The core is slowly rotating and contracting, and over time becomes gravitationally unstable. The collapse begins at the centre and spreads outwards, a process commonly referred to as the inside-out collapse. At this stage, the material becomes transparent to its own thermal radiation allowing it to efficiently radiate away energy. As the core continues to collapse, it eventually becomes dense enough for infrared radiation to play a significant role in further evolution, and both the temperature and the pressure will rise. This process continues until the collapse slows and stops and at the centre, a so called *first core* forms. This first core is still in equilibrium while it gathers material from its environment. It has a mass of a few hundredths of a solar mass and a size of an astronomical unit (AU). The first core is composed of mainly molecular hydrogen, but the hydrogen molecules will dissociate due to the increasing temperature and mass accretion. Eventually, the first core becomes unstable and collapses rapidly, leading to the formation of a *protostar* about 10 000 years after the initial gravitational collapse. At this stage, the protostar contains ionised hydrogen, has a mass of a few tenth of solar masses, and a size of a few solar radii.

Due to the non-zero angular momentum of the initial cloud core, the surrounding material cannot fall directly onto the central protostar. Instead, it forms a disk-like structure around the protostar (see lower panel of Figure 1.2). The size of a disk is typically comparable to that of the Solar System, usually extending to less than a few hundred AU. Within this disk, material

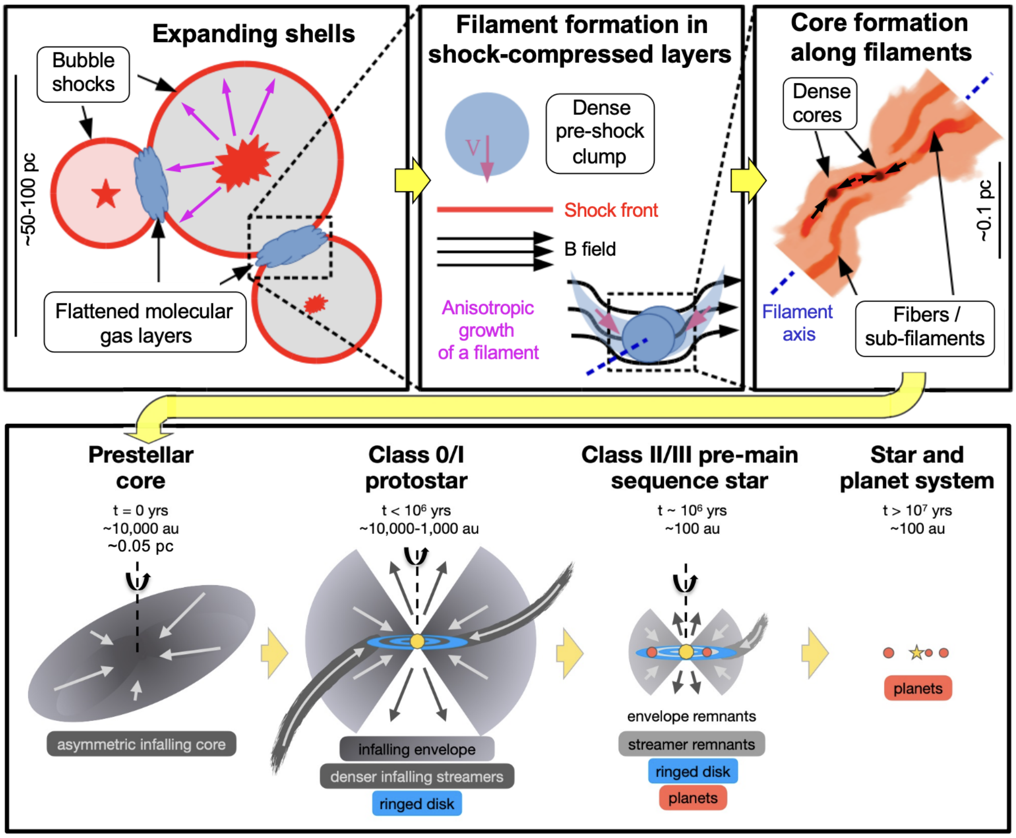

Figure 1.2: Sketch illustrating the star formation process across multiple scales, from dense structures in the interstellar medium to the formation and evolution of stars and planetary systems. Figure from (Pineda et al., 2023).

gradually spirals inward toward the central protostar, continuously feeding it with more material. This stage when the protostar and its accretion disk are still deeply embedded in the surrounding envelope is known as the *Class 0* stage (second panel in Figure 1.2). These Class 0 objects emit far-infrared radiation, which makes them observable in the far-infrared wavelength range. As the protostar accretes material from the disk, some material is expelled from the system via bipolar outflows. These outflows emanate from the poles of the protostar and begin to clear away the envelope. This marks the *Class I* stage and happens in about 100 000 years after the initial gravitational collapse. Objects in this stage are seen in Figure 1.1 as reddish-yellowish dots in the Rho Opchiuchi star forming region. During the Class I stage, the protostar begins deuterium fusion, and later, hydrogen fusion takes over as its primary energy source. These objects are visible in the optical wavelengths and appear at a specific location in the Hertzsprung-Russel diagram, known as the *birthline*. In general, young stars are classified into two groups based on their masses: from a fraction of a solar mass up to $2\,M_\odot$ are known as T Tauri stars, and those with masses ranging from $2\,M_\odot$ to $8\,M_\odot$ are the Herbig Ae/Be stars. Eventually, the accretion rate decreases after the envelope no longer supplies additional material to feed the disk. As the stellar wind begins to blow, the young star disperses most of the remaining material in the disk. This process is slow, but eventually, the disk transitions into something called a passive disk (as opposed to an active disk), where the central star's irradiation becomes the main source of energy. This is the *Class II* stage, and occurs approximately 1 million years after the initial gravitational collapse. During the *Class II* stage, planetesimals may also form. Eventually, within a few million years, the gas and dust content of the disk either disperses or condenses into larger bodies such as planetesimals or planets. This is the *Class III* stage (Figure 1.2). The disk will eventually disperse within a few million years. Any existing planetesimals or planets may trigger a collisional cascade, leading to the formation of a debris disk from the second generation of dust grains. It is important to mention that the classes are based on the spectral energy distribution (SED) slope and not on the physical processes. As a result, they may not accurately reflect the evolutionary stage of young stars, particularly in the case of outbursting YSOs discussed in this Thesis (see, e.g., Quanz et al., 2007b).

For a more detailed description of star formation and its processes, I recommend the foundational work of Stahler & Palla (2004) to any interested reader.

1.2 Observing the Circumstellar Structure around Young Stars

The circumstellar material around young stars typically forms a disk surrounding the central protostar with an envelope extending around the disk. The spectral energy distribution (SED), which is a plot of energy versus frequency or wavelength, of a young star is influenced by the material in its circumstellar environment. The light from the central protostar can be scattered by this surrounding material, illuminating a reflection nebula that is visible in the optical wavelengths, as scattering is more efficient at shorter wavelengths. The dust grains within the circumstellar material emit thermal radiation in the infrared and submillimeter wavelengths, with temperatures ranging from about 10 K to 1000 K (e.g., see Dullemond & Monnier, 2010, and references therein).

It is clear that the material surrounding a young star is diverse in the sense that it consists of different components with varying densities and temperatures. This diversity allows for the collection of data from specific regions of the disk at different wavelengths or frequencies, using various measurement techniques and telescopes. This is illustrated in Figure 1.3 by Dullemond & Monnier (2010). As Figure 1.3 demonstrates, the disk extends from close to the protostar at about 0.1 AU up to 100 AU. The outer regions of the disk can extend from a few ten AU to over a hundred AU while the innermost parts are only a few stellar radii in size, typically a few hundredths of an AU, located close to the central protostar. Due to these substantial size differences between the inner and outer parts of the disk, the various processes occurring within the disk take place on different time scales. In addition to the size differences, there are significant temperature gradients within the disk. For example, the innermost regions typically have temperatures around 1000 K while moving outwards, the temperature decreases to about 10 K or even lower in the outer regions. Observations at longer wavelengths, such as far-infrared and millimeter ranges, allow us to study the outer regions of the disk, covering scales from approximately 10 AU to a few hundred AU. The mid-infrared range provides insight into the inner regions on scales of few tens of AU to a few AU. The shorter wavelengths give us information of the innermost regions of the disk on scales of only a few AU to the central star. In these inner regions, we can observe the flow of material from the disk onto the star through accretion. Finally, optical and ultraviolet observations offer insights about the central protostar itself (Dullemond & Monnier, 2010).

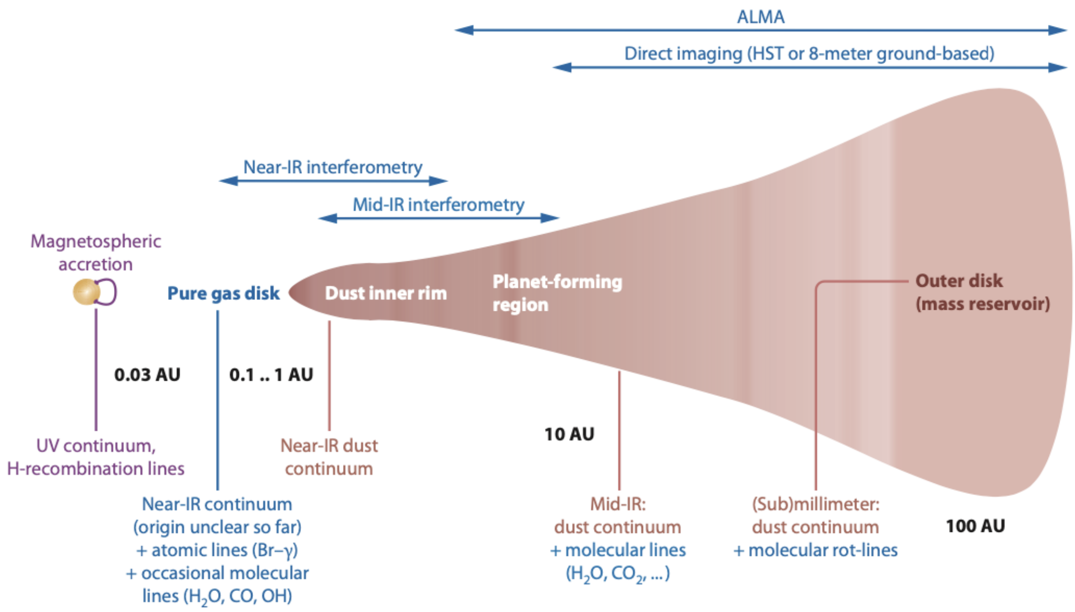

Figure 1.3: Schematic diagram of the structure and spatial scales of the disk around a young star, as presented by Dullemond & Monnier (2010). The different regions of the disk are observable at various wavelengths using a range of telescopes, both ground-based and space-based, as indicated above the pictogram. Figure from Dullemond & Monnier (2010).

1.3 Variations in Light and Accretion

Accretion refers to the process in which particles accumulate onto an object, typically in the form of gas, within an accretion disk, playing a crucial role in both star formation and evolution. The material falling onto the central star does happen in a non-uniform rate, with the accretion rate fluctuating over time (for accretion rate calculations see, e.g., Natta et al., 2006, and references therein). Sometimes more material is being accreted onto the central protostar, and at other times less. As a consequence of stronger accretion flow, more energy is released, causing the star to appear brighter (see the recent review of Fischer et al., 2023, and references therein). These fluctuations and instabilities of the accretion process can be observed on human timescales with light variations which can be categorised into annual, monthly, daily, but even hourly intervals. There are two primary classes of objects that exhibit extreme light variations: the FU Orionis- and the EX Lupi-type objects (see the recent review of Fischer et al., 2023, and references therein). The common characteristic of both types is that their outbursts are driven by the enhanced accretion from the circumstellar disk onto the protostar (Bell et al., 1995; Hartmann & Kenyon, 1996; Fischer et al., 2023).

Episodic accretion is a process in which the typical accretion rate, experiences a significant increase due to an influx of material from the envelope to the disk or from the disk to the star, leading to instability that channels additional matter onto the protostar. This increased material flow cause the accretion rate and luminosity to increase by an order of magnitude or more over a short period of time (e.g., Fischer et al., 2023). Episodic accretion events can lead to a significant growth in the mass of the protostar. For instance, during an FU Orionis-type outburst, the bolometric luminosity of the star can reach between $100\,L_\odot$ and $300\,L_\odot$, while the accretion rate can rise from a typical T Tauri star of 10^{-9}–$10^{-7}\,M_\odot\,yr^{-1}$ up to 10^{-5}–$10^{-4}\,M_\odot\,yr^{-1}$ (Hartmann & Kenyon, 1996). Because of the enhanced accretion, the temperature of the disk becomes high enough to radiate energy in the optical wavelengths, making it visible. As a result, FU Orionis objects serve as observable examples of episodic accretion. Figure 1.4 illustrates the variation of the accretion during the early stages of stellar evolution. This schematic diagram by Schulz (2005) shows the time development of accretion rates, based on calculations that relate to the observed phenomena in low-mass star formation. The dotted horizontal line corresponds to the standard star formation model (Shu et al., 1987), the hatched curve shows the results of more realistic calculations, and the solid thick curve highlights the additional features during accretion processes, such as the FU Orionis and the EX Lupi-type outbursts, and the normal or quiescent T Tauri disk accretion phase (Hartmann, 2001; Schulz, 2005). Since those earlier works, more recent studies have introduced models that focus on episodic accretion (see, e.g., Offner & McKee, 2011; Dunham & Vorobyov, 2012).

In the context of accretion variability it is important to mention the 'luminosity problem', originally referring to the discrepancy that protostars are statistically under-luminous (1 $L_\odot$, e.g., Kenyon et al., 1990), compared to the expectations (50 $L_\odot$, see also Fischer et al., 2023) based on accretion models (e.g., Kenyon & Hartmann, 1995). To address this issue, the FU Orionis- and EX Lupi-type objects undergoing episodic accretion bursts were considered. The core idea is based on the observed phenomena that accretion is not continuous but occurs in bursts, during which the luminosity can rise dramatically (up to 100 $L_\odot$), contributing for most of the star's mass growth (e.g., Hartmann & Kenyon, 1996; Audard et al., 2014). The problem has been revisited with extensive observational data (e.g., Dunham et al., 2013) further suggesting that all or most stars undergo episodic accretion events and highlights that other accretion scenarios and histories may further solve the problem (see, e.g., Vorobyov & Basu, 2005, 2006, 2010; Offner & McKee, 2011; Dalba & Stahler, 2012; Dunham et al., 2013, and references therein).

Accretion variability in eruptive YSOs is thought to be driven by a combination of physical mechanisms within their circumstellar disk. These include gravitational instabilities (GI), which can develop in cool, massive disks and lead to fragmentation or enhanced angular momentum transport, and thermal instabilities (TI), triggered by changes in disk opacity and ionization that cause localized heating and elevated accretion rates (see, e.g., Fischer et al., 2023, and references within). These mechanisms are not only central to explaining episodic accretion events observed in FUors and EXors, but also fundamental in planet formation models, as they affect disk structure and evolution, dust growth, and the emergence of gaps and rings (see, e.g., Bell et al., 1995; Armitage et al., 2001; Zhu et al., 2009; Audard et al., 2014; Fischer et al., 2023, and references therein).

In the following, I will introduce the FU Orionis- and EX Lupi-type objects and summarise their key characteristics in preparation for the upcoming chapters of my thesis.

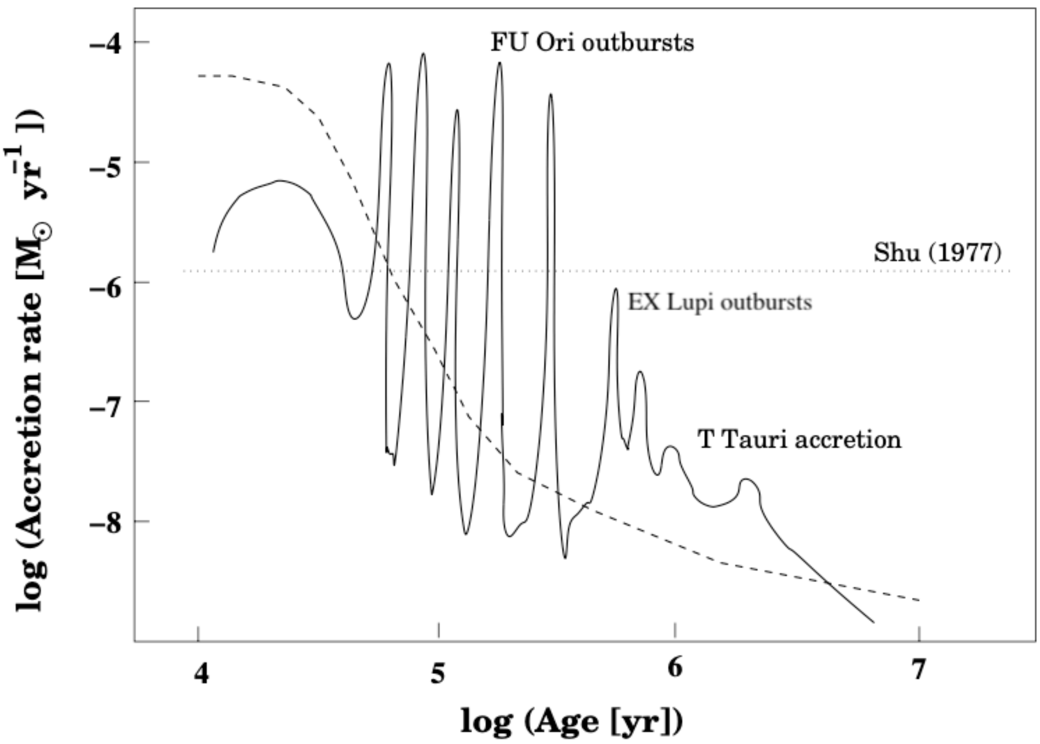

Figure 1.4: Schematic diagram from Schulz (2005) illustrating the time evolution of accretion rates based on calculations related to the observed phenomena in low-mass stars. The dotted straight line represents the standard star formation model (which assumes a time-independent process, with the star's radius and mass being infinitely large, resulting in a flat line throughout the entire time interval Shu et al., 1987). The hatched curve is the results of more realistic calculations (Schulz, 2005, and references therein). The solid thick line highlights additional features in the accretion processes, such as FU Orionis- and EX Lupi-type outbursts, as well as the normal T Tauri disk accretion phase (Hartmann, 2001; Schulz, 2005).

1.4 The FU Orionis-type Objects

The FU Orionis class, commonly referred to as FUors, bears the name of its protoype star, FU Orionis. In 1936, FU Orionis started its outburst, reaching maximum brightness in February 1937 and appearing in the dark nebula of B35 in the Orion star forming region (Wachmann, 1954). Prior to its outburst, the object had a magnitude of around 16.4 to 15.3 mag, but it brightened by approximately 5 magnitudes within a year, and its brightness still remains above 11 magnitudes since its discovery. Initially, it was speculated that the object had either emerged from a previously obscuring nebula or that it was a slow nova-type outburst. However, both hypotheses were ruled out by Herbig (1966), who proposed that the brightening of FU Orionis represented a new type of phenomena in the early stages of stellar evolution. In the 1970s, two additional objects, V1057 Cyg and V1515 Cyg, exhibited similar characteristics to FU Ori. As a result, Herbig (1977) defined this group of objects as FU Orionis-type objects, or FUors, which are young stellar objects (YSOs). Figure 1.5 shows the optical (*B*-band) light curves of the first three FUors, where the x-axis represents the time since the start of the outburst and the y-axis shows the brightness in the *B*-band. The original light curves (black points) were presented by Hartmann & Kenyon (1996) and have more recently been updated (red points) by Szabó et al. (2021) and Szabó et al. (2022) for V1057 Cyg and V1515 Cyg, and by Lykou et al. (2022) for FU Ori. V1057 Cyg and V1515 Cyg together with the later discovered V1735 Cyg (Elias, 1978) are often referred to as classical FUors.

Figure 1.6 shows a schematic picture of an FUor system described by Hartmann & Kenyon (1996). In this diagram, a young low-mass protostar is surrounded by an accretion disk, from which the central star is accreting material at a typical accretion rate for a typical T Tauri star, ranging from 10^{-9} to $10^{-7}\,M_\odot\,yr^{-1}$. The generally low accretion rate can temporarily increase by more than an order of magnitude during outbursts, reaching accretion rates as high as 10^{-5}–$10^{-4}\,M_\odot\,yr^{-1}$. During an outburst, the disk becomes hot enough to emit in the optical wavelengths, and the central protostar can accumulate about $0.01 M_\odot$ of mass over a century-long outburst (Hartmann & Kenyon, 1996). During the outburst, high-velocity winds are generated, reaching speeds of hundreds of $km\,s^{-1}$ (see e.g., the case of V1057 Cyg, Szabó et al., 2021), carrying away roughly 10% of the accreted material. Meanwhile, the protostellar envelope continues to supply the disk with additional material, either to sustain the ongoing outburst or to replenish the disk with more material for the next event (Hartmann & Kenyon, 1996).

As of this writing, there are over a dozen known FUors, with their numbers continuing to

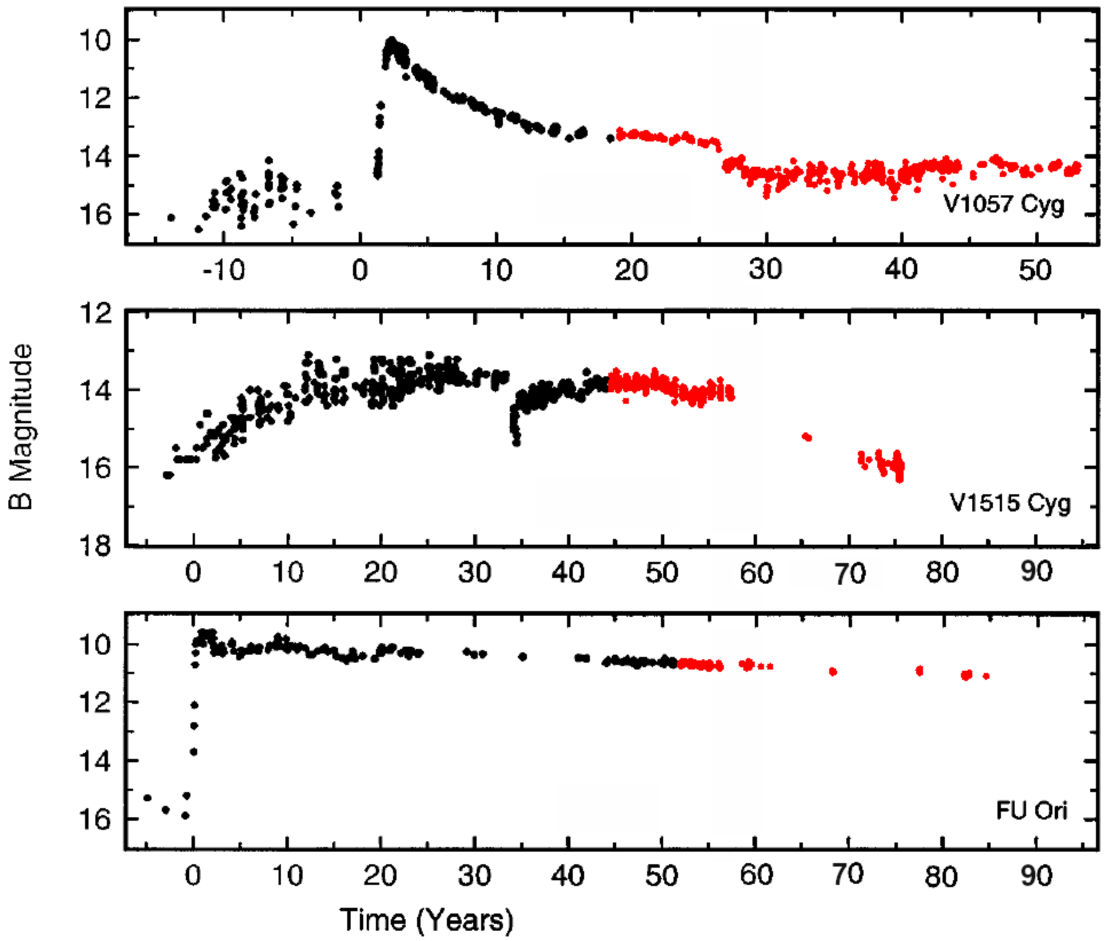

Figure 1.5: Optical (*B*-band) light curves of the first few outbursting FUors, including the prototype star, FU Ori (third panel from the top). The black points are from Hartmann & Kenyon (1996) for all objects, where x-axis shows time since the outburst. The light curves were recently updated by Szabó et al. (2021, 2022); Lykou et al. (2022), respectively shown in red. This figure was remade for a conference talk by Ágnes Kóspál.

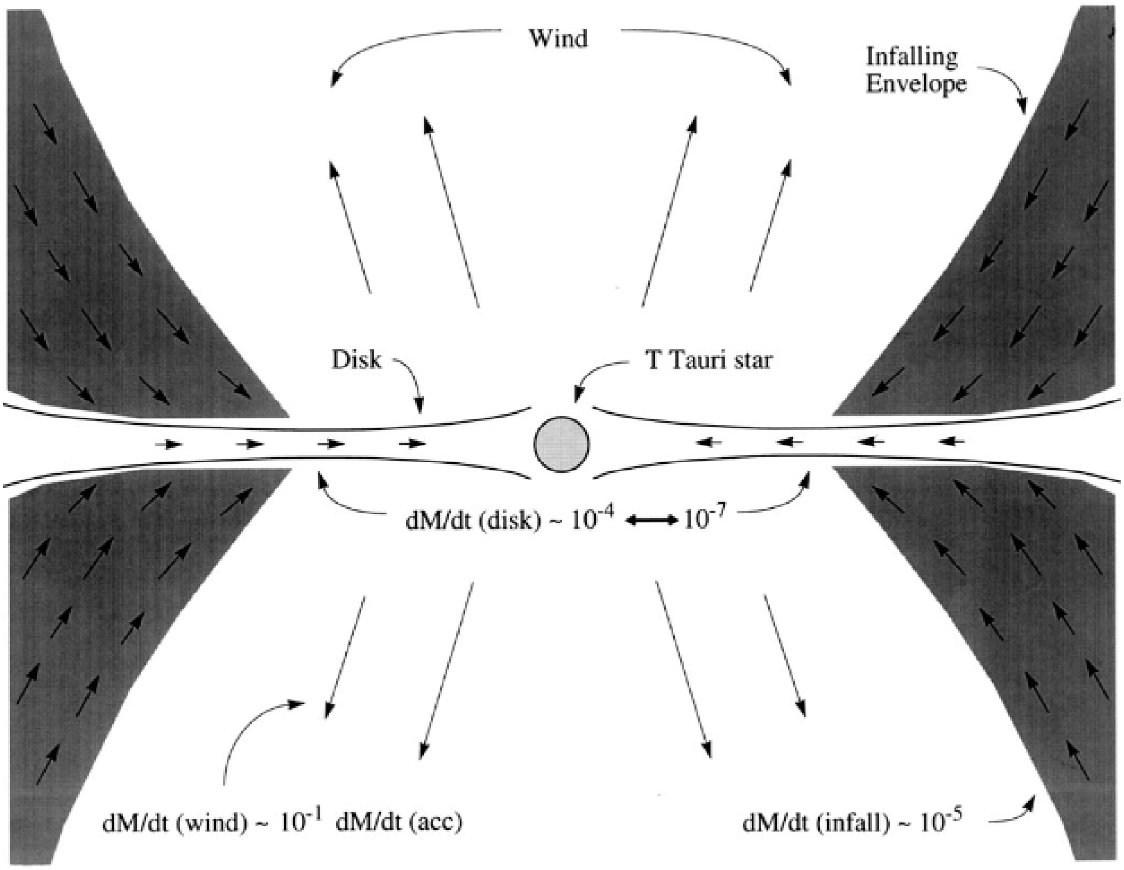

Figure 1.6: A schematic diagram of a FUor system from Hartmann & Kenyon (1996). The material flows inwards in the disk, feeding the protostar, while material from the protostellar envelope provides additional material to sustain the enhanced accretion during the outburst and to replenish the disk between events. Some of the accreted material is expelled form the system via high-velocity winds in the disk. Figure from Hartmann & Kenyon (1996).

grow thanks to space telescopes like *Gaia* (e.g., Hillenbrand et al., 2018; Szegedi-Elek et al., 2020; Nagy et al., 2023, and references therein). With the increasing number of FUors, their light curves exhibit a wide variety of behaviours, including differences in rise time to peak brightness, duration of peak brightness, and decay from the peak brightness. However, FUors are known to undergo rapid, multi-magnitude increases in brightness at optical and near-infrared wavelengths, known to result from a sudden increase in the accretion flow from the disk onto the protostar. This process can last for several decades, possibly centuries (e.g., Paczynski, 1976; Lin & Papaloizou, 1985; Kenyon et al., 1988; Kenyon & Hartmann, 1991; Bell et al., 1995; Turner et al., 1997; Audard et al., 2014; Kadam et al., 2020; Borchert et al., 2021; Hillenbrand & Rodriguez, 2022; Fischer et al., 2023, latter for the most recent review). FUors are commonly found in star-forming regions and often illuminate surrounding reflection nebulae. Figure 1.7 present colour images of HBC 722 (also known as V2493 Cyg) before and after its outburst (Semkov et al., 2019). The spectroscopic features of FUors during outbursts are typically attributed to viscous heating in the accretion disk (the disk is heated by viscosity, which converts angular momentum into thermal energy; see e.g., Bai, 2011; Labdon et al., 2021), which dominates their spectrum and their spectral types differ with wavelength. In the optical wavelengths, FUors exhibit characteristics of spectral types of F/G supergiants, with broad blueshifted absorption lines that indicate strong and, in some cases, variable winds. These features include P Cygni profile of Hα, and strong Li absorption of the 6707 Å line (Hartmann & Kenyon, 1996; Herbig et al., 2003). In contrast, in the near-infrared wavelengths, FUors resemble K/M giants or supergiants, with weak metal absorption (for example iron), as well as absorption lines from water (H_2O), titanium (TiO), and strong CO bandhead absorption (Connelley & Reipurth, 2018). In the ultraviolet, their spectrum shows characteristics of supergiants (Kravtsova et al., 2007). A rare pre-outburst spectrum of V1057 Cyg reveals characteristics of a T Tauri star, suggesting that the precursors of FUors are likely T Tauri stars undergoing episodic accretion events (e.g., Herbig, 1977). V1057 Cyg has been in outburst for over 50 years and still does not exhibit the spectroscopic characteristics typical of those observed in T Tauri stars (e.g., Herbig et al., 2003; Szabó et al., 2021).

1.5 The EX Lupi-type Objects

There is another type of young stars that can exhibit similar eruptions in magnitude but with shorter durations: these are known as EX Lupi-type object, or briefly (and hereafter) *EXors*. The characterisation of EXors is largely based on the prototype object, EX Lupi, and often compared

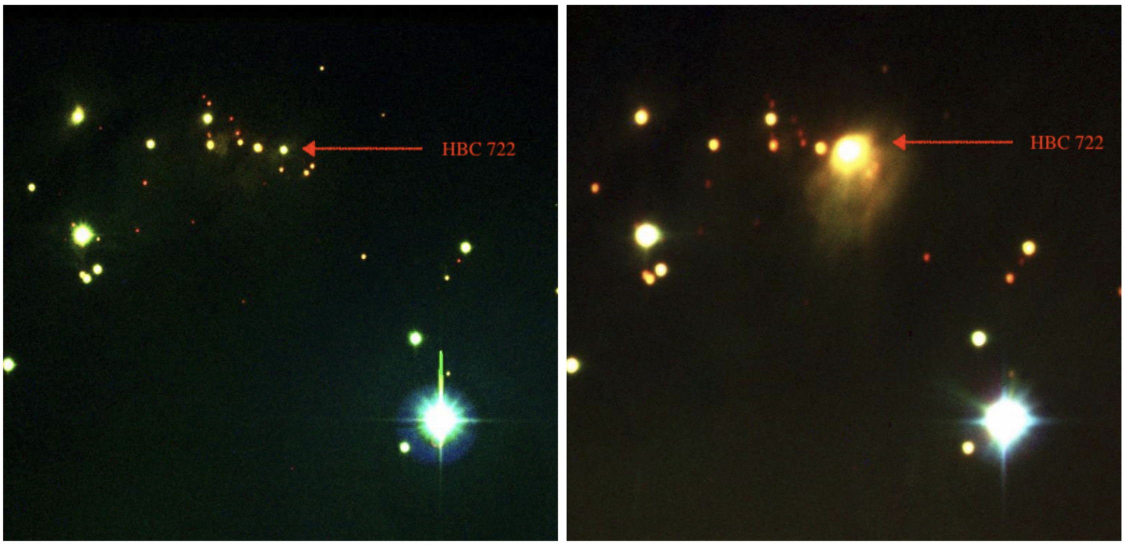

Figure 1.7: Optical colour images of HBC 722, a FUor that went into outburst in 2010, depicting the object before (2007) and after (2013) the outburst, as seen in the left and right panels, respectively. Figure from Semkov et al. (2019).

with FUors, where classical FUors helped define the characterisation scheme (e.g., Herbig, 1977). EXors are distinguished by repeated, short-duration outbursts. In their quiescent state, their spectral type is similar to that of M dwarfs, and they do not exhibit the spectroscopic features typical of outbursting FUors. One advantage of studying EXors is that due to the shorter duration of their outbursts, we have the opportunity to observe them in their quiescent state between eruptions, as these bursts are recurrent (Fischer et al., 2023). These quiescent states have allowed to, for example, directly observe silicate crystallisation in EX Lupi when its famous 2008 outburst happened (Kóspál et al., 2008; Aspin et al., 2010; Juhász et al., 2012). In comparison to FUors, the number of known EXors has not increased as rapidly (Herbig, 1989; Audard et al., 2014), although new sources have been identified in the past five years, thanks to *Gaia* (e.g., Hodapp et al., 2019; Cruz-Sáenz de Miera et al., 2022a; Park et al., 2022). Generally, photometric observations of EXors before and after smaller amplitude bursts ($\sim$1 magnitude variations) and larger outbursts ($\sim$2 magnitude, such as the 2008 outburst of EX Lupi, e.g., Kóspál et al., 2008) show their brightness tends to increase by a few orders of magnitude for a period of a few months (Coffey et al., 2004; Audard et al., 2010; Cruz-Sáenz de Miera et al., 2023a). Figure 1.8 shows the historic light curve of EX Lupi with observational data, showing smaller bursts and larger outbursts (such as its famous 2008 eruption). The first outburst of this source dates back to the late 1930s with the most recent burst recorded in 2022 (Wang et al., 2023).

The bolometric luminosity of EXors during outbursts typically increases from around 1–2 $L_\odot$

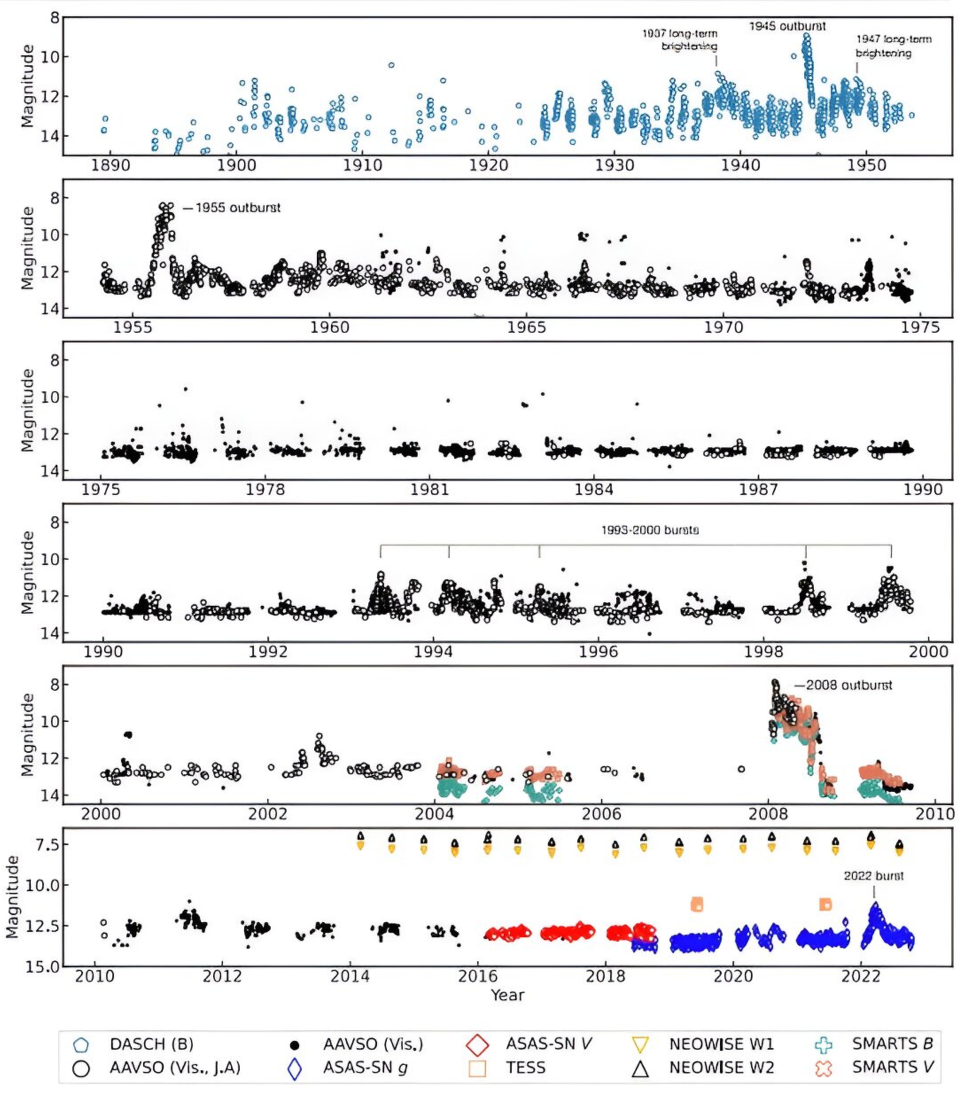

Figure 1.8: The historic light curve of EX Lupi, the prototype object of the EXors class, multiple smaller amplitude bursts and larger outbursts. Figure from Wang et al. (2023).

to several tens of $L_\odot$ (e.g., Lorenzetti et al., 2006; Sipos et al., 2009; Audard et al., 2010, 2014; Cruz-Sáenz de Miera et al., 2023a). In post-outburst, data are generally less available, likely because the sources become faint, making observations more challenging (e.g., more telescope time is needed for faint sources). This lack of data can make it difficult to precisely determine the length and frequency of the bursts. Luckily, sources such as EX Lupi (see Figure 1.8) are bright enough for monitoring even in quiescence, allowing studies in the quiescent states. The burst of a given EXor can typically recur every few years, with durations of 1–2 years (e.g., Herbig, 2008, and references therein).

In their quiescent state or in between bursts, EXors exhibit characteristics of K or M dwarfs, with absorption lines (Herbig, 2008). Signs of infall and outflow are observed through Na I D lines, similar to FUors and T Tauri stars (Lorenzetti et al., 2009). In the near-infrared, EXors typically show atomic lines, hydrogen recombination lines, and CO absorption bandhead features (e.g., Lorenzetti et al., 2009; Cruz-Sáenz de Miera et al., 2023a).

1.6 Intermediate or Hybrid Eruptive Stars

The past two decades has led to an increase in the number of eruptive stars observed. However, as is often the case in science, the situation is not black and white, and it has been shown that not all eruptive stars can be easily categorised as either FUors or EXors, and each system may exhibit unique characteristics. For example, some candidates fit the spectroscopic criteria for FUors (e.g., Herbig et al., 2003; Connelley & Reipurth, 2018), but they lack the dramatic increase in brightness that originally made these sources so distinguishable. Objects like, for example, V2775 Ori or HBC 722, both show spectroscopic characteristics of FUor, but their peak luminosity only reached $\sim$12 $L_\odot$ and $\sim$51 $L_\odot$, respectively (see, e.g., Miller et al., 2011; Fischer et al., 2012, 2023). Interestingly, sources like OO Ser and V1647 Ori have exhibited outbursts with timescales intermediate between FUor and EXor events. The outburst of OO Ser lasted about 8 years, which is longer than the typical EXor outbursts but much shorter than a typical FUor outburst, while V1647 Ori has already undergone two outbursts since 2004 (Hodapp et al., 1996, 2012; Aspin & Reipurth, 2009). Furthermore, it is worth nothing that accretion in young stars is variable across all timescales, from days to months to years, particularly on the rotational timescales (1–10 days, see, e.g., Herbst et al., 2007; Costigan et al., 2014).

1.7 Chemical Tracers

In the following, I summarise the key chemical tracers I've used for my surveys, which serve as powerful tools for probing different physical scales around YSOs. Ammonia is an effective tracer of the large-scale environment, capturing emission from the cold, dense environments surrounding these young stars. On smaller scales, water masers provide valuable insight into the extreme conditions within the inner regions, including the accretion disk, where dynamic processes such as infall and outflow are actively playing a role in the evolution of the targeted YSOs.

1.7.1 Ammonia as a Tracer of Dense Cores around Young Stars

Ammonia (NH_3) is a key tracer of dense cores in star-forming regions, widely used to probe temperatures and column densities in interstellar gas, dense cores, and low-mass star-forming regions (e.g., Walmsley & Ungerechts, 1983; Ungerechts & Guesten, 1984; Tafalla et al., 2004). As a molecular thermometer, ammonia provides valuable insights into these environments. It was first detected in space by Cheung et al. (1968), who observed its inversion transition at 23.6 GHz in emission towards the Galactic centre. The detection of ammonia, a molecule already well-known on Earth, marked a significant advancement in molecular astronomy.

The structure of ammonia is depicted in Figure 1.9, where the schematic illustration depicts three hydrogen atoms bounded to a single nitrogen atom. Ammonia molecules can exist in two distinct states: para and ortho states, which differ based on the alignment of the spins of the hydrogen atoms. In the ortho state, the three hydrogen nuclei have parallel spins, giving a total nuclear spin of $3/2$. The ortho state is important for understanding the excitation of ammonia molecules in hot regions of space, including young stars with protoplanetary disks, where higher temperatures promote the population of ortho states. These molecules are excited and observed in rotational transitions with odd J values, for example $J = 1, 3, 5$. On the other hand, in the para state, the hydrogen nuclei have anti-parallel spins, giving a total nuclear spin of $1/2$. The para state of ammonia is typically more stable at lower temperatures (e.g., in cold molecular clouds), and is usually observed in rotational transitions with even J values, for example $J = 0, 2, 4$ (e.g., Watson, 1976; Ho & Townes, 1983).

The rotational energy levels are defined by the quantum numbers J and K, where J is the total angular momentum, and K is its projection along the molecular symmetry axis. During the inversion transition of the ammonia molecule (J, K), the nitrogen atom passes through the plane

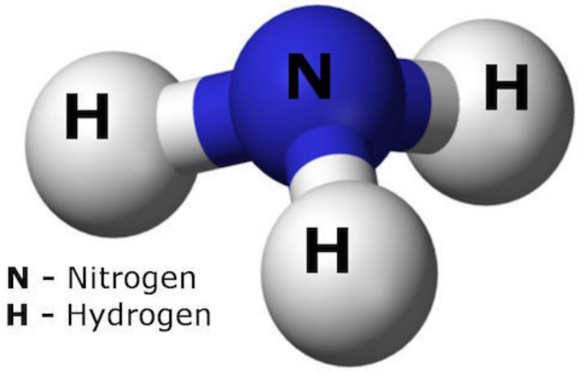

Figure 1.9: The structure of an ammonia molecule: three hydrogen (H) atoms are bound to a single nitrogen (N) atom. The figure is available here.

formed by the three hydrogen atoms bound to it. While the quantum numbers remain unchanged, this transition causes the spectral line to split into five groups: one main group and four minor ones. These groups can further split due to spin-spin interactions between the hydrogen atoms, resulting in a total of eighteen components (e.g., Ho & Townes, 1983; Walmsley & Ungerechts, 1983). The optical depth (τ, which describes how far light can travel through a partially transparent medium) can be obtained from the intensity ratios of the inversion transitions. Similarly, the rotational temperature ($T_{\rm rot}$), which reflects the temperature at which the population of excited rotational energy levels becomes significant, can be determined using the intensity ratios of inversion transitions between different rotational states of the molecules. The most commonly detected transitions are those of NH_3 (1,1), (2,2), (3,3), and higher transitions (e.g., Ho & Townes, 1983; Walmsley & Ungerechts, 1983; Ungerechts & Guesten, 1984, and references therein). By analysing the inversion transitions, it is possible to estimate the temperature and column density, which represents the number of atoms or molecules per square centimetre (cm^2) along the line of sight in a given direction. For my research, I have followed the methodology outlined in Ho & Townes (1983), whose work provides a detailed description of the techniques. In the following Chapter, I will highlight only the relevant technical details applied to my research.

The evolution of young eruptive stars begins in their dense cores, essentially their birthplaces. While we have detailed information on FUors and EXors at optical and near-infrared wavelengths, there is very limited data available on their natal environments in the radio regime. Pioneering studies have shown that more evolved young stellar objects (YSOs), such as T Tauri stars (which are thought to be closest in evolutionary stage to young eruptive stars) and Herbig Ae/Be stars (the intermediate mass counterparts of T Tauri stars, Waters & Waelkens, 1998) are often still associated with their dense cores, which can be traced by the ammonia inversion transitions of the (1,1), (2,2), and (3,3) emission (e.g., Ho & Townes, 1983; Jijina et al., 1999). Although the evolution of young eruptive stars similarly starts in their dense cores, no systematic survey has yet been conducted to gather more information about this early phase. One of the goals of my research was to perform observations of the ammonia (1,1), (2,2), and (3,3) transitions, aiming to create a comprehensive survey of the host environments of FUors and EXors.

1.7.2 Water Masers as Indicators of Star Formation

1.7.2.1 Maser Emission in Astrophysics

Maser is an acronym that stands for microwave amplification by stimulated emission of radiation (MASER). Maser emission plays a crucial role in astrophysics, particularly in probing small-scale structures and dynamics in various cosmic environments. The emission arises in highly energetic regions, where conditions like high densities and temperatures enable the amplification of specific microwave wavelengths through a process similar to the operation of lasers (LASER as the acronym for light amplification by stimulated emission of radiation) in the optical wavelengths. In cosmic settings, maser emission is commonly observed in molecular clouds, star-forming regions (including low- and high-mass star-forming regions), and the surroundings of compact objects like active galactic nuclei (AGN) and supernova remnants (e.g., Gray, 2012, and references therein). Notable examples for masers include hydroxyl (OH), water (H_2O), and methanol (CH_3OH) masers, which have been detected in various galactic and extragalactic environments. Maser sources serve as valuable probes of small-scale physical processes due to their high luminosity and directional emission properties, allowing us to resolve small-scale structures and measure velocities in regions where other observational techniques may be insufficient. For example, in the circumstellar environment of YSOs and evolved stars, masers can trace the motion of gas in accretion disks or outflows with high precision. In the cores of active star-forming regions, masers can provide insights into the dynamics of the interstellar medium (ISM), including the kinematics of molecular gas (e.g., Gray, 2012, and references therein). Additionally, maser emission of water in galaxies can measure proper motions and distances, further correcting the determination of the Hubble constant and cosmological parameters (e.g., Reid et al., 2009). The high spatial resolution observations of masers with interferometric techniques like Very Long Baseline Interferometry (VLBI), can allow the study of small-scale structures and velocities in regions as small as a few astronomical units, making masers extremely valuable tools for probing dynamical behaviours of compact systems (e.g., Greenhill et al., 1995; Peck & Taylor, 2001).

Water masers (H_2O masers) are a crucial tool for probing the physical conditions and dynamics in both low- and high-mass star-forming regions. These masers, which emit at the 22.2 GHz (or 1.35 cm) transition of the H_2O molecule, are typically associated with low- and high-mass YSOs (e.g., Gray, 2012, and references therein). The study of water masers in such regions provides valuable insight into the processes of mass accretion, outflow dynamics, and the structure of circumstellar environments. For my research, I focused on water masers in low-mass star-forming regions, and the following material is centred on these types of environments. The study of astrophysical masers is a relatively young field of science, with the first cosmic masers discovered in the mid-1960s. For a thorough overview of the subject, I recommend the reader Malcolm Gray's book "Maser Sources in Astrophysics" (Gray, 2012) which I often refer to.

1.7.2.2 Formation and Excitation Mechanisms of Water Masers

The pumping mechanism of water masers involves a combination of collisional excitation, radiative pumping, and, in some cases, additional processes like magnetic fields or shock interactions (Gray, 2012). Water masers are typically observed in high-density regions, such as star-forming regions (low- and high-mass), the envelopes of evolved stars, and the environments around AGNs (Gray, 2012).

Collisional excitation can occur in dense regions, where the water molecules can be excited to higher energy states via collisions with, for example, electrons or nearby molecules (e.g., with H_2). The collisions transfer energy to the water molecules, promoting them from their ground state to higher rotational and vibrational levels. This excitation is particularly important in molecular clouds or near the hot gas in the vicinity of young stars or supernova remnants, where high densities and temperatures allow frequent collisions to occur (Goldsmith & Langer, 1999; Neufeld & Melnick, 1991; Gray, 2012). *Radiative excitation* (or pumping by infrared radiation) occurs when water molecules are excited by absorbing infrared radiation from nearby hot stars or from the thermal emission of warm dust. This form of excitation is important in the envelopes of evolved stars or close to AGNs, where intense ultraviolet and infrared radiation fields are present (Gray, 2012). The photons excite the water molecules to a higher energy state, which can undergo spontaneous or stimulated emission when they return to lower energy levels. This pumping mechanisms can occur in regions with strong radiation fields, such as dense gas around YSO and accretion disks (Gray, 2012, and references therein). For maser emission to occur, *population inversion* must take place, which occurs when there are more water molecules in excited states (higher energy) than in the ground (lower energy) state. See Figure 1.10 for a schematic graph showing the stimulated emission process. When the inversion is created, water molecules in excited states can be stimulated to emit coherent radiation, leading to the amplification of specific microwave wavelengths. The stimulated emission process results in the characteristic narrow-line maser emission observed in astrophysical settings (Gray, 2012). The efficiency of the maser depends on the relative balance between the collisional excitation, radiative pumping, the density of the gas, and the physical conditions in the environment (Neufeld & Melnick, 1991; Gray, 2012).

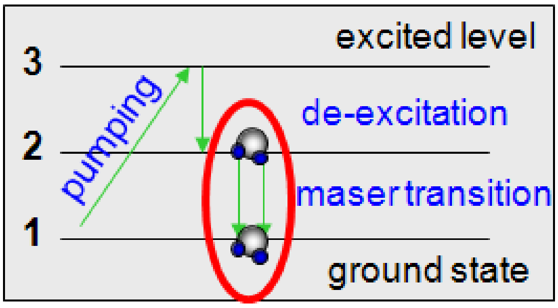

Figure 1.10: A schematic graph showing the stimulated emission process: the molecule is excited and then decays non-radiatively to a metastable state, creating a population inversion. An incoming photon of the same frequency stimulates the emission of a second photon with the same frequency, phase and direction. Both are emitted simultaneously, thus amplifying the incident radiation field. The figure is available here.

The rotational transitions involved in water maser emission typically fall in the microwave to millimeter wavelength range, with the most commonly observed transition being at 22.2 GHz ($J_{K_a K_c} = 6_{16} - 5_{23}$; e.g., Gray, 2012, and references therein). In particular, the interaction of stellar outflows with the surrounding molecular cloud creates shock fronts where the temperature can increase up to thousands of Kelvin, providing conditions ideal for exciting water molecules to higher rotational states (Hollenbach & McKee, 1989; Gray, 2012). Radiative pumping from the central YSO or nearby hot regions can also play a significant role in exciting water molecules in lower-density regions surrounding the outflows (Neufeld & Melnick, 1991; Gray, 2012). This combination of shock and radiative excitation mechanisms allows maser emission to occur in environments where the gas is dense and sufficiently warm.

1.8 Telescopes and Instruments Utilised in This Thesis

My research is primarily observational, and to obtain the necessary data on FUors and EXors, I have utilised various telescopes and facilities. Below, I provide an overview of these instruments and observatories. Since this thesis contains data only from single-dish telescopes, first I will give the basics of single-dish radio astronomy.

1.8.1 Introduction to Single-Dish Radio Astronomy

Observing in certain wavelength regimes can be quite challenging, as not all parts of the electromagnetic (EM) spectrum are able to pass through Earth's atmosphere. Figure 1.11 illustrates the varying opacity of the atmosphere to different types of radiation. One way to emphasise this issue, is the reader imagines the atmosphere as a curtain with varying-sized holes, made up of molecules such as water vapour (H_2O), carbon dioxide (CO_2), ozone (O_3), and others. The areas of the curtain that are intact (where the atmosphere absorbs radiation) are referred to as "absorption bands", while the gaps in the curtain represent the "atmospheric windows" through which certain wavelengths can pass through to us. Following this analogy, the Earth's atmosphere completely blocks gamma rays, X-rays, and ultraviolet light, making it impossible to observe these wavelengths from the ground. To observe these parts of the spectrum, space telescopes are required, though they are highly costly to build. Additionally, the atmosphere absorbs much of the infrared and long-wavelength radio emissions, further restricting ground-based observations. The optical, near-infrared, radio, and submillimeter regimes are observable using ground-based telescopes. However, the submillimeter regime is particularly affected by atmospheric absorption, especially from water vapour. In order to avoid this issue, ground-based telescopes observing in the submillimeter range must be located at high altitudes and in dry environments. One of the best locations for such observations is the Atacama Desert in Chile, where the telescopes lie at an altitude of 5000 meters.

The electromagnetic (EM) spectrum within the radio range spans a broad range of frequencies, leading to considerable variation in the shape, size, design, and configuration of the antennas used to observe these wavelengths, especially when multiple antennas are employed. For example, in the 10–100 MHz (or 30 m–3 m) wavelength range, antennas similar to TV antennas, with movable focal points, are typically used. Due to the long wavelengths in this regime, the reflector surface can be relatively coarse. A good example of such a system is the LOw-Frequency ARray (LOFAR van Haarlem et al., 2013) antennas (e.g., Wilson et al., 2009, and references therein). For shorter wavelengths, classic parabolic "dish" antennas are employed. According to diffraction theory, the angular resolution of a telescope is determined by the ratio of the wavelength (λ) to the diameter of the dish (D; e.g., Wilson et al., 2009). This relationship dictates the physical size of the antenna

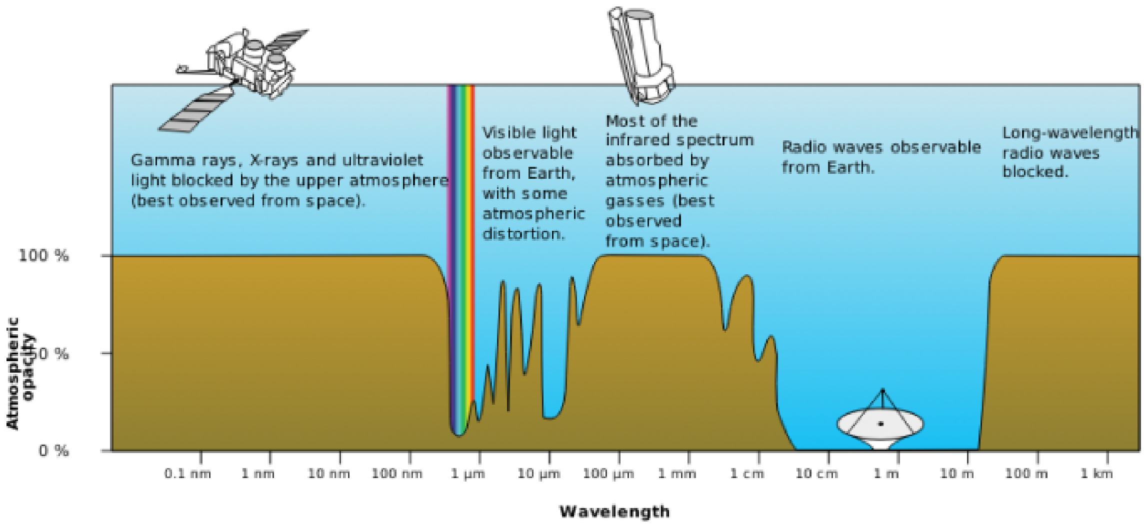

Figure 1.11: Schematic figure of the atmospheric window illustrating how opaque the Earth's atmosphere is to radiation at different wavelengths. Image credit: NASA/Public domain, taken from Wikipedia (available here).

required to achieve a desired resolution. For radio telescopes operating in the 100 MHz to 1 GHz range (wavelengths between 3 m and 30 cm), antennas can go over 100-m in diameter (e.g., the Arecibo Observatory). For wavelengths shorter than this, telescopes with diameters from a few meters up to around 90-m are used, such as the APEX telescope.

The radio telescopes relevant to my research are steerable parabolic reflectors, so in this Thesis I will focus only on this type of telescope. Figure 1.12 illustrates how a single-dish radio telescope observes radio waves. The most common design features a curved dish that reflects radio waves to a focal point. In this illustration, incoming radio waves from a distant radio source (such as a galaxy) are reflected by the primary reflector (the surface of the dish) to a secondary reflector (located above the dish). The secondary reflector then directs the waves back down to the focal point. At this point, feeds, which are devices that convert the radio waves into electrical signals, are typically placed to capture the signal and send it to the receiver (Wilson et al., 2009). From there, the signal is transmitted to the control room for further processing (as shown by the yellow lines in Figure 1.12).

Single-dish radio telescopes are used for two primary types of observations: continuum and spectral line observations. Continuum observations measure the total radio power received over a broad frequency range. These observations are useful for studying the thermal emission from ionized gas (e.g., HII regions, planetary nebulae), synchrotron radiation from supernova remnants, radio galaxies, and cosmic background radiation, and dust and free-free emission, for instance in star-forming regions (Wilson et al., 2009). Spectral line observations focus on detecting and analysing emission or absorption from specific atomic or molecular transitions. This is particularly important for CO and other molecular line observations, which trace molecular clouds and star-forming regions. This also includes masers to study the high-energy processes occurring in star-forming regions and evolved stars (Gray, 2012). Single-dish telescopes are also well-suited for mapping large-scale structures, such as HI emission in the Galaxy (e.g., HI4PI Collaboration et al., 2016), mapping of molecular lines such as CO to provide insight into the interstellar medium (ISM) and star-forming regions (e.g., Dame et al., 2001). Single-dish telescopes are commonly used to detect and characterize molecular spectral lines, providing crucial information on the chemical composition, kinematics, and physical conditions of the emitting gas. In star-forming regions they can be used to trace gas kinematics of CO, NH_3, HCN. For astrochemistry studies single-dish telescopes are often used to detect complex organic molecules (e.g., methanol, formaldehyde) in star-forming regions and circumstellar envelopes both in low- and high-mass star forming regions (see Wilson et al., 2009, and references therein).

Observational techniques include different switching techniques which are used to remove unwanted noise from the atmosphere, ground radiation, and instrumental drift. Position switching is the technique where the telescope alternates between the target source and a nearby reference position (called off-source). The difference between the two measurements removes atmospheric and instrumental contributions, and it is suitable for compact sources in regions with minimal background emission. Frequency switching is when the receiver alternates between two closely spaced frequencies (one on the spectral line and one off-line). This technique is effective for removing baseline variations but requires stable local oscillators. For mapping, on-the-fly (OTF) mode is used, which is a fast-scanning technique, where the telescope continuously moves across the sky while collecting data. Instead of stopping at specific positions to take measurements (traditional pointing mode), the OTF mode records signals in real-time as the telescope scans over a target region. This technique is highly effective to conduct maps over a specific area on the sky (Wilson et al., 2009).

1.8.2 Radio Telescopes Utilised for My Research

1.8.2.1 The Effelsberg 100-meter Telescope

The Effelsberg 100-meter radio telescope is currently the largest fully steerable radio telescope in Europe. It is located in Effelsberg, approximately 40 km southwest of Bonn, Germany, and is

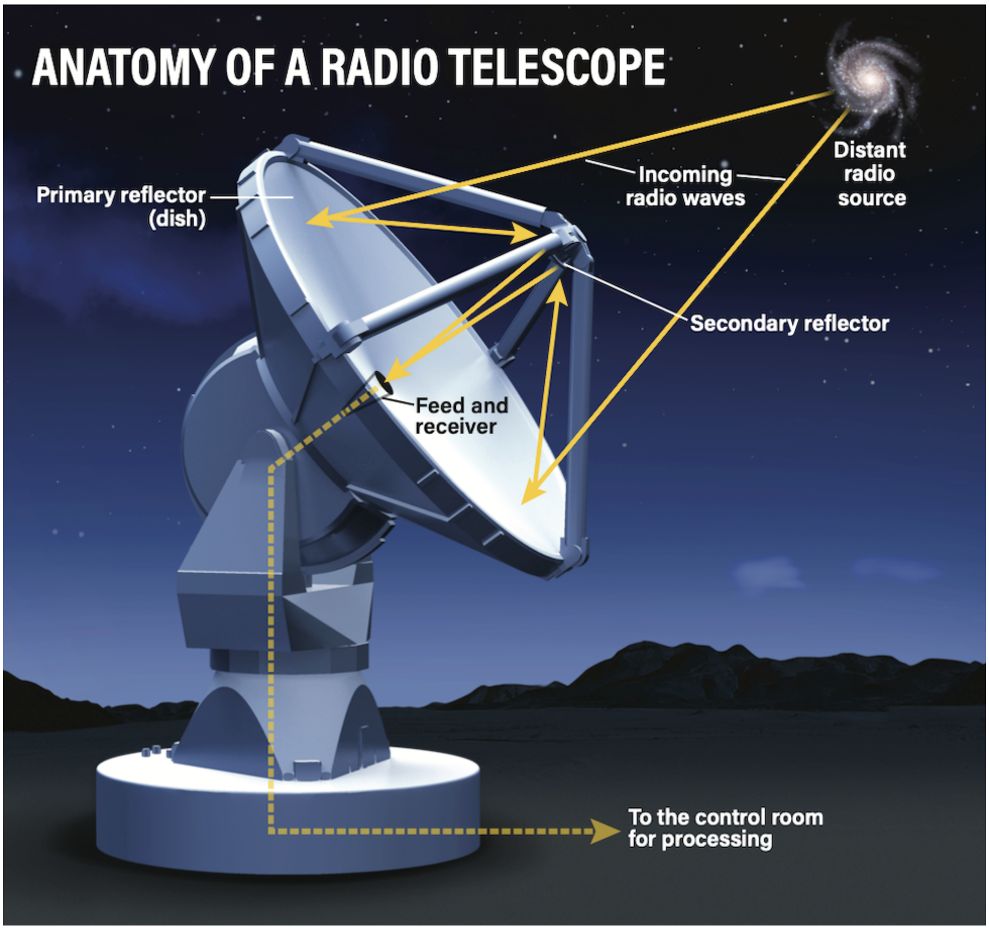

Figure 1.12: The anatomy of a radio telescope. Incoming signals from a radio source arrive at the primary reflector (the dish), which then reflects them to the secondary reflector (located above the dish). This directs the waves back down to the focal point. The signals are then converted by feeds and transmitted to the control room for processing. Image credit: Astronomy: Roen Kelly, 3d Model: ALMA (ESO/NAOJ/NRAO)/David Chorlton, available here.

operated by the Max-Planck-Institute for Radio Astronomy (MPIfR). The telescope began observations in August 1972 and has been in operation for over 50 years. This telescope is equipped with receivers capable of detecting radio waves across a broad range of wavelengths, from 90 cm to 3.5 mm. The dish itself is mounted on a 64 m diameter ring base, with a total steel structure weighing over 3000 tons. The telescope can rotate horizontally through 360 degrees, allowing it to scan the entire sky above the horizon (see e.g., Wielebinski et al., 2011).

Figure 1.13: Aerial view of the valley showing the Effelsberg 100-meter radio telescope in Effelsberg, Germany. The LOw-Frequency ARray (LOFAR) is visible behind the 100-meter telescope. On the right side of the image, the roof of the control building can be seen. Image credit: Dr. G. Schmitz, available here.

The large surface area of the 100-m antenna allows it to collect very weak signals, and its size enables it to achieve the desired angular resolution, which is the smallest angular separation at which the telescope can distinguish between two objects in the sky. The horn feeds, equipped with low-noise amplifiers, detect the incoming radiation that has been focused by the primary reflector. Multiple detecting devices can be used simultaneously to capture various aspects of the signal. The registering and processing equipments are housed in a building adjacent to the telescope (see Figure 1.13). This building contains the control room, where computers are used to operate the telescope, and where an astronomer is always on duty to monitor and manage the observations.

An extensive range of receivers is available for observations at Effelsberg, covering frequencies from 0.4 GHz to 95 GHz. For a detailed and up-to-date list of these receivers, I recommend the reader to visit the Effelsberg Wikipedia page which is regularly updated by the staff. For the research presented in this Thesis, I used the 1.3 cm double-beam secondary focus receiver, which operates within the 18 to 26 GHz frequency window, also known as the *K*-band (from approximately 18 to 26 GHz, but not to be confused with the infrared *K*-band from approximately 1.25 to 2.5 μm.).

1.8.2.2 The IRAM 30-meter Telescope

The IRAM 30-meter telescope, located in the Spanish Sierra Nevada, is operated by the Instituto de Radioastronomía Milimétrica (IRAM) and supported by the Spanish Instituto Geográfico Nacional, the German Max-Planck Gesellschaft and the French CNRS. Commonly referred to simply as the "30-m telescope", I will adopt this shorthand as well. Situated at nearly 3000 meters above sea level, the telescope is positioned above much of the atmospheric water vapour, enabling it to observe across the full millimeter wavelength range. Since its commissioning in the mid-1980s, it has remained one of the largest and most sensitive instruments for studying the millimeter domain. Figure1.14 shows the 30-m telescope, with its control room and living quarters for visiting astronomers in the adjacent building. A detailed technical summary can be found on the IRAM webpage. The 30-m telescope is a powerful instrument for observing a wide variety of astronomical objects, ranging from star-forming regions to extragalactic sources. One of its key areas of research is molecular spectroscopy, and it has played a pivotal role in the first detections of many molecules in space. For example, amino acetonitrile ($N_2H_2CH_2CN$), an organic molecule closely related to an amino acid has been discovered using the 30-m telescope towards the so called "Large Molecule Heimat", a very dense, hot gas clump within the star forming region Sagittarius B2 (Sgr B2(N)) towards the Galactic centre (Belloche et al., 2008). This success is largely due to the telescope's highly sensitive receivers, as well as its excellent angular resolution. Observations can be made down to wavelengths as short as 1 mm (around 280 GHz), where the telescope achieves an angular resolution of 10$''$.

For my research, I utilised the EMIR (Eight MIxer Receiver) instrument, which operates across four atmospheric windows at 3, 2, 1.3 and 0.9 mm. The bands are labelled as E090, E150, E230, and E330, based on their approximate centre frequencies in GHz. A detailed description of the

EMIR receiver can be found in Carter et al. (2012a), and a user guide is also available at the EMIR webpage.

Figure 1.14: The IRAM 30-m telescope in the Spanish Sierra Nevada. Image credit: IRAM/K. Zacher (available here)

1.8.2.3 The APEX 12-meter Telescope

The Atacama Pathfinder EXperiment (APEX) telescope is situated at one of the highest observatory sites on Earth, with an elevation of nearly 5100 meters on the Chajnantor Plateau in the Atacama Desert in Chile. Hosted by the European Southern Observatory (ESO) on behalf of the MPIfR, APEX was inaugurated in September 2005. Originally, the goal was to build and adapt an ALMA (Atacama Large Millimeter/Submillimeter Array) prototype antenna on the Chajnantor site. APEX is located just about 1 km from the ALMA array, and it plays a crucial role in Very Long Baseline Interferometry (VLBI) observations, particularly for calibration purposes, as it provides the shortest baseline between two systems. This capability was vital in imaging black holes with the Event Horizon Telescope (EHT; Event Horizon Telescope Collaboration et al., 2019). The APEX telescope has a 12-meter diameter and is capable of observing in both millimeter and submillimeter wavelengths, bridging the gap between infrared and radio waves. Figure 1.15 shows the APEX telescope alongside the author of this Thesis. Submillimeter astronomy is particularly suited for studying cold dust in the Universe, such as the dense regions in cold clouds where stars are born. These signals are strongly absorbed by water vapor, which makes the Atacama Desert an ideal location for such observations, as it is one of the driest places on Earth. For context, APEX is situated 2400 meters higher than the Very Large Telescope (VLT), also located in Chile on Cerro Paranal. APEX is equipped with a wide range of instruments covering a broad frequency range, which can be explored on the APEX webpage. In the following, I provide a brief overview of the specific instruments from which data is presented in this Thesis.

In chronological order (see later Chapter 4), used data obtained in 2021 with the new First Light APEX Submillimeter Heterodyne (nFLASH[1]) dual-sideband dual-polarization receiver with the Fast Fourier Transform Spectrometer (FFTS, Klein et al., 2006) backend, providing a bandwidth of 32 GHz and a spectral resolution of 61 kHz, covering frequencies between ~213 and ~245 GHz. This instrument was optimised for observation of point sources, offering great science opportunities for various astronomical objects. In 2022, I used data gathered with the Large APEX sub-Millimetre Array (LAsMA[2]), a seven-pixel dual-sideband single-polarization heterodyne receiver, consisting of a hexagonal array of six pixels surrounding a central pixel. The backend consisted of Fast Fourier Transform Spectrometers (FFTSs) covering an intermediate-frequency (IF) bandwidth of 4 – 8 GHz. LAsMA is a great instrument for mapping molecular line emission in the environments of young stars and other objects. Finally, I used data from the Swedish-ESO PI receiver for APEX (SEPIA[3]) dual-sideband dual-polarization receiver. The upper and lower sidebands each cover the IF range 4 – 12 GHz, giving a total IF bandwidth of 32 GHz in which each sideband was recorded by two FFTS units. SEPIA was used because it was possible to cover a frequency range that was not covered with the IRAM 30-m telescope nor with the other instruments on APEX.

1.9 Thesis Overview

This Thesis explores the natal environments of young stars undergoing accretion burst and outburst events, with a particular emphasis on radio and (sub)millimeter wavelengths, areas that are still poorly explored systematically in the study of these objects. The primary objective of my PhD research is to investigate the host environments of eruptive young stellar objects, aiming to fill in gaps in our current understanding of their host environments. The research involves multi-wavelength observational data analysis, complemented with modelling where relevant, to gain

[1] https://www.apex-telescope.org/ns/nflash/
[2] https://www.apex-telescope.org/ns/observing-run/observing/the-telescope/instruments/lasma-large-apex-sub-millimetre-array/
[3] https://www.apex-telescope.org/ns/observing-run/observing/the-telescope/instruments/sepia/

Figure 1.15: The APEX 12-m telescope located in the Atacama Desert in Chile with the author of this Thesis.

insights into the underlying physical processes driving these phenomena.

The core of the dissertation is structured into three chapters, each addressing a distinct aspect of the research. Chapter 2 presents the research on ammonia emission as a tracer of the natal environments of eruptive YSOs, while Chapter 3 focuses on water maser emission linked to the accretion disks and/or the outflows of these objects. Chapter 4 examines an individual source through a detailed millimetre line survey, with the primary goal of examining the molecular emission associated with the protostar and its natal environment. This thesis highlights the importance of conducting more systematic studies and enhancing current statistical overviews on low-mass eruptive YSOs. By adopting a multidisciplinary approach, it integrates comparisons across different evolutionary stages within the broader context of star formation. The work aims to contribute to the advancement of practical, statistical, and potentially theoretical understanding in the field of eruptive YSO research. Based on these findings, this thesis aims to emphasise the importance of conducting more systematic studies to improve the current statistical understanding of low-mass eruptive YSOs.

In summary, this thesis synthesizes results and insights into the environments of young stars undergoing accretion bursts, contributing to the broader understanding of the diverse processes involved in star formation.

2

Host environments of FU Orionis- and EX Lupi-type objects traced by NH_3

This Chapter is based on Szabó et al. (2023a), published in Astronomy & Astrophysics, Volume 672, A158, April 2023. The article is available at the following DOI.

This Chapter is the first part of a survey carried out using the Effelsberg 100-m radio telescope focusing on FUors and EXors. This research reports observations of the host environments of FUors/EXors traced by the NH_3 (1,1), (2,2), and (3,3) transitions, making this the first dedicated ammonia survey towards these objects. In Chapter 2.1, I introduce the survey. Chapter 2.2 presents the observations and data reduction. In Chapter 2.3 the analysis and results are summarised, while the potential importance of the observational results are discussed in Chapter 2.4. Finally, the conclusions and summary are given in Chapter 2.5.

2.1 Introduction

The evolution of FUors and EXors start in their dense cores, i.e., their birthplaces. However, very little is known in the literature about the host environments of these eruptive objects, despite dense cores being observable using a variety of molecular lines. The paucity of data may be due to the distances of these objects (see, e.g., Audard et al., 2014). Another contributing factor is that FUors and EXors have historically been considered too evolved for their dense cores to influence their central YSOs (i.e., have been classified as Class II or T Tauri stars, see, e.g., Lada, 1987; Herbig, 1977; Hartmann & Kenyon, 1996). Indeed, molecular lines were detected toward only ~38% (13/34) of the target sources in a pioneering ammonia study of T Tauri stars conducted by Lang & Willson (1979), using the 36.6-m reflector at Haystack Observatory with beamwidth of 1.4′ and peak sensitivity of 1 Jy (Lang & Willson, 1979). More recently, however, evidence has emerged that some FUors and EXors are still in more embedded evolutionary phases (e.g., Green et al., 2013; Audard et al., 2014), and that FUors/EXors can also be transition objects (i.e., between Class 0 and Class I or between Class I and Class II), such as Haro 5a IRS (Kóspál et al., 2017a), V1647 Ori (Ábrahám et al., 2004; Principe et al., 2018), and HH 354 IRS (Bronfman et al., 1996; Reipurth & Aspin, 1997; Reipurth et al., 1997). This realisation motivates revisiting the temperatures, densities, and dynamic states of the host environments of FUors and EXors, but focusing on a large sample, which has not been well-characterized to date due to the scarcity of systematic molecular line observations. Many FUors and EXors, for example, V883 Ori, Z CMa, V1057 Cyg, or the prototypes FU Ori and EX Lupi have been well-studied with focus on extensive multi-wavelength and high-resolution studies, from optical to radio regimes, revealing detailed structures such as disks, jets, outflows, and complex chemistry (see, e.g., Ábrahám et al., 2009; Antoniucci et al., 2016; Cieza et al., 2016; Lee et al., 2019; Pérez et al., 2020; Szabó et al., 2021; Lee et al., 2024, and references therein). However, despite these detailed case studies, a large, systematic survey focusing on specific molecular tracers has been lacking.

We have chosen ammonia as the molecular tracer due to being able to probe physical conditions in a range of environments and evolutionary stages. The rotational temperature of the gas can be obtained from the intensity ratios of the inversion transitions, and can be used to estimate the kinetic temperature of molecular gas (see for details Ho & Townes, 1983). Ammonia allows the study of a wide range of properties (i.e. line widths, temperatures, densities, molecular abundances) and may, in combination with dust continuum observations, reveal the presence of dense circumstellar envelopes. The results of a large-scale ammonia survey will help to identify sources with line emission strong enough for follow-up higher angular resolution interferometric observations, which in turn will allow us to investigate the relationship between circumstellar envelopes and disk accretion, which can further help in understanding the eruption mechanisms of FUors and EXors. For the survey, we have chosen the Effelsberg 100-m radio telescope (see Section 1.8.2.1 in Chapter 1). The radio telescope is located close to Bonn, where I have been for the first half of my PhD programme, and I had the immense privilege to learn from Yan Gong and Wenjin Yang (postdocs at the Millimeter Department at the time) how to prepare the proposal, execute the observations, reduce, analyse, and interpret the data.

The sample (see Table 2.8) consists of 33 FUors, 13 EXors, and a small sample of five *Gaia* alerted YSOs (see Hodgkin et al., 2021): these are objects with optical variability identified by the *Gaia* satellite, which are yet to be classified as either being FUors or EXors, but potentially neither of these classes. The *Gaia* Science Alerts refer to notifications issued by the *Gaia* mission when it detects transient astronomical events: objects which suddenly change in brightness. The Alert System is designed to inform the astronomical community in almost real-time so that follow-up observations from ground-based telescopes can be made quickly (Hodgkin et al., 2021). In the sample, the source Gaia18dvy is listed with its *Gaia* alert name (see Table 2.1), but this source was classified as a FUor by Szegedi-Elek et al. (2020) and therefore is not counted within the 5 *Gaia* alert sources. The criteria for including *Gaia* alerts in the sample were based on their light curves and luminosity at the time of the proposal submission in 2021 September. In recent years, the *Gaia* alert system has become an important tool in identifying new outbursting systems (see e.g, Hillenbrand et al., 2018, 2019; Szegedi-Elek et al., 2020; Cruz-Sáenz de Miera et al., 2022b; Nagy et al., 2022) as well as studying new events in known sources (see, e.g., Nagy et al., 2021). For this sample, I specifically selected objects with light curves resembling those of FUors and EXors, considering potential interest in these sources within the Star Formation Department at Konkoly Observatory, where members of the group work on *Gaia* alerted YSOs and their classification.

2.2 Observations and data reduction

The three metastable NH_3 $(J, K) = (1, 1), (2, 2)$, and $(3, 3)$ lines were measured simultaneously with the $J_{K_a K_c} = 6_{16} - 5_{23}$ water maser transition on 2021 November 18, 23, and 2022 January

25 using the Effelsberg 100-m telescope in Germany[1] (PI: Szabó, project ID: 95-21). The observations were performed in position-switching mode with the off-position at an offset of 5′ east of each target in azimuth. The 1.3 cm double beam and dual polarization secondary focus receiver was adopted as the frontend. Fast Fourier Transform Spectrometers (FFTSs) were used as the backend, and each FFTS provides a bandwidth of 300 MHz and 65536 channels, which gives a channel width of 4.6 kHz, corresponding to a velocity spacing of 0.06 $\mathrm{km\,s^{-1}}$ at ~23.7 GHz. The actual spectral resolutions are coarser by a factor of 1.16 (Klein et al., 2012a). NGC 7027 was used to obtain the pointing and focus corrections at the beginning of each observing session, then W75N was targeted for its well known H_2O and NH_3 transitions in order to verify our spectral setup. The pointing was regularly checked on nearby continuum sources, and was found to be accurate to about 5″. We also used NGC 7027 as our flux calibrator, which has a continuum flux density of 5.7 Jy at 23.7 GHz (Ott et al., 1994). For the spectral calibration, we used the method introduced by Winkel et al. (2012a), and the calibration uncertainty is about 15%. The half-power beam width (HPBW) is about 37′, and the main beam efficiency is 58.9% at 24 GHz. The conversion factor from flux density (S_ν) to main beam temperature (T_{mb}) is T_{mb}/S_ν=1.73 K/Jy. The main beam temperature is a measure of the observed intensity of a radio signal, normalized to account for the telescope's efficiency. The main beam temperature does not necessarily reflect the physical temperature of the gas (Wilson et al., 2009). Velocities are presented with respect to the local standard of rest (LSR) throughout this Chapter and in Table 2.1. The on-source integration time was 2.5 minutes per spectrum, and during each observing epoch, four spectra per source were obtained.

For the data reduction, we used the GILDAS/CLASS software developed by the Institut de Radioastronomie Millimétrique [2] (IRAM; Pety, 2005a). Spectra were averaged for the same target to achieve better sensitivities, and linear baselines were subtracted. This refers to the removal of a linear fit to the spectral baseline around the molecular lines, which helps to isolate the line emission by correcting for any residual instrumental or atmospheric effects in the baseline region adjacent to the spectral features of interest, in our case the ammonia transitions.

[1]The 100-m telescope at Effelsberg is operated by the Max-Planck-Institut für Radioastronomie (MPIFR) on behalf of the Max-Planck-Gesellschaft (MPG).
[2]`https://www.iram.fr/IRAMFR/GILDAS/`

2.2.1 Sources with non-detections

In Table 2.1, we list 3σ upper limits for sources without ammonia detections. Gaia alerts were chosen based on their light curves and luminosities at the time of our proposal submission. These objects were chosen because their light curves resembled those of FUors/EXors. Interestingly, no ammonia was detected towards any of the Gaia alert sources.

Table 2.1: Sources without ammonia detections in our survey.

Name	R.A. (J2000) ($^{h}:^{m}:^{s}$)	Dec. (J2000) ($^{\circ}:':''$)	Type FUor/EXor	$3\sigma_{(1,1)}$ (K)	$3\sigma_{(2,2)}$ (K)	$3\sigma_{(3,3)}$ (K)	N_{H_2} (cm^{-2})	T_{dust} (K)	Reference
V1180 Cas	02:33:01.53	+72:43:26.8	EXor	0.32	0.32	0.33	–	–	–
XZ Tau	04:31:40.08	+18:13:56.6	EXor	0.34	0.33	0.32	–	–	–
UZ Tau E	04:32:43.02	+25:52:30.9	EXor	0.34	0.33	0.31	–	–	–
VY Tau	04:39:17.42	+22:47:53.3	EXor	0.24	0.25	0.26	–	–	–
DR Tau	04:47:06.21	+16:58:42.8	EXor	0.33	0.33	0.35	–	–	–
V582 Aur	05:25:51.97	+34:52:30.0	FUor	0.34	0.33	0.33	–	–	–
V1118 Ori	05:34:44.98	−05:33:41.3	EXor	0.38	0.45	0.41	3.9×10^{21}	21.9	1, 2
NY Ori	05:35:36.0	−05:12:25.2	EXor	0.41	0.42	0.39	6.6×10^{21}	28.8	1, 2
Gaia21arx	05:36:24.80	−06:17:30.52	unknown	0.32	0.33	0.31	–	–	–
V1143 Ori	05:38:03.89	−04:16:42.8	EXor	0.39	0.44	0.48	5.4×10^{20}	19.7	1, 2
V883 Ori	05:38:18.09	−07:02:25.9	FUor	0.02	0.02	0.03	1.5×10^{22}	18.8	1, 2
HBC 494	05:40:27.45	−07:27:30.0	FUor	0.38	0.42	0.42	–	–	–
FU Ori	05:45:22.37	+09:04:12.3	FUor	0.35	0.39	0.37	–	–	–
V1647 Ori	05:46:13.13	−00:06:04.8	FUor	0.02	0.02	0.02	1.3×10^{22}	17.4	1, 3
V900 Mon	06:57:22.22	−08:23:17.6	FUor	0.57	0.55	0.57	–	–	–
Gaia20bdk	07:10:14.92	−18:27:01.04	unknown	0.62	0.72	0.67	–	–	–
Gaia21aul	18:30:06.18	00:42:33.30	unknown	0.34	0.37	0.36	–	–	–
Gaia21aru	19:00:56.41	18:48:29.20	unknown	0.33	0.31	0.31	–	–	–
Parsamian 21	19:29:00.84	+09:38:43.4	FUor	0.32	0.31	0.33	–	–	–
Gaia18dvy	20:05:06.02	+36:29:13.5	FUor	0.26	0.26	0.28	–	–	–
V1515 Cyg	20:23:48.01	+42:12:25.7	FUor	0.32	0.33	0.33	1.1×10^{22}	17.4	1, 4
PV Cep	20:45:53.9	+67:57:38.6	EXor	0.33	0.30	0.31	1.5×10^{22}	16.3	1, 5
Gaia19bpg	21:41:50.43	51:55:45.48	unknown	0.27	0.27	0.29	–	–	–

Notes. 1 – André et al. (2010), 2 – Pezzuto et al. (2021), 3 – Könyves et al. (2020), 4 – Cao et al. (2019), 5 – Di Francesco et al. (2020)

2.3 Results and analysis

Out of the sample of 51 sources, the NH_3 (1,1) transition was detected (i.e., at least 3× the rms) in 28 sources and the (2,2) transition in 12 sources, while the (3,3) transition was only detected in two sources (namely RNO 1B/1C and V512 Per). This corresponds to detection rates of 54%, 23%, and 4% for NH_3 (1,1), (2,2), and (3,3), respectively. Ammonia emission was not detected toward any of the Gaia alert sources.

The hyperfine structure (HFS) lines of the NH_3 (1,1) transition were fitted using the hyperfine fitting method in CLASS. The independent parameters from the fitting are the LSR velocity (v_{LSR}), line width (Δv) at the full width at half maximum (FWHM) of a Gaussian profile, and the optical depth of the main HFS line (τ_m). The satellite lines of the (2,2) and (3,3) transitions were too weak to be detected. Therefore, only the main lines of these transitions were fitted, assuming a Gaussian function: the derived parameters are the LSR velocity ($v_{\rm LSR}$) and FWHM line width (Δv) of the main lines. Figure 2.1 shows examples of the reduced and calibrated spectra.

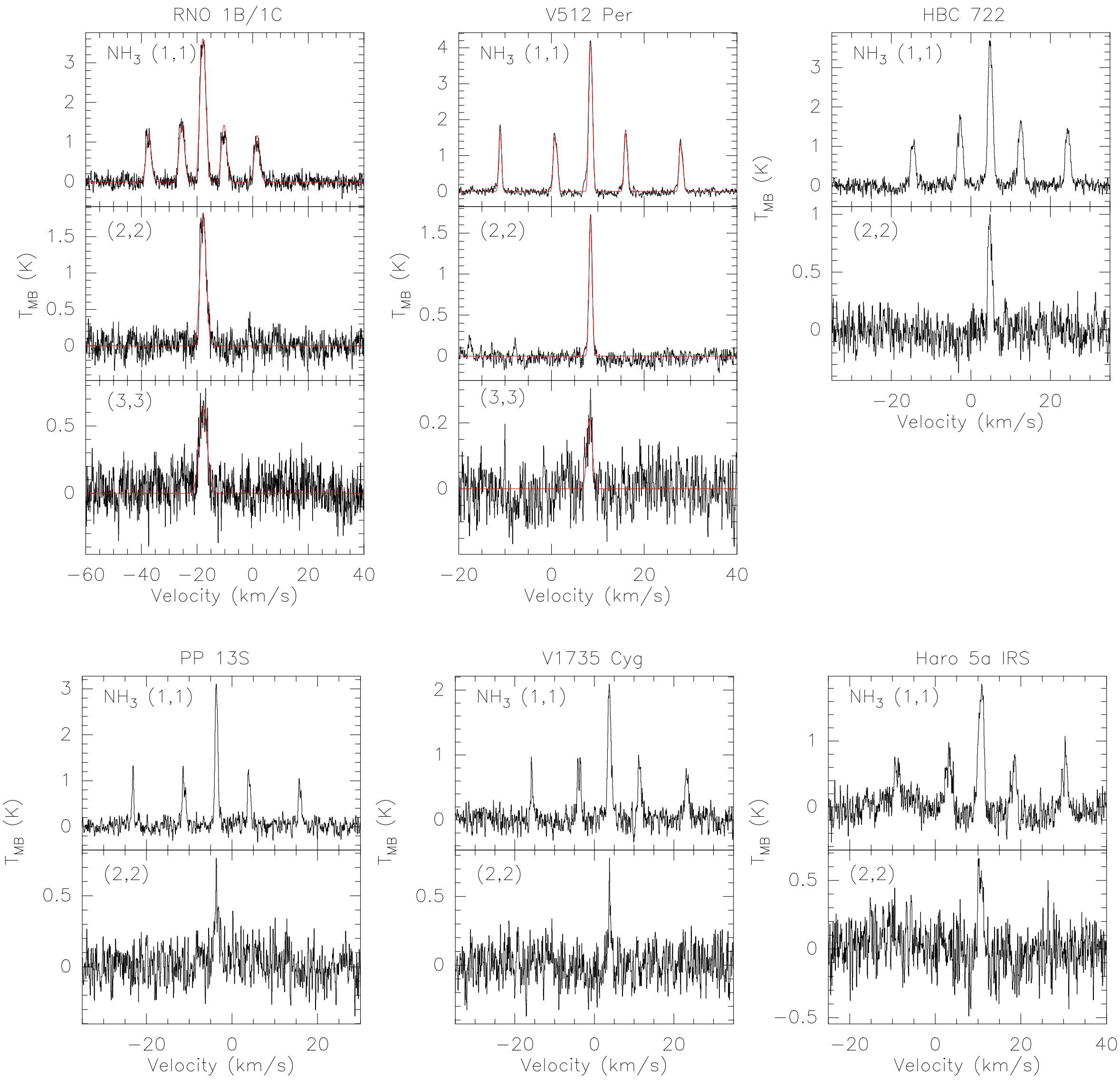

Figure 2.1: Examples of reduced and calibrated spectra for the NH_3 (1,1), (2,2), and (3,3) transitions. The transition is indicated in the upper left corner of each panel. For the first two sources the fits are shown in red. The (3,3) transition was detected only towards RNO 1B/1C and V512 Per (SVS 13A). Figures from Szabó et al. (2023a).

The peak main beam brightness temperatures of the NH_3 (1,1), (2,2) and (3,3) transitions were derived from the peak intensity of the Gaussian fit to the main line. For undetected lines, three times the rms noise (3σ) was adopted as an upper limit (given in Table 2.1). In Tables 2.2 and 2.3, I list the properties of the detected (1,1) transitions for the FUors and EXors, respectively. In each case, their name, position, optical depth (τ), LSR velocity ($v_{\rm LSR}(1,1)$), line width ($\Delta v(1,1)$), and the main beam brightness temperature ($T_{\rm MB}(1,1)$) are given. The formal errors of the fits are given in parentheses. In Table 2.4 and Table 2.5, I list the $v_{\rm LSR}$, Δv and $T_{\rm MB}$ values for the (2,2) and (3,3) transitions, with 3σ upper limits given in the case of non-detections.

Table 2.2: NH_3 (1,1) line parameters for the FU Orionis-type objects detected in the survey.

Name	R.A. (J2000) ($^{\rm h\ m\ s}$)	Dec. (J2000) ($^{\circ}\ '\ ''$)	$\tau(1,1)^{(a)}$	$v_{\rm LSR}(1,1)^{(b)}$ (km s^{-1})	$\Delta v(1,1)^{(c)}$ (km s^{-1})	$T_{\rm MB}(1,1)^{(d)}$ (K)	$\Delta v_{\rm th}^{(e)}$ (km s^{-1})	$\Delta v_{\rm nt}^{(f)}$ (km s^{-1})	$Ma^{(g)}$
RNO 1B/1C	00 36 46.30	+63 28 54.0	1.16 (0.03)	−17.83 (0.02)	2.39 (0.04)	3.75 (0.32)	0.31	2.36	3.36
PP 13S	04 10 41.09	+38 07 54.5	0.79 (0.05)	−3.62 (0.01)	0.75 (0.01)	3.09 (0.20)	0.24	0.71	1.46
L1551 IRS 5	04 31 34.07	+18 08 04.9	1.93 (0.12)	6.35 (0.01)	0.87 (0.02)	2.78 (0.22)	0.23	0.83	1.78
Haro 5a IRS	05 35 26.74	−05 03 55.0	1.80 (0.16)	10.7 (0.01)	1.19 (0.02)	1.89 (0.26)	0.26	1.16	2.21
V2775 Ori	05 42 48.48	−08 16 34.7	1.07 (0.24)	3.05 (0.01)	0.65 (0.03)	1.98 (0.21)	0.19^h	0.62^h	1.12^h
NGC 2071	05 47 09.80	+00 18 00.0	0.10 (0.18)	10.4 (0.01)	0.52 (0.03)	1.06 (0.14)	0.19^h	0.48^h	0.92^h
V899 Mon	06 09 19.24	−06 41 55.8	0.42 (0.19)	9.63 (0.01)	0.46 (0.02)	1.62 (0.15)	0.19^h	0.41^h	0.79^h
IRAS 06297+1021W	06 32 28.70	+10 19 0	0.86 (0.22)	4.17 (0.01)	0.43 (0.02)	1.64 (0.16)	0.19^h	0.38^h	0.73^h
AR 6A/6B	06 40 59.30	+09 35 49.0	0.70 (0.11)	5.06 (0.02)	2.31 (0.05)	1.71 (0.25)	0.27	2.29	4.10
IRAS 06393+0913	06 42 08.13	+09 10 30.0	0.10 (0.11)	7.72 (0.02)	0.49 (0.04)	0.68 (0.14)	0.19^h	0.45^h	0.87^h
V960 Mon	06 59 31.58	−04 05 27.7	0.27 (0.47)	23.8 (0.02)	0.70 (0.10)	0.93 (0.26)	0.19^h	0.67^h	1.29^h
Z CMa	07 03 43.15	−11 33 06.2	0.10 (0.27)	13.8 (0.02)	1.22 (0.04)	1.35 (0.19)	0.19^h	1.21^h	2.34^h
iPTF 15AFQ	07 09 21.39	−10 29 34.5	1.14 (0.28)	13.3 (0.01)	0.71 (0.04)	1.77 (0.30)	0.19^h	0.68^h	1.31^h
IRAS 18270-0153W	18 29 36.90	−01 51 02.0	2.95 (0.11)	7.61 (0.01)	0.55 (0.01)	3.80 (0.32)	0.23	0.49	1.06
OO Ser	18 29 49.13	+01 16 20.6	1.68 (0.08)	8.31 (0.01)	0.77 (0.01)	3.43 (0.28)	0.26	0.73	1.37
IRAS 18341-0113S	18 36 45.70	−01 10 29.0	2.82 (0.17)	9.27 (0.01)	0.41 (0.01)	2.65 (0.16)	0.22	0.34	0.74
HBC 722	20 58 17.00	+43 53 43.0	1.98 (0.06)	4.93 (0.01)	1.08 (0.01)	3.64 (0.34)	0.24	1.05	2.09
V1057 Cyg	20 58 53.73	+44 15 28.4	1.89 (0.57)	4.35 (0.02)	0.72 (0.06)	0.49 (0.16)	0.19^h	0.69^h	1.33^h
V2495 Cyg	21 00 25.24	+52 30 16.9	0.86 (0.37)	4.71 (0.02)	0.80 (0.05)	0.74 (0.15)	0.19^h	0.77^h	1.49^h
RNO 127	21 00 31.80	+52 29 17.0	2.37 (0.65)	−2.90 (0.01)	0.37 (0.02)	0.72 (0.16)	0.19^h	0.31^h	0.59^h
CB 230	21 17 38.62	+68 17 34.0	2.56 (0.15)	2.79 (0.01)	0.46 (0.01)	2.21 (0.19)	0.19^h	0.41^h	0.79^h
V1735 Cyg	21 47 20.66	+47 32 03.8	1.97 (0.17)	3.80 (0.01)	0.69 (0.02)	2.01 (0.21)	0.24	0.64	1.29
HH 354 IRS	22 06 50.37	+59 02 45.9	2.35 (0.33)	−1.52 (0.01)	0.36 (0.01)	1.36 (0.16)	0.19^h	0.30^h	0.58^h
V733 Cep	22 53 33.25	+62 32 23.6	2.32 (0.43)	−8.93 (0.01)	0.36 (0.02)	0.98 (0.15)	0.19^h	0.30^h	0.58^h

Notes. $^{(a)}$ Optical depth of the (1,1) transition main line. $^{(b)}$ LSR velocity. $^{(c)}$ Line width determined using the HFS fitting method. $^{(d)}$ Main beam brightness temperature. $^{(e)}$ Thermal line width. $^{(f)}$ Non-thermal line width. $^{(g)}$ Mach number. $^{(h)}$ Source with the assumed $T_{\rm kin}$ value of 14.6 K.

Table 2.3: NH_3 (1,1) line parameters for the EX Lupi-type objects detected in the survey.

Name	R.A. (J2000) ($^{\rm h\ m\ s}$)	Dec. (J2000) ($^{\circ}\ '\ ''$)	$\tau(1,1)^{(a)}$	$v_{\rm LSR}(1,1)^{(b)}$ (km s^{-1})	$\Delta v(1,1)^{(c)}$ (km s^{-1})	$T_{\rm MB}(1,1)^{(d)}$ (K)	$\Delta v_{\rm th}^{(e)}$ (km s^{-1})	$\Delta v_{\rm nt}^{(f)}$ (km s^{-1})	$Ma^{(g)}$
V512 Per (SVS 13)	03 29 03.75	+31 16 03.9	1.77 (0.03)	8.45 (0.01)	0.64 (0.01)	4.23 (0.35)	0.27	0.58	1.03
LDN 1415 IRS	04 41 37.50	+54 19 22.0	1.26 (0.62)	−5.77 (0.02)	0.48 (0.04)	0.63 (0.16)	0.19^h	0.44^h	0.85^h
V371 Ser	18 29 51.21	+01 16 39.4	2.20 (0.03)	8.34 (0.01)	0.78 (0.01)	3.76 (0.34)	0.23	0.74	1.54
V2492 Cyg	20 51 26.23	+44 05 23.8	0.86 (0.37)	4.71 (0.02)	0.70 (0.05)	0.74 (0.15)	0.19^h	0.67^h	1.29^h

Notes. $^{(a)}$ Optical depth of the (1,1) transition main line. $^{(b)}$ LSR velocity. $^{(c)}$ Line width determined using the HFS fitting. $^{(d)}$ Main beam brightness temperature. $^{(e)}$ Thermal line width. $^{(f)}$ Non-thermal line width. $^{(g)}$ Mach number. $^{(h)}$ Source with the assumed $T_{\rm kin}$ value of 14.6 K.

Table 2.4: NH_3 (2,2) and (3,3) line parameters for the FU Orionis-type objects detected in NH_3 (1,1).

Name	$v_{LSR}(2,2)^{(a)}$ (km s^{-1})	$\Delta v(2,2)^{(b)}$ (km s^{-1})	$T_{MB}(2,2)^{(c)}$ (K)	$v_{LSR}(3,3)^{(d)}$ (km s^{-1})	$\Delta v(3,3)^{(e)}$ (km s^{-1})	$T_{MB}(3,3)^{(f)}$ (K)
RNO 1B/1C	−17.80 (0.01)	2.55 (0.03)	1.82 (0.11)	−17.75 (0.05)	3.19 (0.11)	0.64 (0.11)
PP 13S	−3.57 (0.04)	1.32 (0.12)	0.74 (0.11)	–	–	< 0.11
L1551 IRS 5	6.30 (0.03)	0.62 (0.08)	0.59 (0.11)	–	–	< 0.10
Haro 5a IRS	10.53 (0.04)	1.27 (0.09)	0.59 (0.14)	–	–	< 0.16
V2775 Ori	–	–	< 0.12	–	–	< 0.13
NGC 2071	–	–	< 0.11	–	–	< 0.10
V899 Mon	–	–	< 0.10	–	–	< 0.11
IRAS 06297+1021W	–	–	< 0.12	–	–	< 0.14
AR 6A/6B	5.28 (0.07)	2.48 (0.19)	0.73 (0.13)	–	–	< 0.16
IRAS 06393+0913	–	–	< 0.10	–	–	< 0.10
V960 Mon	–	–	< 0.18	–	–	< 0.18
Z CMa	–	–	< 0.12	–	–	< 0.13
iPTF 15AFQ	–	–	< 0.19	–	–	< 0.21
IRAS 18270−0153W	7.62 (0.01)	0.87 0.05)	1.14 (0.11)	–	–	< 0.14
OO Ser	8.33 (0.02)	1.07 0.05)	1.07 (0.11)	–	–	< 0.11
IRAS 18341−0113S	9.20 (0.02)	0.42 0.05)	0.59 (0.12)	–	–	< 0.12
HBC 722	4.82 (0.02)	1.16 0.04)	0.98 (0.11)	–	–	< 0.11
V1057 Cyg	–	–	< 0.10	–	–	< 0.10
V2495 Cyg	–	–	< 0.15	–	–	< 0.10
RNO 127	–	–	< 0.10	–	–	< 0.10
CB 230	–	–	< 0.10	–	–	< 0.10
V1735 Cyg	3.84 (0.03)	0.78 (0.10)	0.77 (0.12)	–	–	< 0.33
HH 354 IRS	–	–	< 0.10	–	–	< 0.11
V733 Cep	–	–	< 0.10	–	–	< 0.10

Notes. [(a)] LSR velocity of the (2,2) transition. [(b)] Line width determined using a single Gaussian. [(c)] Main beam brightness temperature. The upper limits are 3σ. [(d)] LSR velocity of the (3,3) transition. [(e)] Line width determined using a single Gaussian. [(f)] Main beam brightness temperature. The upper limits are 3σ. The errors are given in parentheses.

2.3.1 Molecular excitation

The rotational (T_{rot}) and kinetic (T_{kin}) temperatures, as well as the ammonia column density (N_{NH_3}), were determined using the standard method introduced in the works of Ho & Townes (1983); Ungerechts & Guesten (1984). The results are given in Tables 2.6 and 2.7 for the FUors and EXors, respectively. The rotational temperature refers to the energy levels of a molecule's rotational motion and is inferred from the population of molecules in different rotational states. It is estimated by comparing the intensities of two or more rotational transitions of a molecule and gives information about the excitation conditions (Goldsmith & Langer, 1999). The kinetic temperature is the true physical temperature of the gas and is related to the thermal motion of particles (e.g., Walmsley & Ungerechts, 1983).

The rotational temperature can only be determined for sources in which both the (1,1) and (2,2) transitions were detected. To calculate the T_{rot} values, we used the following relation (Ho & Townes, 1983):

$$T_{rot} = \frac{-41.5}{\ln\Big(\frac{-0.282}{\tau_m(1,1)}\ln\Big(1 - \frac{T_{MB}(2,2)}{T_{MB}(1,1)}\Big(1 - \exp(-\tau_m(1,1))\Big)\Big)\Big)}\,, \quad (2.1)$$

using the optical depth of the (1,1) main line, $\tau_m(1,1)$, and the main beam brightness temperatures, $T_{\rm MB}$, of the (1,1) and (2,2) main lines derived from the Gaussian fitting. The derived rotational temperatures in our sample range from 11 K to 18 K, with an average $T_{\rm rot}$ of 13.2 K.

Once the rotational temperature is determined, the kinetic temperature can be calculated using the relation of Tafalla et al. (2004) valid for temperatures below ∼20 K,

$$T_{\rm kin} = \frac{T_{\rm rot}(1,2)}{1 - \frac{T_{\rm rot}(1,2)}{42\,{\rm K}} \ln\left(1 + 1.1\exp\left(\frac{-16\,{\rm K}}{T_{\rm rot}(1,2)}\right)\right)}\,, \tag{2.2}$$

where $T_{\rm rot}$(1,2) is the rotational temperature determined from the (1,1) and (2,2) inversion transitions, and 42 K is the energy difference between the (1,1) and (2,2) levels. We find that the host environments are characterised by kinetic temperatures of 12–21 K with an average kinetic temperature of 14.6 K, with the highest kinetic temperature found towards RNO 1B/1C. These kinetic temperatures are lower than those found towards Class II sources (26–37 K), but are similar to low-mass and high-mass dense clumps in early evolutionary stages (e.g., Benson & Myers, 1989; Pillai et al., 2006; Zhang et al., 2011; Wienen et al., 2012).

To calculate the ammonia column density, the rotational temperature derived from Eq. 2.1, $T_{\rm rot}$(1,2), the optical depth, τ_m(1,1), and the linewidth, Δv(1,1), of the (1,1) inversion transition are needed. We calculated the $N_{\rm tot}$ values using the column density of the (1,1) level, assuming that the energy levels are populated according to the Boltzmann distribution (see, e.g., Wilson et al., 2009; Wienen et al., 2012). For the calculation of the total column density, we used the relation given by Wilson et al. (2009), with the assumption that the lowest metastable levels dominate in the population

$$N_{\rm tot} \approx N(1,1)\left(\frac{1}{3}\exp\left(\frac{23.1}{T_{\rm rot}(1,2)}\right) + 1 + \frac{5}{3}\exp\left(-\frac{41.2}{T_{\rm rot}(1,2)}\right) + \frac{14}{3}\exp\left(-\frac{99.4}{T_{\rm rot}(1,2)}\right)\right), \tag{2.3}$$

where $T_{\rm rot}$(1,2) is the rotational temperature, and N(1,1) is the column density of the (1,1) level,

$$N(1,1) = 4.14 \times 10^3 \frac{g_l\, \nu^2\, T_{\rm rot}(1,2)}{g_u\, A_{\rm ul}} \left(1 + \exp(\frac{h\nu}{kT_{\rm ex}})\right) \tau_{\rm m}(1,1)\, \Delta v$$
$$\approx 2.72 \times 10^{13} T_{\rm rot}(1,2) \tau_{\rm m}(1,1)\, \Delta v \ {\rm cm}^{-2}, \qquad (2.4)$$

where g_l, g_u are the statistical weights of the lower/upper levels, A_{ul} is the Einstein coefficient, ν is the frequency in units of GHz, T_{ex} is the excitation temperature of the (1,1) transition, and Δv is the linewidth in units of km s^{-1}. We have used the approximation that $\frac{h\nu}{kT_{ex}}$ $\ll$1 in Eq. (2.4). Assuming local thermodynamic equilibrium (LTE), we used the rotational temperature as the excitation temperature (e.g., Goldsmith & Langer, 1999; Wilson et al., 2009). The values for g_l, g_u, A_{ul}, and ν were taken from the Leiden Atomic and Molecular Database (LAMDA, Schöier et al., 2005).

The average rotational temperature for all sources (with detected (1,1) and the (2,2) emission) was found to be 13.2 K. For sources detected only in the (1,1) transition, we adopt T_{rot} = 13.2 K in order to estimate their NH_3 column densities and abundances. The results are given in Tables 2.6 and 2.7, for the FUors and EXors respectively. Since we find rotational temperatures between 11 K and 18 K, we assume an uncertainty for the average rotational temperature of ~30%.

The ammonia column densities in the sample range from 5.2×10^{13} cm^{-2} (IRAS 06393+0913) to 3.2×10^{15} cm^{-2} (RNO 1B/1C), with an average of 1.18×10^{15} cm^{-2} and a median of 1.15×10^{15} cm^{-2}, respectively. I compared the results from this survey with those found in infrared dark clouds (IRDCs), which are cold and dense MCs, discovered in the mid-infrared (MIR) surveys conducted with the Infrared Space Observatory (ISO, see also Perault et al., 1996). In IRDCs ammonia column densities were found to range from 7.6×10^{14} cm^{-2} to 6.04×10^{15} cm^{-2}, with an average value of 3×10^{15} cm^{-2} (Pillai et al., 2006). Approximately 2/3 of our sample (18/28 objects, ~64%) falls within this range, with the remaining sources having NH_3 column densities lower than observed in IRDCs (see Table 2.6 and 2.7).

2.3.2 Beam filling factor

The beam filling factor, η, gives the fraction of the beam filled by the observed emission (Wilson et al., 2009), and it can be derived from the radiative transfer equation when the excitation temperature and optical depth of the transition can be determined. For ammonia, optical depths can be derived from the HFS fitting and we assume local thermodynamic equilibrium (LTE) in order to

Table 2.5: NH_3 (2,2) and (3,3) line parameters for the EX Lupi-type objects detected in NH_3 (1,1).

Name	$\upsilon_{LSR}(2,2)^{(a)}$ (km s^{-1})	$\Delta\upsilon(2,2)^{(b)}$ (km s^{-1})	$T_{MB}(2,2)^{(c)}$ (K)	$\upsilon_{LSR}(3,3)^{(d)}$ (km s^{-1})	$\Delta\upsilon(3,3)^{(e)}$ (km s^{-1})	$T_{MB}(3,3)^{(f)}$ (K)
V512 Per (SVS 13)	8.45 (0.01)	0.84 (0.03)	1.71 (0.06)	8.23 (0.05)	1.36 (0.12)	0.21 (0.06)
LDN 1415 IRS	–	–	< 0.11	–	–	< 0.12
V371 Ser	8.43 (0.02)	0.97 (0.06)	0.80 (0.06)	–	–	< 0.11
V2492 Cyg	–	–	< 0.10	–	–	< 0.10

Notes. $^{(a)}$ LSR velocity of the (2,2) transition. $^{(b)}$ Line width determined using a single Gaussian. $^{(c)}$ Main beam brightness temperature. The upper limits are 3σ. $^{(d)}$ LSR velocity of the (3,3) transition. $^{(e)}$ Line width determined using a single Gaussian. $^{(f)}$ Main beam brightness temperature. The upper limits are 3σ. The errors are given in parentheses.

Table 2.6: Derived parameters for FU Orionis-type objects detected in NH_3 emission.

Name	$T^{(a)}_{rot}$ (K)	$T^{(b)}_{kin}$ (K)	$N^{(c)}_{NH_3}$ (cm^{-2})	$N^{(d)}_{H_2}$ (cm^{-2})	$T^{(e)}_{dust}$ (K)	$[NH_3 / H_2]^{(f)}$	$\eta^{(g)}$	Outflow (Y/N)	Ref.
RNO 1B/1C	17.9 (0.9)	21.3 (1.1)	$(3.2 \pm 0.2) \times 10^{15}$	2.1×10^{23}	14.5	1.5×10^{-8}	0.16	Y	1
PP 13S	11.9 (0.9)	12.8 (1.1)	$(6.6 \pm 1.0) \times 10^{14}$	2.6×10^{22}	15.6	2.5×10^{-8}	0.18	Y	1
L1551 IRS 5	11.3 (0.8)	12.1 (0.8)	$(1.9 \pm 0.2) \times 10^{15}$	6.5×10^{22}	16.4	2.9×10^{-8}	0.27	Y	1
Haro 5a IRS	13.6 (1.5)	15.1 (1.7)	$(2.8 \pm 0.5) \times 10^{15}$	6.2×10^{22}	18.1	4.5×10^{-8}	0.14	Y	1
V2775 Ori	13.2*	–	$(7.5 \pm 1.9) \times 10^{14}$	2.6×10^{22}	14.0	2.8×10^{-8}	0.15	Y/N**	2, 3
NGC 2071	13.2*	–	$(0.6 \pm 1.0) \times 10^{14}$	9.8×10^{21}	21.8	6.1×10^{-9}	0.01	–	2, 4
V899 Mon	13.2*	–	$(2.2 \pm 1.0) \times 10^{14}$	9.1×10^{21}	13.8	2.4×10^{-8}	0.05	Y	1
IRAS 06297+1021W	13.2*	–	$(4.1 \pm 1.1) \times 10^{14}$	1.5×10^{22}	13.8	2.7×10^{-8}	0.09	Y	1
AR 6A/6B	15.2 (1.9)	17.2 (2.2)	$(1.8 \pm 0.4) \times 10^{15}$	5.1×10^{22}	15.8	3.5×10^{-8}	0.06	N	1
IRAS 06393+0913	13.2*	–	$(5.2 \pm 5.8) \times 10^{13}$	1.1×10^{22}	13.6	4.7×10^{-9}	0.01	Y?	1
V960 Mon	13.2*	–	$(2.1 \pm 3.5) \times 10^{14}$	1.3×10^{22}	14.9	1.6×10^{-8}	0.02	Y	1
Z CMa	13.2*	–	$(1.3 \pm 3.5) \times 10^{14}$	–	–	–	0.01	Y	7
iPTF 15AFQ	13.2*	–	$(8.8 \pm 2.3) \times 10^{14}$	2.1×10^{22}	11.8	1.3×10^{-8}	0.11	Y	1
IRAS 18270−0153 W	11.2 (0.5)	12.1 (0.5)	$(1.8 \pm 0.1) \times 10^{15}$	5.2×10^{22}	12.6	3.4×10^{-8}	0.42	–	1
OO Ser	13.8 (0.6)	15.3 (0.6)	$(1.4 \pm 0.1) \times 10^{15}$	7.1×10^{22}	14.7	1.9×10^{-8}	0.25	Y	2, 5
IRAS 18341−0113 S	11.1 (0.6)	11.7 (0.7)	$(1.3 \pm 0.1) \times 10^{15}$	2.4×10^{22}	14.7	5.4×10^{-8}	0.29	–	2, 5
HBC 722	12.6 (0.6)	13.8 (0.7)	$(2.3 \pm 0.2) \times 10^{15}$	5.5×10^{22}	13.2	4.1×10^{-8}	0.31	Y	1
V1057 Cyg	13.2*	–	$(1.5 \pm 0.5) \times 10^{15}$	1.0×10^{22}	16.1	1.5×10^{-7}	0.03	Y	1
V2495 Cyg	13.2*	–	$(1.8 \pm 0.3) \times 10^{15}$	3.2×10^{22}	12.6	5.6×10^{-8}	0.12	Y	1
RNO 127	13.2*	–	$(9.5 \pm 2.9) \times 10^{14}$	2.1×10^{22}	11.8	4.5×10^{-8}	0.06	Y	1
CB 230	13.2*	–	$(1.3 \pm 0.1) \times 10^{15}$	2.1×10^{22}	15.3	6.2×10^{-8}	0.19	–	1
V1735 Cyg	12.5 (1.5)	13.6 (1.6)	$(1.5 \pm 0.3) \times 10^{15}$	2.3×10^{22}	15.3	6.5×10^{-8}	0.17	Y	2, 6
HH 354 IRS	13.2*	–	$(9.3 \pm 1.7) \times 10^{14}$	1.8×10^{22}	16.5	5.1×10^{-8}	0.11	Y	1
V733 Cep	13.2*	–	$(9.2 \pm 2.1) \times 10^{14}$	1.6×10^{22}	13.8	5.7×10^{-8}	0.08	Y	1

Notes. $^{(a)}$Rotational temperature. $^{(b)}$Kinetic temperature. $^{(c)}NH_3$ column density. $^{(d)}H_2$ column density. $^{(e)}$Dust temperature. $^{(f)}$Ammonia abundance. $^{(g)}$Beam filling factor. References are: 1 – from SED fitting (this work), 2 – André et al. (2010), 3 – Roy et al. (2013), 4 – Schneider et al. (2013), 5 – Fiorellino et al. (2021), 6 – Arzoumanian et al. (2011), 7 – Evans et al. (1994), and references in Table 2.8; *Assumed T_{rot} value.; **The system is seen through a remnant outflow (Zurlo et al., 2017).

Table 2.7: Derived parameters for EX Lupi-type objects detected in NH_3 emission.

Name	$T_{\rm rot}^{(a)}$ (K)	$T_{\rm kin}^{(b)}$ (K)	$N_{\rm NH_3}^{(c)}$ (cm^{-2})	$N_{\rm H_2}^{(d)}$ (cm^{-2})	$T_{\rm dust}^{(e)}$ (K)	$[NH_3 / H_2]^{(f)}$	$\eta^{(g)}$	Outflow (Y/N)	Ref.
V512 Per (SVS 13A)	15.1 (0.6)	17.1 (0.7)	$(1.2 \pm 0.1) \times 10^{15}$	$8.6{\times}10^{22}$	17.5	1.4×10^{-8}	0.41	Y	2, 3
LDN 1415 IRS	13.2*	–	$(6.6 \pm 3.4) \times 10^{14}$	–	–	–	0.04	Y	4
V371 Ser	11.4 (0.4)	12.2 (0.4)	$(1.9 \pm 0.1) \times 10^{15}$	$6.5{\times}10^{22}$	13.4	9.1×10^{-9}	0.38	Y	2, 5
V2492 Cyg	13.2*	–	$(6.5 \pm 2.9) \times 10^{14}$	$3{\times}10^{22}$	13.4	2.1×10^{-8}	0.04	Y	1

Notes. $^{(a)}$Rotational temperature. $^{(b)}$Kinetic temperature. $^{(c)}NH_3$ column density. $^{(d)}H_2$ column density. $^{(e)}$Dust temperature. $^{(f)}$Ammonia abundance. $^{(g)}$Beam filling factor. References are: 1 – from SED fitting (this work), 2 – André et al. (2010), 3 – Pezzuto et al. (2021), 4 – Stecklum et al. (2007); 5 – Fiorellino et al. (2021); *Assumed $T_{\rm rot}$ value.

approximate the excitation temperature (see, e.g., Wienen et al., 2012; Condon & Ransom, 2016; Yan et al., 2021). The η value was determined for each source detected in the sample using the following equation, with the Rayleigh-Jeans approximation,

$$\eta = \frac{T_{\rm MB}(1,1)}{\left(T_{\rm ex} - T_{\rm bg}\right) \times \left(1 - \exp(-\tau_{\rm m}(1,1))\right)}\ , \tag{2.5}$$

where $T_{\rm MB}(1,1)$ is the main beam brightness temperature of the (1,1) transition, $\tau(1,1)$ is the optical depth of the (1,1) main line, and $T_{\rm bg} = 2.73$ K. Assuming LTE, the rotational temperature was used as the excitation temperature (e.g., Goldsmith & Langer, 1999; Wilson et al., 2009). We found that the η values in the sample range from 0.06 to 0.42 with an average of 0.25 and a median of 0.26 (see Tables 2.6 and 2.7).

The low beam filling factors may indicate clumpiness on small scales, which indeed has been revealed by interferometric observations of these ammonia transitions towards dark clouds and high-mass starless cores (see, e.g., Olmi et al., 2010; Devine et al., 2011; Ragan et al., 2011). We find no significant differences between the η values in the sampled low-mass objects compared to those in high-mass clumps (Wienen et al., 2012).

2.3.3 LSR velocities

Table 2.8 presents a comparison of the $\upsilon_{\rm LSR}$ results from the NH_3(1,1) observations with published $\upsilon_{\rm LSR}$ values from the literature. For most sources, the literature LSR velocities were derived from ^{12}CO and its rarer isotopologues. Where other lines or CO observations of nearby clouds were used, this is noted in brackets in Table 2.8.

The observations in this Thesis have yielded the first systemic $\upsilon_{\rm LSR}$ measurements for five sources. Due to the sensitivity of the observations, I was also able to derive more precise υ_{LSR} values for a number of sources (see Table 2.8), which could be helpful for follow-up studies (e.g., comparisons with stellar velocities). The differences between the NH_3 (1,1) velocities and the CO literature values are generally less than 1 km s^{-1}, while the velocities derived from the NH_3 (1,1), (2,2), and (3,3) lines agree within the errors of the fits, generally <0.03 km s^{-1}.

2.3.4 Classification and υ_{LSR}

In Table 2.8 we list all FUors/EXors from our sample including both ammonia detections and non-detections. We tabulate whether each source is an FUor or EXor and previously determined v_{LSR} velocities, with the line(s) used to determine these velocities noted in brackets (a dash indicates no available data). We also list the v_{LSR} results from our ammonia observations, where a dash indicates a non-detection. We list classifications if available in the literature, and give the references. Finally in the last column we give the distances if available, which except for RNO 1B/1C, V512 Per, Z CMa, and HH 354 IRS are adopted from the study of Audard et al. (2014). For these four sources we use updated distances, because of water maser detections associated with these sources in our Paper II. In the case of V512 Per (more commonly known as SVS 13), the source is a resolved binary, consisting of VLA 4A and 4B (e.g., Diaz-Rodriguez et al., 2022). We found CO line data for both sources, from which we find an average value of 8.35 km s^{-1}, similar to our unresolved single dish result.

2.3.5 Line widths

The line widths of the (1,1) inversion transition (where the HFS fitting method was used) range from 0.36 km s^{-1} to 2.39 km s^{-1}. For the (2,2) transition (where the Gaussian fitting was used), the line widths are between 0.42 km s^{-1} and 2.55 km s^{-1}. The derived line widths for the (2,2) transition are broader than those for the (1,1) transition. The ratios of line width, $\Delta\upsilon(2,2)/\ \Delta\upsilon(1,1)$, are between 1.02 and 2.58, with a median of 1.23 and a dispersion of 0.16. This is consistent with previous results that the line widths obtained from the hyperfine structure fitting are generally smaller than those from the Gaussian fitting method (Wienen et al., 2012). In the following analysis I only used the line width of the (1,1) transition.

In the sample, RNO 1B/1C and AR 6A/6B have the broadest lines, and both have kinetic temperatures >17 K. For RNO 1B/1C, the broad line width may be the result of shock heating and shock-driven turbulence caused by this source's powerful outflow action (see, e.g., Anglada

Table 2.8: Reference classification and v_{LSR} for the FUors/EXors in the sample, including NH_3 detections and non-detections.

Name	Type	v_{LSR} (km s^{-1})	v_{LSR} (NH_3) (km s^{-1})	Classification (Class 0 – II)	References	Distance* (pc)
RNO 1B/1C**	FUor	−17.83 (^{13}CO)	−17.83 (0.02)	1B: Class 0/II,1C: Class II	1, 2	965
V1180 Cas	EXor	–	–	–	–	600
V512 Per (SVS 13)	EXor	8.35 (^{12}CO)	8.45 (0.01)	Class I	3	275
PP 13S	FUor	−3.5 (^{12}CO)	−3.62 (0.01)	Class I	4	350
L1551 IRS 5	FUor	6.46 (^{13}CO)	6.35 (0.01)	Class I	5, 6	–
XZ Tau	EXor	6.8 (^{12}CO)	–	Class II	7, 8	140
UZ Tau E	EXor	–	–	Class II	9	140
VY Tau	EXor	+18 or +19 (^{12}CO)	–	Class II	10	140
LDN 1415 IRS	EXor	−5.2 (^{12}CO)	−5.77 (0.02)	Class I	11	170
DR Tau	EXor	–	–	Class II	12	–
V582 Aur	FUor	−10.85 (^{13}CO)	–	Class II	5, 13	–
V1118 Ori	EXor	–	–	Class II	14	414
Haro 5a IRS	FUor	10.90 (^{13}CO)	10.7 (0.01)	Class 0/I	5, 16	450
NY Ori	EXor	–	–	–	–	414
V1143 Ori	EXor	–	–	Class II	17	500
V883 Ori	FUor	4.10 (^{13}CO)	–	Class I	5, 18	460
HBC 494	FUor	~4.6 (^{12}CO)	–	Class I	19	–
V2775 Ori	FUor	3.08 (^{13}CO)	3.05 (0.01)	late Class I	5, 20	420
FU Ori	FUor	11.96 (^{13}CO)	–	Class II	5, 21	450
V1647 Ori	FUor	10.06 (^{13}CO)	–	Class I/II	5, 22, 23	400
NGC 2071	FUor	9.2 (^{13}CO)	10.4 (0.01)	–	24	–
V899 Mon	FUor	9.57 (^{13}CO)	9.63 (0.01)	Class II	5, 25	–
IRAS 06393+0913	FUor	4.3 (0.2) (^{12}CO)	7.72 (0.02)	Class I	26, 27	–
AR 6A/6B	FUor	5.02 (^{13}CO)	5.06 (0.02)	Class II	5, 28	800
IRAS 06297+1021W	FUor	5.1 (0.2) (^{12}CO)	4.17 (0.01)	Class I	26, 27	–
V900 Mon	FUor	13.77 (^{13}CO)	–	Class I	5, 29, 30	1100
V960 Mon	FUor	23.81 (^{13}CO)	23.8 (0.02)	Class II	5, 31	–
Z CMa	FUor	13.91 (^{13}CO)	13.8 (0.02)	Class I	5, 32	1125
iPTF 15AFQ	FUor	14.04 (^{13}CO)	13.3 (0.01)	Class I	5, 33	–
IRAS 18270-0153W	FUor	–	7.61 (0.01)	Class I	34	–
OO Ser	FUor	8.36 (^{13}CO)	8.31 (0.01)	Class I	5, 35	311
IRAS 18341-0113S	FUor	–	9.27 (0.01)	Class I	34	–
V371 Ser	EXor	–	8.34 (0.01)	–	–	311
Parsamian 21	FUor	27 (Li I, Fe I)	–	Class I/ II	36	400
Gaia 18dvy	FUor	–	–	Class II	37	–
V1515 Cyg	FUor	5.80 (^{13}CO)	–	–	1	1000
PV Cep	EXor	−3 (nearby cloud)	–	–	38	325
V2492 Cyg	EXor	4.97 (^{13}CO)	4.71 (0.02)	Class I	1, 39	600
HBC 722	FUor	4.05 (^{13}CO)	4.93 (0.01)	Class II	1, 40	600
V1057 Cyg	FUor	4.3 (^{13}CO)	4.35 (0.02)	Class II	1, 41	600
V2495 Cyg	FUor	–	−3.83 (0.02)	Class I/II	42	800
RNO 127	FUor	–	−2.90 (0.01)	–	–	800
CB 230	FUor	2.78 (N_2H^+)	2.79 (0.01)	Class 0/I	27, 43	–
V1735 Cyg	FUor	4.05 (^{13}CO)	3.80 (0.01)	Class II	1, 44, 45	900
HH 354 IRS	FUor	−1.1 (CS)	−1.52 (0.01)	Class 0/I	46, 47	750
V733 Cep	FUor	−17.83 (^{13}CO)	−8.93 (0.01)	Class II***	1, 27	800

Notes. The first column lists the name, the second the type of object, while third and fourth columns we list v_{LSR} from literature observations (primarily of CO) and our v_{LSR} derived from ammonia observations. The fifth column lists the classification (if available), sixth the references, and finally the distances. Errors are given in parentheses.

* – Adopted from Audard et al. (2014), exceptions are: RNO 1B/1C (Bailer-Jones et al., 2021), V512 Per (Bailer-Jones et al., 2021), Z CMa (Dong et al., 2022), HH 354 IRS (Reipurth et al., 1997). In these cases we detected water masers, and adopted updated distance values in our Paper II.

** – RNO 1B/1C is counted into the Class II statistics in Section 2.4.2.

1 – Fehér et al. (2017), 2 – Quanz et al. (2007a), 3 – Diaz-Rodriguez et al. (2022), 4 – Sandell & Aspin (1998), 5 – Cruz-Sáenz de Miera et al. (2022a), 6 – Fuller et al. (1995), 7 – ALMA Partnership et al. (2015), 8 – Zapata et al. (2015), 9 – Mathieu et al. (1996), 10 – Herbig (1990), 11 – Stecklum et al. (2007), 12 – Banzatti et al. (2014), 13 – Ábrahám et al. (2018), 14 – Giannini et al. (2016), 15 – Kóspál et al. (2017a), 16 – Kóspál et al. (2021), 17 – Parsamian & Mujica (2004), 18 – White et al. (2019), 19 – Ruíz-Rodríguez et al. (2017b), 20 – Zurlo et al. (2017), 21 – Herbig (1977), 22 – Ábrahám et al. (2004), 23 – Principe et al. (2018), 24 – Stojimirović et al. (2008), 25 – Park et al. (2021), 26 – Wouterloot & Brand (1989), 27 – Connelley & Reipurth (2018), 28 – Moriarty-Schieven et al. (2008), 29 – Reipurth et al. (2012), 30 – Takami et al. (2019), 31 – Kóspál et al. (2015), 32 – Gramajo et al. (2014), 33 – Miller et al. (2015), 34 – Connelley & Greene (2010), 35 – Kóspál et al. (2006), 36 – Kóspál et al. (2008), 37 – Szegedi-Elek et al. (2020), 38 – Torrelles et al. (1986), 39 – Hillenbrand et al. (2013), 40 – Kóspál et al. (2016), 41 – Szabó et al. (2021), 42 – Liu et al. (2018), 43 – Chen et al. (2007), 44 – Harvey et al. (2008), 45 – Kóspál et al. (2011), 46 – Bronfman et al. (1996), 47 – Reipurth & Aspin (1997)

*** – Based on the extreme similarities to FU Ori from optical and NIR spectra et al., 1994; Quanz et al., 2007a; Bae et al., 2011). In contrast, previous observations suggest that AR 6A/6B does not have a CO outflow (Moriarty-Schieven et al., 2008). Based on its environment, which shows large concentration of dense material offset from the source (compared to that around RNO 1B/1C; see Figure 2.2), it may be possible that its increased line width and elevated kinetic temperature are caused by turbulence from the nearby structures, which are in the beam of the observations. The spectral energy distributions (SEDs) are discussed in Section 2.3.6.

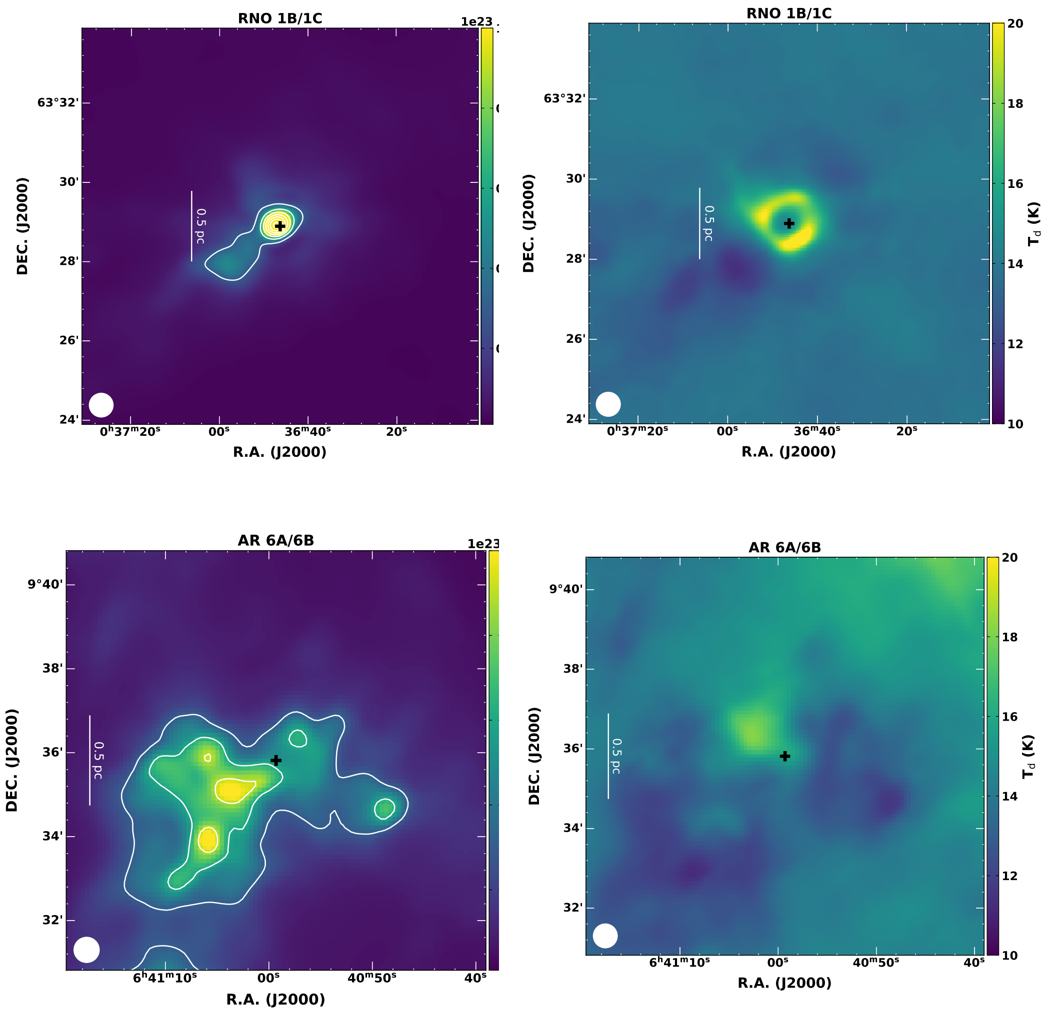

Figure 2.2: H_2 column density (left) and dust temperature (right) maps derived from the pixel-by-pixel SED fitting of the *Herschel* data, convolved to the Effelsberg beam (shown in the bottom left corner) of RNO 1B/1C and AR 6A/6B. The field of view is the same for all sources, corresponding to $10'' \times 10''$, + symbols represent the pointing positions listed in Tables 2.2, 2.3 and 2.8, respectively. The physical scale is presented for sources with known distances, taken from the study of Audard et al. (2014) or described in the notes of Table 2.8. The color scale is not the same for the two sources. Figures from Szabó et al. (2023a)

The observed line width, $\Delta v(1,1)$, is related to the velocity dispersion, $\sigma_{\rm obs}$, as $\Delta v = \sqrt{8 \ln 2} \cdot \sigma_{\rm obs}$. The observed line widths or velocity dispersions of the inversion lines have contributions from both thermal and non-thermal motions (e.g., Hacar et al., 2016),

$$\Delta v_{\rm obs} = \sqrt{\Delta v_{\rm th}^2 + \Delta v_{\rm nt}^2}\,, \quad \sigma_{\rm obs} = \sqrt{\sigma_{\rm th}^2 + \sigma_{\rm nt}^2}\,, \tag{2.6}$$

where $\Delta v_{\rm th}$ and $\sigma_{\rm th}$ are the thermal line width and velocity dispersion, respectively, and $\Delta v_{\rm nt}$ and $\sigma_{\rm nt}$ are the non-thermal line width and velocity dispersion, respectively. The thermal line width and velocity dispersion can be calculated from

$$\Delta v_{\rm th} = \sqrt{\frac{8\ln(2)\,{\rm k}\,T_{\rm kin}}{m}}\,, \quad \sigma_{\rm th} = \sqrt{\frac{{\rm k}\,T_{\rm kin}}{m}} \tag{2.7}$$

where k is the Boltzmann constant, $T_{\rm kin}$ is the kinetic temperature, and m is the molecular weight of the given molecule, in this case $m_{\rm NH_3} = 17$. According to Eq. 2.6, the non-thermal motions can be derived by subtracting the thermal motions from the total. The kinetic temperatures derived from ammonia are used to derive thermal line widths for sources with both NH_3 (1,1) and NH_3 (2,2) detections. For sources with only an NH_3 (1,1) detection, we assume the average kinetic temperature of 14.6 K (derived earlier in Section 2.3.1) to calculate the contribution of thermal motions. The results are listed in Tables 2.2 and 2.3, respectively. Based on these results, it can be concluded that the line widths of most sources are dominated by non-thermal contributions.

Once $\sigma_{\rm nt}$ is determined, the Mach number can be derived in order to distinguish between sonic ($Ma \leq 1$), transonic ($1 < Ma \leq 2$) and supersonic ($Ma > 2$) environments. When calculating the Mach number, $Ma = f(T_{\rm kin}) = \sigma_{\rm nt}/{\rm c_s}$, where c_s is the sound speed of the molecular gas, both terms depend on $T_{\rm kin}$. Typically, the same $T_{\rm kin}$ is adopted for evaluating $\sigma_{\rm nt}$ and the sound speed (e.g., Hacar et al., 2016). I calculated the Mach numbers for all sources with detections of both the (1,1) and (2,2) transitions using the values of $T_{\rm kin}$ derived from our observations; the results are listed in Tables 2.2 and 2.3 for FUors and EXors, respectively. Using the average kinetic temperature of 14.6 K, the Mach numbers are also derived for sources with only (1,1) detections, which are marked in Tables 2.2 and 2.3. Based on these calculations, 10 sources have Mach numbers of <1, indicative of sonic motions, while 13 sources show transonic motions. Finally, five FUors in our sample have Mach numbers larger than 2, indicating supersonic environments. Because these 5 FUors are associated with molecular outflows (see Table 2.6), their higher Mach numbers may be attributable to turbulence driven by outflow shocks. Notably, in the case of Z CMa from high-resolution SPHERE observations Antoniucci et al. (2016) have revealed a massive outflow which aligns with our finding of supersonic motions in this source. Interestingly, for the EXors, there is no indication of supersonic environments. It is also worth noting that there are several examples of sources that have Mach numbers <1 despite being known to host outflows (i.e., V899 Mon, V2495 Cyg, HH 354 IRS, etc). Our results show that the host environments of most of the eruptive stars in our sample are dominated by sonic and transonic motions on the scales sampled with the Effelsberg beam (∼37″), indicating that most eruptive stars reside in rather quiescent host environments.

2.3.6 Spectral Energy Distributions (SEDs)

The H_2 column densities are needed in order to determine ammonia abundances for sources detected in ammonia. For seven sources with NH_3 (1,1) detections in the survey, H_2 column density and dust temperature maps derived from the *Herschel Gould Belt* survey (André et al., 2010) were already available in the literature. For these sources, we measured column density and dust temperature values for our targets from the published maps, and these adopted values with the literature references are given in Tables 2.6 and 2.7. Where H_2 column density and dust temperature maps were available in the literature for sources undetected in NH_3 in our survey, these parameters were still measured for the targets, included in Table 2.1.

For the remaining sources with NH_3 (1,1) detections, we derived H_2 column density and dust temperature maps using archival *Herschel* SPIRE data at 250 μm, 350 μm, and 500 μm [3] using the same methods as previous studies (e.g., André et al., 2010; Elia et al., 2017). Prior to pixel-by-pixel spectral energy distribution (SED) fitting, the archival data were convolved to a common angular resolution of 36.″3 (i.e., the beamsize of Herschel/SPIRE at 500 μm), which is comparable to the angular resolution of our ammonia observations, and then projected onto the same grid as the 500 μm data.

Assuming that the SED of the dust emission follows the modified-blackbody model, the flux density, S_ν, at frequency ν can be expressed as

$$S_\nu = (1 - e^{-\tau_\nu}) B_\nu(T_d) \Omega \,, \tag{2.8}$$

where τ_ν is the optical depth at the frequency ν, $B_\nu(T_d)$ is the Planck function evaluated at the dust temperature T_d, and Ω is the solid angle of the beam. The H_2 column density, N_{H_2}, is proportional

[3] The data have been downloaded from `http://archives.esac.esa.int/hsa/whsa/`

to τ_ν with the relationship:

$$N_{H_2} = \frac{\tau_\nu}{\kappa_\nu \mu m_H} , \tag{2.9}$$

where μ is the molecular weight per hydrogen molecule, taken to be 2.8 (Kauffmann et al., 2008), κ_ν is the dust opacity per unit (dust+gas) mass, and m_H is the mass of hydrogen. The dust opacity per unit mass, κ_ν, is approximated by the power law $\kappa_\nu = 0.1(\nu/1000\mathrm{GHz})^\beta \mathrm{cm}^2/\mathrm{g}$ (e.g., Hildebrand, 1983), where β is the dust emissivity index and the canonical gas-to-dust ratio of 100 has been applied. Following previous studies (e.g. André et al., 2010; Elia et al., 2017), β is assumed to be 2 here. The SED fitting was performed using the "LMFIT"[4] python package (Newville et al., 2014) to fit the two free parameters, N_{H_2} and T_d, for every pixel. The results are shown in Figure 2.3, and the corresponding beam averaged values are given in Tables 2.6 and 2.7.

For sources with NH_3 (1,1) detections, the dust temperatures range from 11.8 K to 21.8 K and the derived H_2 column densities range from 9.0×10^{21} cm^{-2} to 2.2×10^{23} cm^{-2}. We compared the dust temperatures and gas kinetic temperatures for sources in the sample with T_{kin} measurements (i.e., those with both NH_3 (1,1) and (2,2) detections), and found that in most cases the dust temperature and gas kinetic temperature agree within 3 K. The only exception is RNO 1B/1C, which has a gas kinetic temperature that is much higher than its dust temperature (T_{kin} = 21.3 K, T_d = 14.5 K). Such a scenario could be caused by inefficient gas-to-dust coupling and gas cooling if the density was < $10^{3.5}$ cm^{-3} (Goldsmith, 2001). However, RNO 1B/1C is surrounded by deeply embedded objects, forming a small cluster (Quanz et al., 2007a). Based on the dust temperature map of the source (see Figure 2.3) there is significantly warmer dust within <1′ of the source position, and this warmer material likely contributes to the higher temperature measured in the beam of the 100-m telescope.

Interestingly, based on the derived H_2 column density maps (Figure 2.3), the host environments of the eruptive stars detected in NH_3 (1,1) are quite diverse on scales larger than the Effelsberg beam (~37″). A few sources are relatively isolated, while others are associated with larger, extended cloud structures.

[4]`https://lmfit.github.io/lmfit-py/`

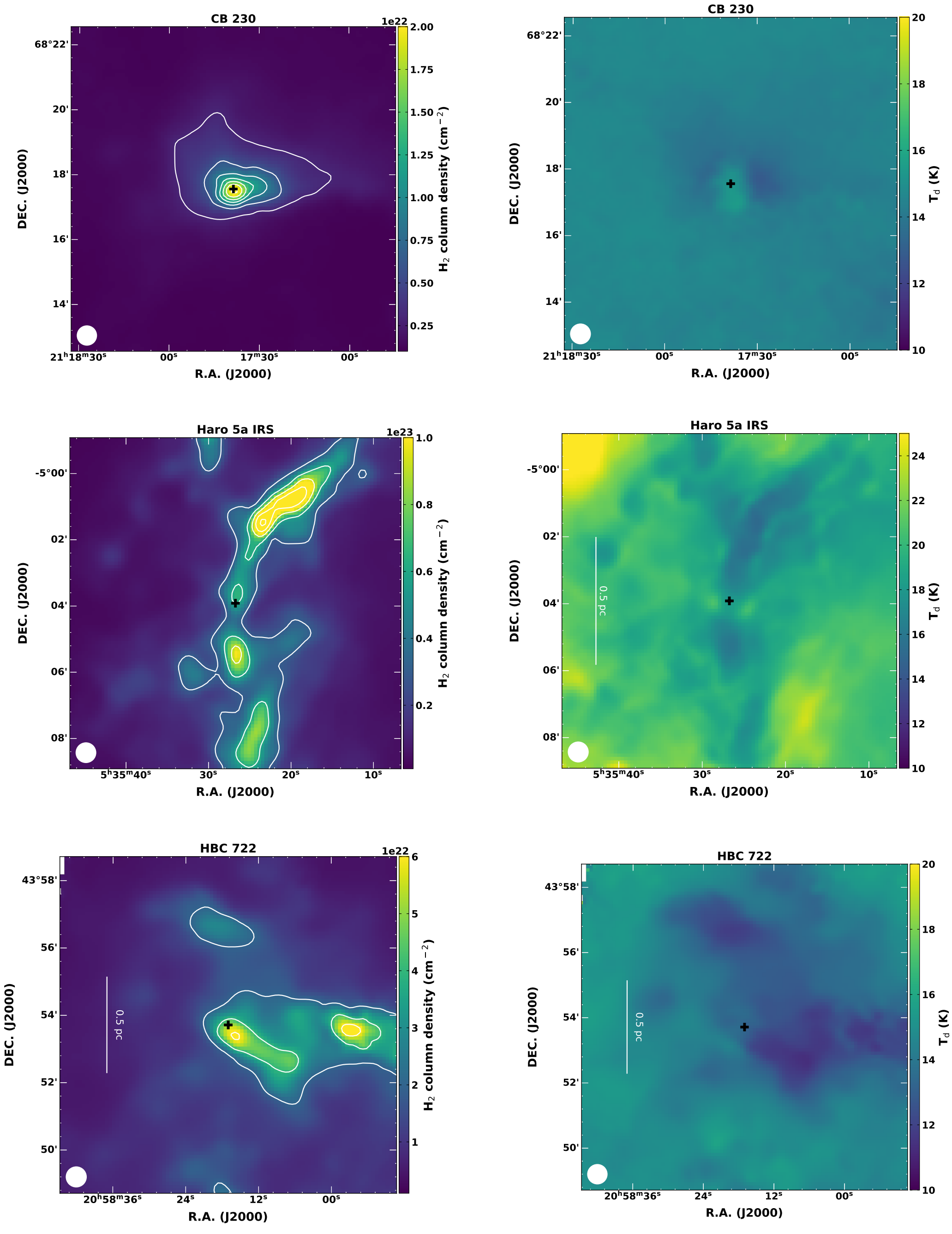

Figure 2.3: H_2 column density (left) and dust temperature (right) maps derived from the pixel-by-pixel SED fitting of the *Herschel* data, convolved to the Effelsberg beam (shown in the bottom left corner). Figures from Szabó et al. (2023a).

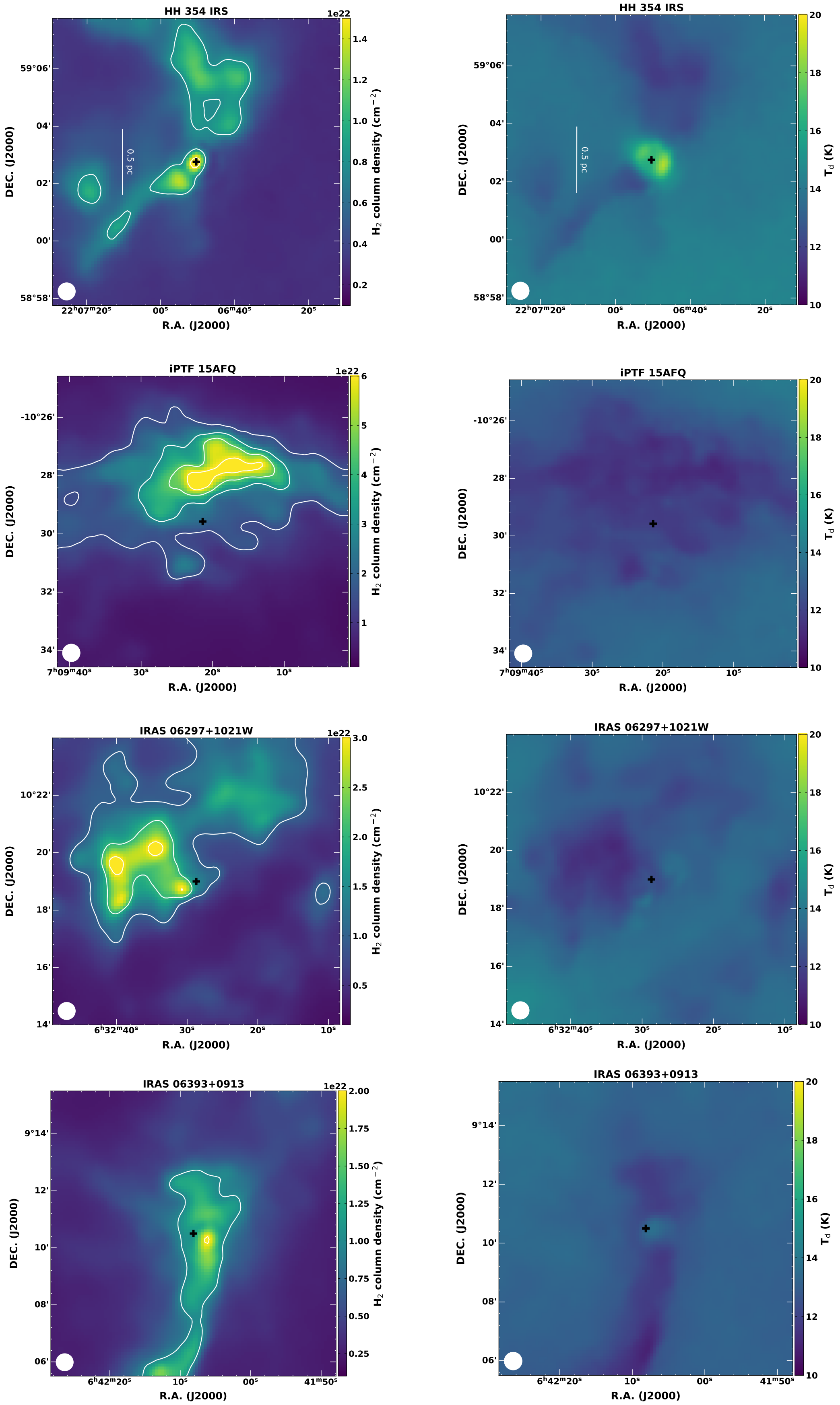

Figure 2.3: (Continued.)

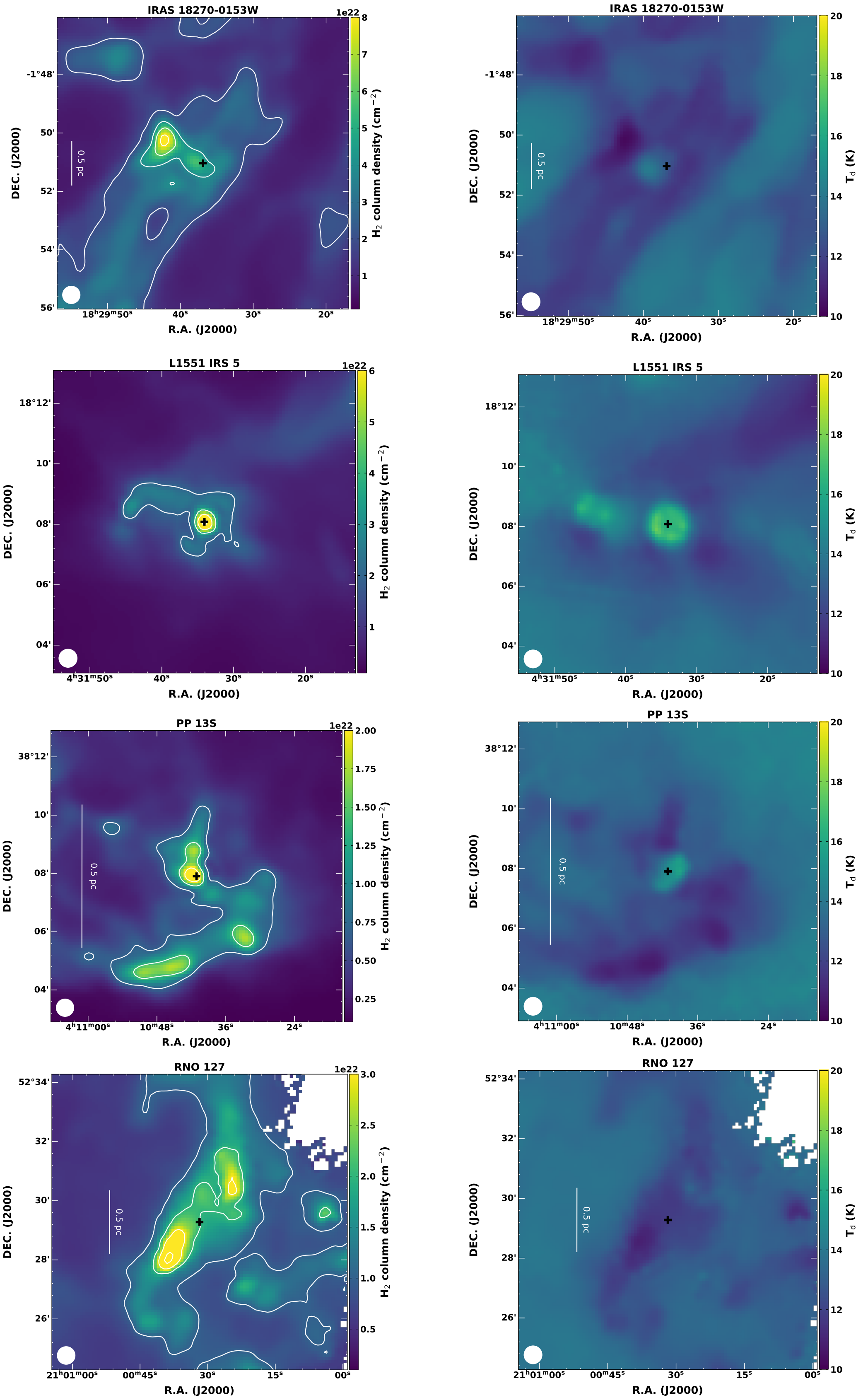

Figure 2.3: (Continued.)

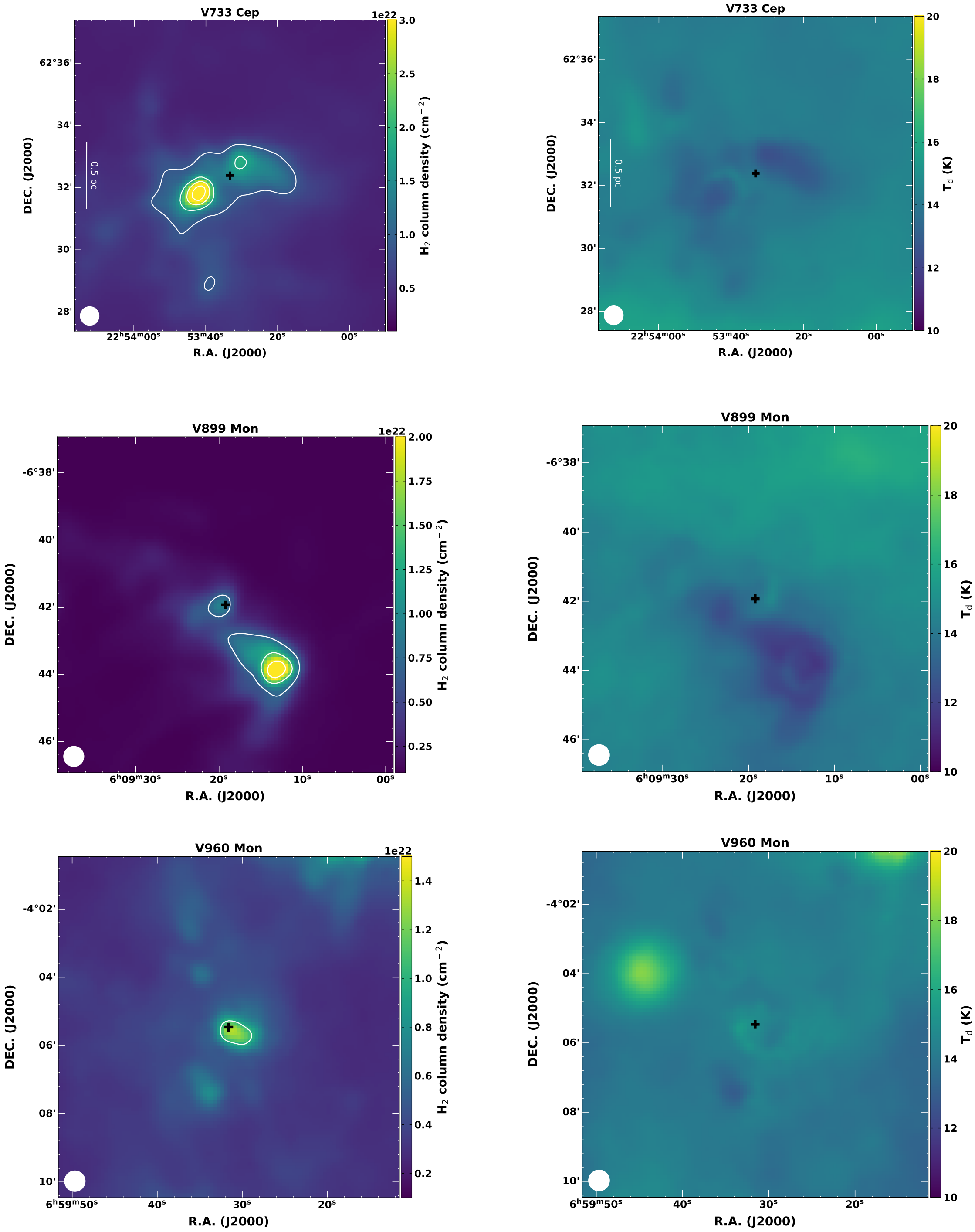

Figure 2.3: (Continued.)

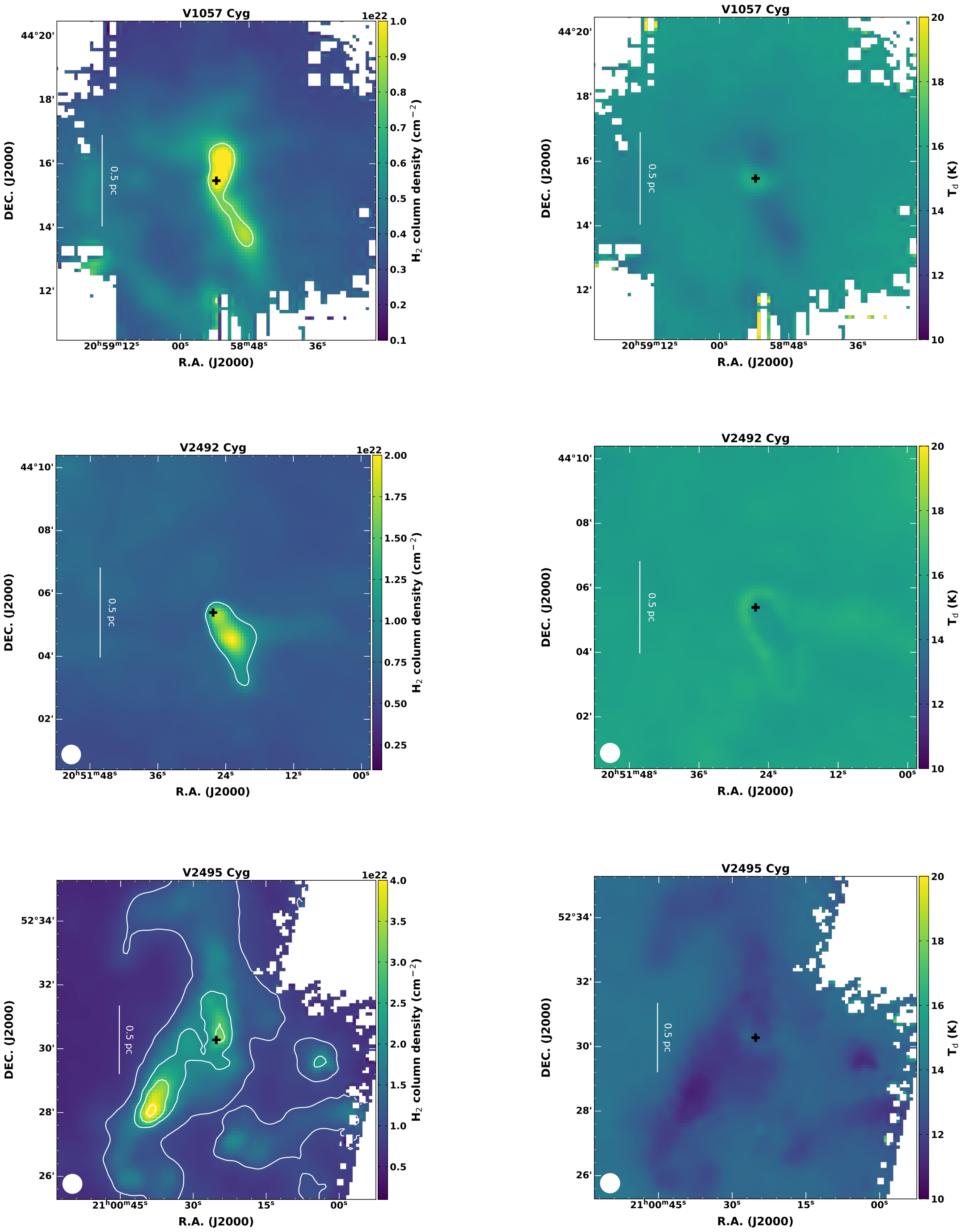

Figure 2.3: (Continued.)

2.3.7 Ammonia abundance

I used the NH_3 and H_2 column densities from Sections 2.3.1 and 2.3.6 respectively to derive ammonia abundances, $\chi = N_{NH_3}/N_{H_2}$. The derived abundances, listed in Tables 2.6 and 2.7, range from 4.7×10^{-9} to 1.5×10^{-7}, with an average of 3.6×10^{-8} and a median of 2.8×10^{-8}, respectively.

The results can be compared with NH_3 abundances from other studies, which focus on low-, intermediate-, and high-mass star forming regions. The derived NH_3 abundances are similar to values found in cold, dark clouds (see, e.g., Ohishi et al., 1992). With very few exceptions, the derived NH_3 abundances fall within the range observed towards IRDCs (e.g., 0.7×10^{-8} to 15.9×10^{-8}; Pillai et al., 2006; Zhang et al., 2011). (The exceptions are NGC 2071 and IRAS 06393+0913, which have abundances of $\sim 0.6 \times 10^{-8}$ and $\sim 0.5 \times 10^{-8}$, respectively; see Table 2.6.) The average abundance of 3.6×10^{-8} is also similar to the average values reported for IRDCs by Pillai et al. (2006) ($\sim 4 \times 10^{-8}$) and for high-mass clumps by Dunham et al. (2011) (4.6×10^{-8}). Interestingly, NH_3 abundances observed towards Herbig Ae/Be stars, which are intermediate-mass pre-main sequence stars, range from 1×10^{-8} to 4×10^{-8} (Fuente et al., 1990), on the lower end of the range observed towards IRDCs and towards our sample.

2.4 Discussion

2.4.1 Ammonia in the neighbourhood of outbursting systems

Based on previous studies, ammonia emission can have different origins, corresponding to grain surface and gas-phase chemistry (see Jørgensen et al. 2020 for the most recent review, and references therein). In the following, I compare our observations with these different scenarios. First, I discuss ammonia release from grains, then examine the formation of NH_3 via gas-phase chemistry.

During an outburst, the whole disk experiences a temperature increase due to the energy released in the very inner few 0.1 au of the disk (e.g., Fischer et al., 2023). The temperature increase in the outer part of the disk could easily sublimate ammonia molecules off the grains, releasing them back into the gas phase (Guesten & Fiebig, 1988) and enhancing the ammonia abundance. However, any ammonia set free in this way should not make a significant contribution to our observed ammonia emission: because our FWHM beam size of $\sim 37''$ (i.e., 5000 au at 140 pc) is much larger than typical disk sizes (~ 60 au; Maury et al., 2019), beam dilution effects should result in only a very minor contribution to the ammonia signals we observe. Such enhancements would be better constrained with higher angular resolution observations of ammonia transitions toward the disks around eruptive stars, especially during the bursting phase.

Alternatively, chemical models suggest that ammonia molecules on dust grains can be released into the gas phase through the passage of shocks produced by molecular outflows (e.g., Holdship et al., 2017). Such effects have already been confirmed by observations of outflows (e.g., Tafalla & Bachiller, 1995; Umemoto et al., 1999; Feng et al., 2022), and could explain the relatively high ammonia abundances in some sources, such as RNO 1B/1C. In fact, almost all of the sources in our sample with ammonia (1,1) detections possess CO outflows (see Tables 2.6 and 2.7).

As suggested by early studies (e.g., Herbst & Klemperer, 1973; Galloway & Herbst, 1989), ammonia can also form in cold molecular gas via successive hydrogenation of N^+ by H_2 and the subsequent electron recombination of NH_4^+. Hence, it is also possible that the observed ammonia emission is dominated by circumstellar envelopes and/or ambient clouds; as discussed in Section 2.3.7, we find that the eruptive stars in our sample generally have NH_3 abundances similar to those of IRDCs. A circumstellar envelope is an important part of any YSO system, being a reservoir of material, replenishing a disk with more matter (e.g., Hartmann & Kenyon, 1996). For example, previous observations of a deeply embedded Class 0 protostar suggest that the ammonia emission is dominated by the circumstellar envelopes on scales of 10^4 au, revealed from interferometric observations (Tanner & Arce, 2011; Jhan & Lee, 2021). Based on Figure 2.3, we find that CB 230, HH 354 IRS, L1551 IRS 5, PP 13S, RNO 1B/1C, V960 Mon, and V1057 Cyg coincide with dense dust concentrations, indicative of the presence of dense circumstellar envelopes. In several cases, our observations are the first NH_3 detections of dense circumstellar envelopes identified in other datasets. The dense circumstellar envelopes of RNO 1B/1C and V1057 Cyg have been confirmed by an interferometric ^{13}CO and $C^{18}O$ survey (Fehér et al., 2017), with further evidence for an envelope in V1057 Cyg from its SED, using the extensive multi-wavelength data available for this source (Szabó et al., 2021). Similarly, we detect NH_3 (1,1) and (2,2) toward the EXor-type object V371 Ser (also known as EC 53), known to have a dense circumstellar envelope based on millimeter observations and radiative transfer modelling (e.g., Baek et al., 2020; Lee et al., 2020, and references therein).

The ammonia detections in the survey, combined with the *Herschel* column density maps, suggest that V2492 Cyg and V2495 Cyg are also associated with dense material. However, it is clear they do not possess the highest column densities/most concentrated peaks. In the case of AR 6A/6B, our NH_3 (1,1) and (2,2) detections are tentative evidence for the presence of dense gas. In the H_2 column density map (Figure 2.3), however, the dust concentrations appear offset from the target source. Kóspál et al. (2017a) found that the CO emission peak at $\upsilon_{\rm LSR}$ = 5.3 $km\,s^{-1}$ (similar to the 5.06 $\rm km\,s^{-1}$ derived from the ammonia (1,1) transition) was offset from AR 6A/6B, and suggested, based on the *Herschel*/SPIRE 250 μm image, that this source lies in a cavity. Based on these results and our H_2 column density map (Figure 2.3), it is most likely that the NH_3 emission picked up by the Effelsberg beam originates from material offset from the source and may not be physically associated with the object. Therefore the velocity discrepancy is likely due to the two lines tracing different physical components along the line of sight, rather than a fitting error. For other sources with NH_3 detections but without associated dense dust concentrations, their ammonia emission might arise from ambient clouds.

The non-detections of ammonia transitions in our survey could indicate that dense circumstellar envelopes are not present or that the objects are too far away for their envelopes to be detected. The distances are known for the majority of sources in the sample (e.g., Audard et al., 2014), allowing the investigation of the second possibility. Interestingly, RNO 1B/1C is the farthest source in our sample, yet (relatively strong) NH_3 emission was still detected in multiple transitions. Similarly, at least NH_3 (1,1) was detected towards other sources with large distances, such as Z CMa, V1735 Cyg and V2495 Cyg, suggesting that distance is unlikely to be a main explanation for NH_3 non-detections. Instead, the non-detections may indicate that dense circumstellar envelopes have already been dispersed. For instance, the ammonia non-detection in the case of V1515 Cyg is consistent with a recent multiwavelength SED analysis that found no clear sign of a massive circumstellar envelope (Szabó et al., 2022). This is in contrast to the results we have found for V1057 Cyg (see also, Szabó et al., 2021).

It is important to note that many of the targeted sources are known binaries or multiples, often with strong outflows. Given the 5″ pointing accuracy and the 37″ beam size of the observations, it is likely that the emission we detect includes contributions from all components in known binary or multiple systems. This encompasses not only the individual disks and envelopes of the sources, but also any shared circumstellar material and potentially overlapping outflows. This is notable in sources, for example, RNO 1B/1C (e.g., Sepúlveda et al., 2020, and references therein), V960 Mon (Weber et al., 2025), FU Ori (Pérez et al., 2020), and Z CMa (e.g., Dong et al., 2022, and references therein), where in all cases multiple sources are present within a few arcseconds.

2.4.2 Is the standard classification scheme reliable for outbursting systems?

Based on the standard classification scheme (e.g., Greene et al., 1994; Evans et al., 2009), the sources in the sample have been classified as Class I, Class II, or transition objects (i.e. Class 0/I or Class I/II, see Table 2.8). Because Class II objects are thought to be beyond the embedded phase (see the recent review by Fischer et al., 2023, and references therein), their host environments are not expected to harbor as much dense gas as those of younger sources. In the survey, the Class 0/I and Class I sources have the highest ammonia detection rates: 16 sources (3 Class 0/I and 13 Class I) are detected in NH_3 (1,1), corresponding to detection rates of 100% for Class 0/I sources and 81% for Class I sources. Seven of these sources are also detected in NH_3 (2,2). Notably, however, NH_3 (1,1) was detected toward 9 sources classified as older than Class I, 4 of which are also detected in (2,2) emission. Ammonia was detected towards 1 Class I/II and 8 Class II objects in the survey, corresponding to detection rates of 33% and 47%, respectively. Some of the Class II sources (namely HBC 722, V1057 Cyg, V1735 Cyg, and RNO 1B/1C) have higher NH_3 and H_2 column densities than some sources classified as Class I or Class 0/I or Class I/II transition objects.

The results show that, as expected, the younger systems have significantly higher ammonia detection rates. However, based on the dust and ammonia evidence, some sources classified as older systems, i.e. Class II sources, can still be associated with high concentrations of their dense cores, indicative of a younger evolutionary stage. Interestingly, it is puzzling that many younger sources were not detected in ammonia in the survey (see Table 2.8). It is important to emphasize the need for future interferometric studies to better understand the effects of the outbursts on the dense cores of young eruptive stars. Higher-angular resolution NH_3 observations could potentially probe whether there is a connection/ongoing accretion from cloud/filament down to core scales (e.g., Redaelli et al., 2022), since NH_3 can be used to identify the presence of dense gas. As already proposed by Quanz et al. (2007b), the standard classification scheme for low mass YSOs might not be able to adequately classify FUors, since they might represent an in-between evolutionary stage in the standard classification scheme. Furthermore, FUors might undergo several outburst events (Herbig, 1977; Hartmann & Kenyon, 1985), just like EXors. After several outbursts, the envelope vanishes in about several hundred thousand years (as discussed above supplying the accretion disk with more material, e.g., Fischer et al., 2023). As a consequence, the objects enter a low accretion state permanently (i.e. become T Tauri stars), as discussed by Takami et al. (2018, 2019). Weintraub et al. (1991) and Sandell & Weintraub (2001) also suggest that

FUors are younger than T Tauri stars and might be an important link between the more embedded Class I and the more evolved Class II stages (the latter closer to or being T Tauri stars.) Additionally, some FUors have features of both Class I and Class II sources: warm continuum consistent with Class II sources, but rotational line emission typical of Class I, far higher than Class II sources with similar mass/luminosity (Green et al., 2013).

Compared to the later evolutionary stages, one of the important features of the embedded phase is the presence of dense circumstellar envelopes around YSOs. The appearance of the 10 μm silicate feature in absorption has been regarded as a signature for such a circumstellar envelope (Quanz et al., 2007b), and dust continuum emission also traces the cold envelopes around YSOs. Molecular line tracers like ammonia can provide another tool to investigate the surrounding environments. Because the effective critical densities of the NH_3 (1,1) and (2,2) lines are $7.9{\times}10^2$ cm^{-3} and $1.6{\times}10^4$ cm^{-3}, respectively, the detection of NH_3 (1,1) and (2,2) would suggest the presence of dense gas at a H_2 density of $\sim 1 \times 10^4$ cm^{-3} (Shirley, 2015), which would in turn indicate the embedded phase. The presence of dense gas ($\sim 1 \times 10^4$ cm^{-3}) indicates that some of the eruptive stars in our sample lie at an earlier phase than previously classified (see Table 2.8). For instance, our result from the ammonia observations agrees well with previous studies on V371 Ser (EXor), which was classified as a Class I object based on its spectral index and bolometric temperature (e.g., Dunham et al., 2015), but ALMA observations revealed that its envelope has a much higher mass than its disk and protostar, suggesting that the source might actually be a Class 0 object (Lee et al., 2020). We suggest that incorporating more data regarding the presence of dense material surrounding these peculiar objects into the standard classification scheme could better illuminate the evolutionary stages of eruptive FUors and EXors.

By the original definition, the young eruptive star classes of FUors and EXors are Class II objects, therefore T Tauri stars (see, e.g., Adams et al., 1987; Lada, 1987; Kenyon & Hartmann, 1991; Hartmann & Kenyon, 1996). This was further suggested by the only available pre-outburst spectra for two FUors: V1057 Cyg and HBC 722, which both showed properties reminiscent of classical T Tauri stars (CTTS) prior to their outbursts (Herbig, 1977; Miller et al., 2011). However, nowadays there are many examples of more embedded young eruptive stars, which were also part of our sample, i.e. Haro 5a IRS, HH 354 IRS, L1551 IRS 5 (see, e.g., Audard et al., 2014; Connelley & Reipurth, 2018).

Apart from a single dish study by Lang & Willson (1979), there are no dedicated surveys using ammonia to investigate the dense environments focusing only on T Tauri stars, the closest objects to the ones in our study. The sample of Lang & Willson (1979) consisted of 34 T Tauri stars, located in Taurus-Auriga and the young star cluster NGC 2264, accessible with the Arecibo telescope. Out of the 34 sources they detected at least the (1,1) transition toward 13 sources, a detection rate of 38%. In our case, the sample consisted of 17 Class II sources (see Table 2.8), and we have detected at least the (1,1) transition toward 8 of them, which is ~47%. Lang & Willson (1979) found kinetic temperatures from 26 K to 37 K, and column densities between 1 and 5.9×10^{14} cm^{-2}. In our sample, the Class II sources (see Table 2.8) have kinetic temperatures between 13.63 K and 21.35 K and column densities from $1.3 \times 10^{14}\, cm^{-2}$ to $1.8 \times 10^{15}\, cm^{-2}$. When compared to Lang & Willson (1979), for a few of the Class II sources, namely V899 Mon, V960 Mon, and V733 Cep, the column densities are within the same order of magnitude, i.e., $\sim10^{14}$ cm^{-2}. However, there are other Class II sources which have ~1 order of magnitude higher column density values (*i.e.*, $\sim 10^{15}$ cm^{-2}), namely RNO 1B/1C, AR 6A/6B, HBC 722, V1057 Cyg, and V1735 Cyg. The similar column densities suggest that ammonia does not probe the part of the envelope impacted by the outburst.

I also compared our results to NH_3 observations of Herbig Ae/Be stars, YSOs that are the intermediate mass counterparts of T Tauri stars (see, e.g., Waters & Waelkens, 1998). These YSOs have similar properties to the objects in our sample, such as P Cygni profiles indicating mass loss (Strom et al., 1972), stellar winds (Canto et al., 1984), and are usually illuminating nebulosities (just like the first few FUor examples) (Herbig, 1960), however outflows are more typical and better understood in low-mass YSOs (e.g., Pezzuto et al., 1997; Tambovtseva & Grinin, 2016; Fischer et al., 2023). Towards three Be Herbig stars, a small survey conducted by Fuente et al. (1990), found ammonia column densities ranging between 0.5×10^{14} and 2.9×10^{14} cm^{-2}, which values are within the same range for 5 sources (NGC 2071, V899 Mon, IRAS 06393+0913, V960 Mon and Z CMa) in our sample (see Tables 2.6 and 2.7). In their study Fuente et al. (1990) also obtained maps and found that in HD 200775, a source illuminating an extended reflection nebula in NGC 7023, three different clumps could be traced with the NH_3 emission, with varying rotational temperatures and column densities. High-angular resolution observations in the future of a selected sample of eruptive objects could reveal similar clumpiness of the ammonia emission in the host environments of FUors/EXors.

The classification of sources based on ammonia observations provide valuable insight, and its significance may be further enhanced by linking it to potential eruption mechanisms such as gravitational instabilities (GI), stellar flybys, or binary interactions. These mechanisms likely influence not only the eruptive behaviour but also the surrounding physical and chemical environments, and ammonia emission may show differences depending on the dominant mechanism. This highlights the importance of high-resolution interferometric observations to disentangle these effects, particularly in systems with known dynamical interactions, such as Z CMa with a known flyby event (Dong et al., 2022), where ammonia has been detected.

2.5 Conclusions

We carried out the first dedicated ammonia survey of a large sample of FUors and EXors in order to investigate their host environments. For this survey, we used the Effelsberg 100-m radio telescope, where I had the opportunity to also observe the full survey. The observations resulted in the detection of NH_3 (1,1) in 28 sources (24 FUors, 4 EXors), NH_3 (2,2) in 12 sources (10 FUors, 2 EXors), and NH_3 (3,3) in 2 sources (the FUor-type object RNO 1B/1C and the EXor-type object V512 Per, the latter more commonly known as SVS 13). Ammonia emission was not detected toward any of the Gaia alert sources. The analysis of the data has lead to the following conclusions:

- Based on the results for the 12 sources with both NH_3 (1,1) and NH_3 (2,2) detections the kinetic temperatures range from ~12 K to ~21 K, which is slightly lower than the $T_{\rm kin}$ values reported toward classical T Tauri stars. The ammonia column densities for sources in our sample detected in NH_3 (1,1) range from $5.2 \times 10^{13}\ cm^{-2}$ to $3.2 \times 10^{15}\ cm^{-2}$. The average value for our sample, $1.18 \times 10^{15}\ cm^{-2}$, is higher than the ammonia column densities found toward T Tauri stars. The ammonia abundances with respect to H_2 for our sample range from 4.7×10^{-9} to 1.5×10^{-7} with an average of 3.6×10^{-8} and a median of 2.8×10^{-8}, comparable to IRDCs.

- Most of the eruptive stars in our sample reside in rather quiescent (sonic or transonic) host environments, with the exception of 5 FUors (RNO 1B/1C, Haro 5a IRS, AR 6A/6B, Z CMa and HBC 722) that exhibit supersonic motions. The supersonic motions might be caused by associated outflows.

- We investigate the origin of the observed ammonia emission in the outbursting systems. Comparing with dust-based H_2 column density maps, we find that circumstellar envelopes are present and likely contribute to the observed ammonia emission in seven sources: CB 230, HH 354 IRS, L1551 IRS 5, PP 13S, RNO 1B/1C, V960 Mon, and V1057 Cyg. Outflow shocks could contribute to the relatively high ammonia abundances in sources like RNO 1B/1C.

- Additional eruptive stars potentially harbour dense gas based on their NH_3 (2,2) detections, which could indicate an earlier phase than originally classified. Our results add to the growing evidence that low-mass young eruptive stars occupy a wide range of evolutionary stages (see also e.g., Green et al., 2013).

The Effelsberg ammonia observations have investigated the host environments of eruptive low-mass stars on scales of $\sim$37″, much larger than the disks surrounding these targets (e.g., Cieza et al., 2018; Kóspál et al., 2021; Liu et al., 2021). For the majority of these young eruptive stars, their environments are still poorly constrained on small scales and further high angular resolution observations are needed to shed light on the relationship between young eruptive stars, their disks, and their potential circumstellar envelopes. Such observations will be important for expanding the standard classification scheme of YSOs, and for studying the effects of the outburst on the host environments of young eruptive stars.

3

H_2O maser observations of FU Orionis and EX Lupi objects

This Chapter is based on Szabó et al. (2023b), published in Astronomy & Astrophysics, Volume 674, A202, June 2023. The article is available at the following DOI.

3.1 Introduction

Interstellar masers are powerful tools for studying the physics of star formation on small-scales, frequently probing regions of enhanced density and temperature (e.g., Elitzur, 1992; Reid & Honma, 2014). While masers have been substantially used to probe both low- and high-mass star formation regions (e.g., Abraham et al., 1981; Omodaka et al., 1999; Hirota et al., 2011; Furuya et al., 2001, 2003), so far little information exists on masers in FUors/EXors, or more generally focusing on low-mass eruptive YSOs. Pioneering studies found compact maser emission in the 1720 MHz hyperfine structure line of hydroxyl (OH) toward the archetypal FUor, V1057 Cyg (Lo & Bechis, 1973). This emission, which comes from the immediate vicinity of the star (Lo

& Bechis, 1974a) and is highly time variable (Winnberg et al., 1981), is unique in the literature. The 22.2 GHz transition of water (H_2O) is the most widespread interstellar maser (see, e.g., Gray, 2012, and references therein). It has been detected towards numerous low- to high-mass star forming regions in the Milky Way (see e.g., Ladeyschikov et al., 2022). Pumping models indicate that 22.2 GHz water masers are excited at elevated temperatures (~500 K) and densities (10^{8-9} cm^{-3}), which are typically found in the compressed post-shock regions of jets and outflows from YSOs (Elitzur et al., 1989a; Elitzur & Fuqua, 1989; Gray, 2012; Gray et al., 2022). With very-long-baseline interferometry (VLBI), multi-epoch observations of water masers associated with protostellar outflows can be used to study mass accretion and ejection (see, for example, Burns et al., 2016; Moscadelli et al., 2019).

Despite the fact that water masers are closely associated with mass accretion and ejection events in protostars, a systematic search for 22.2 GHz H_2O masers in FUors and EXors has not yet been performed. Hence, the overall incidence of 22.2 GHz water masers in these classes of eruptive objects is unknown. The following sections present the first dedicated 22.2 GHz water maser survey of low-mass young eruptive stars, also using the Effelsberg 100-m (see also Chapter 1). This single-dish survey is a first step in investigating water masers in low-mass outbursting systems, aimed at investigating the existence and prevalence of water masers in these objects and identifying targets for follow-up interferometric observations.

3.2 Observations

The H_2O $J_{K_a,K_c} = 6_{16} - 5_{23}$ transition (rest frequency 22235.0798 MHz, from the JPL Molecular Spectroscopy database[1], Pickett et al. 1998a) was observed simultaneously with the three lowest metastable NH_3 transitions ($(J, K) = (1, 1), (2, 2)$ and $(3, 3)$), presented in Chapter 2. The observations were carried out on 2021 November 18, November 23, and 2022 January 25 using the Effelsberg 100-m telescope in Germany[2] (project id: 95-21, PI: Szabó). The sample is the same as described in Chapter 2, consisted of 51 sources: 33 FUors, 13 EXors, and 5 Gaia alerts.

The observations were performed in position-switching mode with an off-position at an offset of 5′, east of our targets in azimuth. During our observations, the 1.3 cm double beam and dual polarization secondary focus receiver was employed as the frontend, while the fast Fourier transform

[1] https://spec.jpl.nasa.gov/

[2] The 100-m telescope in Effelsberg is operated by the Max-Planck- Institut für Radioastronomie (MPIfR) on behalf of the Max-Planck Gesellschaft (MPG).

spectrometers (FFTSs) were used as the backend. Each FFTS provides a bandwidth of 300 MHz and 65536 channels, which gives a channel width of 4.6 kHz, corresponding to a velocity spacing of 0.06 $km\,s^{-1}$ at 22.2 GHz. The actual spectral resolution is coarser by a factor of 1.16 (Klein et al., 2012b).

At the beginning of each observing session, pointing and focus were verified towards NGC 7027. On 2021 November 18 we also targeted W75N, known for its H_2O and NH_3 emission, to make sure that the system was working properly. Because W75N is a different type of object than those I focus in this Thesis, the observations and results conducted on this source are summarised in see Appendix A.1. Pointing was regularly checked on nearby continuum sources and was found to be accurate to about 5″. NGC 7027 was also used as our flux calibrator, assuming a flux density of ~5.6 Jy at 22.2 GHz (Ott et al., 1994). The on-source integration time was the same as mentioned in Chapter 2, since they are the same dataset.

The majority of the sources were observed on 2021 November 18 and 23 (see Tables 3.2 and 3.3). On 2021 November 18, H_2O maser emission was detected toward V512 Per (SVS 13A), RNO 1B/1C, and HH 354 IRS. To study the time variability of the maser emission, we re-observed the detected sources in as many subsequent epochs as possible (see Table 3.2). For Z CMa, which was known to have water maser emission (Moscadelli et al., 2006) but could not be observed in November 2021 due to time constraints, we searched for short-term maser variability by observing this source for two 4×2.5 minute blocks separated by 2.5 hours in January 2022. No variability was detected on this timescale, so all eight spectra of Z CMa were averaged for the subsequent analysis. Due to the weak detection of the water maser in HH 354 IRS, the spectrum was spectrally smoothed by a factor of 2 using the `smooth` built-in function in CLASS. The smoothed spectrum is presented throughout this thesis. Having detected unusually high-amplitude (factor of ~4 with respect to the previous observation) and rapid variability in the H_2O maser spectra towards V512 Per (SVS 13A see Section 3.3.3), we requested additional time to observe this source and carried out nine-point observations and 1′×1′ on-the-fly (OTF) mapping of this source on 2022 February 5 to investigate whether emission from nearby sources in the telescope sidelobes could be contributing to the observed emission. The beam is not a perfect point source, but rather has a distribution of sensitivity across the sky. The main lobe is the region where the telescope's sensitivity is the highest, typically aligned with the direction of the source being observed. However, due to imperfections in the design or characteristics of the antenna, the beam pattern extends beyond the main lobe and can have sidelobes at various angles. The sidelobes can pick up signals from unwanted sources outside the main field of view, contaminating the measurements of the target source (e.g., radio emission from a nearby source Wilson et al., 2009, see also references within). Consequently, we had serendipitously detected strong water maser emission toward a source called H_2O(B) (SVS 13C), which is 30″ south of V512 Per (SVS 13A) (see Sections 3.3.3 and 3.3.4.1). We also performed single-pointing observations towards H_2O(B) during this epoch to check the strength of the water masers towards this source.

We adopted the method introduced by Winkel et al. (2012b) for our spectral calibration which resulted in a calibration uncertainty of about 15%. The half-power beam width (HPBW) was about 40″ at 22 GHz and the main beam efficiency was 60.2% at 22 GHz. The conversion factor from flux density, S_ν, to main beam brightness temperature, T_{mb}, was T_{mb}/S_ν=1.73 K/Jy. Typical rms noise levels for the observations of detected sources are given in Table 3.2 and the 3σ upper limits for non-detections are given in Table 3.3.

The data were reduced using the GILDAS/CLASS package developed by the Institut de Radioastronomie Millimétrique (IRAM) [3] (Pety, 2005b; Gildas Team, 2013). For each target, spectra observed on the same day were averaged to improve the signal-to-noise ratio prior to subtracting a linear baseline. Velocities are presented with respect to the local standard of rest (LSR) throughout this chapter, similarly to Chapter 2.

3.3 Results

Out of the 51 targets, we detected $>3\sigma$ water maser emission towards two FUors (namely Z CMa and HH 354 IRS) and one EXor (V512 Per or SVS 13A), corresponding to a detection rate of only ~6%. For 31 sources in our sample, no previous observations of the 22.2 GHz water maser line have been reported in the literature. We also serendipitously detected water maser emission towards two non-eruptive embedded protostars (discussed in Sections 3.3.4.1 and 3.3.4.2). The basic parameters of sources with maser detections, including their types (either FUor or EXor), coordinates, distances, and evolutionary classifications are listed in Table 3.1. Altogether, water masers were detected in two Class 0 sources, which are currently not known as eruptive YSOs, (namely IRAS 00338+6312 and H2O(B)/SVS 13C) and in one Class 0/I (HH 354 IRS) and two Class I (V512 Per/SVS 13A and Z CMa) eruptive objects, using the standard classification scheme (see e.g., Greene et al., 1994; Evans et al., 2009).

[3] `https://www.iram.fr/IRAMFR/GILDAS/`

For sources with water maser detections, I fit each velocity component with a Gaussian to obtain its LSR velocity ($v_{\rm LSR}$), line width (Δv), and peak flux density (S_ν), which are given in Table 3.2. The peak flux densities of detected water masers vary from 0.11 Jy to 498.7 Jy, spanning over three orders of magnitude. The observed maser velocities are within 10 km s^{-1} of the systemic cloud velocities measured from NH_3 emission. While shock velocities of $\gtrsim$50 km s^{-1} are expected in theoretical models (e.g. Elitzur et al., 1989b), the modest velocity offsets between water masers and dense gas observed in the sample are generally consistent with observations of water masers towards high-mass YSOs (e.g. Urquhart et al., 2009; Cyganowski et al., 2013, Figures 4 and 16, respectively). Isotropic H_2O maser luminosities, $L_{\rm H_2O}$, were calculated as (e.g., Anglada et al., 1996; Urquhart et al., 2011; Cyganowski et al., 2013)

$$\left[\frac{L_{\rm H_2O}}{L_\odot}\right] = 2.3 \times 10^{-8} \left[\frac{\int S_\nu {\rm d}v}{\rm Jy\ km\ s^{-1}}\right]\left[\frac{D}{\rm kpc}\right]^2 , \tag{3.1}$$

where D is the distance to the target (see Table 3.1). Estimating the isotropic H_2O maser luminosities of individual velocity components separately, we find a range of $L_{\rm H_2O}$ of $7.9{\times}10^{-10} L_\odot$ to $6.1{\times}10^{-7} L_\odot$ (see Table 3.2).

Table 3.1: Basic information about the sources towards which water maser emission was detected at 22.2 GHz.

Name	Type FUor/EXor	R.A. (J2000) ($^{\rm h\ m\ s}$)	Dec. (J2000) ($^\circ\ '\ ''$)	Distance (pc)	Classification	Reference
Z CMa	FUor	07 03 43.15	−11 33 06.2	1125	Class I	1, 2, 3
HH 354 IRS	FUor	22 06 50.37	+59 02 45.9	750	Class 0/I	1, 4, 5, 6
V512 Per (SVS 13A)	EXor	03 29 03.75	+31 16 03.9	275	Class I	1, 7, 8
IRAS 00338+6312 (close to RNO 1B/1C)	–	00 36 46.30	+63 28 54.0	965	Class 0	7, 9
H_2O(B) (SVS 13C)*	–	03 29 01.35	31 15 40.4	275	Class 0	7, 10

Notes. *The coordinates given for H_2O(B) were derived from the OTF mapping. References for distance and classification: 1 – Audard et al. (2014); 2 – Dong et al. (2022); 3 – Gramajo et al. (2014); 4 – Reipurth et al. (1997); 5 – Bronfman et al. (1996); 6 – Reipurth et al. (1997); 7 – Bailer-Jones et al. (2021); 8 – Diaz-Rodriguez et al. (2022); 9 –Quanz et al. (2007a); 10– Plunkett et al. (2013).

3.3.1 Non-detections in the survey

Here, I present the non-detections, where Table 3.3 lists the targeted sources along with their types, coordinates, 3σ upper limits, whether they were previously searched to find their 22.2 GHz maser emission, and, if so: the reference, the date of observation in the current survey, their classification and reference, and distances. In the following subsections, I discuss the results for sources with detected water masers.

Table 3.2: Properties of observed water maser features.

Source	Date	H_2O					NH_3 (1,1)
	yyyy-mm-dd	v_{LSR} (km s^{-1})	Δv (km s^{-1})	RMS (Jy)	S_ν (Jy)	L_{H_2O} ($L_\odot$)	v_{LSR} (km s^{-1})
V512 Per (SVS 13A)*	2021-11-18	6.31 (0.06)	1.20 (0.06)	0.07	20.20 (0.07)	3.7×10^{-8}	
V512 Per*	2021-11-18	8.46 (0.06)	0.86 (0.06)	0.07	19.24 (0.07)	3×10^{-8}	
V512 Per*	2021-11-18	10.91 (0.06)	0.74 (0.06)	0.07	19.02 (0.07)	2.4×10^{-8}	8.45 (0.01)
V512 Per*	2021-11-18	11.68 (0.06)	0.56 (0.06)	0.07	16.88 (0.07)	1.6×10^{-8}	
V512 Per*	2021-11-18	13.23 (0.06)	1.56 (0.06)	0.07	1.72 (0.07)	3.6×10^{-9}	
V512 Per*	2021-11-23	6.30 (0.03)	1.08 (0.01)	0.04	55.81 (0.05)	9.7×10^{-8}	
V512 Per*	2021-11-23	8.42 (0.03)	0.95 (0.01)	0.04	86.38 (0.05)	1.5×10^{-7}	
V512 Per*	2021-11-23	10.95 (0.03)	0.81 (0.01)	0.04	16.14 (0.05)	2.8×10^{-8}	8.45 (0.01)
V512 Per*	2021-11-23	11.11 (0.03)	1.28 (0.01)	0.04	15.85 (0.05)	3.1×10^{-8}	
V512 Per*	2021-11-23	13.40 (0.03)	0.88 (0.01)	0.04	2.91 (0.05)	4.1×10^{-9}	
V512 Per*	2022-02-05	5.15 (0.01)	0.74 (0.03)	0.06	2.09 (0.01)	2.8×10^{-9}	
V512 Per*	2022-02-05	6.13 (0.01)	0.67 (0.01)	0.06	21.31 (0.01)	2.7×10^{-8}	
V512 Per*	2022-02-05	7.21 (0.01)	0.69 (0.01)	0.06	4.33 (0.01)	5.3×10^{-9}	8.45 (0.01)
V512 Per*	2022-02-05	8.63 (0.01)	0.97 (0.01)	0.06	7.99 (0.01)	1.4×10^{-8}	
V512 Per*	2022-02-05	9.64 (0.01)	1.12 (0.01)	0.06	5.81 (0.01)	1.2×10^{-8}	
V512 Per*	2022-02-05	11.82 (0.01)	1.11 (0.01)	0.06	2.49 (0.05)	4.5×10^{-9}	
H_2O(B) (SVS 13C)**	2022-02-05	5.07 (0.01)	0.63 (0.01)	0.06	41.45 (0.05)	4.8×10^{-8}	
H_2O(B)**	2022-02-05	6.14 (0.01)	0.66 (0.01)	0.06	498.7 (0.05)	6.1×10^{-7}	
H_2O(B)**	2022-02-05	7.22 (0.01)	0.76 (0.01)	0.06	98.30 (0.05)	1.3×10^{-7}	8.33 (0.01)
H_2O(B)**	2022-02-05	8.62 (0.01)	0.92 (0.01)	0.06	182.34 (0.05)	3.1×10^{-7}	
H_2O(B)**	2022-02-05	9.61 (0.01)	0.96 (0.01)	0.06	126.73 (0.05)	2.3×10^{-7}	
IRAS 00338+6312	2021-11-18	−28.78 (0.01)	1.72 (0.01)	0.05	2.61 (0.09)	1.1×10^{-7}	
IRAS 00338+6312	2021-11-18	−15.79 (0.05)	0.96 (0.05)	0.05	0.37 (0.09)	6.2×10^{-9}	
IRAS 00338+6312	2021-11-23	−28.78 (0.01)	1.70 (0.01)	0.04	2.75 (0.09)	1.1×10^{-7}	−17.90 (0.06)
IRAS 00338+6312	2021-11-23	−15.88 (0.02)	0.69 (0.05)	0.04	0.39 (0.09)	5.6×10^{-9}	
IRAS 00338+6312	2022-01-25	−28.48 (0.01)	1.75 (0.02)	0.04	1.10 (0.09)	4.1×10^{-8}	
IRAS 00338+6312	2022-02-05	−28.43 (0.01)	1.69 (0.02)	0.05	1.63 (0.09)	6.3×10^{-8}	
HH 354 IRS	2021-11-18	1.18 (0.06)	0.81 (0.10)	0.07	0.18 (0.03)	2.1×10^{-9}	
HH 354 IRS	2022-01-25	−10.51 (0.02)	0.54 (0.05)	0.02	0.11 (0.02)	7.9×10^{-10}	−1.52 (0.01)
HH 354 IRS	2022-01-25	5.04 (0.02)	0.63 (0.05)	0.02	0.18 (0.02)	1.6×10^{-9}	
Z CMa	2022-01-25	7.82 (0.01)	1.36 (0.01)	0.01	2.36 (0.01)	1.1×10^{-7}	13.8 (0.02)

Notes. *From the pointed observations towards V512 Per. The possible contamination by H_2O(B) is discussed in Section 3.3.4.1.
**From the pointed observations towards H_2O(B) (see also Section 3.3.4.1).

In total, our survey consisted of 51 objects: 33 Fuors, 13 EXors and 5 Gaia alerts accessible with the Effelsberg 100-m telescope. The chosen Gaia alerts are part of the Piszkéstető Monitoring Program, in Hungary, which started a few years ago with the aim of following the optical wavelength brightness variations of Gaia alert sources with light curves that resemble those of FUors and EXors (see e.g. Szegedi-Elek et al., 2020; Nagy et al., 2021; Cruz-Sáenz de Miera et al., 2022b). We chose Gaia alerts for inclusion in our sample based on their having light curves and luminosities similar to those of FUors and EXors. Water masers were detected in only four out of our 51 targeted sources, however, the emission in one of those target pointings is not attributed to the targeted eruptive star (see Section 3.3.4.2). The 48 non-detections, within a velocity range from -100 to $+100\,\mathrm{km\,s^{-1}}$, are reported in Table 3.3.

3.3.2 FUors

3.3.2.1 Z CMa

Z CMa consists of an FUor (southwest component) and a Herbig Ae/Be star (northeast component) that are only 0.1″ apart (Koresko et al., 1991; Bonnefoy et al., 2017). Figure 3.1 shows the H_2O maser spectrum observed toward Z CMa, the only source among those detected observed at only one epoch (Section 3.2). As shown in Figure 3.1, there is only one bright maser feature, at υ_{LSR} =7.82 $\mathrm{km\,s^{-1}}$, blueshifted by ∼6 $\mathrm{km\,s^{-1}}$ with respect to the thermal NH_3 emission. Although Z CMa has been observed in many previous water maser studies (Blitz & Lada, 1979; Thum et al., 1981; Deguchi et al., 1989; Scappini et al., 1991; Palla & Prusti, 1993; Moscadelli et al., 2006; Sunada et al., 2007; Bae et al., 2011; Kim et al., 2018), maser emission was detected only on 2003 March 14 (Moscadelli et al., 2006), with a flux density of ∼2 Jy at $\upsilon_{\mathrm{LSR}} = 14.3\,\mathrm{km\,s^{-1}}$. The maser component at $\upsilon_{\mathrm{LSR}} = 7.82\,\mathrm{km\,s^{-1}}$ is therefore detected and reported for the first time.

3.3.2.2 HH 354 IRS

HH 354 IRS, also known as IRAS 22051+5848 and L1165-SMM1 (e.g. Visser et al., 2002), was classified as a FUor based on its CO first-overtone bandhead feature at ∼2.3 μm (Reipurth & Aspin, 1997; Connelley & Reipurth, 2018). This FUor was searched for H_2O maser emission multiple times between 1985 and 2005 (Wouterloot et al., 1993; Persi et al., 1994; Sunada et al., 2007), but no maser emission was reported.

As shown in Figure 3.2, we detected weak H_2O maser emission (peak flux densities <0.2 Jy, Table 3.2) towards HH 354 IRS in two epochs. These are the first detections of water maser emis-

Table 3.3: H_2O maser non-detections in the survey.

Source	Type (FUor/EXor/ Gaia alert)	R.A. (J2000) ($^{h\ m\ s}$)	Dec. (J2000) ($^{\circ}\ '\ ''$)	Upper limit$^{(a)}$ (Jy)	Previous survey$^{(b)}$ (No/Yes/ Unknown)	Date$^{(c)}$ (A/B/C)	Classification (Class 0 – II)	Ref.	D$^{(d)}$ (pc)
V1180 Cas	EXor	02 33 01.53	+72 43 26.8	0.17	Unk.		–	–	908 [51]
PP 13S	FUor	04 10 41.09	+38 07 54.5	0.18	Yes [1]		I	21	350
L1551 IRS 5	FUor	04 31 34.07	+18 08 04.9	0.17	No [2,3]		I	22	–
XZ Tau	EXor	04 31 40.08	+18 13 56.6	0.18	Unk.		II	23	140
UZ Tau E	EXor	04 32 43.02	+25 52 30.9	0.18	Unk.		II	24	130 [51]
LDN 1415 IRS	EXor	04 41 37.50	+54 19 22.0	0.21	Unk.		I	25	170
DR Tau	EXor	04 47 06.21	+16 58 42.8	0.17	Unk.		II	26	192 [51]
V582 Aur	FUor	05 25 51.97	+34 52 30.0	0.15	Unk.		II	27	2401 [52,53]
V1118 Ori	EXor	05 34 44.98	−05 33 41.3	0.21	Unk.		II	28	414
Haro 5a IRS	FUor	05 35 26.74	−05 03 55.0	0.21	Unk.		0/I	29	450
NY Ori	EXor	05 35 36.00	−05 12 25.2	0.22	Unk.		–	–	403 [51]
V1143 Ori	EXor	05 38 03.89	−04 16 42.8	0.22	Unk.		II	30	395 [51]
V883 Ori	FUor	05 38 18.09	−07 02 25.9	0.20	No [4,5]		I	31	417 [54]
HBC 494	FUor	05 40 27.45	−07 27 30.0	0.21	Unk.		I	32	–
V2775 Ori	FUor	05 42 48.48	−08 16 34.7	0.25	No [6]		late I	33	420
FU Ori	FUor	05 45 22.37	+09 04 12.3	0.22	Unk.		II	34	407 [51]
V1647 Ori	FUor	05 46 13.13	−00 06 04.8	0.23	Unk.		I/II	35	412 [51]
AR 6A/6B	FUor	06 40 59.30	+09 35 49.0	0.23	Unk.	A	II	36	800
Parsamian 21	FUor	19 29 00.84	+09 38 43.4	0.16	Unk.		I/II	37	400
I 18270-0153W	FUor	18 29 36.90	−01 51 02.0	0.19	No [7]		I	38	–
OO Ser	FUor	18 29 49.13	+01 16 20.6	0.18	No [3,8]		I	38	311
V371 Ser	EXor	18 29 51.21	+01 16 39.4	0.18	No [3,8]		–	–	311
Gaia21aul	Gaia alert	18 30 06.18	00 42 33.30	0.17	No [9,10]		–	–	378 [55]
I 18341-0113S	FUor	18 36 45.70	−01 10 29.0	0.19	No [3,7]		I	38	–
Gaia21aru	Gaia alert	19 00 56.41	18 48 29.20	0.16	Unk.		–	–	–
V1515 Cyg	FUor	20 23 48.01	+42 12 25.7	0.18	Unk.		–	–	900 [55]
PV Cep	EXor	20 45 53.90	+67 57 38.6	0.17	Yes [5,11] No [10,12,13,14,15]		–	–	325
V2492 Cyg	EXor	20 51 26.23	+44 05 23.8	0.16	No [16]		I	39	804 [51]
V1057 Cyg	FUor	20 58 53.73	+44 15 28.4	0.17	Yes [11] No [3,10,12,13,14]		II	40	891 [55]
HBC 722	FUor	20 58 17.00	+43 53 43.0	0.17	Unk.		II	41	757 [55]
V2495 Cyg	FUor	21 00 25.24	+52 30 16.9	0.16	No [9]		I/II	42	800
RNO 127	FUor	21 00 31.80	+52 29 17.0	0.17	Unk.		–	–	800
CB 230	FUor	21 17 38.62	+68 17 34.0	0.15	No [3,7,17,18]		0/I	43	339 [18]
V1735 Cyg	FUor	21 47 20.66	+47 32 03.8	0.18	No [1,3,12]		II	43	663 [55]
V733 Cep	FUor	22 53 33.25	+62 32 23.6	0.16	Unk.		I/II	43	724 [55]
VY Tau	EXor	04 39 17.42	+22 47 53.3	0.11	Unk.		II	44	153 [55]
Gaia21arx	Gaia alert	05 36 24.80	−06 17 30.52	0.15	Unk.		–	–	361 [55]
NGC 2071	FUor	05 47 09.80	+00 18 00.0	0.15	Yes [1,3,6]		–	–	–
I 06297+1021W	FUor	06 32 28.70	+10 19 0	0.16	Unk.	B	I	43	–
I 06393+0913	FUor	06 42 08.13	+09 10 30.0	0.15	Unk.		I	43	–
Gaia18dvy	FUor	20 05 06.02	+36 29 13.52	0.14	Unk.		II	45	1880 [45]
Gaia19bpg	Gaia alert	21 41 50.43	+51 55 45.48	0.12	Unk.		–	–	–
V899 Mon	FUor	06 09 19.24	−06 41 55.8	0.10	Unk.		II	46	809 [51]
V900 Mon	FUor	06 57 22.22	−08 23 17.6	0.13	Unk.		I	47	1304 [51]
V960 Mon	FUor	06 59 31.58	−04 05 27.7	0.12	Unk.	C	II	48	2189 [51]
iPTF 15AFQ	FUor	07 09 21.39	−10 29 34.5	0.13	Unk.		I	49	1315 [51]
Gaia20bdk	Gaia alert	07 10 14.92	−18 27 01.04	0.15	Unk.		–	–	–
RNO 1B/1C	FUor	00 36 46.30	+63 28 54.0	0.05 0.04 0.04 0.05	No [1,7,8,10,19,20]	A B C D	1B: 0/I–II, 1C: II	50	965 [55]

Notes. Source types and coordinates are taken from Audard et al. (2014), except for Gaia alerts, whose positions are taken from the Gaia alerts system. $^{(a)}$Upper limits are 3 × RMS. $^{(b)}$Previous surveys: No – Source was observed, but no H_2O maser detected; Yes – H_2O maser detected; Unk. (Unknown) – To our knowledge, previously not searched for water masers. $^{(c)}$Our observations were carried out on: A – 2021-11-18; B – 2021-11-23; C – 2022-01-25.; D – 2022-02-05. $^{(d)}$Distance – the default values are from Audard et al. (2014), but in case of more recent data (i.e. *Gaia*), the values are then updated with references.

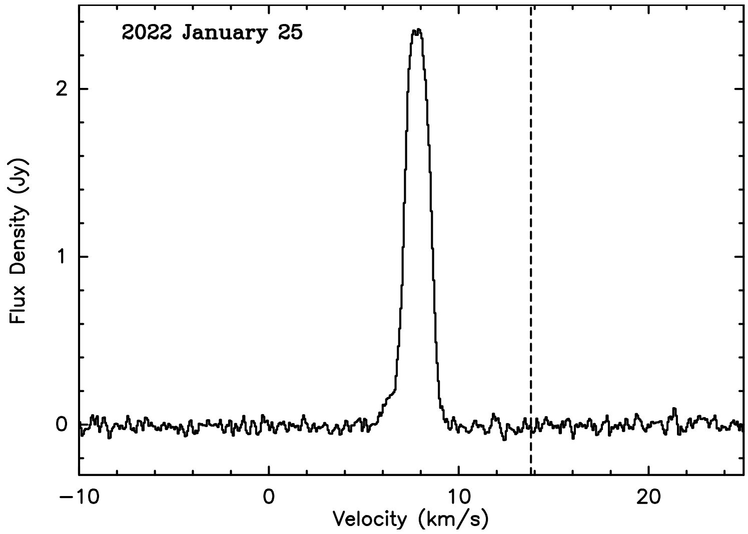

Figure 3.1: H_2O maser spectrum of Z CMa observed on 2022 January 25. The dashed vertical line indicates the v_{LSR} of 13.8 km s^{-1} from the NH_3 (1,1) transition (Szabó et al., 2023a). Figure from Szabó et al. (2023b).

sion towards this source. On 2021 November 18, we detected a weak H_2O maser at v_{LSR} =1.18 km s^{-1}. On 2022 January 25 we detected two features at v_{LSR} = −10.51 and v_{LSR} = 5.04 km s^{-1} but the 1.18 km s^{-1} feature had disappeared. This variability is consistent with the findings of Claussen et al. (1996), namely, that water maser features associated with low-mass YSOs can have lifetimes of $\lesssim$2 months.

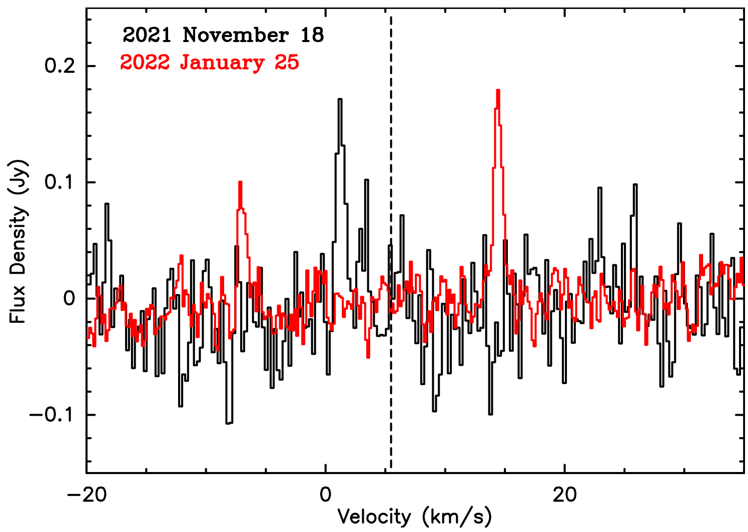

Figure 3.2: Spectrally smoothed line profile of H_2O maser emission observed in HH 354 IRS on 2021 November 18 and 2022 January 25. The dashed vertical line indicates the average v_{LSR} of −1.47 km s^{-1} derived from the NH_3 (1,1) and (2,2) transitions (Szabó et al., 2023a). Figure from Szabó et al. (2023b).

3.3.3 EXors – V512 Per (SVS 13A)

Located in the low-mass star-forming region NGC 1333, V512 Per (commonly known as SVS 13 or SVS 13A, e.g.,Plunkett et al. 2013) has been the subject of extensive multi-wavelength studies, resulting in a complex nomenclature. The source was discovered during an infrared survey (SVS76 NGC 1333 13A, Strom et al., 1976). An optical outburst was detected in the late 1980's (Mauron & Thouvenot, 1991) and observations by Eisloeffel et al. (1991) confirmed it showed EXor properties. The variable name of V512 Per was assigned in the 71st Name-List of Variable Stars by Kazarovets et al. (1993), who noted SVS 13 and V512 Per were the same source. A radio counterpart of the optical/near-infrared source, named VLA 4, was first detected by Rodríguez et al. (1997) and later resolved into a binary (VLA 4A and 4B; Anglada et al., 2000). Rodríguez et al. (2002) noted that SVS 13 (therefore V512 Per) and VLA 4 are the same source, which is consistent with other studies (see, e.g. Goodrich, 1986; Fujiyoshi et al., 2015). The source is also commonly known as SVS 13A (see, e.g. Plunkett et al., 2013, and references therein) and is associated with several Herbig/Haro objects (HH 7–11; e.g. Rodríguez et al., 1997; Bachiller et al., 2000). I refer to the source as V512 Per in this thesis, noting that this name might be more familiar to the variable star community (e.g. Kazarovets et al., 1993; Audard et al., 2014), while SVS 13, VLA 4, or SVS 13A may be more familiar to the radio astronomy community (e.g. Rodríguez et al., 2002; Plunkett et al., 2013).

Figure 3.3 shows the spectra obtained towards V512 Per in 2021 November. On 2021 November 18, we detected at least six maser features towards V512 Per (see Figure 3.3), with the brightest one being 20.2 Jy. Only five of them are shown in Table 3.2, since the additional feature on the main component at 6.31 $\mathrm{km\,s^{-1}}$ cannot be reliably fit with a Gaussian. Five days later, two velocity features, at 6.3 $\mathrm{km\,s^{-1}}$ and 8.4 $\mathrm{km\,s^{-1}}$, had increased in flux density by factors of ~3 and ~4, respectively. Previous H_2O maser observations of the V512 Per region revealed three maser positions, H_2O(A), H_2O(B), and H_2O(C) (Haschick et al., 1980). H_2O(A) is associated with V512 Per. H_2O(B), also known as HH 7–11(B), VLA 2, SVS 13C, or MMS3, is a Class 0 source located ~0.5′, to the southwest (Cesaroni et al., 1988; Segura-Cox et al., 2018; Chen et al., 2013; Plunkett et al., 2013), while H_2O(C) is ~2.5′ southeast of V512 Per (Haschick et al., 1980).

To investigate which of the observed velocity components may be associated with V512 Per, we carried out a nine-point grid of observations centred on V512 Per on 2022 February 5 (with pointings separated by 20″). The results indicate that the strong water maser features at 5–

10 km s^{-1} are brightest at an offset position (−20″,−20″), rather than toward V512 Per (0″,0″), suggesting that these maser features do not arise mainly from V512 Per. The ~12 km s^{-1} component, in contrast, is strongest towards V512 Per and is likely associated with the eruptive binary source (Figure 3.4, see also Figure 3.5).

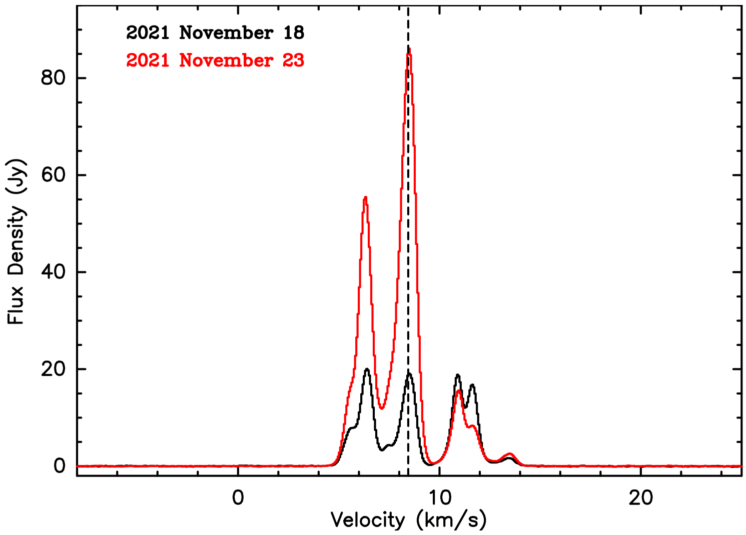

Figure 3.3: H_2O maser spectra toward V512 Per in November 2021: the two epochs are indicated at upper left. The dashed line indicates the average υ_{LSR} of 8.39 km s^{-1} derived from the NH_3 (1,1), (2,2), and (3,3) transitions (Szabó et al., 2023a). Figure from Szabó et al. (2023b).

3.3.4 Serendipitous detections towards Class 0 protostars

3.3.4.1 A water maser flare in H_2O(B)

In addition to the nine-point map described above (Section 3.3.3), we also performed OTF mapping towards V512 Per and H_2O(B), shown in Figure 3.5. As illustrated by the channel maps in Figure 3.5, spectral features at υ_{LSR} ≤11 km s^{-1} peak around H_2O(B) while spectral features at υ_{LSR} >11 km s^{-1} peak around V512 Per. Figure 3.4 compares the pointed observations toward V512 Per and H_2O(B) on 2022 February 5: the spectra show very similar profiles between 4 km s^{-1} and ~10 km s^{-1} but the intensities are different by a factor of ~20. This similarity suggests that the pointed observations of V512 Per, including those shown in Figure 3.3, have significant contributions from H_2O(B). We estimate this contribution for our 2022 February 5 observations assuming a perfect Gaussian beam pattern with a beam size of 40″. A source at an offset of 38.7″ (the angular separation between V512 Per and H_2O(B) derived from our observations, see Table 3.1) will fall at the 7.5% response level of the beam, or between the 3.7–14% levels assuming a typical pointing error of 5″. Thus H_2O(B), with a flux density of 498.7 Jy, would contribute 18.4–69.8 Jy to the spectrum observed towards V512 Per, comparable to the observed value of 21.3 Jy (Table 3.2).

Notably, in the pointed 2022 February 5 observations, the peak flux density of the water maser in H_2O(B) is 498.7 Jy at $v_{\rm LSR}$ = 6.1 km s^{-1}. This is the highest flux density reported for this source to-date (c.f. Haschick et al., 1980; Lyo et al., 2014), indicative of a maser flare (see also Section 3.4.1).

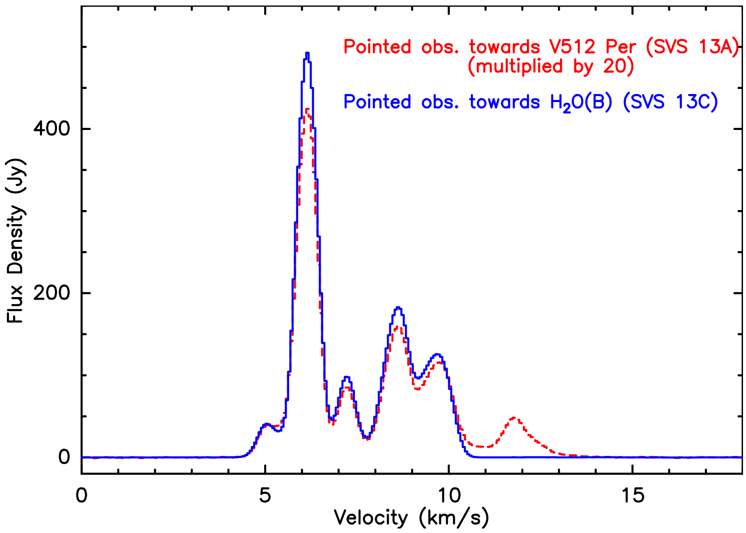

Figure 3.4: Pointed H_2O maser spectra towards V512 Per and H_2O(B) observed on 2022 February 5. The spectrum of V512 Per is multiplied by 20 to better match the spectrum of H_2O(B). Figure from Szabó et al. (2023b).

3.3.4.2 RNO 1B/1C and IRAS 00338+6312

RNO 1B/1C (V710 Cas) is a double FUor system, with both RNO 1B and 1C classified as FUors (Staude & Neckel, 1991; Kenyon et al., 1993). The binary is part of a cluster of deeply embedded YSOs (e.g., Quanz et al., 2007a) that has been targeted by numerous water maser studies (e.g., Fiebig, 1995; Furuya et al., 2003; Sunada et al., 2007; Bae et al., 2011, and references therein). Previous VLA observations of the clustered region suggest that the water masers between $v_{\rm LSR}$ ~ −30 km s^{-1} and $v_{\rm LSR}$ ~ −5 km s^{-1} originate from the deeply embedded Class 0 object IRAS 00338+6312, rather than RNO 1B or RNO 1C (see, e.g., Fiebig, 1995; Fiebig et al., 1996, and references therein). IRAS 00338+6312 is only ~4″ northeast of RNO 1C, but is a separate object (e.g., Mookerjea et al., 1999; Quanz et al., 2007a). The blueshifted and redshifted masers are thought to arise from the bipolar outflow or an accretion disk (Fiebig et al., 1996).

In the pointing towards RNO 1B/1C, we detected water maser emission in four epochs, as shown in Figure 3.6. During the first observations on 2021 November 18, we detected two maser

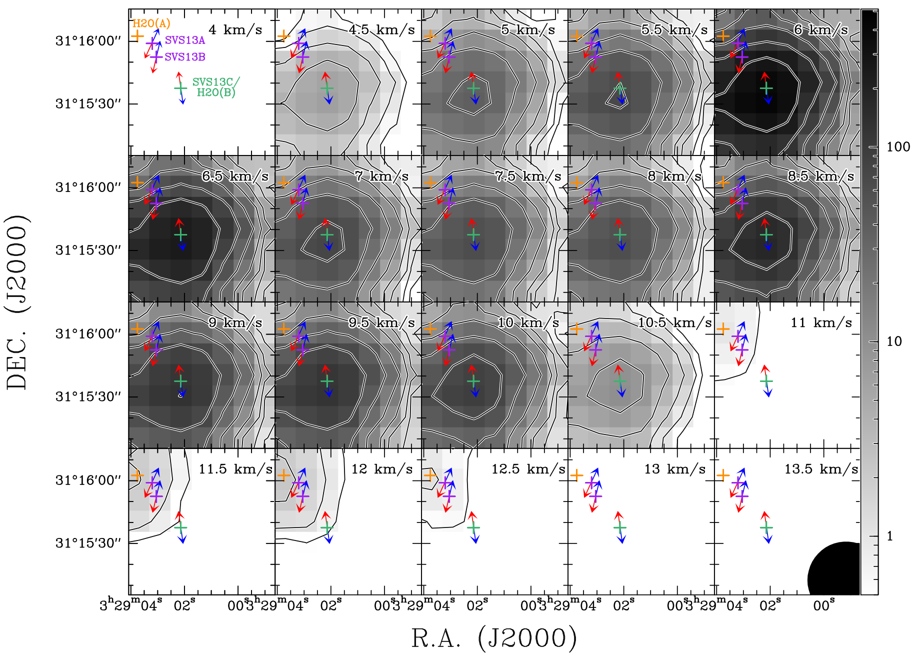

Figure 3.5: Channel maps of H_2O masers in H_2O(B) (SVS 13C) and V512 Per (SVS 13A). The contours start at 0.5 Jy, and then increase by a factor of two. The plus signs represent the positions of the two H_2O masers (orange and green) previously detected by Haschick et al. (1980) and of YSOs (purple; e.g. Plunkett et al., 2013). Based on previous observations (Plunkett et al., 2013; Podio et al., 2021), the outflow directions are indicated by red and blue arrows. The beam size is shown in the lower right corner of the last panel. The colour bar represents the flux density in units of Jy. Figure from Szabó et al. (2023b).

features at $\upsilon_{\rm LSR} = -28.78\,{\rm km\,s^{-1}}$ and $\upsilon_{\rm LSR} = -15.79\,{\rm km\,s^{-1}}$; five days later the flux densities and LSR velocities of the two maser features were nearly unchanged. The source was observed again on 2022 January 25 and February 5: in these observations, the $\upsilon_{\rm LSR} \sim -15.8\,{\rm km\,s^{-1}}$ feature had disappeared and the blueshifted maser was weaker and had slightly shifted in velocity to $\upsilon_{\rm LSR} \sim -28.48\,{\rm km\,s^{-1}}$. The 3σ upper limits for the $\upsilon_{\rm LSR} \sim -15.8\,{\rm km\,s^{-1}}$ feature are 0.12 Jy and 0.15 Jy for the observations on 2022 January 25 and February 5, respectively. The $\upsilon_{\rm LSR} \sim -28\,{\rm km\,s^{-1}}$ feature has the largest velocity offset with respect to the cloud among our detections, $\sim$10 km s^{-1} (see Table 3.2). Based on comparing the results to the literature, the water maser features detected in the survey are most likely to originate from IRAS 00338+6312 rather than RNO 1B/1C. The velocities of the detected masers are similar to those of the masers associated with IRAS 00338+6312 in the VLA observations (Fiebig, 1995; Fiebig et al., 1996) and also match the velocity range of the molecular outflow (about $-30\,{\rm km\,s^{-1}}$ to $-5\,{\rm km\,s^{-1}}$ Snell et al., 1990; Yang et al., 1991) driven by IRAS 00338+6312 (Henning et al., 1992; Wouterloot et al., 1993; Anglada et al., 1994; Furuya et al., 2003; Bae et al., 2011). We therefore do not count the water maser emission in the RNO 1B/1C pointing as a detection towards an eruptive star and the 3σ upper limits are given in Table 3.3.

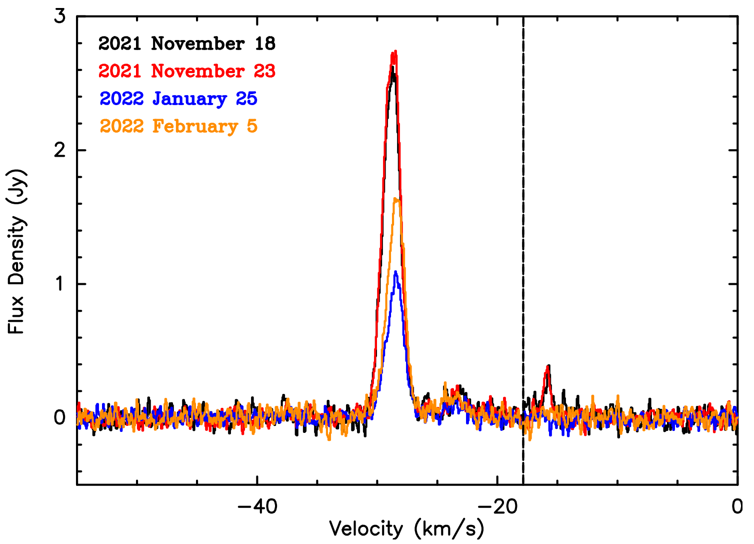

Figure 3.6: H_2O maser observed in IRAS 00338+6312 at four epochs in 2021 November, 2022 January and February. The dashed vertical line indicates the systemic $\upsilon_{\rm LSR}$ of $-17.83\,{\rm km\,s^{-1}}$ derived from the NH_3 (1,1), (2,2), and (3,3) transitions (Szabó et al., 2023a). Figure from Szabó et al. (2023b).

3.4 Discussion

3.4.1 Long-term time variation

Water maser flares have been recognised in star-forming regions for decades (e.g., Boboltz et al., 1998; Kramer et al., 2018), with recent observations suggesting that water maser flares can accompany ejection events associated with accretion bursts in massive and intermediate-mass stars (e.g., MacLeod et al., 2018; Brogan et al., 2018; Chen et al., 2021; Bayandina et al., 2022). Hence, it is reasonable to expect such water maser flares from FUors or EXors. We investigated whether our targets have experienced water maser flares previously.

Figure 3.7 presents long-term time series for the water masers detected in the survey, which show that these masers are quite variable in both flux density and LSR velocity. Based on data from the literature, Z CMa appears to be in a relatively active phase, with the flux density of 2.4 Jy seen during our observations, the highest observed to date (c.f. Blitz & Lada, 1979; Thum et al., 1981; Deguchi et al., 1989; Scappini et al., 1991; Palla & Prusti, 1993; Moscadelli et al., 2006; Sunada et al., 2007; Bae et al., 2011; Kim et al., 2018). For HH 354 IRS, no water maser emission was detected by previous observations (Wouterloot et al., 1993; Persi et al., 1994; Sunada et al., 2007). The water maser detections toward this source is therefore the first in the literature. Since the upper limits of previous observations are comparable to the detected flux densities (see Figure 3.7), we cannot conclude whether the maser was in its active or quiescent phase during our observations. For V512 Per, Figure 3.7 compares the velocity component in our observations that likely arises from V512 Per (see Section 3.3.3) to archival data that include both single-dish and interferometric measurements (Haschick et al., 1980; Claussen et al., 1996; Rodríguez et al., 2002; Furuya et al., 2003).We note that in the case of the Claussen et al. (1996) data, the results were measured from the published figures. Based on this comparison, we can identify three water maser flares, in 1978, 1992, and 1998, which reached peak flux densities of ~310 Jy, 660 Jy, and 244 Jy on 1978 February 17, 1992 November 28, and 1998 June 22, respectively. The observations spanning these dates were performed with single-dish telescopes with large beams (>1′), so H_2O(B) could potentially contribute to the observed flux densities (see Section 3.3.3). Claussen et al. (1996) noted, however, that the maser features detected in their 1991–92 observations all had velocities consistent with those of H_2O(A)/V512 Per, suggesting that this flare was associated with the eruptive star.

For H_2O(B), I found no suggestion in the literature of this source being an eruptive variable at optical or near-infrared wavelengths, but our comparison with previous water maser observations (Figure 3.7; Haschick et al., 1980; Lyo et al., 2014) shows three maser flares with peak flux densities of >100 Jy, on 1975 November 30, 2012 May 28, and with the new observations on 2022 February 5. As for V512 Per, Figure 3.7 compares the velocity components in our observations that likely arise from H_2O(B) (Section 3.3.3 and 3.3.4.1) with historical data. Again, the large single dish beams encompass both H_2O(B) and V512 Per, meaning that we cannot rule out a contribution from V512 Per to the historical flares. For instance, the observations of Lyo et al. (2014) had a HPBW of 120″. As noted in Section 3.3.4.1, the water maser flare detected in our observations on 2022 February 5 is the brightest to date, with a peak flux density of 498.7 Jy.

For IRAS 00338+6312, there is similarly no suggestion in the literature of this object being an eruptive source in the optical or near-infrared, but Figure 3.7 suggests its water maser emission was in a more active phase in 1998 and then again in 2004 (Cesaroni et al., 1988; Henning et al., 1992; Wouterloot et al., 1993; Persi et al., 1994; Fiebig, 1995; Codella et al., 1995; Furuya et al., 2003; Sunada et al., 2007; Bae et al., 2011), but relatively quiescent during the new observations. The highest flux density reached was ∼31 Jy on 1998 January 5 (Furuya et al., 2003).

Periodic variations have been reported in some velocity components of the 22.2 GHz H_2O (and the 6.7 GHz Class II CH_3OH) masers associated with the intermediate-mass YSO G107.298+5.639 and cyclic accretion instabilities have been invoked to explain this peculiar behaviour (Szymczak et al., 2016). Low-mass stars such as FUors and EXors might also experience cyclic accretion events, but no evidence is found for periodic variations in Figure 3.7. Perhaps a long-term monitoring program could improve on the currently available data .

3.4.2 Scarcity of water masers in selected eruptive systems

The water maser detection rate of 6% in FUors and EXors is perhaps surprising in light of the close connection between water maser emission and mass accretion and ejection in protostars (see Section 3.1). In this section, I summarise possible explanations for the low detection rate.

First, the low detection rate could be caused by an evolutionary effect. Previous observations indicate that the water maser detection rate decreases from Class 0 to Class II objects (e.g., Furuya et al., 2001). Since the selected FUors and EXors are mainly Class I and Class II objects (see Tables 3.1 and 3.3), we would expect a lower detection rate compared to Class 0 objects. Furthermore, our detection rate is comparable to that (6.3%) for Class I objects in Furuya et al. (2001). No

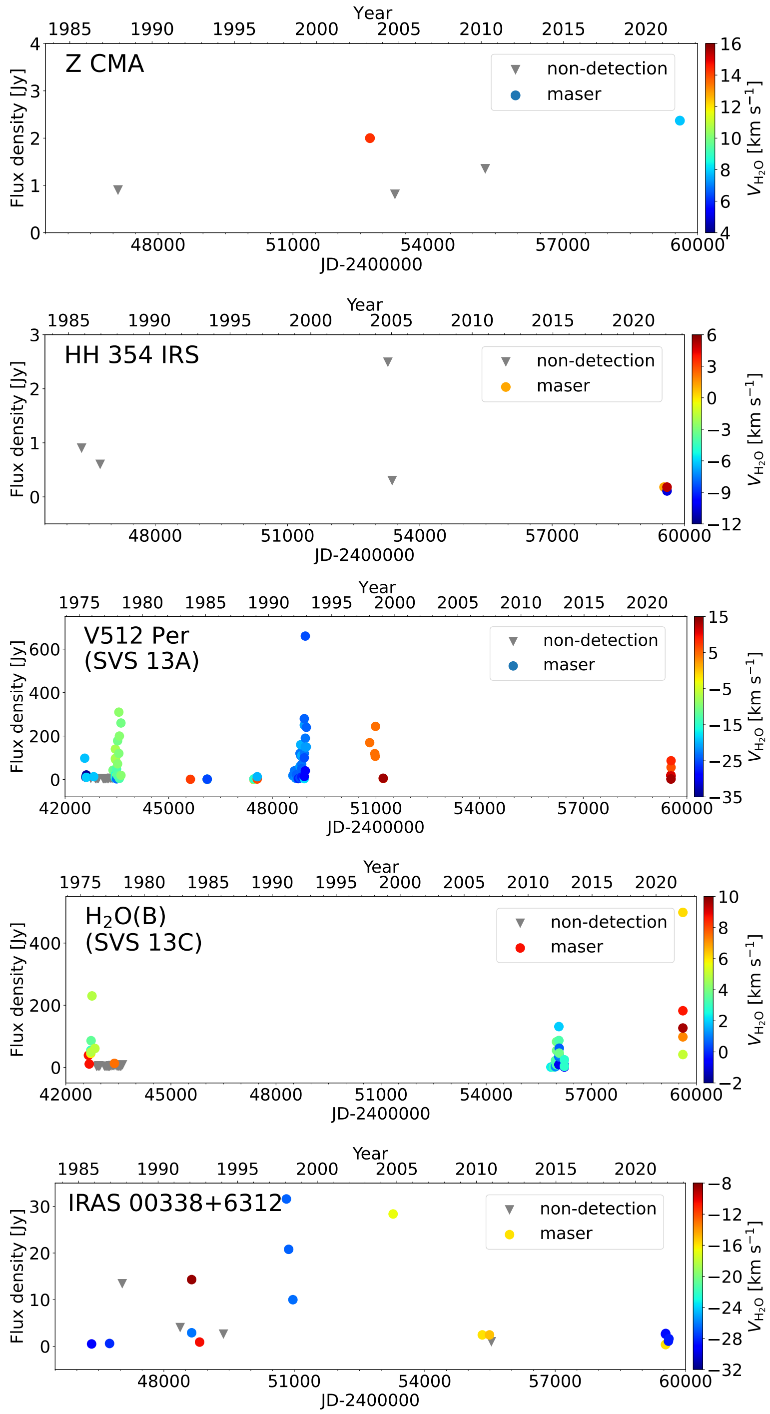

Figure 3.7: Long-term variations in flux density of detected water masers. The colour-coded dots and grey triangles represent flux densities for maser detections, colour-coded by velocity (see colour-bar at right), and upper limits for non-detections, respectively. References for archival data are given in Section 3.4.1. Figure from Szabó et al. (2023b). The typical error is around 1 Jy or below and are smaller than the markers.

water masers were detected toward any of the Class II objects in the survey, which further supports the evolutionary trend proposed by Furuya et al. (2001).

Second, water masers have relatively low luminosities in low-mass star formation regions. Statistical studies have shown that the maser luminosities are correlated with bolometric luminosities (e.g., Figure 16 in Urquhart et al., 2011). This suggests lower maser luminosities in low-mass star formation regions, so lower flux densities would be expected. This could contribute to the low detection rate toward low-mass eruptive stars. This is supported by previous water maser surveys toward the Serpens South and Orion molecular clouds (Kang et al., 2013; Ortiz-León et al., 2021), which give detection rates of $\lesssim$2% for low-mass protostars.

Third, water masers show rapid time variations. The time variability of water masers is evident in this study (see also Figures 3.2, 3.4 and 3.7). Water masers can be in a quiescent phase for about five years (Claussen et al., 1996), meaning that maser emission would not be detected during that time even for sources known to be associated with water masers. This is consistent with the fact that several water masers reported by previous studies are not detected in the new observations (see Table 3.3). It is possible that non-detection of water masers is due to their inactive state. Indeed, when including historical detections, the detection rate of water masers in eruptive stars in the sample is ~15% (excluding the unclassified Gaia alerts), which is higher than the survey detection rate of 6%. This suggests that previously detected water masers were in an inactive phase during the observations.

Overall, the detection rate in this survey is comparable to non-outbursting YSOs (Furuya et al., 2001), suggesting that water maser emission may not be strongly associated with eruptive activity in low-mass outbursting YSOs.

3.5 Conclusions

In this chapter, I summarised the results of the first dedicated water maser survey towards FUors and EXors, two classes of low-mass young eruptive stars. We detected H_2O masers toward five objects, of which three are young eruptive stars: Z CMa (FUor; Class I), HH 354 IRS (FUor; Class 0/I), V512 Per (EXor; Class I), IRAS 00338+6312 (Class 0), and H_2O(B) (Class 0). The detection presented here is the first report of water maser emission in HH 354 IRS. The observations reveal the highest peak flux density yet reported towards H_2O(B) (498.7 Jy), indicative of a recent H_2O maser flare. Overall, the observations reveal a detection rate of ~6% for young eruptive stars in our survey. An analysis of the long-term time series of the water masers suggests that V512 Per and H_2O(B) have experienced multiple water maser flares.

Despite the low detection rate, these observations confirm the presence of 22.2 GHz water maser emission in FUors and EXors, meaning that follow-up radio interferometric observations can be used to probe the environments of eruptive stars on small scales (see, e.g. Haschick et al., 1980; Rodríguez et al., 2002). If water masers are generally weak in FUors and EXors (Section 3.4.2), deeper observations would also potentially find more of them. Expanding on optical and near-infrared knowledge of FUors/EXors with more radio observations, especially future VLBI measurements, will be crucial to improve our understanding of the underlying physics (e.g., mass accretion and ejection) of such peculiar objects, as well as the eventual formation of Sun-like stars.

4

Molecular inventory of the host environment of V1057 Cyg

This Chapter is based on Szabó et al. (2025), published in Astronomy & Astrophysics, Volume 694, A329, February 2025. The article is available at the following DOI.

4.1 Introduction

The powerful and energetic FUor outbursts potentially have a long-lasting influence on the chemistry and molecular inventory of the disks around eruptive stars. The elevated temperatures can, temporarily, increase the abundances of complex organic molecules (COMs), which are carbon-bearing molecules with six or more atoms (e.g., Herbst & van Dishoeck, 2009; Ceccarelli et al., 2017; van 't Hoff et al., 2018; Lee et al., 2019; Jørgensen et al., 2020; Ceccarelli et al., 2022). Improvements in observational techniques and the sensitivity of instruments allow the chemistry of FUors and FUor-like objects to be studied in a new way, covering different frequency regimes (e.g., L1551 IRS5, Fridlund et al., 2002; Bianchi et al., 2020; Mercimek et al., 2022; Andreu et al., 2023; Marchand et al., 2024) and providing small-scale views of the inner regions around these objects. Among the most noteworthy results from interferometric observations is the direct evidence of the outburst affecting the location of the water snow-line, shifting it from a typical few au to ~40–120 au observed in the FUor V883 Ori (see Cieza et al., 2016; van 't Hoff et al., 2018; Leemker et al., 2021, and references therein). Observational studies (both single-dish and interferometric) of young eruptive stars in the (sub)millimeter regime targeting both molecular line emission and dust continuum radiation provide more in-depth views of the small-scale structures and kinematics of the disk, and the envelope surrounding YSOs: transitions of ^{12}CO and its rarer isotopic species ^{13}CO and C^{18}O can be used to detect low- and high-density circumstellar material (e.g., Kóspál, 2011; Kóspál et al., 2016, 2017b; Fehér et al., 2017; Cruz-Sáenz de Miera et al., 2023b). HCO$^+$ and HCN emission can trace cavity walls, while SiO and SO trace the shocked material in outflows (Hogerheijde et al., 1999), and finally, the line wings of ^{12}CO emission trace the outflow itself (Evans et al., 1994).

Despite the growing number of observational studies in the millimeter regime including FUors and FUor-like objects (e.g., McMuldroch et al., 1995; Fridlund et al., 2002; White et al., 2006; Fehér et al., 2017; Lee et al., 2019; Bianchi et al., 2020; Wendeborn et al., 2020; Mercimek et al., 2022; Ruíz-Rodríguez et al., 2022; Lee et al., 2024) and model predictions on molecules as outburst tracers in eruptive systems (Visser et al., 2015; Rab et al., 2017; Molyarova et al., 2018; Zwicky et al., 2024), wide-band spectral line surveys at (sub)mm wavelengths of more evolved FUors do not yet exist. The lack of studies could be (primarily) due to the distances of many of these sources, highlighted by Audard et al. (2014) and revised recently by Szabó et al. (2023a,b). Broad frequency coverage is needed to cover multiple transitions of a given species, which is crucial to determine the physical properties of the gas using population diagrams (e.g., Goldsmith & Langer, 1999).

Historically FUors, especially FU Orionis and the classical FUors (see Chapter 1) have been well-studied at optical and near-infrared wavelengths. This resulted in comprehensive analyses that are utilised to identify and characterise new members of the class (e.g., Herbig, 1977; Herbig et al., 2003; Clarke et al., 2005; Connelley & Reipurth, 2018; Hillenbrand et al., 2018; Szegedi-Elek et al., 2020; Szabó et al., 2021; Nagy et al., 2022; Szabó et al., 2022; Nagy et al., 2023). Millimeter wavelength observations of spectral lines and modelling have addressed their molecular content (e.g., Rab et al., 2017; Molyarova et al., 2018; Zwicky et al., 2024). Eruptive stars appear to be still close to their natal cores, whose chemistry can be investigated well through (sub)mm and radio wavelength observations (e.g., Szabó et al., 2023a,b, and references therein), which indicate the presence of high concentrations of dense material in the vicinity of many of these protostars. A line survey covering wide frequency regimes, aiming to provide an in-depth view of the molecular inventory of the environment of an FUor can motivate interferometric studies, which may allow further study of the outburst effects on the chemical composition of the stars' close environments.

This Chapter presents a study of V1057 Cyg, a classical FUor in the Class II evolutionary phase (e.g., Herbig, 1977; Herbig et al., 2003), the second FUor discovered. At a distance of 897^{+19}_{-20} pc (Bailer-Jones et al., 2018a,b), V1057 Cyg has the highest peak accretion rate among FUors measured to date (Szabó et al., 2021). The source went into outburst in 1969–1970, brightening by ~6 magnitudes in the V-band (Welin, 1971a,b). The only pre-outburst spectrum shows properties of a T Tauri star (TTS, Herbig, 1977, 2009). The source displays variable and high-velocity wind features of P Cygni profiles blueshifted by up to 100 – 300 km s^{-1} and recently jet tracers were detected, usually rare in FUors, but more common in classical T Tauri stars (Magakian et al., 2013; Takagi et al., 2018; Kóspál et al., 2020; Park et al., 2020; Szabó et al., 2021). V1057 Cyg has exhibited multiple extraordinary flares in the 1720 MHz OH maser transition, remaining the only eruptive star known to show this phenomenon (Lo & Bechis, 1973, 1974b; Winnberg et al., 1981).

In the following, I present the results of a wideband spectral line survey of V1057 Cyg complemented by on-the-fly maps of emission from selected molecules. The line survey was conducted with the IRAM 30-m telescope and has an almost continuous coverage from ~72 GHz (~4.1 mm) to ~263 GHz (~1.1 mm). Other selected frequencies, around 219 GHz – 227 GHz (~1.3 mm), 291 GHz (~1.0 mm), and 344 GHz (~0.8 mm), were observed with the APEX 12-m telescope. Together, this dataset provides an in-depth view of the molecular composition of this young eruptive star's environment. In Section 4.2 I describe the observations as well as the data reduction. In Section 4.3 I present the results and analysis of the data, while in Section 4.4 I compare the findings with results reported in the literature. Finally, in Section 4.5 I summarise the most important findings of this study.

4.2 Observations and data reduction

To acquire the main spectral line survey data of V1057 Cyg we observed the star's position, $(\alpha, \delta)_{\rm J2000} = 20^{\rm h}58^{\rm m}53\overset{\rm s}{.}73$, $+44°15'28\overset{''}{.}4$, with the IRAM 30-m telescope, operated by the Instituto de Radioastronomía Milimétrica (IRAM) on Pico Veleta in the Spanish Sierra Nevada. The observations (project id: 060-23, PI: Menten) took place from 2021 August 4 to 6, with a total observing time of 35.5 hours. We used the Eight Mixer Receiver[1] (EMIR, Carter et al., 2012b) in the E0, E1 and E2 bands, with the fast Fourier transform spectrometers (FFTSs), providing an instantaneous bandwidth of 16 GHz and a spectral resolution of ∼200 kHz. The survey was conducted in the position-switching mode with a reference position at the relative equatorial offset (−600″, 600″). In addition, mapping was conducted using on-the-fly (otf) mode, centered on the position of V1057 Cyg with a reference position at (300″, 300″). NGC 7027 and K3-50A were used to obtain pointing and focus corrections regularly during each observing session. The main parameters of the 30-m observations are summarised in Table 4.1. The main beam efficiencies were computed automatically using the Ruze formula (relating the gain of an antenna to the root mean square, RMS, of the antenna's random surface errors), with parameters taken from the IRAM webpage[2].

The data were reduced using the GILDAS/CLASS software developed by IRAM (Pety, 2005c). Platforming effects, materialising as intensity offsets in the spectra, were identified and corrected by subtracting first order baselines in each subband. In addition, I excluded scans, where careful inspection revealed remaining platforming, which generally stemmed from problems in the outer basebands, or any other issues.

Table 4.1: Information on the IRAM 30-m observations conducted with EMIR.

Date yyyy-mm-dd	Mode	Band	Tuning (GHz)	Frequency range (LSB, USB) (GHz)	Beam (″)	Measured rms noise level[(*)] LO (mK)	 LI (mK)	 UI (mK)	 UO (mK)	Size of otf map (″)
2021-08-04	onOff	E0	73	72 – 78.5, 86.4 – 94.1	34.4 – 26.7	12.5	8	5.5	11.2	–
2021-08-04	onOff	E0	80	77.7 – 85.5, 93.2 – 101.1	32.2 – 22.8	5.1	3.9	4.5	4.7	–
2021-08-06	otf	E0	90	87.7 – 95.5, 103.3 – 111.1	28.2 – 22.6	11.2	10.7	12.3	14.7	300″×300″ 315″×315″
2021-08-04	onOff	E0	94	92.7 – 99.8, 107.7 – 115.5	27.3 – 21.6	4.5	3.5	4.4	6.4	–
2021-08-05	onOff	E1	133	130.7 – 138.5, 146.3 – 154.1	19.1 – 16.31	7.6	5.8	9.3	12	–
2021-08-05	onOff	E1	141	138.7 – 146.5, 154.4 – 162.1	18.1 – 15.51	7.5	5.9	10	9.5	–
2021-08-06	onOff	E2	202	199.7 – 207.5, 215.4 – 223.1	12.5 – 11.2	19.3	36.1	37.3	39.2	–
2021-08-06	onOff	E2	210	207.7 – 215.5, 223.4 – 231.1	12.1 – 10.8	46.5	43.9	43	45.9	–
2021-08-06	onOff	E2	234[(a)]	231.7 – 239.5, 247.4 – 255.1	10.8 – 9.8	37.8	41.6	54	74.8	–
2021-08-06	onOff	E2	242	239.7 – 247.5, 255.4 – 263.1	10.4 – 9.5	52.3	52.4	64.8	67.8	–

Notes. *The rms noise levels were measured separately for the lower outer (LO), lower inner (LI), upper inner (UI), and upper outer (UO) bands of the lower and upper side bands.
[(a)]The 234 GHz tuning observations are not presented.

In addition to the IRAM 30-m observations we conducted observations with the Atacama Pathfinder EXperiment (APEX) 12-m submillimeter telescope at selected frequencies centered around 227, 291, and 344 GHz (project ids: M9530C_107, M9515A_108, M9523C_109; PI:

[1]https://publicwiki.iram.es/EmirforAstronomers#Overview
[2]https://publicwiki.iram.es/Iram30mEfficiencies

Menten). The APEX data were obtained using several instruments, summarised here in chronological order of their use (see also Table 4.2).

We used the dual-sideband, dual-polarization receiver nFLASH230[3] with the Fast Fourier Transform Spectrometer (FFTS, Klein et al., 2006) backend, providing a bandwidth of 32 GHz and a spectral resolution of 61 kHz, covering frequencies between ~213 and ~245 GHz (see also Table 4.2). The observations were carried out on 2021 July 20, 21, and 31 with a total observing time of ~5.5 hours. For the July 20 and 21 observations the wobbler switching mode was used with a single pointing toward the position of the source and a wobbler throw of 200″ in azimuth, and for the July 31 observation mapping was conducted with a reference position at the relative equatorial offset (6000″, 4000″).

We also used LAsMA[4], a 7-pixel, dual-sideband, single-polarization, heterodyne receiver, consisting of a hexagonal array of six pixels surrounding a central pixel. The backend consisted of Fast Fourier Transform Spectrometers (FFTSs) covering an intermediate frequency (IF) bandwidth of 4 – 8 GHz (see Table 4.2 for the covered frequency range). The observing time with LAsMA was ~8.5 hours. The LAsMA observations were conducted using the on-the-fly mapping mode with reference position at (400″, 400″).

Finally, we used the dual-sideband, dual-polarization receiver SEPIA345[5] (see Table 4.2 for the covered frequency range). The upper and lower sidebands each cover the IF range 4 – 12 GHz, giving a total of 32 GHz IF bandwidth, with each sideband recorded by two FFTS units. The observations were conducted with the position-switching mode with a reference position at (300″, 300″). The observing time was ∼1 hour with SEPIA. The total observing time with APEX was ∼15 hours.

For all APEX observations, the antenna temperature, T_{A}^{*}, was converted to main-beam temperature, T_{MB}, using the relationship $T_{\mathrm{MB}} = T_{\mathrm{A}}^{*}\ \eta_{\mathrm{f}}/\eta_{\mathrm{mb}}$ where η_{f} and η_{mb} are the forward and main-beam efficiencies, respectively, from the APEX website[6]. The main parameters of the observations are listed in Table 4.2. The data obtained with APEX were also reduced using the GILDAS/CLASS software.

[3]https://www.apex-telescope.org/ns/observing-run/observing/the-telescope/instruments/nflash/
[4]https://www.apex-telescope.org/ns/observing-run/observing/the-telescope/instruments/lasma-large-apex-sub-millimetre-array/
[5]https://www.apex-telescope.org/ns/observing-run/observing/the-telescope/instruments/sepia/
[6]https://www.apex-telescope.org/telescope/efficiency/

Table 4.2: Information on the APEX 12-m observations.

Date	Receiver	Mode	Band	Tuning	Frequency range	Beam	Measured rms noise level				Size of otf
yyyy-mm-dd				(GHz)	(GHz)	($''$)	LO (mK)	LI (mK)	UI (mK)	UO (mK)	($''$)
2021-07-20	nFLASH	onOff	nFLASH230	219.2	213.2 – 221.1, 229.3 – 237.2	29.5 – 26.5	20.3	38.5	21	122.5	–
2021-07-21	nFLASH	onOff	nFLASH230	227.2	221.1 – 229, 237.3 – 245.2	28.4 – 25.6	19.7	67.9	20.2	67.8	–
2021-07-31	nFLASH	otf	nFLASH230	227.2	213.2 – 221.1, 229.3 – 237.2	28.4 – 25.6	101	350	138	–*	$600''\times600''$
2021-11-19	LAsMA	otf	LAsMA345	344.2	342.2 – 346.3, 354.2 – 358.2	18.3 – 17.5	30.4[(a)]		59.3[(b)]		$120''\times120''$
2021-11-20	LAsMA	otf	LAsMA345	344.2	342.2 – 346.3, 354.2 – 358.2	18.3 – 17.5	31.1[(a)]		105.1[(b)]		$120''\times120''$
2022-05-28	SEPIA	onOff	SEPIA345	291.0	272.9 – 280.8, 289.2 – 297	23.0 – 21.1	69.9	29.5	38	41.5	–

Notes. *Due to high noise level and deep atmospheric lines the rms of the UO cannot be measured accurately. [(a)]Measured rms noise level for the whole LSB. [(b)]Measured rms noise level for the whole USB.

4.3 Results and analysis

4.3.1 Line detection and identification

Figure 4.1 presents the complete spectrum obtained towards V1057 Cyg with the IRAM 30-m telescope, with frequencies of prominent molecular lines marked with vertical lines. Line identifications were based on spectroscopic data from the Cologne Database for Molecular Spectroscopy[7] (CDMS, Müller et al., 2001, 2005) and the Jet Propulsion Laboratory catalog[8] (JPL, Pickett et al., 1998b). A line is considered detected if its peak intensity is $\geq 3\,\sigma$, where σ is the rms noise level measured in the portion of the spectrum surrounding the candidate line. I only report lines of molecules with at least 2 detected transitions within the coverage of our line survey. In general, the detected lines are relatively narrow (<2.5 km s^{-1}, FWHM), and well isolated, thus their identification is straightforward compared to line-rich sources such as hot cores or hot corinos (Belloche et al., 2013; Bianchi et al., 2020; Busch et al., 2024). The terms hot core (in high-mass star-forming regions) and hot corinos (in low-mass star-forming regions) refer to the warm, dense inner region of the envelope of massive young stellar objects and YSOs where complex organic molecules (e.g.,CH_3OH) are located (Belloche et al., 2013; Yamamoto, 2017; Bianchi et al., 2020).

Figure 4.2 shows examples of the detected line profiles for several molecules observed with the 30-m telescope. These examples illustrate the identification of a certain molecular species with a particular transition (e.g., DCO^+), hyperfine structure components (e.g., CN), multiple transitions within a narrow frequency range (e.g., CH_3OH), and the presence of broad line wings indicating outflow activity (e.g., ^{13}CO). The complete list of identified lines is given in Table B.1 (due to the length of this table) with upper energy levels, Einstein coefficients, and the parameters derived

[7]https://cdms.astro.uni-koeln.de
[8]https://spec.jpl.nasa.gov

from Gaussian fits (discussed in Section 4.3.2), while each detected line is displayed in a narrow frequency window in Figures B.1–B.9. There are several cases where the data suggest potential detections of molecules, however, these identifications remain uncertain due to low signal-to-noise ratios (with candidate lines detected $<3\sigma$) or because they only rely on a single, weakly detected transition (below $<3\sigma$). These occurrences are not included in the final line identification and fit results in Table B.1, but are instead marked with green labels in Figures B.1–B.9 (e.g., some molecules with a particular transition, in the case of H_2CO, H_2CN, H_5CN, CH_3OH in Figure B.7). The list of identified lines from the APEX observations is given in Table B.2 and the detected lines are displayed in Figures B.10–B.13.

We detect emission of molecules ranging from simple neutral molecular species to COMs. Identified species are listed in Table 4.3, with the molecules organised from the simplest to the most complex. In total, 35 molecular species are detected (including isotopologues) in the spectrum of V1057 Cyg. We detect *C*-, *N*-, *O*-, *S*-bearing molecules (e.g., CO, CN, CS, CCS, HCN, HNC, H_2CO, H_2CS), deuterated species (e.g., DCN, DNC), molecular ions (e.g., HCO^+, HCS^+), carbon-chain molecules (e.g., C_2H, HC_3N), a cyclic molecule (e.g., c-C_3H_2), COMs (e.g., CH_3OH), and in many cases some of their isotopologues (see Table B.1).

The spectral energy distribution (SED) of V1057 Cyg implies a flared disk and envelope geometry (e.g., Kenyon & Hartmann, 1991), while an envelope with an estimated size of 7000 au was confirmed from Spitzer/IRS observations (Green et al., 2006). Later, 50–670μm far infrared/submilllimeter wavelength imaging with *Herschel* also indicated a reservoir of cold dust (Green et al., 2013). From ^{13}CO observations using the Plateau de Bure Interferometer (with a beam of $2.7'' \times 2.2''$), Fehér et al. (2017) reported a rotating envelope around V1057 Cyg, with a radius of $5''$ (3000 au). Thus it is likely that our single-dish data, with a beam size larger than $9''$, corresponding to ~8100 au at the 897 pc distance to the target, traces emission both from the disk and the envelope around the source. For instance, CO and its isotopologues likely trace the disk and outflow, while CS (2–1), HCN (1–0), and the hyperfine structure components of CN (2–1) and C_2H (1–0) could sample the cold gas closer to the midplane (seen in T Tauri stars, e.g., Dutrey et al., 2014). We also detected other dense gas tracers, such as CS, CCS, HCO^+, including their isotopologues ^{13}CS, $C^{33}S$, $C^{34}S$, and $H^{13}CO^+$, as well as N_2H^+ (e.g., Shirley, 2015; Yamamoto, 2017, and references therein).

For most molecular species, several transitions with different upper-level energies are detected,

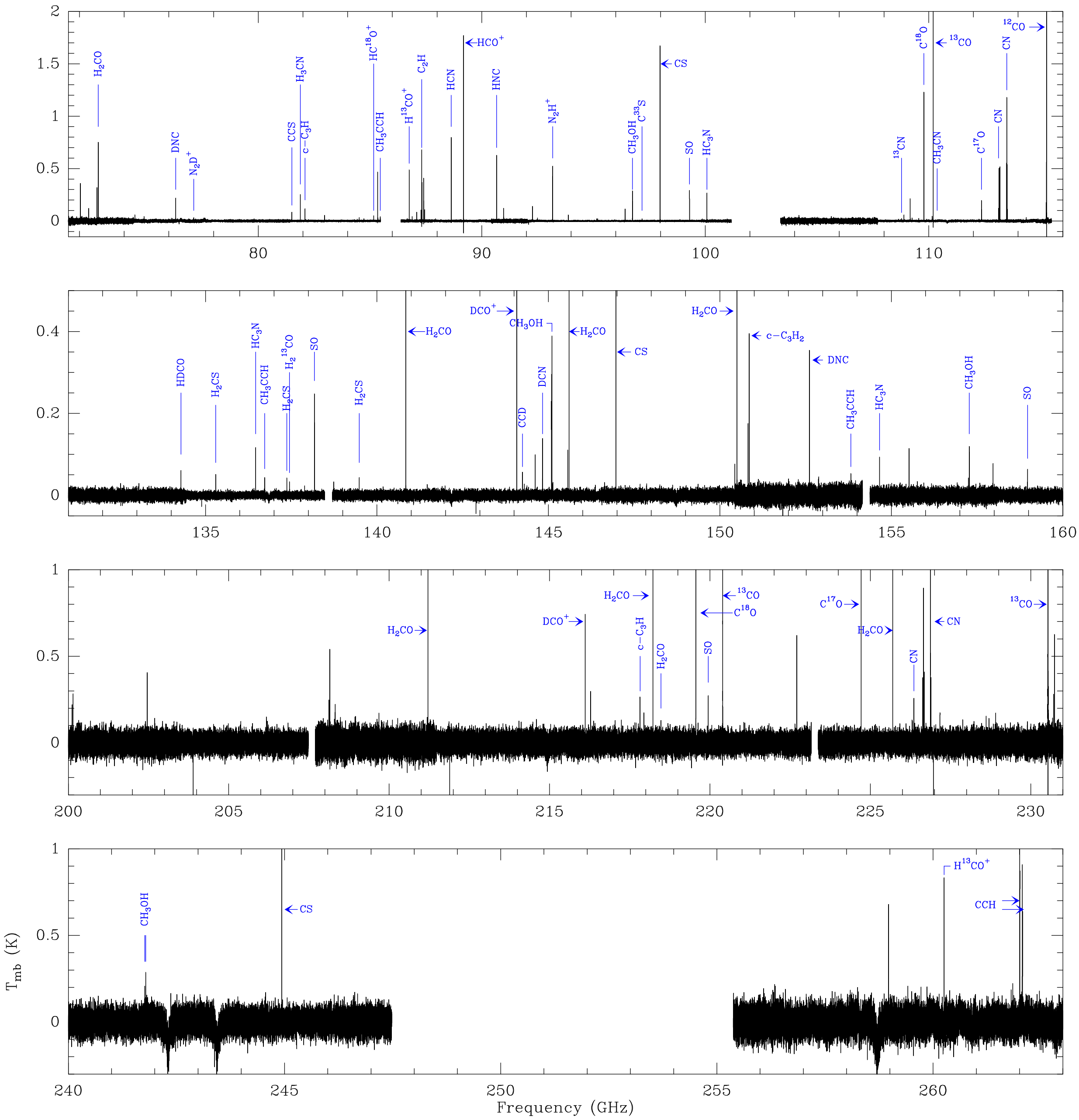

Figure 4.1: Complete spectrum of V1057 Cyg obtained with the IRAM 30-m telescope, with selected lines labelled with the name of the molecular species. The complete list of identified lines is provided in Table B.1 and zoom views of all lines are displayed in Figure 4.2 and Figures B.1 – B.9. The deep absorption features around 242–244 GHz and 258–259 GHz represent residual atmospheric absorption. Figure from Szabó et al. (2025).

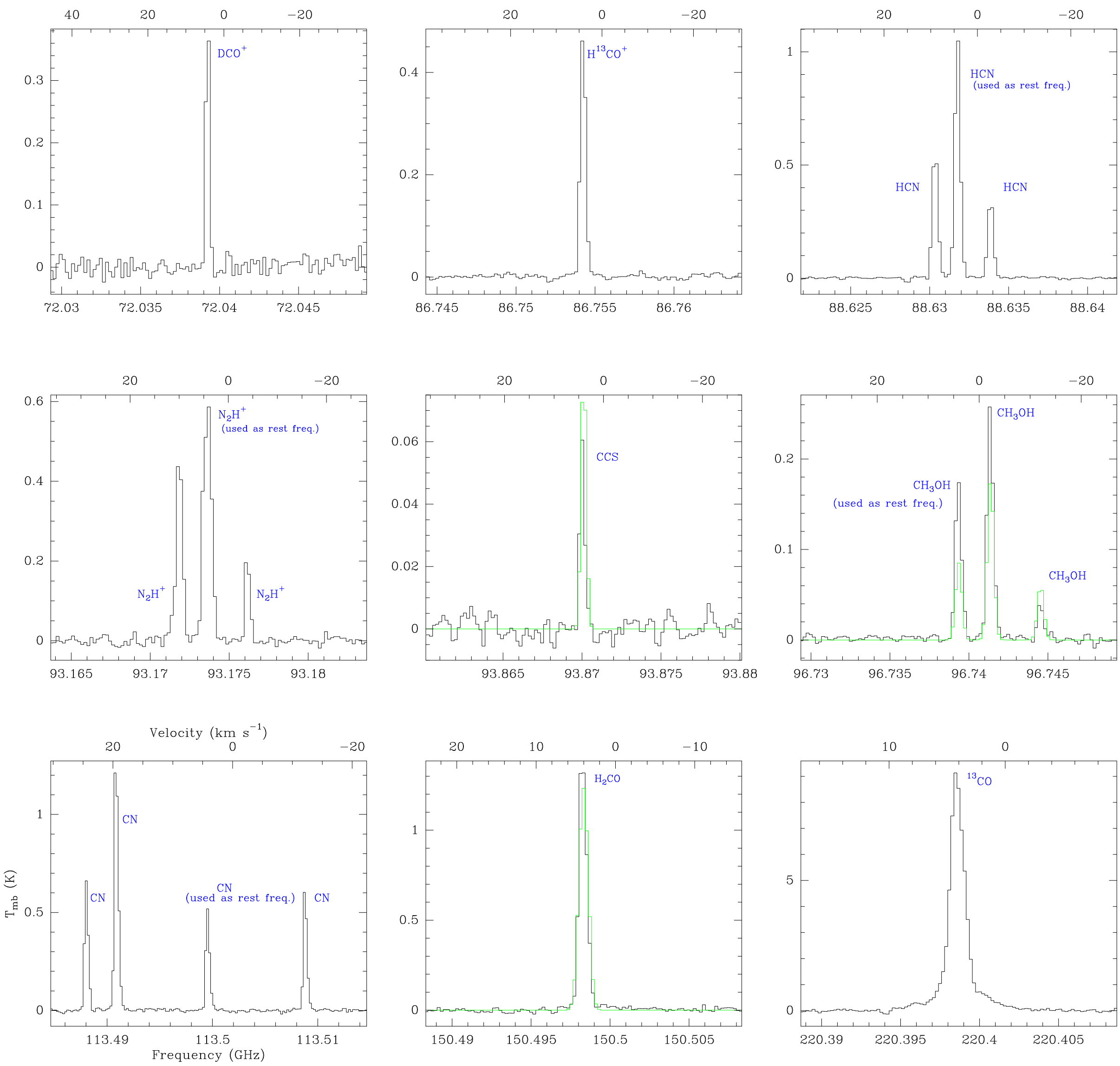

Figure 4.2: Selection of lines detected with the IRAM 30-m telescope, labelled with the molecular species name in blue; the other lines are shown in Figures B.1–B.9. LTE synthetic spectra are overlaid in green for selected species (see Sections. 4.3.4 and 4.3.5). In each panel, the bottom and top axes are labelled in frequency and velocity, respectively. Figure from Szabó et al. (2025).

Table 4.3: Overview of molecules and isotopic species detected towards V1057 Cyg in this survey.

Simple neutral molecules:
CN, ^{13}CN, CO, ^{13}CO, $C^{17}O$, $C^{18}O$, SO, CS, ^{13}CS, $C^{33}S$, $C^{34}S$, HCN, HNC, H_2CO, $H_2{}^{13}CO$, H_2CS
Deuterated species:
CCD, DCN, DCO^+, DNC, N_2D^+, HDCO
Molecular ions:
HCO^+, $H^{13}CO^+$ HCS^+, N_2H^+
Carbon chain molecules:
C_2H, CCS, C_4H, CH_3CCH, HC_3N
Cyclic molecules:
c-C_3H_2
Complex organic molecules:
CH_3OH, CH_3CN
Other molecules:
HNCO

which allows a more detailed analysis including simple radiative transfer modelling and the construction of population diagrams, presented in Sections 4.3.4 and 4.3.5, respectively.

4.3.2 Line profiles, LSR velocities, and line widths

Based on single-dish observations, it can be challenging to distinguish emission from foreground or background clouds and from different physical structures within a source (e.g., disk, envelope) unless these components have different velocities. In this survey, only molecules with similar velocities were detected, suggesting that the observed line emission is associated with V1057 Cyg and its environment.

Most of the detected lines show narrow single-peaked profiles that can be fitted by a single Gaussian. In the case of outflow tracers (e.g., ^{13}CO) the line profiles are also single-peaked (except ^{12}CO, see below), but show broader wings, suggesting outflow activity. For the spectrum at the source position, I fitted each line profile with a single Gaussian component using the built-in function in CLASS, and the results are presented in Tables B.1 and B.2. The Gaussian fitting method does not yield good results for the ^{12}CO transitions because they show self-absorption, suggesting that these lines are optically thick (see examples for other FUors in Evans et al., 1994; Kóspál et al., 2017a; Kóspál, 2011; Cruz-Sáenz de Miera et al., 2023b). Therefore, these lines are only reported as detected in Tables B.1 and B.2, while Gaussian fit results are not presented. The LSR velocities obtained from the Gaussian fits range from 2.45 to 4.80 $\mathrm{km\,s^{-1}}$ for the 30-m, and from 3.95 to 4.46 km s^{-1} for the APEX data. Comparing to single-dish and interferometric observations from the past decade, I find that the previously reported velocities of, for example, ^{13}CO (1–0) (4.6 and 4.05 km s^{-1}, Kóspál, 2011; Fehér et al., 2017), C^{18}O (1–0) (4.10 km s^{-1}, Kóspál, 2011), and NH_3 (1,1) (4.35 km s^{-1}, Szabó et al., 2023a, see also Chapter 2 Section 2.3 of this Thesis) are generally within ~0.5 km s^{-1} of the $v_{\rm lsr}$ values derived in this study, further indicating that the molecular species detected in our survey are associated with V1057 Cyg and its environment. Notably, I find that the measured velocities of dense gas tracers such as CS, CCS, H^{13}CO^{+}, N_2H^+ and HC_3N coincide within ~0.3 km s^{-1} (within the uncertainties of the Gaussian fits) with the systemic velocity of V1057 Cyg derived from the most recent ammonia observations (4.35 ± 0.02 km s^{-1}, Szabó et al., 2023a, see also Chapter 2 Section 2.3 of this Thesis).

From the Gaussian fits, FWHM line widths are between 0.67 and 3.43 km s^{-1} for the 30-m, and from 0.71 to 1.78 km s^{-1} for the APEX data. In general, lines that show wings, indicating outflow activity, have FWHM line widths broader than the other species (e.g., ^{12}CO and its isotopologues). The line widths of more than 50% of the fitted lines cluster around 1.3–1.5 km s^{-1} mainly transitions of CH_3OH, HC_3N, and H_2CO. Narrower widths are mainly found for CN and c-C_3H_2 lines, the former clustered around 1.1 km s^{-1} and the latter around 0.9 – 1 km s^{-1}.

I note that the transition of methanol (CH_3OH) at 84.5 GHz is a well-known Class I maser line (e.g., Batrla & Menten, 1988; Breen et al., 2019, and references therein). However, the line emission detected towards V1057 Cyg does not show clear maser characteristics (such as strong, narrow features in comparison to other transitions), thus not suggesting maser activity. The well-known Class I CH_3OH maser line at 95.1 GHz (Plambeck & Menten, 1990; Chen et al., 2011; Yang et al., 2023) was not detected in this survey, which I discuss more in Section 4.3.5.

4.3.3 Line mapping

Figures 4.3 and 4.4 present integrated intensity maps for lines mapped in the otf mode with the IRAM 30-m and APEX 12-m telescopes, respectively. In most cases (except ^{13}CO 1–0 and 2–1, see Figures 4.3i and 4.4b), the molecular line emission does not peak on V1057 Cyg itself. The HCN (1–0), HNC (1–0), HC_3N (10–9), HCO^{+} (1–0), and N_2H^+ (1–0) maps show a primary concentration of emission offset from V1057 Cyg towards the north, while a secondary peak is distributed towards the southwest, connected with a ridge that traces a pc-scale filamentary structure (Figure 4.3c,d,f,g,h). The northern peak is offset by approximately 14.7″ (~0.06 pc) to the north, while the southern peak is located approximately 1.8′ (~0.46 pc) to the southwest of V1057 Cyg.

The offset of the northern concentration relative to V1057 Cyg corresponds to only half a beam width in the 3 mm maps, but given the high signal-to-noise ratio of most maps, it is significant. The offset is unlikely the result of an optical depth effect because ^{13}CO (1–0) does peak towards the source. Moreover, the offset is larger than the pointing error and this peak is also visible in the dust-based H_2 column density map (Szabó et al., 2023a, see also Figure 2.3 in Chapter 2). The larger-scale ridge structure is well traced by the 1–0 and 2–1 transitions of ^{13}CO and C^{18}O (see Figures 4.3i,j and 4.4b,c). The ridge towards the southwest appears fainter compared to the northern peak in the maps of the 1–0 transitions of HCN, HCO^+, and N_2H^+. Notably, the extent of the emission from some transitions (e.g., HC_3N 10–9, HNC 1–0) to the southwest seems comparable in size and intensity to that of the northern peak in these transitions. The integrated intensity maps of CCS (7–6), H_2CS (3–2), and HC_3N (12–11) have lower signal-to-noise ratios but appear to trace the same extensions toward the north and southwest. The mapped molecular emission trace a large-scale structure (e.g., see emission of HCN (1–0), HC_3N (10–9), HNC (1–0)), with a ridge extending through the position of V1057 Cyg to the north and the south. This structure shows signs of fragmentation on smaller scales, suggesting the presence of dense material which may indicate the presence of a dense core or an embedded protostar. This is further discussed in Section 4.4 of this Chapter.

The molecular outflow of V1057 Cyg was first reported by Evans et al. (1994) on the basis of the strong blueshifted wing emission detected in their ^{12}CO 3–2 spectrum obtained with the Caltech Submillimeter Observatory 10.4 m telescope (CSO). These authors also mentioned the existence of maps towards this source as a private communication from S. McMuldroch but I could not find any publication reporting them. The APEX spectrum has a similar line profile as the CSO spectrum, with a slightly more pronounced self-absorption, however, our more sensitive spectrum reveals the redshifted wing for the first time. The APEX map of the ^{12}CO 3–2 emission, presented in Figure 4.5, reveals a bipolar outflow that appears to originate from V1057 Cyg. The outflow appears to be more collimated on the redshifted side, with discrete peaks to the south of the source position. Figure 4.6 shows a ^{12}CO (3–2) position-velocity (p-v) diagram taken along the cut shown in Figure 4.5. The p-v diagram shows several peaks (labelled R1, R2, and B1; R for red and B for blue), which are more prominent in the redshifted emission. The highest velocity extensions are revealed by the first contour close to R1, which may mark an episodic ejection event (e.g., as seen in non-eruptive YSOs; Plunkett et al., 2015). Peak R1 appears close to the systemic velocity of the source, while peak R2 is located around 5 km s^{-1}. The fainter blueshifted peak,

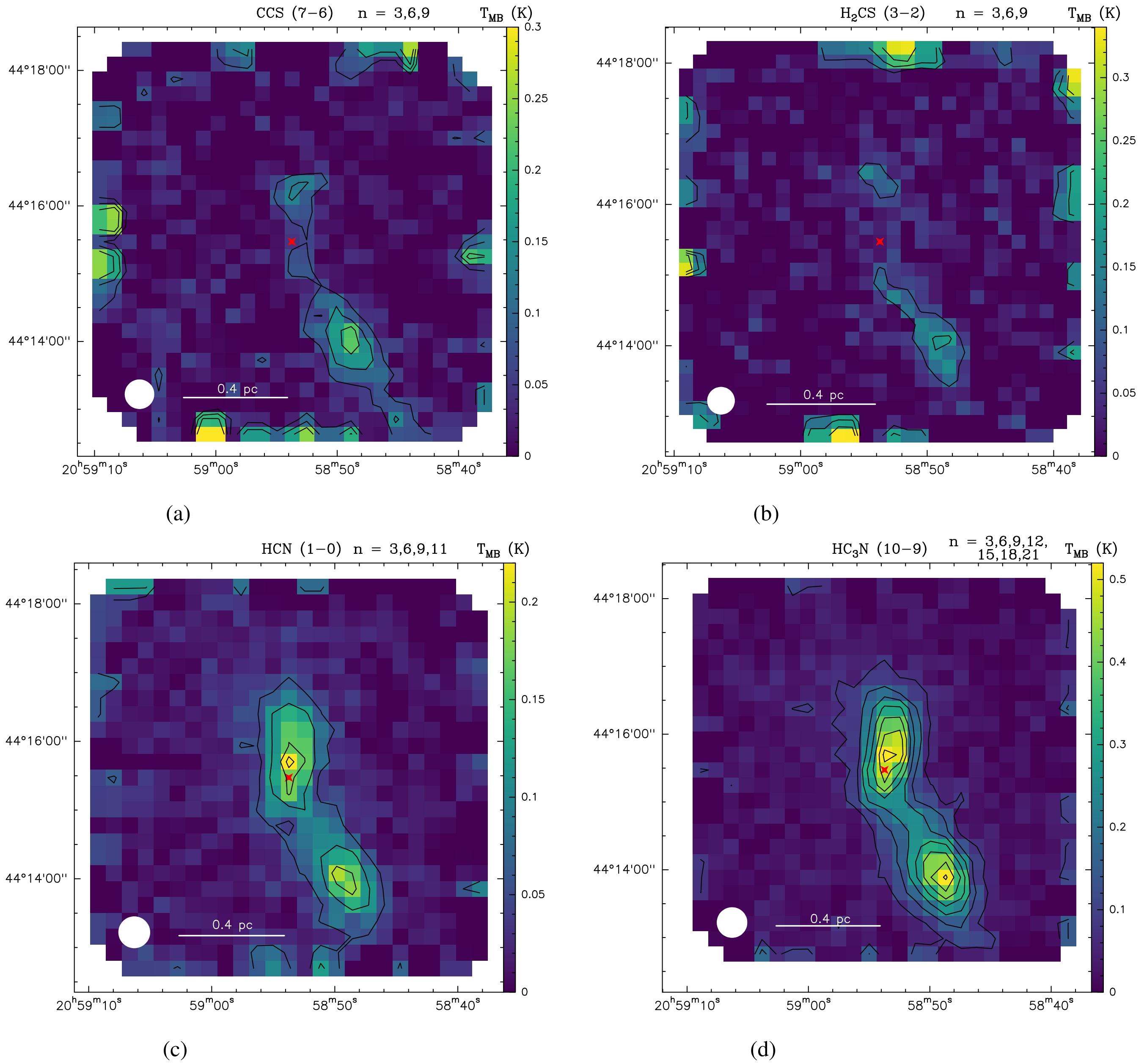

Figure 4.3: Integrated intensity maps of molecular lines obtained with the IRAM 30-m telescope. The red cross marks the position of V1057 Cyg and the white circle shows the telescope beam size at the line frequency. The physical scale is presented near the beam size. Contour levels are $n\sigma_{int}$ (multiples of the noise level in each map, between ~0.02 and ~0.03), with the corresponding values of n given above each panel. Figures from Szabó et al. (2025).

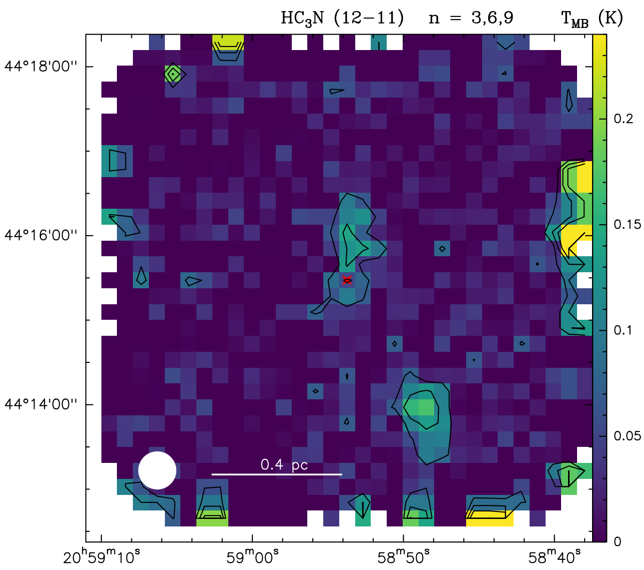

(e)

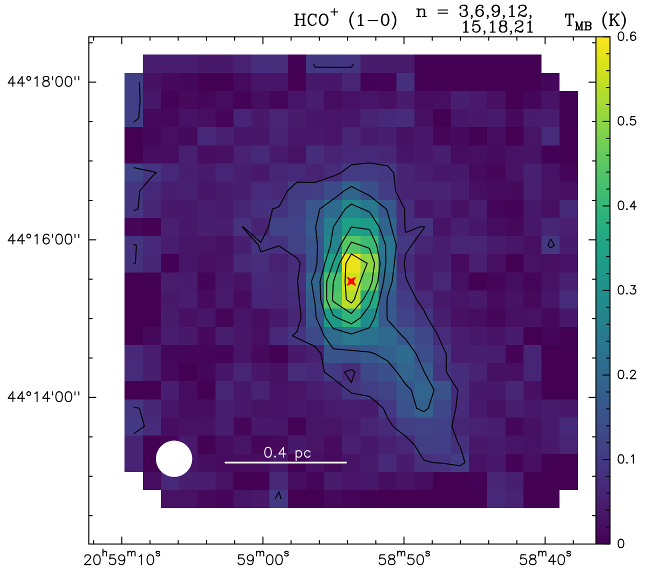

(f)

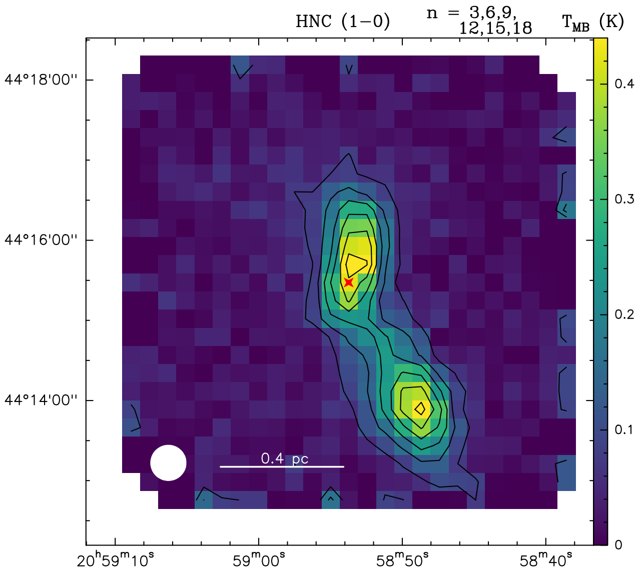

(g)

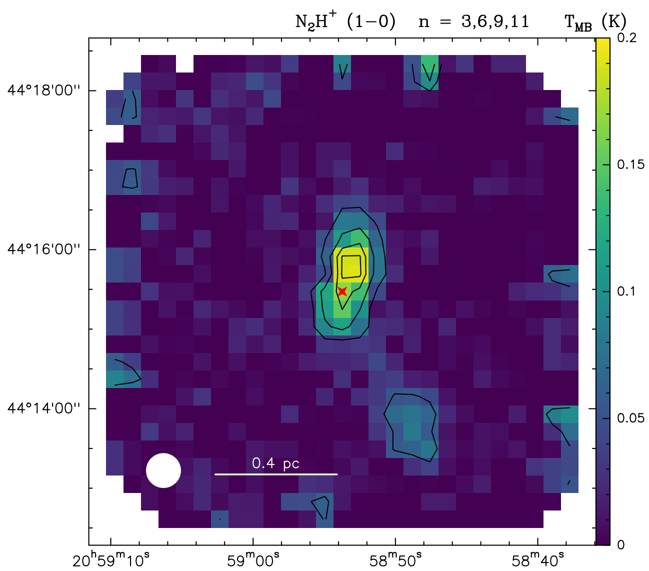

(h)

Figure 4.3: Continued.

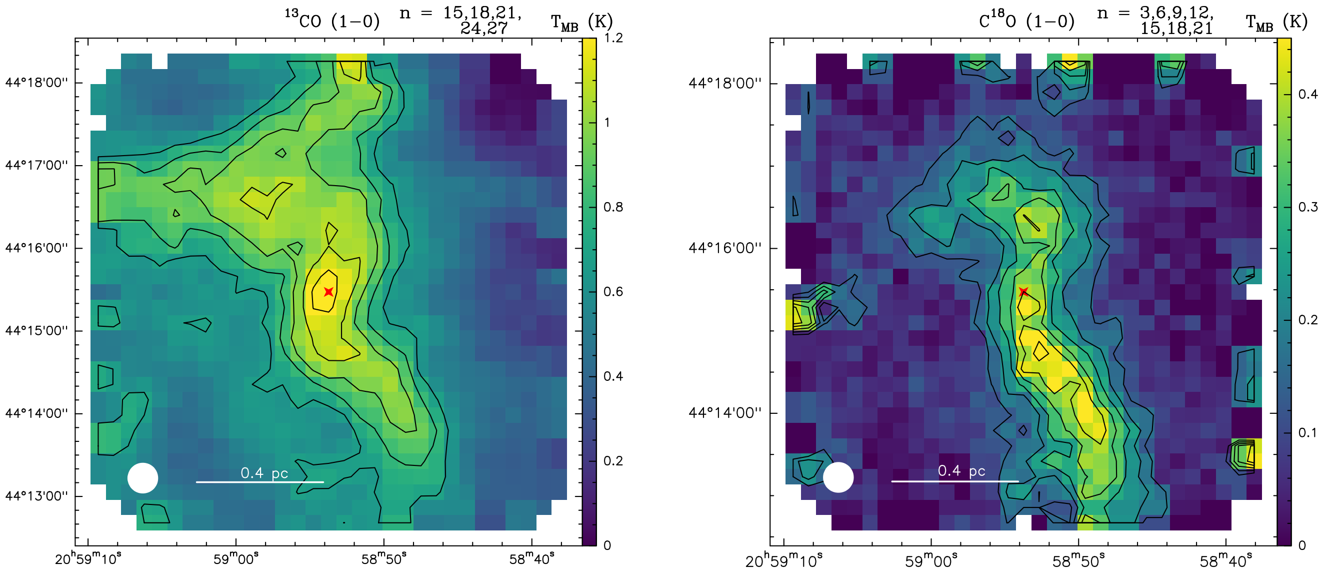

(i) (j)

Figure 4.3: Continued.

B1, appears at a velocity around 1 km s^{-1}. The p-v diagram also shows weak "fingers" (indicated by white arrows) revealed by the lowest contours of the ^{12}CO emission. These results are further discussed in Section 4.4.2.

4.3.4 Radiative transfer modelling

I modelled the observed 30-m data using Weeds (a GILDAS/CLASS extension for the analysis of millimeter and submillimeter data, Maret et al., 2011) to create synthetic spectra with the assumption of local thermodynamic equilibrium (LTE). The spectroscopic information required for the synthetic spectra was taken from the CDMS database (Müller et al., 2005; Endres et al., 2016). Multiple transitions are detected from molecules such as methanol (CH_3OH), formaldehyde (H_2CO), cyclopropenylidene (c-C_3H_2), carbon monosulfide (CS), thioethenylidene (CCS), cyanoacetylene (HC_3N), and thioformaldehyde (H_2CS) (see Tables 4.4 and B.1). These species were chosen for modelling because several of their lines show significant emission (i.e., $> 3\sigma$) and their profiles do not show indication of outflow (i.e., extended wings, as seen in lines from ^{12}CO and its isotopologues). I used only transitions detected with the IRAM 30-m telescope with a signal-to-noise ratio higher than 3σ for the following analysis. The radiative transfer model presented here, along with the population diagrams in Section 4.3.5, provides initial estimates of the temperatures and column densities of the molecular emission towards V1057 Cyg as observed in

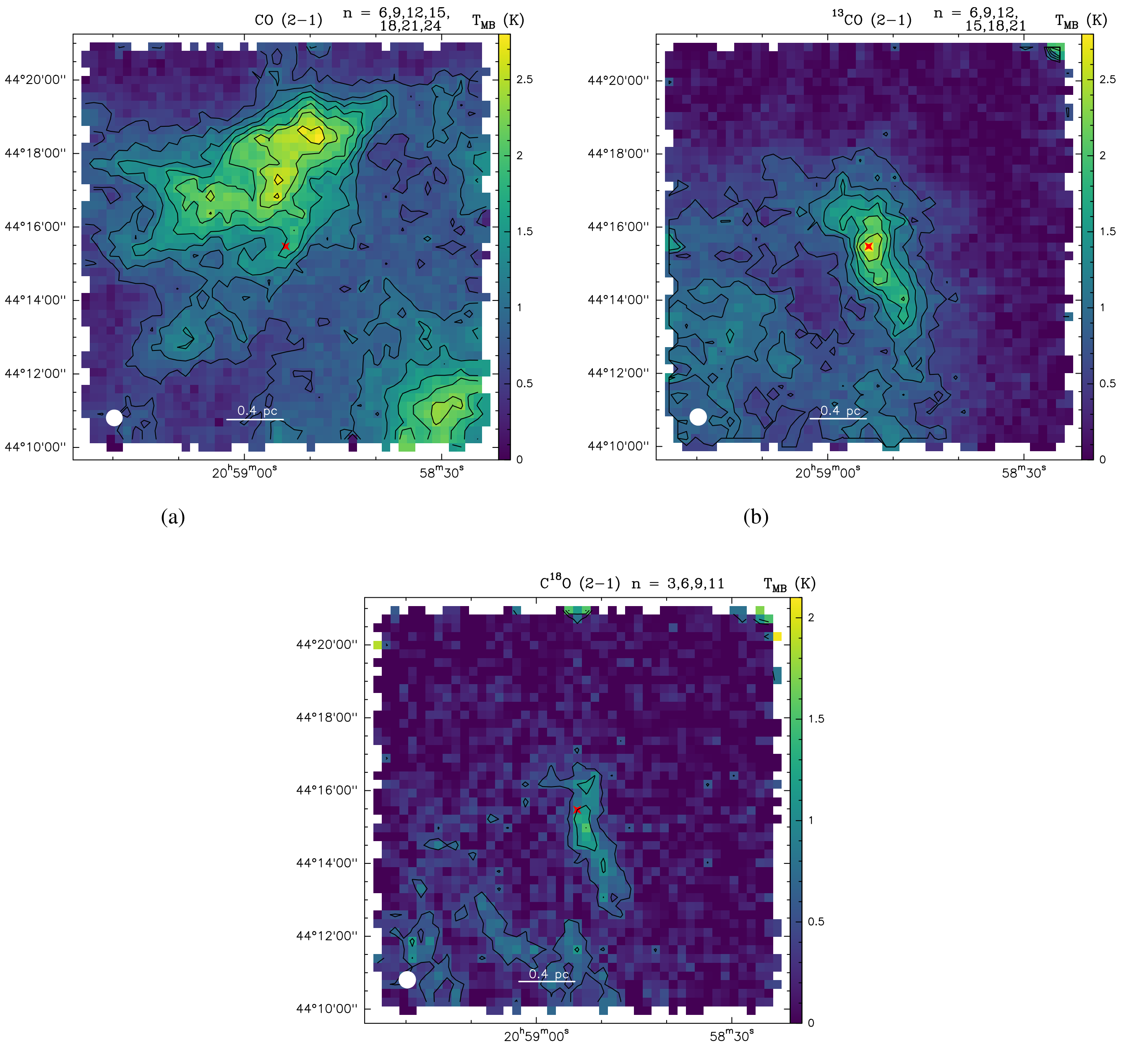

Figure 4.4: Same as Figure 4.3, but for the maps of (a) ^{12}CO, (b) ^{13}CO, and (c) C^{18}O (2–1) obtained with APEX. Contour levels are $n\sigma_{int}$ (multiples of the noise level in each map, from 0.10 to 0.16), with the corresponding values of n given above each panel. Figures from Szabó et al. (2025).

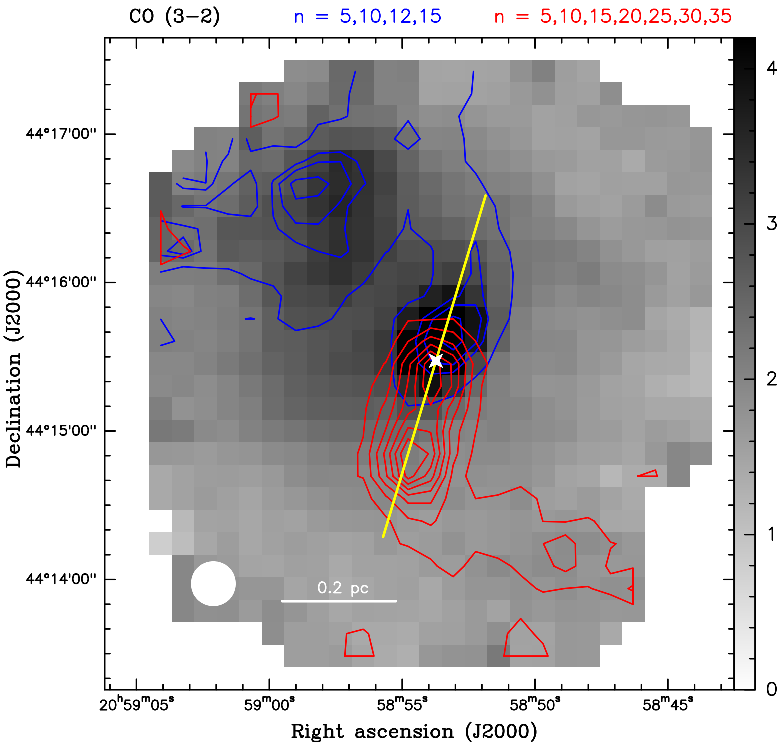

Figure 4.5: Integrated intensity map of ^{12}CO (3–2) (grey-scale image). The blue and red contours represent the blueshifted and redshifted wing emission integrated over the velocity ranges of $[-6, 2]\,\mathrm{km\,s^{-1}}$ and $[5.5, 12]\,\mathrm{km\,s^{-1}}$. The HPBW is shown in the bottom left corner in white. The position of V1057 Cyg is marked with a white cross. The yellow line shows the cut used for the position-velocity diagram shown in Figure 4.6. The position angle (PA) of the cut is $-17°$ (East from North). Figure from Szabó et al. (2025).

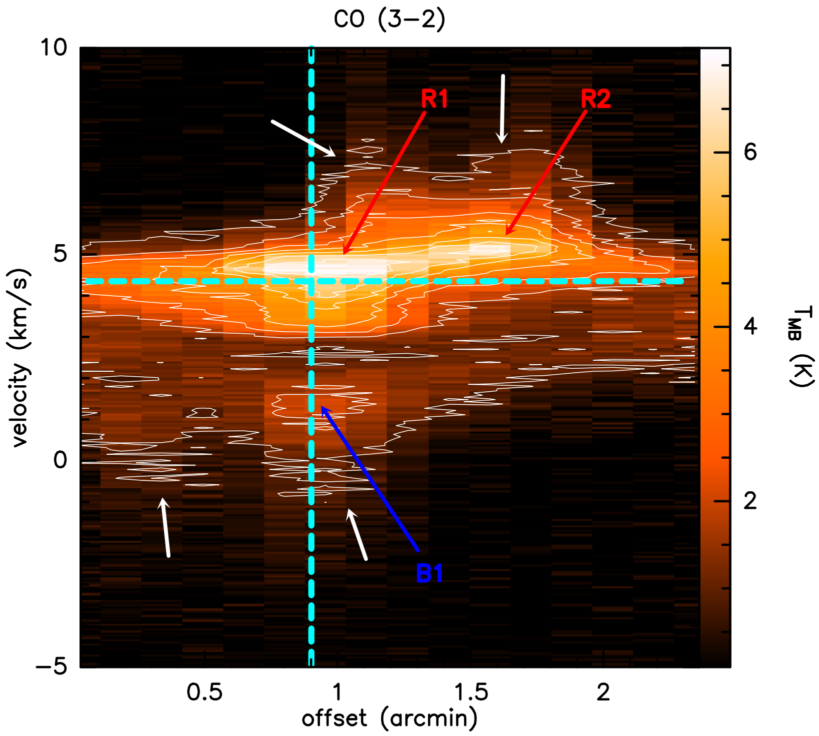

Figure 4.6: Position-velocity (p-υ) diagram along the yellow line shown in Figure 4.5. The horizontal dashed cyan line corresponds to the systemic $\upsilon_{\rm lsr}$ velocity of 4.35 km s^{-1} (Szabó et al., 2023a), while the vertical one corresponds to the source position. The contours start at 5σ and end at 35σ with 5σ steps in between. Peaks of redshifted emission are labeled R1 and R2 and the peak of blueshifted emission is labeled B1. The white arrows highlight the presence of weak "fingers" that may trace episodic ejection events. Figure from Szabó et al. (2025).

the single-dish data.

The purpose of applying a Weeds model to the chosen molecules is to improve the line identification and to investigate whether the spectrum is well-represented by an LTE model. The radiative transfer is computed by accounting for the line optical depth and the angular resolution of the observations. Weeds requires five input parameters for each molecule: the size of the emitting region (θ_s) in arcseconds, column density (N_{tot}), temperature (T_{rot}), line width ($\Delta \upsilon$ in km s^{-1}), and velocity offset (υ_{off}, with respect to the systemic velocity of the source). For each molecule, the line width was set to the average value of the line widths determined from the Gaussian fits of its detected transitions. The column density and rotational temperature are set by eye, and subsequently adjusted until the best-fit was achieved. The population diagrams described in Section 4.3.5 were used to optimise the temperature, emission size, and, in turn, the column density, of the Weeds models to reach the best fits possible. The column density provides a measure of the amount of a specific molecular species along the line of sight, while the abundance is derived by comparing this values to the column density of hydrogen. The molecular abundances offer insights into the chemical composition and physical conditions of the gas. I discuss the abundances later in this Section and in Section 4.3.5 of this Chapter.

I explored a range of source sizes between 1.5″ (e.g., Calahan et al., 2024) and 35″ (larger than the largest beam size) and found the best fits with a source size of 25″ for HC_3N and 30″ for the rest of the molecular species. These results are consistent with the integrated intensity maps of the different species (see Figure 4.3), and are further discussed in Section 4.3.5. Calahan et al. (2024) detected methanol emission, coincident with the source position of V1057 Cyg using the NOEMA interferometer, which remained unresolved. They derived the column density and temperature of methanol with a similar LTE analysis, assuming a size of 1.5″ (private communication with Calahan). Using the same parameters in our Weeds model of the single-dish data results in methanol lines that are much weaker than those detected with the 30-m telescope. The 218.44 GHz methanol line is detected in both the interferometric and the single-dish data. The peak intensity of this line is 53 mJy/beam in the NOEMA data (private communication with Calahan) and 440 mJy/beam in the IRAM 30-m telescope spectrum, ~8.3 times higher. Since the CH_3OH emission in the NOEMA data was unresolved (Calahan et al., 2024), this difference implies that the single-dish observations trace extended emission that is not detected by the interferometer. With the single-dish telescope, we are likely capturing several components blended together, including disk, envelope, and surrounding cloud emission.

The best-fit column densities from our LTE modeling are used to derive abundances relative to H_2. With the help of Yan Gong, we derived values for the H_2 column density by following the method used in Szabó et al. (2023a), see also Chapter 2 Section 2.3.6. I used archival *Herschel* data at 160, 250, and 350 μm to fit a spectral energy distribution (SED) to the data and derive H_2 column densities at 25″ and 30″ resolution (corresponding to the sizes mentioned above) using the same method we Szabó et al. (2023a) (see also Chapter 2 Section 2.3.6). The *Herschel* data is used to derive the H_2 column density toward V1057 Cyg with angular resolutions comparable to both the observations and the source size inferred from the best-fit radiative transfer model. However, unlike in Szabó et al. (2023a), the 500 μm data was not used because of relatively poor angular resolution (37″). Based on the SED fit, I find H_2 column densities of 1.14×10^{22} cm^{-2} and 1.21×10^{22} cm^{-2} at the angular resolution of 30″ and 25″, respectively (beam centered on the optical stellar position), with typical uncertainties of about 10%. The derived column densities and abundances are further discussed in Section 4.3.5 and listed in Table 4.4. In a number of cases (especially for certain transitions of methanol) the LTE synthetic spectra do not match the observed spectra well. This may be due to deviating from LTE. Non-LTE modelling is beyond the scope of this work, but an idea for the future (see Chapter 5).

4.3.5 Population diagrams and abundances

The transitions used for the population diagrams are well isolated in the spectrum of V1057 Cyg, therefore it was not necessary to discard any transitions owing to contamination by other species (a potential issue in line-rich sources; e.g., Belloche et al., 2009, 2016). The population diagrams were constructed using the integrated intensities of the observed profiles (from the Gaussian fits), and are presented in Figure 4.7, while the fit results are given in Table 4.4. The population diagrams presented here account for beam dilution, using the sizes determined in Section 4.3.4, including the changing beam size through the frequency coverage. Additionally, the diagrams are also corrected for optical depth, using the opacity correction factor $C_\tau = \frac{\tau}{1-e^{-\tau}}$ (see Goldsmith & Langer, 1999) from the Weeds model.

In the case of methanol, I separated the *A*- and *E*-type transitions (using two shades of green) to check for any systematic difference seen in Figure 4.7a. The *A*- and *E*-type methanol refers to two symmetry species due to the internal rotation of the methyl group (CH_3) relative to the hydroxyl (OH) group. The *A*-type methanol corresponds to states where the total spin of the three hydrogen nuclei in the methyl group is aligned to form a symmetric spin configuration, while *E*-

Table 4.4: Parameters of our best-fit LTE model and population diagram fit of methanol, formaldehyde, thioethenylidene, cyanoacetylene, thioformaldehyde, carbon monosulfide, and cyclopropenylidene.

Molecule	Parameters of the best-fit LTE model					Results of the population diagram method	
	Source size[(a)] ($''$)	N_{Weeds}[(b)] ($\mathrm{cm^{-2}}$)	T_{rot}[(c)] (K)	Δv[(d)] ($\mathrm{km\,s^{-1}}$)	$N_{\mathrm{X}}/N_{\mathrm{H_2}}$[(e)]	N_{pop}[(f)] ($\mathrm{cm^{-2}}$)	T_{rot}[(g)] (K)
CH_3OH	30$''$	3.3×10^{13}	12.0	1.42	2.8×10^{-09}	$2.8\times10^{13}\pm1.0\times10^{13}$	11.7 ± 1.9
H_2CO	30$''$	2.0×10^{13}	9.7	1.27	1.7×10^{-09}	$1.6\times10^{13}\pm4.2\times10^{12}$	10.6 ± 1.3
CCS	30$''$	3.0×10^{12}	9.4	1.14	2.8×10^{-10}	$3.3\times10^{12}\pm1.2\times10^{12}$	8.1 ± 0.8
HC_3N	25$''$	5.0×10^{12}	14.5	1.19	3.5×10^{-10}	$4.2\times10^{12}\pm5.7\times10^{11}$	14.4 ± 0.7
H_2CS	30$''$	1.5×10^{12}	14.0	1.29	1.2×10^{-10}	$1.4\times10^{12}\pm1.5\times10^{12}$	14.8 ± 9.5
CS	30$''$	2.2×10^{13}	10.5	1.33	1.9×10^{-09}	$1.7\times10^{13}\pm5.4\times10^{12}$	10.5 ± 1.5
c-C_3H_2	30$''$	6.0×10^{12}	9.0	1.09	4.7×10^{-10}	$5.5\times10^{12}\pm1.5\times10^{12}$	8.6 ± 0.7

Notes. [(a)]Emission diameter (FWHM). [(b)]Column density. [(c)]Temperature. [(d)]Average line width of all detected transitions. [(e)]Abundance values with respect to the H_2 column density using N_{Weeds} values from the best-fit LTE model. [(f)]Column density from the population diagram method. [(g)]Rotational temperature from the population diagram method.

type methanol represents the antisymmetric spin configuration. The population diagram is also a good way to see hints of maser activity of known maser species. The methanol emission in the 84.5 GHz transition does not show deviation from the rest of the transitions in Figure 4.7(a), so does not indicate maser activity. However, the best-fit model with Weeds underestimates its line strength. The other common maser transition at 95.1 GHz was not detected in this survey.

In all cases, a linear trend is present in the population diagrams without significant departure from linearity that could indicate the effect of optically thick emission or sub-thermal excitation (e.g., Velilla Prieto et al., 2017). The assumed emission size can affect the spread of data points in the population diagram due to the frequency-dependent beam size, while the opacities were found to be $\ll 1$ for all transitions, and thus do not affect the shape of the diagrams. We checked emission from CH_3OH, from which multiple lower-frequency transitions (below 120 GHz, ~3 mm window) are detected, and we found that assuming emission sizes smaller than 30$''$ increases the spread of the data points. This leads to a larger gap between the low- and high-frequency transitions, which in turn compromises the fit to the data.

From the population diagram method, we find column densities ranging from $2.8\times10^{13}\ \mathrm{cm^{-2}}$ for CH_3OH, down to $1.4\times10^{12}\ \mathrm{cm^{-2}}$ for H_2CS, and rotational temperatures ranging from 8.1 K to 14.8 K. The Weeds models were optimised on the basis of the population diagram results and the two methods agree within the errors of the population diagram method for both the column density and rotational temperature values.

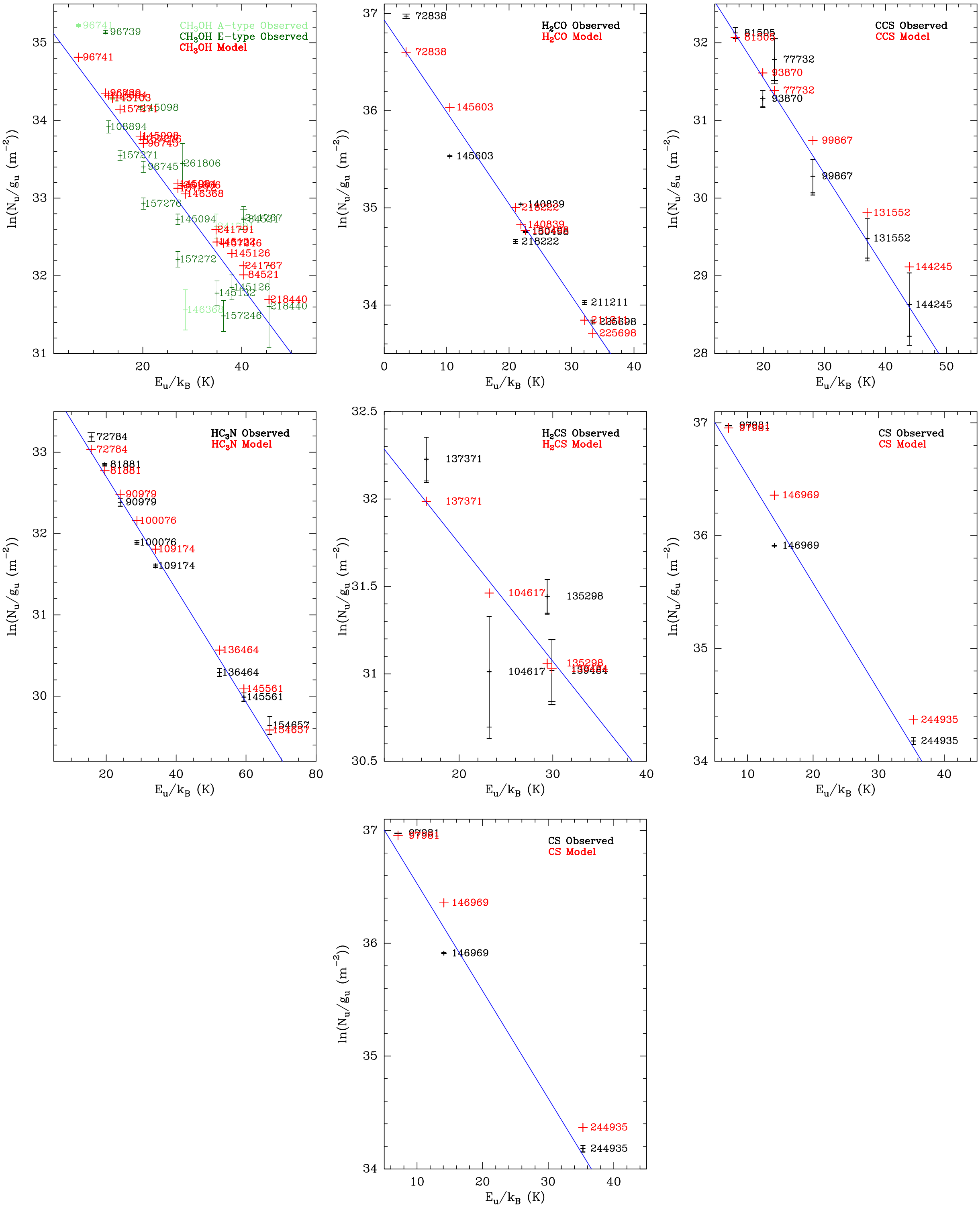

Figure 4.7: Population diagrams of: (a) CH_3OH; (b) H_2CO; (c) CCS; (d) HC_3N, (e) H_2CS; (f) CS; (g) c-C_3H_2. The black points (green in the case of CH_3OH) represent the observations while the red points correspond to the Weeds synthetic spectra computed with the parameters given in Table 4.4. For CH_3OH, the *A*- and *E*-types were separated (using two shades of green) to check for any systematic difference (see Section 4.3.5). The blue line is a fit to the observed data points in all cases. Figures from Szabó et al. (2025).

4.4 Discussion

4.4.1 Large- and small-scale structures in the environment of V1057 Cyg

In Section 4.3.3 I presented the integrated intensity maps of several molecular species, in most cases tracing lower energy transitions (Figures 4.3 and 4.4). Now, I discuss the different structures traced in our single-dish observations in the environment of our target and compare these findings with those in the literature.

The observed molecular emission traces a ridge structure seen in most of the integrated intensity maps with two peaks offset from V1057 Cyg: one towards $\sim$14.7″ to the north and one towards $\sim$1.8′ to the southwest offset from V1057 Cyg. The interferometric ^{13}CO (1–0) data presented by Fehér et al. (2017) show a structure to the north of V1057 Cyg, referred to as clump B, with a similar offset to that seen in the single-dish data. Their maps show the close vicinity of V1057 Cyg and do not cover the southwestern extension. Extended 850 μm emission distributed over large scales (larger than 1′) has been reported by Sandell & Weintraub (2001), who used the Submillineter Common User Bolometer Array (SCUBA) on the James Clerk Maxwell Telescope. These authors found V1057 Cyg to be located in a narrow ridge, traced by the dust continuum emission, extending to the north and southwest of the star. Our single-dish data extend further to the southwest providing more information. The ridge to the southwest seen in our molecular line data is visible in *Herschel* dust-based H_2 column density maps (Szabó et al., 2023a). The *Herschel* dust map, along with our integrated intensity maps, further suggests a large-scale morphology of a filamentary cloud, in which V1057 Cyg is located, as proposed by Sandell & Weintraub (2001).

Ridge structures or filaments, similar to what is seen around V1057 Cyg, are typically found in star forming regions (e.g., André et al., 2010; Hacar et al., 2023, for a recent review). A famous example is the Taurus Molecular Cloud 1 (TMC-1), where numerous cloud cores are located along a ridge structure (e.g., Hirahara et al., 1992; Langer et al., 1995). Naturally, the sizes of the TMC-1 filaments are much larger ($\sim$10 pc with cores around 0.1 pc in size, e.g., L1495 in TMC-1, Schmalzl et al., 2010) than the ridge we see around V1057 Cyg ($\sim$1–1.5 pc) within our field of view. Ridges with similar sizes to that seen around V1057 Cyg are found in many low-mass star forming regions, with NGC 1333 being a prominent example (e.g., Hacar et al., 2017). We speculate that the condensation detected to the southwest of V1057 Cyg in high density tracers (see Section 4.3.3) represents a secondary, possibly protostellar, dense core in the vicinity of V1057

Cyg. The spatial extent of the 850 μm data of Sandell & Weintraub (2001) does not extend far enough to the south to localise the soutwest peak, however, the *Herschel* derived H_2 column density map shows a peak at the position of the southwestern peak seen in our single-dish molecular line data (see, e.g., Green et al., 2013; Szabó et al., 2023a, and Figure C.1 in the latter).

Previously, the NH_3 (1,1) transition towards V1057 Cyg has been detected with a beam size of $\sim 37''$ using the Effelsberg 100-m telescope (see Szabó et al., 2023a, and Chapter 2 Section 2.3). In light of our 30-m single-dish map of, for example, the N_2H^+ (1–0) emission, it is plausible that the NH_3 spectrum is contaminated by the northern peak, located at $\sim 14.7''$ from V1057 Cyg. High-angular resolution observations of high-density tracers with interferometers could probe whether V1057 Cyg is an isolated protostar or a member of a cluster similarly to the RNO 1B/1C FUor system (Quanz et al., 2007a).

4.4.2 Temporal variations in the molecular outflow

Both single-dish and interferometric observations of ^{12}CO (and its isotopologues) have been used to identify molecular outflows associated with FUors and FUor-like objects (e.g., Evans et al., 1994; Kóspál, 2011; Fehér et al., 2017; Kóspál et al., 2017a; Cruz-Sáenz de Miera et al., 2023b, and references therein). As discussed in Section 4.3.3, the molecular outflow of V1057 Cyg was first reported by Evans et al. (1994), based only on the presence of blueshifted wing emission in a single ^{12}CO 3–2 spectrum of the source observed with the Caltech Submillimeter Observatory 10.4-meter telescope (CSO). The new ^{12}CO (3–2) APEX map reveals a clear bipolar outflow morphology (Figure 4.5), with the redshifted component reported here for the first time. The CSO spectrum of Evans et al. (1994), which peaks at 8.7 km s^{-1}, is shifted by about 4.5 km s^{-1} compared to the APEX one, which is puzzling. Although the Gaussian fit is unreliable for the ^{12}CO data, it would still be closer to the ^{13}CO and $C^{18}O$ (1–0) v_{lsr} of 3.86 km s^{-1} and 4.09 km s^{-1}, perspectively, and also to those derived from interferometric data by Fehér et al. (2017) for ^{13}CO and $C^{18}O$ (1–0) (4.05 km s^{-1} and 4.10 km s^{-1}, respectively). We suspect that the frequency axis of the spectrum published in Evans et al. (1994) was not properly calibrated. It is worth to mention that the red- and blue-shifted emission of V1057 Cyg seen in Figure 4.5 does not exhibit the typical hourglass morphology often seen in other eruptive systems such as V2775 Ori (Zurlo et al., 2017), V1647 Ori (Principe et al., 2018) or FU Orionis (Hales et al., 2015). The curved structure in both lobes may indicate a precessing outflow, potentially explaining the observed asymmetry. While the possibility of inflowing gas or streamers cannot be entirely excluded, confirming such scenarios would require higher-resolution interferometric observations. Furthermore, it is worth noting that the earlier data from Evans et al. (1994) does not show the outflow map obtained which limit a direct comparison.

Figure 4.5 reveals the outflow originating from V1057 Cyg, with the redshifted lobe pointing to the South-South-East and the blueshifted one to the North-North-West. I measured the lengths of the lobes, $R_{\rm lobe}$, and maximum velocities, $\upsilon'_{\rm max}$, to estimate the dynamical time, $t_{\rm d}$, of the outflow with the formula (Beuther et al., 2002) $t_{\rm d} = \frac{R_{\rm lobe}}{\upsilon'_{\rm max} \tan i}$, with i the inclination of the outflow axis to the line of sight (summarised in Table 4.5). The outflow map shows bipolar morphology with no overlap between the redshifted and blueshifted emissions, implying an intermediate inclination angle. Therefore I estimated $t_{\rm d}$ assuming a range of inclinations between 10 ° and 80 ° and obtained values ranging from $5{\times}10^3$ yrs to $234{\times}10^3$ yrs. Previous studies analysing the disk of V1057 Cyg derived an inclination of 62 ° (Liu et al., 2018; Szabó et al., 2021). In the following we adopt the dynamical times estimated with i =62 °, which are 15 000 years for the blue lobe, and 22 000 years for the red lobe of the outflow of V1057 Cyg. A recent survey of 20 FUors, also using the APEX 12-m telescope (Cruz-Sáenz de Miera et al., 2023b), found dynamical times on the order of thousands of years, from $3{\times}10^3$ yrs to $130{\times}10^3$ yrs, suggesting that the detected outflows are most likely not related to the current outbursts in the sample. V1057 Cyg has been in outburst for about 50 years (Herbig, 1977; Herbig et al., 2003; Clarke et al., 2005; Szabó et al., 2021), therefore the outflow cannot result from the ongoing outburst alone. High velocity gas may have been ejected in the recent outburst, however, this gas would be confined to small scales, remaining unresolved in single-dish observations (see also the results of Cruz-Sáenz de Miera et al., 2023b). The dynamical timescales derived for V1057 Cyg are consistent with those found for a sample of FUors by Cruz-Sáenz de Miera et al. (2023b), as well as with the timescales reported for a large sample of protostellar outflows such as in the study of Ioannidis & Froebrich (2012).

Signs of potential past ejection activity in V1057 Cyg have not yet been explored. One way to search for historical mass ejection events is to inspect the kinematics of the outflow in a position-velocity (p-υ) diagram, which can be used as a "fossil record" (e.g., Arce & Goodman, 2001; Zhou et al., 2024). The p-υ diagram displayed in Figure 4.6 shows discrete peaks and hints at structures similar to the turbulent jet + jet bow shock model, which can be interpreted as episodic accretion/ejection events (see, e.g., Plunkett et al., 2015). In this model, the episodic variation in the jet velocity produces an internal bow shock driving an internal shell in addition to the terminal shock. The ^{12}CO emission traces cool (i.e., lower than 100 K) swept-up material, providing a record

Table 4.5: Properties of each lobe of the outflow of V1057 Cyg determined from the APEX ^{12}CO 3–2 observations.

Lobe	$\upsilon_{max}{}^{(a)}$ (km s^{-1})	$\upsilon'_{max}{}^{(b)}$ (km s^{-1})	$R_{lobe}^{proj\,(c)}$ ($''$)	$i^{(d)}$ (°)	$t_d{}^{(e)}$ (10^3 years)
Blue	−6	10.35	70	10	163
Red	12	7.65	74	10	235
Blue				45	29
Red				45	41
Blue				62	15
Red				62	22
Blue				80	5
Red				80	7.3

Notes. $^{(a)}$Minimum (blueshifted) and maximum (redshifted) velocities. $^{(b)}$Maximum velocities $\upsilon'_{max} = |\upsilon_{max} - \upsilon_{sys}|$, where $\upsilon_{sys} = 4.35$ km s^{-1}. $^{(c)}$Projected length of a lobe along the outflow axis. $^{(d)}$Input inclination for estimating the dynamical time of the outflow lobe. $^{(e)}$Dynamical time of the outflow lobe.

of the timing history of mass-loss event(s). The p-υ diagram shows red- and blueshifted peaks (R1, R2, and B1 in Figure 4.6), with velocity offsets from the systemic velocity of V1057 Cyg. Moreover, the p-υ diagram shows weak "fingers", revealed by the lowest contour in the blue- and redshifted emission (indicated by white arrows in Figure 4.6). This is reminiscent of the results of Plunkett et al. (2015), who report a saw-like pattern along the extent of the ^{12}CO emission of the Class 0 source CARMA-7. Plunkett et al. (2015) proposed that the peaks may indicate shocks and the fingers (in their case the saw-like structure) may be evidence for a period where the faster ejecta overtakes the slower one. Furthermore, previous ejections could entrain the outflow material, therefore appearing as clumpy (see peaks R1, R2, and B1 in Figure 4.6), creating distinct shocks when a newer ejecta overtakes the previous, older one (Plunkett et al., 2015). The clumpy structure of the ^{12}CO emission of V1057 Cyg might indicate episodic ejection mechanisms, rather than a smooth, continuous/homogeneous outflow. The prominent peaks and weak fingers together with the estimated dynamical times further suggest past outburst activity of V1057 Cyg.

4.4.3 Brief comparison to other FUors

Millimeter-wavelength observations can provide information on both the small- and large-scales in the environments of YSOs. The majority of previous studies of FUors, whether single-dish or interferometric observations, have mainly focused on ^{12}CO and its rarer isotopologues of ^{13}CO and C^{18}O to probe the molecular outflows (e.g., Evans et al., 1994; Fehér et al., 2017; Ruíz-Rodríguez et al., 2017c,a; Hales et al., 2020; Wendeborn et al., 2020; Cruz-Sáenz de Miera et al., 2023b;

Nogueira et al., 2023, and references therein). However, employing other molecular species has been increasing over the past decade using both single-dish and interferometric facilities. Despite being a famous member within its class and a classical FUor, V1057 Cyg had not yet been systematically searched for molecular emission in the millimeter domain, which similar to optical and near-infrared in depth-studies (see, e.g., Herbig et al., 2003; Szabó et al., 2021, 2022) could be valuable when classifying new FUors. Prior to this work, molecular line observations towards this target mainly focused on ^{12}CO (and its isotopic species), which have been observed since the 1970s, following the outburst. ^{12}CO and ^{13}CO 1–0 line emission was first reported by Bechis & Lo (1975), followed by the detection of other transitions of ^{12}CO and its isotopic species throughout the decades, both with single-dishes and interferometers (see Section 4.3.2). Detection of the simple molecule CN (3–2) was also reported towards V1057 Cyg with a peak $\upsilon_{\rm lsr}$ comparable to the ^{12}CO observations (Stäuber et al., 2007).

The recent NOEMA observations by Calahan et al. (2024) show that V1057 Cyg stands out among a small sample of surveyed eruptive YSOs, with detections of several COMs (e.g., CH_3OH, CH_3CN, CH_3OCHO), sulfur-bearing molecules (e.g., SO, SO_2), and others. I give a brief overview of the most relevant molecular line studies targeting FUors. These include both single-dish and interferometric observations. For the relevant comparison, I chose RNO 1B/1C, L1551 IRS5, and V883 Ori. Beam dilution is an important factor when comparing single-dish and interferometric studies, since it limits the capability of single-dish telescopes to detect compact emission. For the overview, I present Table 4.6, which lists a selection of species ranging from simple molecules to COMs. The table indicates for each molecule the sources for which a detection has been reported. The FUor binary RNO 1B/1C, is one of the earliest documented examples of molecular emission associated with FUors (apart from CO, Evans et al., 1994), which includes detections of SiO (5–4), H_2CO (3–2), CH_3OH (4–3), $C^{18}O$ (2–1), CS (7–6 and 2–1), and HCO^+ (4–3) emission (McMuldroch et al., 1995). In this case, the CO emission was found to trace the bipolar outflow and CS (2–1) to probe the dense cloud core around the binary. In all cases, (McMuldroch et al., 1995) find relatively cold (below $T_{\rm kin}$ 35 K) emission tracing the environment of RNO 1B/1C, which is similar to the cold molecular emission detected towards V1057 Cyg, however the rotational temperatures that we derived toward V1057 Cyg are lower than toward RNO 1B/1C. The column densities are about an order of magnitude lower for V1057 Cyg than in RNO 1B/1C. Similarly to RNO 1B/1C, we also detect further indication of dense material (e.g., Shirley, 2015; Yamamoto, 2017, and references therein) from a number of transitions of CS, CCS, HCO^+ (and

Table 4.6: Brief overview of molecular emission reported from both single-dish and interferometric observations towards RNO 1B/1C, L1551 IRS5, V883 Ori, and V1057 Cyg discussed in Sect 4.4.4. For the table L1551 IRS5 is abbreviated as L1551. Only the main isotopologues are listed below, in many cases the secondary isotopologues of the main ones are also detected.

Species	Detected (source name/names)	Species	Detected (source name/names)
CN	L1551, V1057 Cyg	HDO	L1551, V883 Ori, V1057 Cyg
CO	RNO 1B/1C, L1551, V883 Ori, V1057 Cyg	HDCO	L1551, V883 Ori, V1057 Cyg
SO	L1551, V883 Ori, V1057 Cyg	NH_2D	L1551
SiO	RNO 1B/1C, V883 Ori	N_2D^+	L1551
CS	RNO 1B/1C, L1551, V883 Ori, V1057 Cyg	C_2DCCH	L1551
NS	L1551	CCH	L1551 IRS5, V1057 Cyg
HCN	L1551, V883 Ori, V1057 Cyg	CCS	L1551, V1057 Cyg
HCO	L1551, V883 Ori, V1057 Cyg	c-C_3H	L1551
H_2S	L1551	l-C_3H_2	L1551
HNC	L1551, V883 Ori, V1057 Cyg	c-C_3H_2	L1551, V1057 Cyg
OCS	L1551, V883 Ori	HC_3N	L1551, V1057 Cyg
SO_2	L1551, V883 Ori	CH_3CCH	L1551, V1057 Cyg
NH_3	RNO 1B/1C, L1551, V1057 Cyg	HC_5N	L1551, V1057 Cyg
H_2CO	RNO 1B/1C, L1551, V883 Ori, V1057 Cyg	CH_3CN	L1551, V883 Ori, V1057 Cyg
H_2CS	L1551, V1057 Cyg	CH_3OH	RNO 1B/1C, L1551, V883 Ori, V1057 Cyg
CH_3	L1551	CH_3CHO	L1551, V883 Ori
HCO^+	RNO 1B/1C, L1551, V883 Ori, V1057 Cyg	CH_3CCH	L1551, V883 Ori, V1057 Cyg
HCS^+	L1551, V883 Ori, V1057 Cyg	CH_3CH_2OH	L1551
N_2H^+	L1551, V1057 Cyg	CH_3OCH_3	L1551, V883 Ori
N_2D^+	L1551	C_2H_3CN	V883 Ori
$HOCO^+$	L1551	HCOOCH	L1551
CCD	L1551, V1057 Cyg	H_2CCO	L1551, V883 Ori
DCN	L1551, V883 Ori, V1057 Cyg	HNCO	L1551, V883 Ori, V1057 Cyg
DCO^+	L1551, V883 Ori, V1057 Cyg		
D_2CO	L1551		
DNC	L1551, V883 Ori, V1057 Cyg		

Notes. The most relevant references for each source. RNO 1B/1C: Evans et al. (1994); McMuldroch et al. (1995). L1551 IRS5: Fridlund et al. (2002); White et al. (2006); Bianchi et al. (2020); Mercimek et al. (2022); Marchand et al. (2024, and references therein). V883 Ori: Ruíz-Rodríguez et al. (2017a); Lee et al. (2019); Ruíz-Rodríguez et al. (2022); Cruz-Sáenz de Miera et al. (2023b, and references therein); Tobin et al. (2023); Lee et al. (2024); Yamato et al. (2024). V1057 Cyg: Bechis & Lo (1975); Levreault (1988); Evans et al. (1994); Stäuber et al. (2007); Kóspál (2011); Fehér et al. (2017); Calahan et al. (2024); and this work.

their isotopologues), and N_2H^+ in V1057 Cyg, traced on single-dish scales.

Probably the most prominent example in the literature for molecular line emission is the FUor-like, Class I protostar, L1551 IRS5 (e.g., Adams et al., 1987; Looney et al., 1997; Connelley & Reipurth, 2018), located in Taurus, at a distance of ~140 pc (Zucker et al., 2019), with a luminosity of $L = 28\,L_\odot$ (Butner et al., 1991). This source might be one of the most line-rich sources associated with the FUor class, and the detections include molecular species ranging from simple to complex molecules (see Table 4.6, and also e.g., Fridlund et al., 2002; White et al., 2006; Mercimek et al., 2022, and references therein). The most notable result toward this source is the interferometric detection of a hot corino (a region around a low-mass protostar bright in emission of COMs, e.g., Yamamoto, 2017) traced by CH_3OH (and its isotopologues), CH_2DOH, $HCOOCH_3$, and CH_3CH_2OH (Bianchi et al., 2020). One of the recent studies on this source reports a survey, covering the 3 mm and 2 mm windows using the 30-m telescope, revealing a total of 75 species, including isotopologues (Marchand et al., 2024). V1057 Cyg is not as line-rich as L1551 IRS5 with a lower number of detected species and in particular only three COMs (CH_3OH, CH_3CCH, and CH_3CN) out of the 15 reported by Marchand et al. (2024). The majority of species detected in the recent survey of L1551 IRS5 trace the cold envelope with temperatures ≤ 10 K, however, the authors report molecules with ≥ 5 atoms and a few S-bearing species (C_3S, SO, SO_2) to trace warmer, ≥ 30 K, regions. In V1057 Cyg, molecular emission above 10 K was not detected, implying that we only trace cold molecular emission towards this source. The column densities derived by Marchand et al. (2024) for L1551 IRS5 are within the same order of magnitude as the column densities we derived for V1057 Cyg, with the exception of c-C_3H_2, which has an order of magnitude lower column density in V1057 Cyg. For V1057 Cyg, the emission detected by the single-dish observations is extended over 25–30″, i.e., ~0.1 pc at the distance of ~900 pc, and likely traces the disk, the envelope, and the surrounding cloud while the observations of L1551 IRS5 and V883 Ori trace smaller scales (see below).

Finally, V883 Ori, is a FUor transitioning from the Class I to the Class II phase, located at a distance of $d = 338$ pc, with a bolometric luminosity of $L \sim 220\,L_\odot$ (e.g., Furlan et al., 2016; Connelley & Reipurth, 2018; Lee et al., 2019). This source has been the focus of a number of interferometric observations, revealing in particular a snow-line shift attributed to the outburst, a complex physical structure of its environment traced by high-density (e.g., HCN, HCO^+, DCN) and shock tracers (e.g., CH_3OH, SiO, SO), a ring-like structure traced by HCO^+ emission, and a rich chemistry traced by COMs (see Table 4.6 and also e.g., Ruíz-Rodríguez et al., 2017a; Lee et al., 2019; Ruíz-Rodríguez et al., 2022; Yamato et al., 2024; Lee et al., 2024). The recent study of Lee et al. (2024) focuses on the detection of simple molecular species and a small list of COMs using ALMA Band 6 data, a frequency regime partly covered by our single-dish observations. We find many molecular species detected in both V1057 Cyg and V883 Ori (see Table 4.6). The interferometric data trace different physical components of the environment of V883 Ori: HDCO and HNCO trace mainly the water sublimation front; HCN emission traces both the inner and outer disk, revealing an arm-like structure; and HNC and DNC trace a ring structure at the outer disk boundary (Lee et al., 2024). With the single-dish data of V1057 Cyg, we are only able to trace the large scale emission (the ridge with the southern peak and the northern concentration, and the outflow, see also Sections 4.3.3, 4.4.1, and 4.4.2). Between these two sources, V883 Ori harbours more COMs, similarly to L1551 IRS5. However, for the more evolved nature of V1057 Cyg it still demonstrates a line-rich environment, motivating follow-up interferometric observations. Furthermore, water lines were not detected in either the IRAM 30-m or the APEX 12-m data (despite transitions covered by the setup) compared to V883 Ori, however, I note that HDO $3_{(1,2)}$–$2_{(2,1)}$ emission has been recently detected by sensitive interferometric NOEMA observations towards V1057 Cyg (Calahan et al., 2024).

4.4.4 Chemical signatures of outbursts and outlook

Episodic outbursts may strongly influence the disks around protostars, introducing changes to the thermal structure and inducing chemical changes (e.g., Fischer et al., 2023), which may be used to identify past outburst events.

Rab et al. (2017) extended the radiation thermo-chemical disk code, PRODIMO (PROtoplanetary DIsk MOdel, Woitke et al., 2009, 2016), to treat envelope structures by using a representative Class I model. They simulated, spatially resolved ALMA $C^{18}O$ 2–1 observations and found this particular transition to be a good tool to probe post-outburst sources. In the model, the spatially resolved $C^{18}O$ 2–1 emission exhibits distinct signatures, such as a gap due to the freeze out of the molecules (see Figure 4 of Rab et al., 2017). In our line survey, we detected and mapped the $C^{18}O$ 2–1 transition with APEX and the emission is resolved in the north-south direction, tracing the ridge, but our observations do not resolve the disk around V1057 Cyg (see Figure 4.4 and Table B.2). Interferometric observations of the $C^{18}O$ 1-0 transition by Fehér et al. (2017) found a rotating envelope with a radius of 5″, or 3000 au at $d = 600$ pc (common distance used before *Gaia*, Bailer-Jones et al., 2018a,b), corresponding to ~4500 au at ~900 pc. With the single-dish observations of this transition having a beam size of 22.4″, we do not resolve the envelope either. The model of Rab et al. (2017) accounts for both disk and envelope emission, and the outburst-induced changes are seen in the radial distribution of the ^{12}CO emission on scales of a few 1000 au, thus much larger than the typical disk scales. The single-dish data have an angular resolution that corresponds to about ~18 000 au and, therefore, cannot resolve the ^{12}CO structures predicted by the model which are at a few 1000 au scales.

The other notable model is by Molyarova et al. (2018), who used the ANDES physical-chemical code (Akimkin et al., 2013) to follow the impact of a FUor outburst on the chemical evolution of the disk and to identify molecular tracers reacting on different timescales to the outburst. Two main groups are specified: species with abundances sensitive to an ongoing outburst but returning quickly (i.e., a few years after the peak outburst) to the quiescent (pre-outburst) values, and species that take longer to return to pre-outburst or even remain overabundant for decades (> 20 yrs). The most notable prediction is formaldehyde (H_2CO), whose gas-phase abundance can grow by up to 4–6 magnitudes, and take 30–120 years to deplete back onto dust grains, making it a good candidate tracer to, in theory, identify post-outburst sources. (Molyarova et al., 2018) modelled the brightest H_2CO transition observed in disks, the 3_{03}–2_{02} transition at 218.222 GHz, with input parameters based on the FUor outburst of V346 Nor, which in 2010 seemed to abruptly finish its outburst (and was thought to be the first FUor to do so, see Kraus et al., 2016). However, the study of Kóspál et al. (2020) showed evidence for the source gradually brightening at near-infrared wavelengths back to almost the same brightness level as prior to the abrupt fading event. They concluded the fading was likely due to different mechanisms, including an increase of the line-of-sight extinction, and appearance of warm material possibly refuelling the outburst. H_2CO (3_{03}–2_{02}) emission is detected toward V1057 Cyg in our 30-m data, however, it is fainter than other transitions of H_2CO detected in the survey. The abundances of H_2CO and CH_3OH (see Table 4.4) are orders of magnitude lower than the abundances predicted by both the medium and grown dust models by Molyarova et al. (2018). However, the abundances presented here correspond to material at the scale of ~30″, while the model abundances are predicted at the much smaller scale of the disk. In contrast, the HC_3N abundance is closer to the model predictions, although its abundance is lower than those of H_2CO and CH_3OH. The HC_3N map shows extended emission, without a peak centered on V1057 Cyg, hence suggesting that the HC_3N line emission detected towards the target is not dominated by compact, unresolved emission. Unluckily, we do not have maps of H_2CO or CH_3OH emission to check whether the emission peaks on the target. The CS abundance derived for V1057 Cyg is higher than the model predictions. The NH_3 abundance derived in Chapter 3 is ~1 order of magnitude lower than the abundance predicted by the model of Molyarova et al. (2018).

Considering that V1057 Cyg has been in outburst for over 50 years, it is plausible that during the peak of the outburst, the abundance values were elevated due to the heat from the central source. The detection of multiple transitions of many molecular species and the lower abundances compared to the model predictions show that many species are still present and not yet frozen-out to dust surfaces. On the other hand, the single-dish data clearly trace large-scale structures (i.e., the ridge), and it is uncertain what fraction of the measured flux is related to a more compact disk around the source and what is related to the extended ridge.

The available chemical models, together with line surveys such as the one presented here, motivate follow-up studies both observational and theoretical. In the case of V1057 Cyg, high-angular resolution observations could resolve the smaller-scale structures (i.e., on scales of the disk and envelope system) and their connection to the larger scale emission traced by the ridge both to the north and south of the source position. Future, spatially resolved observations could reveal structures similar to those predicted in the models due to inside out freeze-out (Rab et al., 2017), snow-line shifts (either water or other molecules) attributed to the outburst, or could help with distinguishing which species trace the different layers in the system, similarly to what has been found in V883 Ori (e.g., Tobin et al., 2023; Yamato et al., 2024). This may allow probing of the impact of the outburst on the physical and chemical structure of the disk and the close environment of V1057 Cyg (e.g., Molyarova et al., 2018; Lee et al., 2024; Andreu et al., 2023). Further detection of indicators of the water snowline (e.g., Molyarova et al., 2018) and information on the D/H ratio in more evolved sources such as V1057 Cyg may add more information on Class II sources, currently absent from the statistics (see Figure 3 of Andreu et al., 2023, and references therein). Despite the single-dish data not being able to resolve the small scales, the line survey shows a richer line emission than might have been expected for a relatively more evolved, classical FUor like V1057 Cyg, and motivates higher-angular resolution studies to determine whether emission from molecules such as H_2CO and CH_3OH is coming from the large-scale ridge or a compact structure around the source. Furthermore, high-angular resolution observations of ^{12}CO could reveal past episodic ejection events in greater detail.

4.5 Conclusions

The first wide-band line survey of the Class II source, V1057 Cyg in the millimeter wavelength regime, spanning an almost continuous frequency coverage from ~72 GHz to ~263 GHz has lead to the following conclusions:

- In the spectra taken with the IRAM 30-m and the APEX 12-m telescopes of V1057 Cyg, I identified (mostly) simple *C*-, *N*-, *O*-, *S*-bearing molecules (e.g., CN, CS, HCN), deuterated species (e.g., DCN), molecular ions (e.g., HCO^+), simple *C*-chain molecules (e.g., C_2H, HC_3N), and complex organic molecules in the single-dish data. V1057 Cyg displays lines from 35 molecular species (including isotopologues). The different spatial distributions of emission in the integrated line intensity maps indicate that the various lines sample different regions in the environment of the source. Most of the lines detected in this survey have been detected in disks around T Tauri stars (e.g., Dutrey et al., 2014), the closest in evolution to V1057 Cyg and other well studied, but younger FUors and FUor-like objects (e.g., Marchand et al., 2024; Lee et al., 2024).

- Most of the lines show narrow single-peaked line profiles that are well-described by single Gaussian fits, with the exception of outflow tracers that show broader line wings, indicating outflow activity. The LSR velocities in all cases indicate that the line emission is associated with the circumstellar environment of V1057 Cyg.

- Population diagrams of molecules detected in several transitions (CH_3OH, H_2CO, CCS, HC_3N, H_2CS, CS, c-C_3H_2) were constructed, indicating rotational temperatures ($T_{\rm rot}$) ranging from 8.1 K to 14.8 K. We derived column densities ($N_{\rm tot}$) of these molecules under the assumption of LTE with values ranging from 1.4×10^{12} cm^{-2} to 2.8×10^{13} cm^{-2}. The derived column densities are ~1 order of magnitude lower than those derived for younger, line rich FUors, but our single-dish survey probes larger scales compared to previous studies on FUors.

- The emission of several molecular species was mapped with the IRAM 30-m or the APEX 12-m telescope. The integrated intensity maps trace a parsec-scale ridge that runs from the Southwest to the North, going through the position of V1057 Cyg. This ridge coincides with the ridge seen in earlier dust continuum emission (Sandell & Weintraub, 2001; Green et al., 2013; Szabó et al., 2023a), however, our molecular line maps cover a larger area towards the southwest. Two clumps of molecular emission, clearly visible in the integrated intensity maps of HCN, HNC, N_2H^+ 1–0, and HC_3N 10–9, are detected along the ridge to the North and Southwest of V1057 Cyg, offset by ~15″ (~0.06 pc), and ~108″ (~0.46 pc) respectively from the source position. These results could indicate that V1057 Cyg is forming as part of a small cluster, similarly to several other FUors (e.g., White et al., 2006; Quanz et al., 2007a), and motivate future interferometric observations to reveal the protostellar content of the filamentary structures.

- The new ^{12}CO 3–2 map reveals a bipolar outflow centered on V1057 Cyg. I estimate a dynamical time for the outflow of tens of thousands of years (15 000 years for the blue lobe and 22 000 years for the red lobe of the outflow), implying that the detected outflow does not result from the current outburst activity alone. The position-velocity diagram shows discrete peaks and hints at structures representing episodic ejection events, further indicating outburst activity in the past evolution of V1057 Cyg.

Despite being at a distance of almost 900 pc and being a more evolved (i.e., Class II) object, V1057 Cyg exhibits a line-rich environment in the single-dish observations. While the molecular emission in the environment of V1057 Cyg does not reveal clear evidence of the imprint of an outburst on the chemistry of the object on the scales traced by the single-dish data, the line-rich spectra motivate future interferometric observations to spatially resolve the emission. The results also motivate similar studies of a larger sample of FUors to study the range of astrochemical properties associated with this class of outbursting protostars, and to improve the current statistics regarding the outbursts' effects on the chemical composition of their close environments, ultimately the future birthplace of planets.

5

Summary and Future Work

5.1 Summary

This Thesis is motivated by the study of the environments surrounding young stars undergoing episodic outbursts. The primary focus of my work has been on analysing observational data, both new data collected during my PhD in collaboration with others, as well as archival datasets. My research specifically targets the millimeter and radio wavelengths. Chapter 1 provides an introduction to the field of low-mass star formation and evolution, with a particular emphasis on the eruptive phenomena. It outlines the observable signatures of such outbursts, the molecular species I have investigated to trace the environments of young stellar objects, and the telescopes used throughout my research. Chapter 2 presents the first and largest dedicated radio survey of eruptive stars, with a focus on ammonia as a tracer for the dense environments and birthplaces of these objects. Chapter 3 reports the results of the first maser survey of low-mass eruptive stars, specifically concentrating on water maser emission, which provides critical insights into the local physical conditions around these objects. Chapter 4 introduces the first millimeter line survey of a more evolved, well-known example of young eruptive stars, V1057 Cyg. Chapter 4 examines the molecular inventory of the star's environment as traced through single-dish observations, offering a comprehensive view of its current state.

Studying the early stages of stellar formation and evolution is crucial for understanding of Sun-like star formation, and the potential later stage planet formation. Particular groups of low-mass Sun-like young stellar objects are of significant interest due to their (unique) accretion-driven outbursts during their early evolutionary stages. These objects experience enhanced accretion rates, resulting in the central protostars accumulating substantial amounts of material during these outbursts. Although FUors and EXors share this common feature, they differ primarily in the duration of their outbursts. Members of the FUor class exhibit longer outbursts, whereas EXors can undergo several smaller bursts followed by longer and larger amplitude outbursts. While their optical and near-infrared properties have been extensively studied through long-term monitoring programs, the environments of these objects remain relatively unexplored systematically at millimeter and radio wavelengths, despite recent advancements and efforts, such as those made with ALMA.

In the ammonia survey using the Effelsberg 100-m radio telescope, out of the 51 sources in total (both FUors and EXors, and additional *Gaia* alerts objects), we detected the NH_3 (1,1) transition in 28 sources, the (2,2) transition in 12, while the (3,3) transition was only detected in two sources, corresponding to detection rates of 54%, 23%, and 4%, respectively. The hyperfine structure of ammonia was only detected in the (1,1) transition, the satellite lines of the (2,2) and (3,3) transitions were too weak to be detected, thus only the main lines were detected. For 12 sources, where both the (1,1) and (2,2) transitions were detected, I derived kinetic temperatures, which are between 12 K and 21 K, slightly lower to the values reported towards classical T Tauri stars (see Chapter 2). I derived ammonia column densities, that range from 5.2×10^{13} cm^{-2} to 3.2×10^{15} cm^{-2}, with an average of 1.8×10^{15} cm^{-2}, higher than the average found towards T Tauri stars. The ammonia abundance is found to range from 4.7×10^{-9} to 1.5×10^{-7} with an average of 3.6×10^{-8} and a median of 2.8×10^{-8}, comparable to those reported towards infrared dark clouds (see Chapter 2). I utilised archival *Herschel* SPIRE observations, to create dust-based H_2 column density maps, of most of the targets in the survey and we found that circumstellar envelopes are present and likely contribute to the observed ammonia emission in seven sources. The first dedicated ammonia survey is sampling large-scale environments in most of the sources with a $\sim37''$ beam, which is much larger than the typical disk sizes around these objects.

The 22.2 GHz water maser survey, conducted simultaneously with the ammonia observations for the same targets, yielded a low detection rate of just 6% towards eruptive young stars, with two detections in FUors and only one in an EXor. The detection of water maser emission in the embedded object HH 354 IRS is the first reported in the literature, despite previous attempts to detect water maser emission from this source. Additionally, we serendipitously observed a strong water maser flare towards the EXor V512 Per, which, upon follow-up, was found to originate from a nearby source, H_2O(B). Despite the overall low detection rate, our findings confirm the presence of 22.2 GHz water masers in eruptive stars. The rarity of water maser detections in these objects may be attributed to evolutionary effects, as most of the sources in our sample are relatively evolved, and water masers typically decrease in intensity from the Class 0 to Class II stage. Previous surveys have suggested that water masers are less luminous in low-mass star forming regions compared to high-mass star-forming regions, which could imply that water masers present in our sample were below the detection threshold of the Effelsberg telescope. Furthermore, the rapid variability of water maser emission observed in the data suggests that sources known to harbour maser activity may have been in a quiescent phase during our observations, contributing to the overall low detection rate.

The study of the molecular inventory of V1057 Cyg focuses on a wide-band line survey of the source, covering a frequency range from approximately 72 GHz to 263 GHz using the IRAM 30-m telescope, with additional observations at selected frequencies made with the APEX 12-m telescope. In the spectra of V1057 Cyg, I identified over 35 molecular species, primarily consisting of simple *C*-, *N*-, *O*-, *S*-bearing molecules (e.g., CN, CS, HCN), deuterated species (e.g., DCN), molecular ions (e.g., HCO^+), simple *C*-chain molecules (e.g., C_2H, HC_3N), and complex organic molecules (e.g., CH_3OH). Despite being a more evolved source, V1057 Cyg displays a rich chemical composition, and the varying spatial distributions of emission in the integrated line intensity maps suggest that different molecular species trace distinct regions within the source's environment. Overall, species detected in the single-dish observations primarily sample cold regions surrounding the target. The emission from several species reveals a large, parsec-scale ridge extending to the north and south of V1057 Cyg. We hypothesize that this feature towards the south, where high-density molecular species could indicate the presence of a secondary dense core near the target, possibly harbouring an embedded protostar.

The observations presented in this Thesis show that the sampled FUors and EXors do not exhibit a clear deviation from the general population of YSOs. In fact, their properties, particularly the ammonia and water maser emission are similar to non-eruptive YSOs and T Tauri stars. The most promising distinguishing feature appears to be in their chemistry. Objects like V883 Ori reveal, for the first time, the shift in the water snow-line within the disk, driven by the increased heating from the high accretion rates during outbursts. Chemical signatures may offer the clearest path to identifying and understanding the unique impact of episodic accretion in these systems.

5.2 Future Work

Based on the research conducted for this Thesis, several promising directions for future work emerge. These directions have significant potential to further our understanding of the eruptive phenomena that occur during the early stages of stellar evolution, as well as their impact on the environments of young stars, including the planet-forming zones, and potentially, the habitability of exoplanets.

In Chapter 2, I presented the results of the first ammonia survey of young eruptive stars, where we identified 28 sources exhibiting the (1,1) transition. Combining these findings with archival *Herschel* data, we found that 7 out of the 28 sources harbour additional large concentrations of dense material. For future work, conducting a similar survey using a radio telescope located in the Southern Hemisphere to observe the eruptive stars that were not covered by the Effelsberg telescope would be highly beneficial to complete a full-sky survey. This would enhance the statistical significance of ammonia detections in eruptive stars, enabling the determination of more accurate temperature and column density estimates, while also leveraging *Herschel* data for additional insights. Additionally, interferometric observations, such as those possible with the Very Large Array (VLA), could be used to target the most interesting detections (e.g., those with high column densities and temperatures). Such observations would provide an opportunity to resolve these systems and gain a deeper understanding of the small-scale properties and interactions of ammonia emission, including potential clumpiness and spatial distribution.

Building on the work presented in Chapter 3, I identify several ways for extending the study of water maser emission in young eruptive stars emerge. Similarly to the ammonia survey, it would be beneficial to observe the remaining YSOs in the Southern Hemisphere for completing the survey and providing a more comprehensive dataset for maser emission in eruptive stars. Another valuable approach would be to gather all available archival data on water masers and investigate potential variability trends in the maser emission. This could help forecast future maser flares, particularly for sources such as V512 Per and its surrounding environment, including the nearby source H_2O(B). Although such work may require a large-scale effort at the Effelsberg telescope a focused monitoring program for a smaller sample of maser sources should yield significant insights. This could be complemented by proposing VLA observations to resolve and study the small-scale properties of the maser emission in objects where water masers have been confirmed these systems.

Although Chapter 4 already presents a comprehensive study of the molecular inventory of V1057 Cyg, several aspects remain that could be explored further in future work. High-resolution interferometric observations, particularly with facilities such as ALMA (or, alternatively, NOEMA), could provide the ability to resolve the smaller-scale emission in the environment of the target. This would include key species like HCO^+, HCN, CS, and CH_3OH, helping to differentiate between emission from the disk, envelope, and surrounding cloud. Such high-resolution observations of various transitions from several molecular species would allow for improved LTE modelling, as well as also the possibility to explore non-LTE modelling, and to derive even more accurate temperature and column density values for this source. Additionally, high-resolution interferometric data would provide the opportunity to study the ^{12}CO (3–2) emission from the outflow on smaller scales, particularly near the source. This would allow investigating the outflow linked to the most recent outburst, and might also reveal concentrations of ^{12}CO emission that suggest previous ejection events on small-scales close to the source. My work on this project, has led to new collaboration with Jenny Calahan (CfA) on a NOEMA proposal, which has been accepted with the highest mark, with the aim of a follow-up, deeper integration on the deuterated water detection towards V1057 Cyg. I am also collaborating with Lis Zwicky (Konkoly Observatory), with the aim of improving the current outburst chemistry models for FUors (Molyarova et al., 2018; Zwicky et al., 2024). The wide-band spectrum of V1057 Cyg may allow the appropriate reconstruction of the observed data in a chemical model to better understand the long-term evolution of the outburst affects on the chemistry of the disk.

A
Appendix of Chapter 3

This section contains the appendix for Chapter 3.

A.1 W75N

During the initial observing run on 2021 November 18, our setup was verified by observing W75N, a well-known massive star-forming region showing bright water masers (Lekht & Sorochenko, 1984; Hunter et al., 1994; Kim et al., 2013, and references therein). Although the survey focused on low- and intermediate-mass young stars, here I briefly present the W75N maser spectrum to make it available for potential future studies of maser variability in this famous and well-studied region. Figure A.1 shows the water maser spectrum observed toward W75N on 2021 November 18. The dashed vertical line indicates the average centroid $\upsilon_{\rm LSR}$ of 9.43 km s^{-1} derived from the NH_3 (1,1), (2,2), and (3,3) transitions. In Table A.1, we list the properties of the water maser features, along with the $\upsilon_{\rm LSR}$ results from the NH_3 transitions.

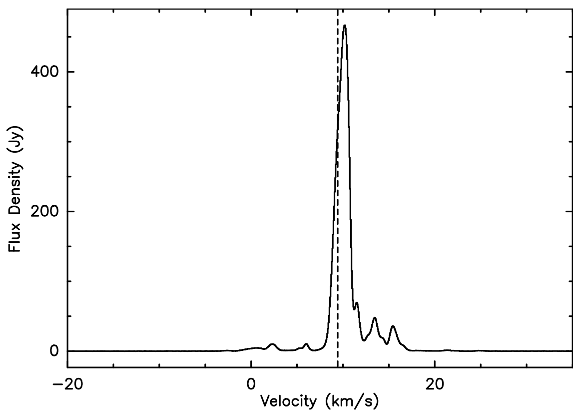

Figure A.1: H_2O maser spectrum observed toward W75N on 2021 November 18. The dashed line indicates the centroid LSR velocity of 9.43 km s^{-1} from the NH_3 (1,1), (2,2), and (3,3) transitions.

Table A.1: H_2O maser velocity components and NH_3 LSR velocities from observations of W75N on 2021 November 18.

H_2O				NH_3 (1,1)	(2,2)	(3,3)
$\upsilon_{\rm LSR}$ (km s^{-1})	RMS (Jy)	S_ν^* (Jy)	$L_{\rm H_2O}$ ($L_\odot$)	$\upsilon_{\rm LSR}$ (km s^{-1})	$\upsilon_{\rm LSR}$ (km s^{-1})	$\upsilon_{\rm LSR}$ (km s^{-1})
0.84 (0.01)	0.08	11.27	3.06×10^{-6}			
5.88 (1.23)	0.08	11.27	3.91×10^{-7}			
9.99 (0.03)	0.08	467.64	3.23×10^{-5}	9.48 (0.03)	9.37 (0.04)	9.46 (0.07)
13.35 (0.06)	0.08	49.71	3.11×10^{-6}			
15.56 (0.06)	0.08	36.50	1.32×10^{-6}			

Notes. *Results from the Gaussian fitting, for more information, see Section 3.2.

B

Appendix of Chapter 4

This appendix contains all the appendices for Chapter 4.

B.1 Line detection

In Tables B.1 and B.2, I list the lines detected above 3σ, with their respective quantum numbers, upper energy levels, Einstein coefficients, and the Gaussian fit results for the IRAM 30-m and the APEX 12-m telescopes, respectively. The lines detected in the 30-m survey are presented in Figures B.1–B.9. In certain tunings contamination from the image band cause false signal. These occurrences are labelled in red indicating rest frequency and peak temperature in the image band. An artifact is labelled on Figure B.7 around ~222.7 GHz, which does not show similarities to any of the line profiles detected (i.e., extremely narrow). Lines are labelled in red and marked as unidentified (~15 lines in the 30-m spectrum) where there is a ≥3 σ detection but line identification does not match anything in the databases. Lines detected in the other selected frequencies covered with the APEX telescope are shown in Figures B.10 and B.11.

Table B.1: Lines detected toward V1057 Cyg with the IRAM 30-m telescope

Rest frequency (GHz)	Molecule	Quantum numbers	$E_{\rm up}^{(a)}$ (K)	$log_{10}A_{\rm ij}^{(b)}$ ($\rm s^{-1}$)	$\upsilon_{\rm LSR}{}^{(*)}$ (km $\rm s^{-1}$)	$\Delta\upsilon^{(*)}$ (km $\rm s^{-1}$)	$T_{\rm MB}{}^{(*)}$ (K)	rms (mK)	Blended? (Y/N)
Tuning: 73 GHz									
72.039	DCO^+	$J = 1-0, F = 0-1$	3.5	−4.65	4.28 (0.01)	1.12 (0.06)	0.45 (0.01)	10.50	N
72.413	DCN	$J = 1-0, F = 1-1$	3.5	−4.88	4.21 (0.06)	0.81 (0.10)	0.12 (0.01)	15.30	N
72.414	DCN	$J = 1-0, F = 2-1$	3.5	−4.88	4.13 (0.12)	1.01 (0.15)	0.12 (0.01)	15.30	N
72.783	HC_3N	$J = 8-7$	15.7	−4.53	4.24 (0.02)	1.15 (0.04)	0.34 (0.05)	10.08	N
72.837	H_2CO	1(0, 1) − 0(0, 0)	3.5	−5.08	4.16 (0.01)	0.81 (0.01)	0.49 (0.01)	10.68	N
76.117	C_4H	$N = 8-7, J = 17/2-15/2$	16.4	−4.97	4.20 (0.16)	2.27 (0.41)	0.02 (0.01)	5.24	Y
76.117	C_4H	$N = 8-7, J = 17/2-15/2$	16.4	−4.97					Y
76.156	C_4H	$N = 8-7, J = 15/2-13/2$	16.5	−4.97	4.50 (0.14)	1.50 (0.35)	0.03 (0.01)	5.31	Y
76.156	C_4H	$N = 8-7, J = 15/2-13/2$	16.5	−4.97					Y
76.305	DNC	$J = 1-0$	3.7	−4.79	4.32 (0.02)	1.56 (0.05)	0.22 (0.01)	5.87	N
77.107	N_2D^+	$J = 1-0$	3.7	−4.68	4.68 (0.17)	1.18 (0.45)	0.03 (0.01)	5.69	N
77.109	N_2D^+	$J = 1-0$	3.7	−4.68	4.49 (0.17)	2.17 (0.34)	0.03 (0.01)	3.59	N
77.731	CCS	$N = 6-5, J = 6-5$	21.8	−4.69	4.07 (0.26)	3.43 (0.64)	0.03 (0.01)	5.91	N
86.670	HCO	1(0, 1) − 0(0, 0), $J = 3/2-1/2$	4.2	−5.32	4.45 (0.12)	1.49 (0.28)	0.02 (0.01)	3.19	N
86.708	HCO	1(0, 1) − 0(0, 0), $J = 3/2-1/2$	4.2	−5.33	4.27 (0.21)	1.96 (0.53)	0.02 (0.01)	4.32	N
86.754	$H^{13}CO^+$	$J = 1-0$	4.2	−4.41	4.13 (0.01)	1.42 (0.01)	0.48 (0.01)	3.91	N
87.090	$HN^{13}C$	$J = 1-0$	4.2	−4.62	4.37 (0.04)	1.46 (0.09)	0.08 (0.01)	3.92	N
87.284	CCH	$N = 1-0, J = 3/2-1/2$	4.2	−6.58	4.17 (0.02)	1.47 (0.07)	0.11 (0.01)	3.65	N
87.316	CCH	$N = 1-0, J = 3/2-1/2$	4.2	−5.81	4.18 (0.01)	1.38 (0.02)	0.75 (0.01)	5.62	N
87.328	CCH	$N = 1-0, J = 3/2-1/2$	4.2	−5.89	4.16 (0.01)	1.35 (0.02)	0.42 (0.12)	3.79	N
87.402	CCH	$N = 1-0, J = 1/2-1/2$	4.2	−5.89	4.17 (0.04)	1.32 (0.10)	0.43 (0.02)	33.94	N
87.407	CCH	$N = 1-0, J = 1/2-1/2$	4.2	−5.81	4.21 (0.20)	1.29 (0.39)	0.18 (0.09)	72.50	N
87.446	CCH	$N = 1-0, J = 1/2-1/2$	4.2	−6.58	4.15 (0.02)	1.46 (0.05)	0.11 (0.01)	3.06	N
87.925	HNCO	4(0, 4) − 3(0, 3)	10.5	−5.05	3.53 (0.08)	1.10 (0.14)	0.03 (0.01)	3.36	N
88.630	HCN	$J = 1-0$	4.3	−4.61	4.21 (0.17)	1.41 (0.43)	0.57 (0.15)	3.48	N
88.631	HCN	$J = 1-0$	4.3	−4.61	4.26 (0.05)	1.38 (0.13)	1.07 (0.09)	3.97	N

Table B.1: Continued.

Rest frequency (GHz)	Molecule	Quantum numbers	$E_{up}^{(a)}$ (K)	$log_{10}A_{\rm ij}^{(b)}$ (s^{-1})	$v_{\rm LSR}^{(*)}$ (km s^{-1})	$\Delta v^{(*)}$ (km s^{-1})	$T_{\rm MB}^{(*)}$ (K)	rms (mK)	Blended? (Y/N)
88.633	HCN	$J = 1 - 0$	4.3	−4.61	4.26 (0.28)	1.27 (0.75)	0.34 (0.18)	98.23	N
89.188	HCO^+	$J = 1 - 0$	4.3	−4.37	4.25 (0.01)	1.46 (0.01)	2.26 (0.01)	3.77	N
90.663	HNC	$J = 1 - 0$	4.4	−4.57	4.30 (0.01)	1.45 (0.01)	1.59 (0.01)	10.08	N
90.979	HC_3N	$J = 10 - 9$	24	−4.23	4.36 (0.02)	1.37 (0.05)	0.26 (0.01)	9.21	N
92.494	^{13}CS	$J = 2 - 1$	6.7	−4.85	3.89 (0.33)	2.26 (0.87)	0.02 (0.01)	9.76	N
93.171	N_2H^+	$J = 1 - 0$	4.5	−4.44	4.11 (0.14)	1.45 (0.36)	0.47 (0.10)	24.52	N
93.173	N_2H^+	$J = 1 - 0$	4.5	−4.44	4.25 (0.09)	2.07 (0.20)	0.60 (0.98)	9.06	N
93.176	N_2H^+	$J = 1 - 0$	4.5	−4.44	3.97 (0.20)	0.77 (0.70)	0.25 (0.99)	9.21	N
93.870	CCS	$N = 7 - 6, J = 8 - 7$	19.9	−4.42	4.44 (0.12)	0.96 (0.21)	0.05 (0.01)	9.65	N
Tuning: 80 GHz									
81.505	CCS	$N = 6 - 5, J = 7 - 6$	15.4	−4.61	4.16 (0.02)	1.34 (0.06)	0.08 (0.01)	3.29	N
81.881	HC_3N	$J = 9 - 8$	19.6	−4.37	4.26 (0.01)	1.53 (0.01)	0.27 (0.01)	2.59	N
82.093	c-C_3H_2	2(0, 2) − 1(1, 1)	6.4	−4.72	4.25 (0.01)	1.48 (0.04)	0.12 (0.01)	2.99	N
82.966	c-C_3H_2	3(1, 2) − 3(0, 3)	16	−5.00	4.26 (0.03)	1.30 (0.08)	0.05 (0.01)	2.21	Y
84.521	CH_3OH	$5_{-1} - 4_0, E$	40.4	−5.71	4.31 (0.07)	1.60 (0.18)	0.03 (0.01)	3.57	N
84.727	c-C_3H_2	3(2, 2) − 3(1, 3)	16.1	−4.98	4.17 (0.12)	1.15 (0.18)	0.02 (0.01)	3.22	N
85.162	$HC^{18}O^+$	$J = 1 - 0$	4.1	−4.43	4.16 (0.04)	1.48 (0.11)	0.05 (0.01)	2.91	N
85.338	c-C_3H_2	2(1, 2) − 1(0, 1)	6.4	−4.63	4.22 (0.01)	1.31 (0.02)	0.47 (0.01)	5.38	N
85.347	HCS^+	$J = 2 - 1$	6.1	−4.95	4.20 (0.07)	1.22 (0.19)	0.03 (0.01)	3.72	N
85.455	CH_3CCH	5(1) − 4(1)	19.5	−5.71	4.11 (0.12)	1.20 (0.31)	0.03 (0.01)	4.07	N
85.457	CH_3CCH	5(0) − 4(0)	12.3	−5.69	4.09 (0.09)	1.37 (0.21)	0.04 (0.01)	4.07	N
93.870	CCS	$N = 7 - 6, J = 8 - 7$	19.9	−4.42	4.31 (0.03)	1.18 (0.06)	0.06 (0.01)	3.26	N
95.150	C_4H	$N = 10 - 9$	25.1	−4.67	4.36 (0.07)	1.32 (0.16)	0.02 (0.01)	3.04	Y
95.150	C_4H	$N = 10 - 9$	25.1	−4.67					Y
95.188	C_4H	$N = 10 - 9$	25.1	−4.68	4.34 (0.09)	1.46 (0.30)	0.02 (0.01)	3.14	Y
95.188	C_4H	$N = 10 - 9$	25.1	−4.67					Y
96.412	$C^{34}S$	$J = 2 - 1$	6.9	−4.79	4.21 (0.01)	1.41 (0.04)	0.11 (0.01)	3.15	N
96.739	CH_3OH	2(1, 2) − 1(1, 1) E	12.5	−4.59	4.08 (0.13)	1.43 (0.31)	0.17 (0.03)	7.20	N
96.741	CH_3OH	2(0, 2) − 1(0, 1) A	7.0	−5.46	4.08 (0.06)	1.45 (0.15)	0.25 (0.02)	2.95	N
96.744	CH_3OH	2(−0, 2) − 1(−0, 1) E	20.1	−5.46	4.07 (0.60)	0.97 (1.57)	0.04 (0.05)	30.24	N
97.172	$C^{33}S$	$J = 2 - 1$	7.0	−4.78	4.56 (0.14)	1.93 (0.30)	0.02 (0.01)	2.93	N
97.980	CS	$J = 2 - 1$	7.1	−4.77	4.25 (0.01)	1.39 (0.01)	1.61 (0.01)	4.37	N
99.299	SO	$J = 2 - 1$	9.2	−4.94	4.17 (0.01)	1.23 (0.02)	0.27 (0.01)	4.14	N
99.866	CCS	$N = 8 - 7, J = 7 - 6$	28.1	−4.35	4.33 (0.08)	1.08 (0.24)	0.02 (0.01)	3.28	N
100.076	HC_3N	$J = 11 - 10$	28.8	−4.11	4.28 (0.01)	1.14 (0.02)	0.25 (0.01)	4.02	N
Tuning: 90 GHz otf (spectrum towards the source position, i.e. (0″,0″))									
88.630	HCN	$J = 1 - 0$	4.3	−4.61	4.06 (0.17)	1.46 (0.40)	0.10 (0.02)	10.36	N
88.631	HCN	$J = 1 - 0$	4.3	−4.62	3.32 (0.07)	1.19 (0.20)	0.15 (0.02)	11.34	N
88.633	HCN	$J = 1 - 0$	4.3	−4.61	4.35 (0.28)	0.75 (0.77)	0.08 (0.03)	20.04	N
89.188	HCO^+	$J = 1 - 0$	4.3	−4.37	4.18 (0.03)	1.53 (0.07)	0.23 (0.01)	10.60	N
90.663	HNC	$J = 1 - 0$	4.4	−4.57	4.12 (0.04)	1.51 (0.11)	0.19 (0.01)	11.58	N
90.979	HC_3N	$J = 10 - 9$	24.0	−4.23	4.29 (0.08)	0.65 (0.10)	0.09 (0.01)	12.14	N
93.171	N_2H^+	$J = 1 - 0$	4.5	−4.44	4.05 (0.17)	1.42 (0.38)	0.03 (0.01)	6.85	N
93.173	N_2H^+	$J = 1 - 0$	4.5	−4.44	4.29 (0.20)	2.38 (0.38)	0.03 (0.01)	8.45	N
93.870	CCS	$N = 7 - 6, J = 8 - 7$	19.9	−4.42	4.29 (0.17)	1.10 (0.53)	0.02 (0.01)	7.73	N
109.782	$C^{18}O$	$J = 1 - 0$	5.3	−7.02	4.09 (0.02)	1.07 (0.04)	0.35 (0.01)	11.89	N
110.201	^{13}CO	$J = 1 - 0$	5.3	−7.19	3.86 (0.01)	1.80 (0.01)	2.36 (0.02)	13.47	N
Tuning: 94 GHz									
92.494	^{13}CS	$J = 2 - 1$	6.7	−4.85	4.12 (0.08)	1.26 (0.19)	0.04 (0.01)	5.21	N
93.171	N_2H^+	$J = 1 - 0$	4.5	−4.44	4.09 (0.09)	1.36 (0.25)	0.55 (0.08)	6.29	N
93.173	N_2H^+	$J = 1 - 0$	4.5	−4.44	4.22 (0.07)	1.92 (0.16)	0.71 (0.01)	6.29	N
93.176	N_2H^+	$J = 1 - 0$	4.5	−4.44	3.91 (0.21)	1.03 (0.46)	0.27 (0.01)	6.29	N
93.870	CCS	$N = 7 - 6, J = 8 - 7$	19.9	−4.42	4.36 (0.02)	0.86 (0.14)	0.08 (0.01)	4.53	N
95.150	C_4H	$N = 10 - 9$	25.1	−5.41	4.32 (0.08)	0.97 (0.14)	0.03 (0.01)	4.49	Y
95.150	C_4H	$N = 10 - 9$	25.1	−5.41					Y
96.412	$C^{34}S$	$J = 2 - 1$	6.9	−5.41	4.14 (0.01)	1.41 (0.03)	0.11 (0.01)	2.46	N
96.739	CH_3OH	2(1, 2) − 1(1, 1) E	12.5	−5.59	4.04 (0.10)	1.48 (0.24)	0.18 (0.01)	5.83	N
96.741	CH_3OH	2(0, 2) − 1(0, 1) A	7.0	−5.46	4.06 (0.05)	1.45 (0.12)	0.27 (0.01)	2.42	N

Table B.1: Continued.

Rest frequency (GHz)	Molecule	Quantum numbers	$E_{up}^{(a)}$ (K)	$log_{10}A_{ij}^{(b)}$ (s^{-1})	$v_{LSR}{}^{(*)}$ ($km\,s^{-1}$)	$\Delta v^{(*)}$ ($km\,s^{-1}$)	$T_{MB}{}^{(*)}$ (K)	rms (mK)	Blended? (Y/N)
96.744	CH_3OH	$2(-0,2)-1(-0,1)\ E$	20.1	−5.46	4.10 (0.49)	1.24 (1.02)	0.04 (0.01)	2.25	N
97.172	$C^{33}S$	$J=2-1$	7.0	−4.78	4.80 (0.09)	1.33 (0.21)	0.02 (0.01)	2.95	N
97.980	CS	$J=2-1$	7.1	−4.77	4.17 (0.01)	1.49 (0.01)	1.52 (0.01)	2.68	N
99.299	SO	$J=3-2$	9.2	−4.94	4.04 (0.01)	1.45 (0.01)	0.27 (0.01)	2.93	N
108.651	^{13}CN	$N=1-0, J=1/2-1/2$	5.2	−5.01	4.16 (0.11)	1.24 (0.25)	0.02 (0.01)	3.72	N
108.780	^{13}CN	$N=1-0, J=3/2-1/2$	5.2	−4.97	4.13 (0.06)	1.01 (0.13)	0.03 (0.01)	3.39	N
108.893	CH_3OH	$0(0,0)-1(-1,1)\ E$	13.1	−4.83	4.05 (0.03)	1.44 (0.07)	0.05 (0.01)	2.82	N
109.173	HC_3N	$J=12-11$	34.1	−3.99	2.45 (0.01)	1.13 (0.01)	0.21 (0.01)	2.47	N
109.252	SO	$2(3)-1(2)$	21.1	−3.97	3.68 (0.05)	1.53 (0.15)	0.03 (0.01)	2.73	N
109.782	$C^{18}O$	$J=1-0$	5.3	−7.20	4.14 (0.01)	0.99 (0.01)	1.12 (0.01)	2.84	N
109.905	HNCO	$5(0,5)-4(0,4)$	15.8	−4.75	4.19 (0.10)	1.61 (0.22)	0.02 (0.01)	3.34	N
110.153	NH_2D	$1(1,1)0-1(0,1)0$	21.3	−4.78	4.46 (0.07)	1.97 (0.28)	0.04 (0.01)	3.16	N
110.201	^{13}CO	$J=1-0$	5.3	−7.19	3.02 (0.01)	1.51 (0.01)	5.66 (0.01)	2.48	N
110.381	CH_3CN	$6(1)-5(1)$	25.7	−3.96	4.15 (0.14)	1.41 (0.31)	0.02 (0.01)	2.99	N
110.383	CH_3CN	$6(0)-5(0)$	18.5	−3.95	3.76 (0.17)	1.66 (0.41)	0.01 (0.01)	3.02	N
112.358	$C^{17}O$	$J=1-0$	5.4	−7.17	3.72 (0.03)	1.29 (0.08)	0.21 (0.01)	4.81	N
112.360	$C^{17}O$	$J=1-0$	5.4	−7.17	4.20 (0.12)	1.13 (0.31)	0.12 (0.01)	5.07	N
113.123	CN	$N=1-0, J=1/2-1/2$	5.4	−5.88	4.26 (0.02)	1.01 (0.05)	0.15 (0.01)	5.93	N
113.144	CN	$N=1-0, J=1/2-1/2$	5.4	−5.97	4.28 (0.01)	1.15 (0.05)	0.56 (0.01)	5.42	N
113.170	CN	$N=1-0, J=1/2-1/2$	5.4	−5.28	4.21 (0.01)	1.16 (0.01)	0.56 (0.01)	5.35	N
113.191	CN	$N=1-0, J=1/2-1/2$	5.4	−5.17	4.22 (0.01)	1.13 (0.01)	0.63 (0.01)	4.68	N
113.488	CN	$N=1-0, J=3/2-1/2$	5.4	−5.17	4.24 (0.10)	1.09 (0.24)	0.65 (0.14)	56.14	N
113.490	CN	$N=1-0, J=3/2-1/2$	5.4	−4.92	4.30 (0.04)	1.05 (0.07)	1.26 (0.12)	84.52	N
113.499	CN	$N=1-0, J=3/2-1/2$	5.4	−4.97	4.27 (0.15)	1.04 (0.32)	0.49 (0.22)	160	N
113.508	CN	$N=1-0, J=3/2-1/2$	5.4	−5.28	4.29 (0.04)	0.99 (0.10)	0.59 (0.07)	56.98	N
113.520	CN	$N=1-0, J=3/2-1/2$	5.4	−5.88	4.31 (0.22)	0.92 (0.59)	0.13 (0.08)	65.04	N
115.271	CO	$J=1-0$	5.5	−7.14	…	…	…	…	…
Tuning: 133 GHz									
131.551	CCS	$N=10-9, J=11-10$	37.0	−3.97	3.67 (0.18)	1.54 (0.49)	0.03 (0.03)	6.62	N
134.284	HDCO	$2(1,1)-1(1,0)$	17.6	−4.33	3.90 0.05)	0.99 (0.12)	0.07 (0.01)	7.15	N
135.298	H_2CS	$4(1,4)-3(1,3)$	29.9	−4.48	3.93 (0.04)	1.53 (0.15)	0.05 (0.01)	4.82	N
136.464	HC_3N	$J=15-14$	52.4	−3.70	4.08 (0.01)	1.17 (0.04)	0.12 (0.01)	3.92	N
136.725	CH_3CCH	$8(1)-7(1)$	36.8	−5.07	4.12 (0.09)	0.95 (0.19)	0.04 (0.01)	5.24	N
136.728	CH_3CCH	$8(0)-7(0)$	29.5	−5.05	3.95 (0.11)	1.68 (0.31)	0.04 (0.01)	5.76	N
137.371	H_2CS	$4(0,4)-3(0,3)$	16.5	−4.43	4.28 (0.06)	1.33 (0.18)	0.04 (0.01)	4.29	N
137.449	$H_2{}^{13}CO$	$2(1,2)-1(1,1)$	21.7	−4.30	3.95 (0.08)	1.67 (0.25)	0.03 (0.01)	4.29	N
138.178	SO	$4(3)-3(2)$	15.9	−4.49	3.96 (0.01)	1.38 (0.02)	0.24 (0.01)	4.78	N
146.635	$H_2^{13}CO$	$2(1,1)-1(1,0)$	22.4	−4.22	4.11 (0.10)	1.24 (0.20)	0.03 (0.01)	7.04	N
146.969	CS	$J=3-2$	7	−4.21	4.18 (0.01)	1.26 (0.01)	1.70 (0.01)	6.87	N
150.436	c-C_3H_2	$2(2,0)-1(1,1)$	9.7	−4.22	4.20 (0.04)	1.03 (0.11)	0.08 (0.01)	8.78	N
150.498	H_2CO	$2(1,1)-1(1,0)$	22.6	−4.18	4.12 (0.01)	1.18 (0.01)	1.41 (0.01)	10.81	N
150.820	c-C_3H_2	$4(0,4)-3(1,3)$	19.3	−3.74	4.19 (0.02)	0.93 (0.05)	0.17 (0.01)	10.44	N
150.851	c-C_3H_2	$4(1,4)-3(0,3)$	19.3	−3.74	4.23 (0.01)	0.97 (0.02)	0.41 (0.01)	9.89	N
152.609	DNC	$J=2-1$	11.0	−3.81	4.32 (0.01)	0.97 (0.03)	0.34 (0.01)	9.61	N
153.814	CH_3CCH	$9(1)-8(1)$	44.1	−4.95	4.28 (0.16)	1.36 (0.31)	0.04 (0.01)	9.94	N
153.817	CH_3CCH	$9(0)-8(0)$	36.9	−4.94	4.12 (0.09)	1.01 (0.21)	0.05 (0.01)	9.14	N
Tuning: 141 GHz									
138.739	^{13}CS	$J=3-2$	13.3	−4.29	4.34 (0.09)	1.18 (0.20)	0.04 (0.0)	7.71	N
139.483	H_2CS	$4(1,3)-3(1,2)$	29.9	−4.44	4.36 (0.07)	1.18 (0.16)	0.05 (0.01)	7.11	N
140.839	H_2CO	$2(1,2)-1(1,1)$	21.9	−4.27	4.08 (0.01)	1.17 (0.01)	1.70 (0.01)	7.76	N
144.077	DCO^+	$J=2-1$	10.4	−3.67	4.21 (0.01)	1.01 (0.01)	0.71 (0.01)	4.00	N
144.241	CCD	$N=2-1, J=5/2-3/2$	10.4	−5.08	4.17 (0.09)	1.35 (0.45)	0.04 (0.01)	4.45	N
144.242	CCD	$N=2-1, J=5/2-3/2$	10.4	−5.20	4.06 (0.06)	1.14 (0.18)	0.05 (0.01)	4.41	N
144.244	CCS	$N, J=11,12-10,11$	43.9	−3.85	4.20 (0.21)	0.97 (0.49)	0.02 (0.01)	4.17	N
144.296	CCD	$N=2-1, J=3/2-1/2$	10.4	−5.17	3.73 (0.17)	2.75 (0.43)	0.03 (0.01)	4.18	N
144.376	CCD	$N=2-1, J=3/2-3/2$	10.4	−5.42	4.38 (0.10)	0.91 (0.25)	0.02 (0.01)	4.59	N
144.617	$C^{34}S$	$3-2$	13.9	−4.23	4.14 (0.02)	1.33 (0.05)	0.10 (0.01)	4.20	N
144.826	DCN	$J=2-1, F=2-2$	10.4	−4.50	3.93 (0.05)	1.23 (0.14)	0.03 (0.01)	3.52	Y

Table B.1: Continued.

Rest frequency (GHz)	Molecule	Quantum numbers	$E_{up}^{(a)}$ (K)	$log_{10}A_{\rm ij}^{(b)}$ (s^{-1})	$v_{\rm LSR}{}^{(*)}$ ($km\,s^{-1}$)	$\Delta v^{(*)}$ ($km\,s^{-1}$)	$T_{\rm MB}{}^{(*)}$ (K)	rms (mK)	Blended? (Y/N)
144.826	DCN	$J = 2-1, F = 1-0$	10.4	−4.15					Y
144.828	DCN	$J = 2-1, F = 2-1$	10.4	−3.89	4.05 (0.02)	1.15 (0.05)	0.13 (0.01)	3.367	N
145.089	c-C_3H_2	$3(1,2)-2(2,1)$	16.0	−4.16	4.18 (0.13)	0.95 (0.70)	0.21 (0.06)	70.95	N
145.093	CH_3OH	$3(-0,3)-2(-0,2)\,E$	27.1	−4.91	3.99 (0.50)	1.07 (1.00)	0.06 (0.07)	57.56	N
145.097	CH_3OH	$3(1,3)-2(1,2)\,E$	19.5	−4.95	4.00 (0.10)	1.23 (0.23)	0.27 (0.06)	33.63	N
145.103	CH_3OH	$3(0,3)-2(0,2)\,A$	13.9	−4.91	4.01 (0.05)	1.07 (0.09)	0.34 (0.06)	46.30	N
145.126	CH_3OH	$3(-2,2)-2(-2,1)\,E$	36.2	−5.16	3.84 (0.12)	1.54 (0.41)	0.03 (0.01)	4.42	Y
145.126	CH_3OH	$3(2,1)-2(2,0)\,E$	39.8	−5.16					Y
145.131	CH_3OH	$3(-1,2)-2(-1,1)\,E$	35.0	−4.95	3.96 (0.11)	1.40 (0.40)	0.03 (0.01)	6.31	N
145.560	HC_3N	$J = 16-15$	59.4	−3.61	4.05 (0.02)	1.10 (0.04)	0.11 (0.01)	4.35	N
145.602	H_2CO	$2(0,2)-1(0,1)$	10.5	−4.10	4.08 (0.01)	1.23 (0.01)	1.16 (0.01)	4.19	N
146.368	CH_3OH	$3(1,2)-2(1,1)\,A$	28.6	−4.96	3.93 (0.10)	1.27 (0.22)	0.02 (0.01)	4.83	N
154.657	HC_3N	$J = 17-16$	66.8	−3.53	4.07 (0.03)	1.25 (0.09)	0.10 (0.01)	7.04	N
155.518	c-C_3H_2	$3(2,2)-2(1,1)$	16.1	−3.95	4.19 (0.02)	0.95 (0.06)	0.11 (0.01)	7.28	N
157.246	CH_3OH	$4(-0,4)-4(1,4)\,E$	36.3	−4.67	4.25 (0.10)	1.46 (0.23)	0.04 (0.01)	7.28	N
157.270	CH_3OH	$1(-0,1)-1(1,1)\,E$	15.4	−4.65	3.99 (0.06)	1.21 (0.14)	0.12 (0.01)	6.85	N
157.272	CH_3OH	$3(-0,3)-3(1,3)\,E$	27.1	−4.66	4.00 (0.16)	1.46 (0.63)	0.07 (0.02)	6.91	N
157.276	CH_3OH	$2(-0,2)-2(1,2)\,E$	20.1	−4.66	3.98 (0.08)	1.26 (0.21)	0.10 (0.02)	6.57	N
158.971	SO	$3(4)-2(3)$	28.7	−4.37	4.12 (0.06)	1.80 (0.17)	0.07 (0.01)	7.01	N
Tuning: 202 GHz									
206.176	SO	$4(5)-3(4)$	38.6	−3.99	4.11 (0.10)	1.54 (0.26)	0.13 (0.03)	26.15	N
216.112	DCO^+	$J = 3-2$	20.7	−3.11	4.11 (0.01)	0.86 (0.02)	0.77 (0.03)	27.50	N
216.278	c-C_3H_2	$3(3,0)-2(2,1)$	19.5	−3.59	4.12 (0.03)	0.97 (0.08)	0.27 (0.03)	23.81	N
216.372	CCD	$N = 3-2, J = 7/2-5/2$	20.8	−3.52					Y
216.373	CCD	$N = 3-2, J = 7/2-5/2$	20.8	−3.57	3.57 (0.10)	1.65 (0.24)	0.11 (0.03)	28.43	Y
216.373	CCD	$N = 3-2, J = 7/2-5/2$	20.8	−3.55					Y
217.238	DCN	$J = 3-2$	20.9	−3.33	4.15 (0.08)	1.09 (0.20)	0.12 (0.03)	24.58	N
217.822	c-C_3H_2	$6(1,6)-5(0,5)$	38.6	−3.26	4.13 (0.03)	1.10 (0.08)	0.27 (0.03)	28.04	N
217.940	c-C_3H_2	$5(1,4)-4(2,3)$	35.4	−3.39	4.15 (0.05)	0.91 (0.10)	0.17 (0.03)	25.74	N
218.222	H_2CO	$3(0,3)-2(0,2)$	21.0	−3.54	4.02 (0.01)	1.16 (0.02)	1.31 (0.03)	24.59	N
218.440	CH_3OH	$4(-2,3)-3(-1,2)\,E$	45.5	−3.32	3.91 (0.10)	0.98 (0.20)	0.09 (0.03)	26.27	N
219.560	$C^{18}O$	$J = 2-1$	15.8	−6.22	4.07 (0.01)	1.09 (0.01)	3.69 (0.05)	32.17	N
219.560	H_2CN	$3(0,3)-2(0,2)$	21.1	−5.05	3.77 (0.14)	0.90 (0.42)	0.10 (0.04)	33.09	N
219.949	SO	$6(5)-5(4)$	35.0	−3.87	4.14 (0.04)	1.23 (0.09)	0.29 (0.04)	33.54	N
220.398	^{13}CO	$J = 2-1$	15.9	−6.21	4.13 (0.01)	1.55 (0.01)	8.75 (0.11)	30.68	N
Tuning: 210 GHz									
211.211	H_2CO	$3(1,3)-2(1,2)$	32.1	−3.64	4.13 (0.01)	1.07 (0.02)	2.048 (0.06)	44.13	N
212.928	H_2CN	$3(1,3)-2(1,2)$	32.3	−3.68	3.92 (0.15)	1.29 (0.36)	0.09 (0.04)	34.86	N
224.714	$C^{17}O$	$J = 2-1$	16.2	−6.34	4.77 (0.01)	1.47 (0.04)	1.04 (0.04)	29.31	N
225.697	H_2CO	$3(1,2)-2(1,1)$	33.4	−3.55	4.09 (0.01)	1.12 (0.01)	1.78 (0.04)	29.47	N
226.298	CN	$N = 2-1, J = 3/2-3/2$	16.3	−5.08	4.53 (0.14)	1.00 (0.23)	0.09 (0.04)	31.07	N
226.303	CN	$N = 2-1, J = 3/2-3/2$	16.3	−5.37	4.03 (0.06)	0.48 (0.17)	0.13 (0.05)	34.72	N
226.314	CN	$N = 2-1, J = 3/2-3/2$	16.3	−5.00	4.09 (0.07)	0.76 (0.17)	0.13 (0.04)	36.27	N
226.359	CN	$N = 2-1, J = 3/2-3/2$	16.3	−4.79	4.11 (0.04)	1.06 (0.09)	0.26 (0.04)	29.72	N
226.632	CN	$N = 2-1, J = 3/2-1/2$	16.3	−4.37	4.11 (0.02)	0.92 (0.05)	0.40 (0.04)	31.92	N
226.659	CN	$N = 2-1, J = 3/2-1/2$	16.3	−4.02	4.13 (0.02)	1.02 (0.06)	0.91 (0.09)	71.64	N
226.663	CN	$N = 2-1, J = 3/2-1/2$	16.3	−4.07	4.10 (0.15)	0.96 (0.33)	0.27 (0.13)	70.84	N
226.679	CN	$N = 2-1, J = 3/2-1/2$	16.3	−4.27	4.12 (0.05)	0.93 (0.11)	0.43 (0.11)	85.94	N
226.874	CN	$N = 2-1, J = 5/2-3/2$	16.3	−4.06	3.59 (0.02)	1.72 (0.06)	1.63 (0.09)	73.74	N
226.887	CN	$N = 2-1, J = 5/2-3/2$	16.3	−4.56	4.25 (0.26)	0.66 (0.45)	0.26 (0.36)	284	N
226.892	CN	$N = 2-1, J = 5/2-3/2$	16.3	−4.74	4.14 (0.27)	0.79 (0.47)	0.28 (0.36)	285	N
227.169	c-C_3H_2	$4(3,2)-3(2,1)$	29.1	−3.51	4.20 (0.05)	0.86 (0.13)	0.18 (0.04)	29.02	N
228.910	DNC	$J = 3-2$	22.0	−3.25	4.18 (0.08)	1.05 (0.18)	0.16 (0.05)	41.83	N
230.538	CO	$J = 2-1$	16.6	−6.16	…	…	…	…	…
Tuning: 242 GHz									
241.767	CH_3OH	$5(1,5)-4(1,4)\,E$	40.4	−4.23	4.22 (0.14)	1.42 (0.47)	0.16 (0.08)	61.14	N
241.791	CH_3OH	$5(0,5)-4(0,4)\,A$	34.8	−4.21	4.08 (0.08)	1.01 (0.18)	0.19 (0.08)	57.21	N
244.935	CS	$J = 5-4$	35.3	−3.52	4.12 (0.01)	1.15 (0.02)	1.23 (0.05)	37.76	N

Table B.1: Continued.

Rest frequency (GHz)	Molecule	Quantum numbers	$E_{up}^{(a)}$ (K)	$log_{10}A_{ij}^{(b)}$ (s^{-1})	$v_{LSR}^{(*)}$ ($km\,s^{-1}$)	$\Delta v^{(*)}$ ($km\,s^{-1}$)	$T_{MB}^{(*)}$ (K)	rms (mK)	Blended? (Y/N)
258.255	SO	6(6) − 5(5)	56.5	−3.66	4.24 (0.09)	1.26 (0.22)	0.18 (0.06)	45.20	N
260.255	$H^{13}CO^+$	$J = 3 - 2$	25.0	−2.87	4.05 (0.02)	0.93 (0.05)	0.84 (0.08)	63.97	N
261.805	CH_3OH	2(−1, 1) − 1(−0, 1) E	28.0	−4.25	4.50 (0.11)	1.17 (0.28)	0.20 (0.08)	58.26	N
261.843	SO	7(6) − 6(5)	47.6	−3.64	4.06 (0.09)	1.20 (0.21)	0.22 (0.08)	61.15	N
262.004	CCH	$N = 3 - 2, J = 7/2 - 5/2$	25.1	−4.27	4.06 (0.03)	1.04 (0.07)	1.20 (0.13)	56.72	N
262.006	CCH	$N = 3 - 2, J = 7/2 - 5/2$	25.1	−4.29	4.12 (0.06)	1.13 (0.15)	0.85 (0.16)	53.22	N
262.064	CCH	$N = 3 - 2, J = 5/2 - 3/2$	25.2	−4.31	4.12 (0.03)	1.06 (0.08)	0.88 (0.11)	61.20	N
262.067	CCH	$N = 3 - 2, J = 7/2 - 5/2$	25.2	−4.34	4.09 (0.06)	0.98 (0.14)	0.67 (0.13)	58.27	N

Notes. $^{(a)}$Upper energy level. $^{(b)}$Einstein coefficient. $^{(*)}$Parameters from the Gaussian fit results, where the formal errors of the fits are given in parentheses. The rms is a result from the baseline fitting.

Table B.2: Lines detected toward V1057 Cyg with the APEX 12-m telescope.

Rest frequency (GHz)	Molecule	Quantum numbers	$E_{up}^{(a)}$ (K)	$log_{10}A_{ij}^{(b)}$ (s^{-1})	v_{LSR} ($km\,s^{-1}$)	Δv ($km\,s^{-1}$)	T_{MB} (K)	rms (mK)	Blended? (Y/N)
Receiver: nFLASH230, Tuning: 219.2 GHz									
216.112	DCO^+	$J = 3 - 2$	20.7	−3.11	4.31 (0.01)	0.76 (0.02)	0.36 (0.02)	18.45	N
216.278	$c\text{-}C_3H_2$	3(3, 0) − 2(2, 1)	19.5	−3.55	4.30 (0.04)	1.07 (0.09)	0.13 (0.02)	19.43	N
218.222	H_2CO	3(0, 3) − 2(0, 2)	21.0	−3.54	4.09 (0.01)	1.26 (0.03)	0.38 (0.02)	20.38	N
217.822	$c\text{-}C_3H_2$	6(0, 6) − 5(1, 5)	38.6	−3.26	4.14 (0.04)	0.77 (0.10)	0.82 (0.02)	20.04	Y
217.822	$c\text{-}C_3H_2$	6(1, 6) − 5(0, 5)	38.6	−3.26					Y
219.560	$C^{18}O$	$J = 2 - 1$	15.8	−6.22	4.15 (0.01)	0.97 (0.01)	1.70 (0.02)	19.27	N
219.949	SO	6(5) − 5(4)	35.0	−3.87	4.12 (0.06)	1.48 (0.14)	0.08 (0.02)	20.01	N
220.398	^{13}CO	$J = 2 - 1$	15.9	−6.21	4.25 (0.01)	1.21 (0.01)	4.77 (0.05)	21.09	N
230.538	CO	$J = 2 - 1$	16.6	−6.16	…	…	…	…	…
231.321	N_2D^+	$J = 3 - 2$	22.2	−3.14	4.45 (0.06)	0.71 (0.19)	0.08 (0.02)	19.79	N
Receiver: nFLASH230, Tuning: 227.2 GHz, Mode: onOff									
224.714	$C^{17}O$	$J = 3 - 2$	16.2	−6.19	4.28 (0.01)	1.51 (0.05)	0.28 (0.02)	18.25	N
225.697	H_2CO	3(1, 2) − 2(1, 1)	33.4	−3.55	4.14 (0.01)	1.21 (0.02)	0.49 (0.02)	18.74	N
226.359	CN	$N = 2 - 1, J = 3/2 - 3/2$	16.3	−4.79	4.24 (0.04)	0.96 (0.12)	0.10 (0.02)	20.78	N
226.632	CN	$N = 2 - 1, J = 3/2 - 1/2$	16.3	−4.37	4.26 (0.03)	0.90 (0.08)	0.11 (0.02)	19.47	N
226.659	CN	$N = 2 - 1, J = 3/2 - 1/2$	16.3	−4.02	4.31 (0.02)	0.78 (0.03)	0.31 (0.04)	30.83	N
226.663	CN	$N = 2 - 1, J = 3/2 - 1/2$	16.3	−4.07	4.24 (0.08)	0.99 (0.20)	0.10 (0.04)	19.41	N
226.679	CN	$N = 2 - 1, J = 3/2 - 1/2$	16.3	−4.27	4.33 (0.08)	0.93 (0.08)	0.12 (0.04)	31.88	N
226.874	CN	$N = 2 - 1, J = 5/2 - 3/2$	16.3	−4.01	4.41 (0.01)	1.78 (0.04)	0.48 (0.03)	18.40	Y
226.875	CN	$N = 2 - 1, J = 5/2 - 3/2$	16.3	−3.94				18.40	Y
226.887	CN	$N = 2 - 1, J = 5/2 - 3/2$	16.3	−4.56	4.18 (0.04)	0.93 (0.10)	0.11 (0.04)	20.60	N
226.892	CN	$N = 2 - 1, J = 5/2 - 3/2$	16.3	−4.74	4.26 (0.04)	0.87 (0.07)	0.13 (0.03)	20.97	N
228.910	DNC	$J = 3 - 2$	22.0	−3.25	4.40 (0.02)	0.61 (0.05)	0.16 (0.03)	21.64	N
241.767	CH_3OH	5(1, 5) − 4(1, 4) E	40.4	−4.23	4.12 (0.05)	1.04 (0.12)	0.08 (0.03)	26.21	N
241.791	CH_3OH	5(0, 5) − 4(0, 4) A	34.8	−4.21	4.01 (0.03)	1.35 (0.07)	0.09 (0.02)	14.66	N
244.935	CS	$J = 5 - 4$	35.3	−3.52	4.16 (0.01)	1.21 (0.02)	0.31 (0.02)	16.86	N
Receiver: nFLASH230, Tuning: 227.2 GHz, Mode: otf									
219.560	$C^{18}O$	$J = 2 - 1$	15.8	−6.22	4.03 (0.03)	0.81 (0.10)	0.20 (0.05)	35.45	N
220.398	^{13}CO	$J = 2 - 1$	15.9	−6.21	3.95 (0.01)	1.36 (0.02)	1.01 (0.05)	34.67	N
230.538	CO	$J = 2 - 1$	16.6	−6.16	…	…	…	…	…
Receiver: LAsMA345, Tuning: 344.2 GHz, Observation date: 2021-11-19, Mode: otf									
345.795	CO	$J = 3 - 2$	33.2	−5.60	…	…	…	…	…
356.734$^{(*)}$	HCO^+	4 − 3	42.8	−2.44	4.05 (0.06)	1.31 (0.12)	2.65 (0.63)	455	N
Receiver: SEPIA345, Tuning: 291 GHz									
279.511	N_2H^+	$J = 3 - 2$	26.8	−2.89	4.46 (0.01)	0.89 (0.02)	0.47 (0.03)	26.47	N

Table B.2: Continued.

Rest frequency (GHz)	Molecular species	Quantum numbers	$E_{\rm up}^{(a)}$ (K)	$log_{10}A_{\rm ij}^{(b)}$	$v_{\rm LSR}$ (km s^{-1})	Δv (km s^{-1})	$T_{\rm MB}$ (K)	rms (mK)	Blended? (Y/N)
290.623	H_2CO	$4(0,4) - 3(0,3)$	34.9	−3.16	4.09 (0.04)	1.36 (0.10)	0.79 (0.02)	18.83	N
293.912	CS	$J = 6 - 5$	49.4	−3.28	4.36 (0.03)	0.99 (0.08)	0.14 (0.02)	20.34	N

Notes. $^{(a)}$Upper energy level. $^{(b)}$Einstein coefficient. $^{(*)}$The spectrum was spectrally smoothed by a factor of 2 using the `smooth` built-in function in CLASS, and presented as such throughout this appendix and Chapter 4.

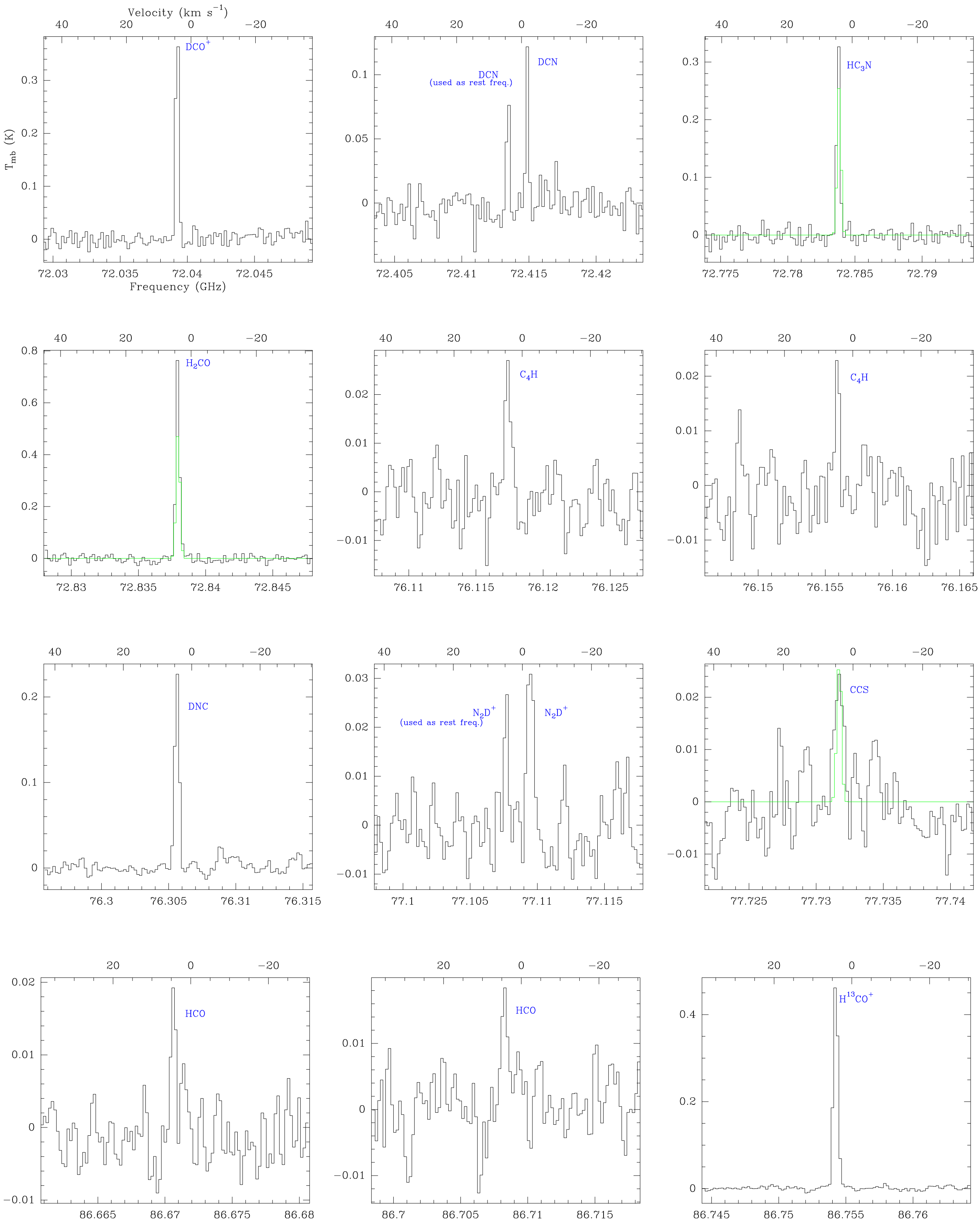

Figure B.1: Spectra of lines detected towards V1057 Cyg with the IRAM 30-m telescope in the 73 GHz tuning, displayed in main-beam temperature scale. Molecule names for identified lines are labelled in blue, the synthetic model (displayed in the population diagrams in Figure 4.7) is overlaid in green, tentative detections are labelled in dark green, and unidentified lines are labelled in red. In certain panels, extra text describes the species or transition used as rest frequency to display the top axis.

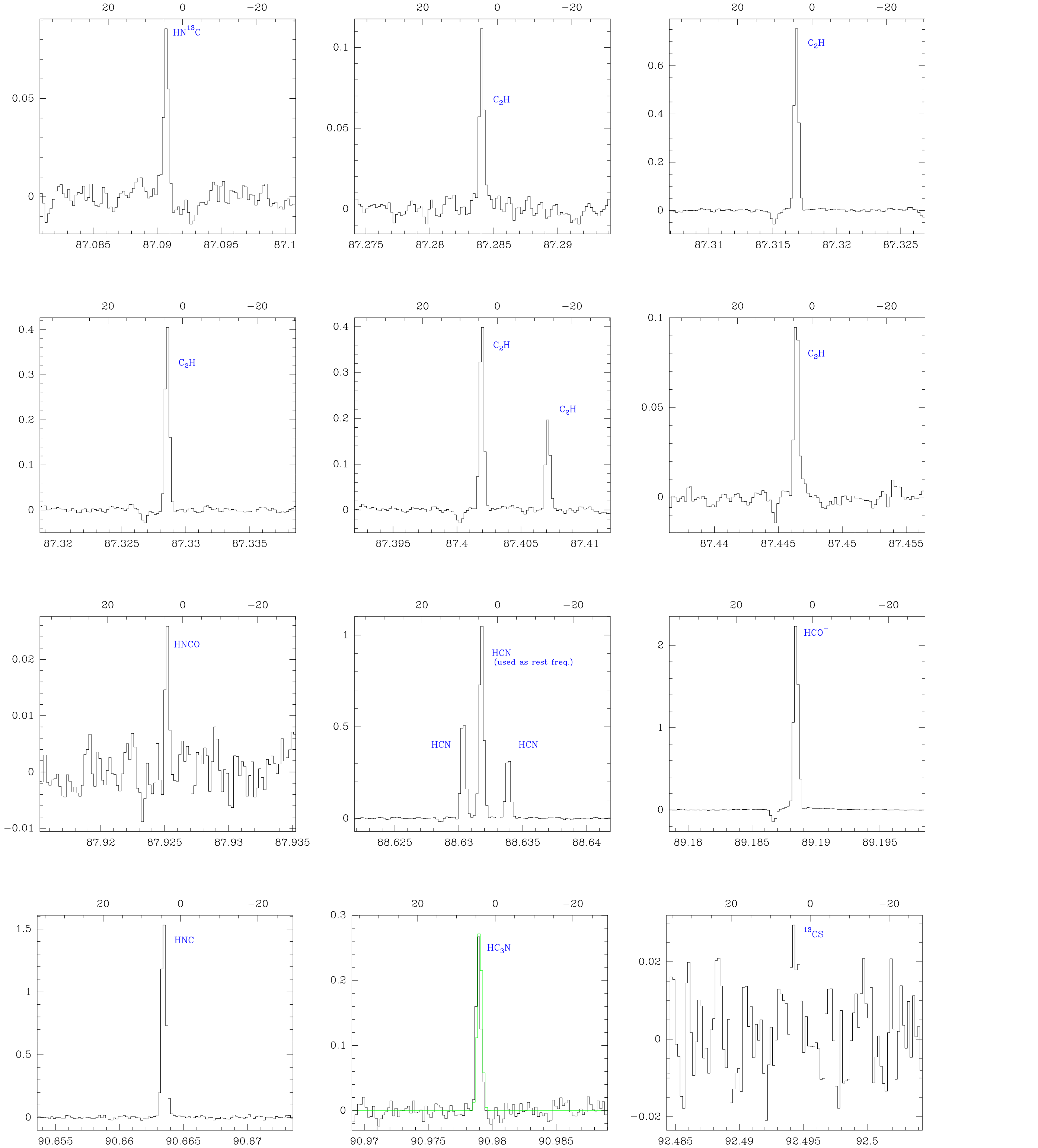

Figure B.1: Continued.

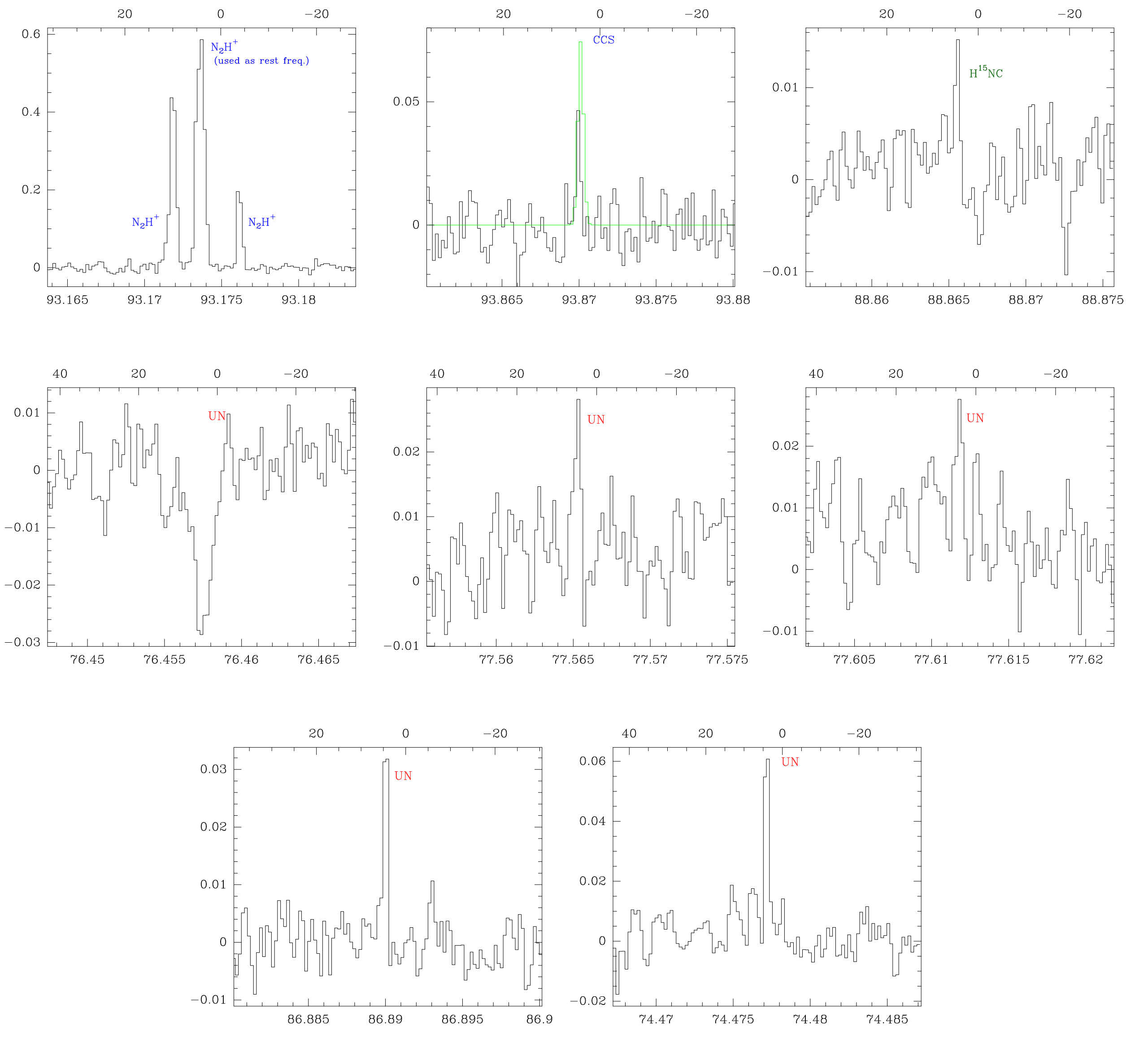

Figure B.1: Continued.

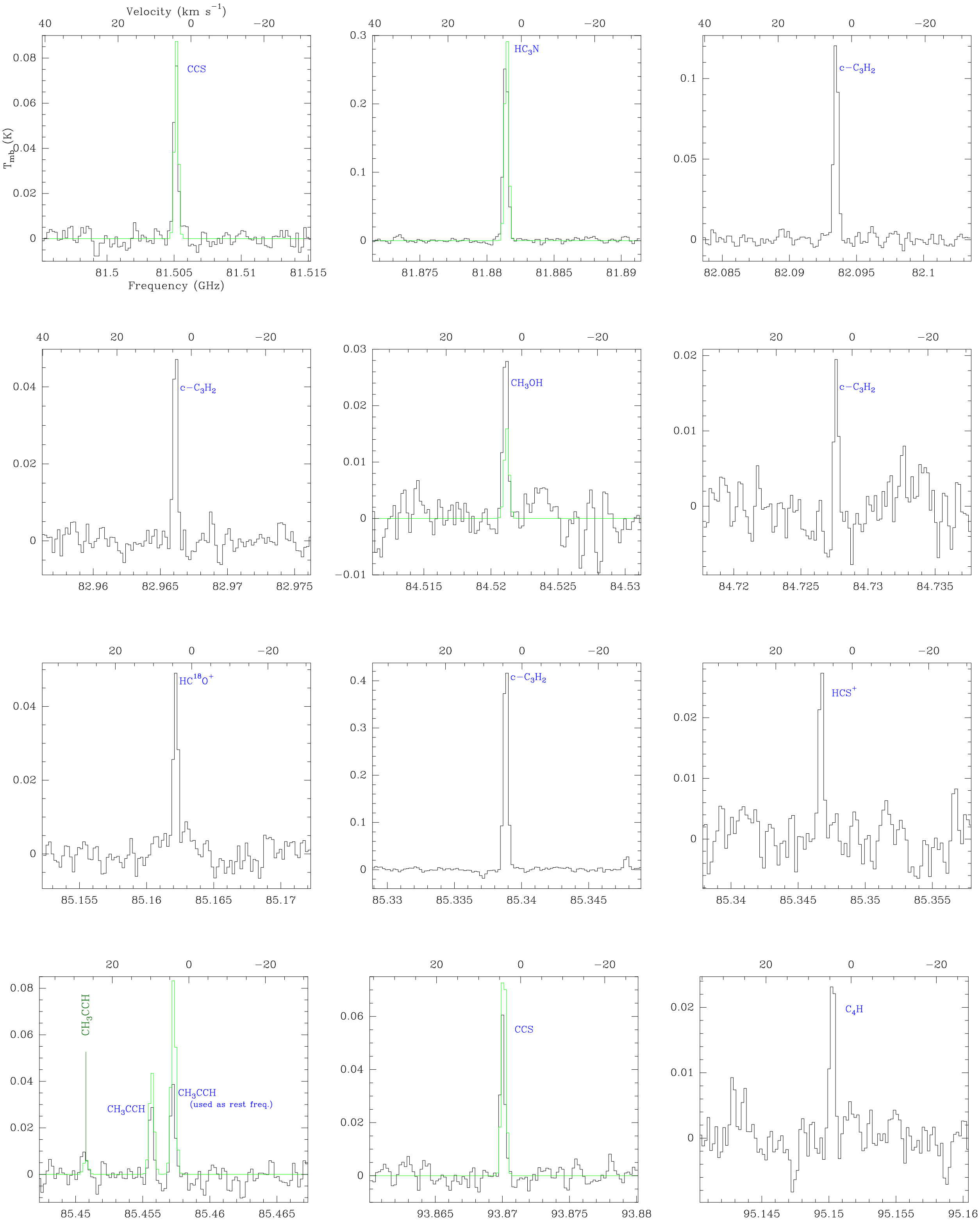

Figure B.2: Same as Figure B.1 but for the tuning at 80 GHz.

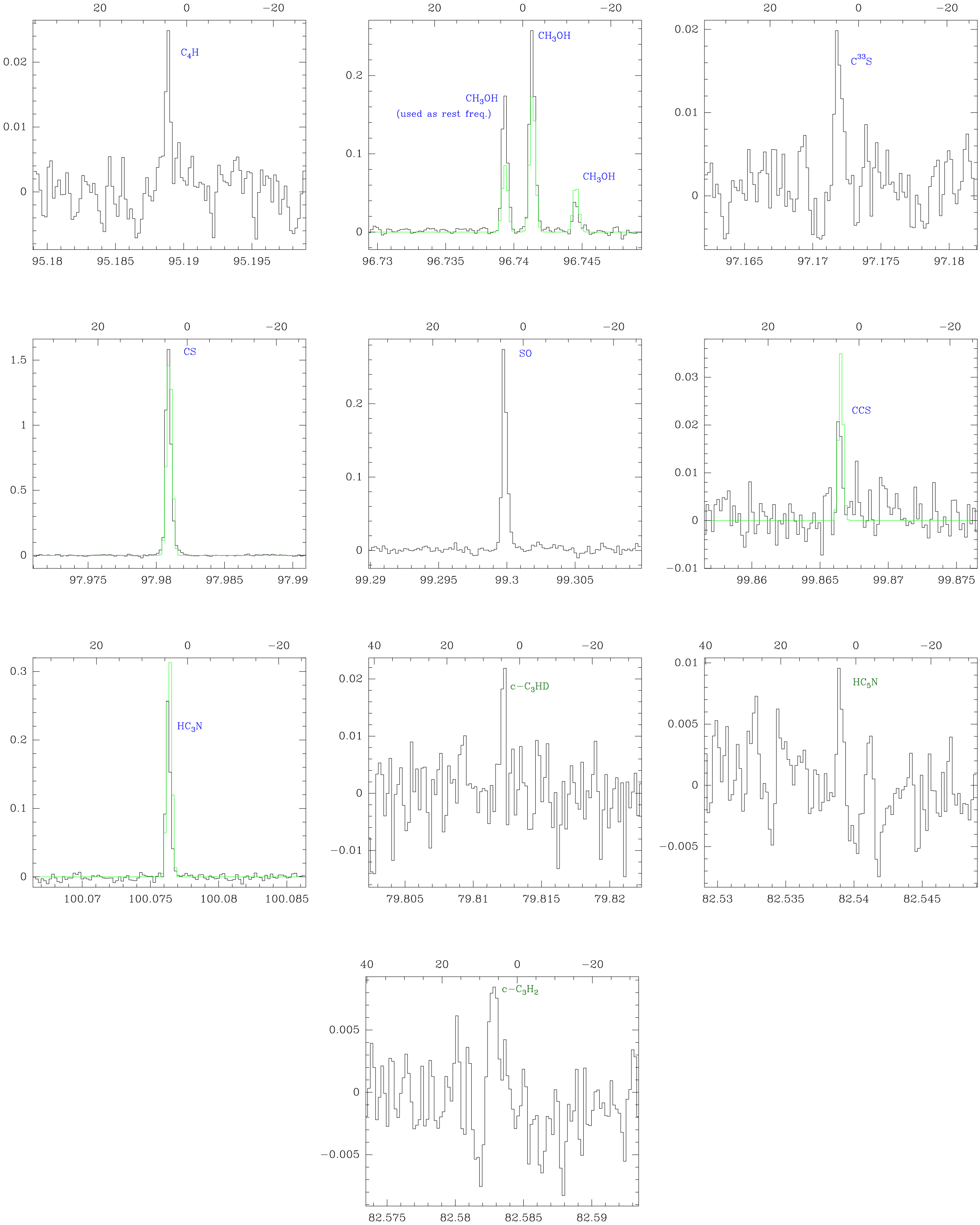

Figure B.2: Continued.

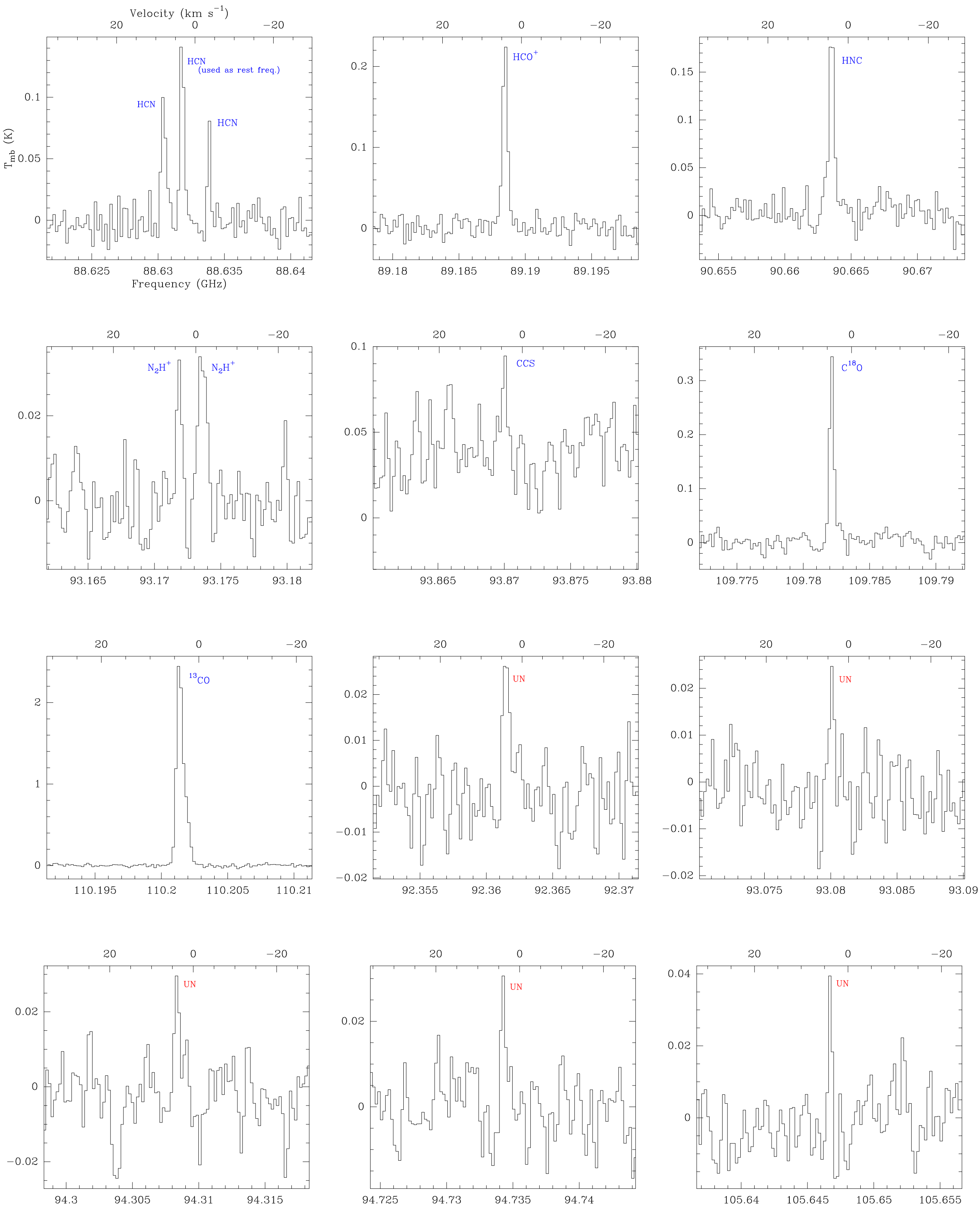

Figure B.3: Same as Figure B.1 but for the tuning at 90 GHz in the otf mode at the source position.

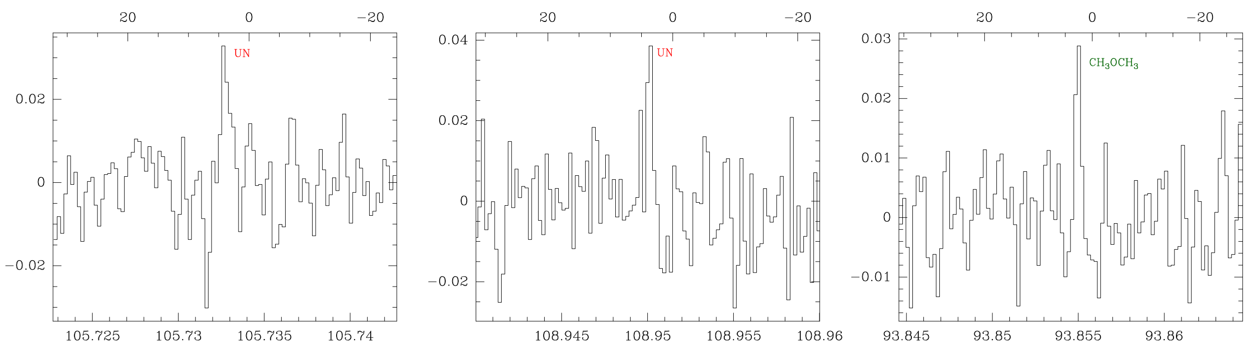

Figure B.3: Continued.

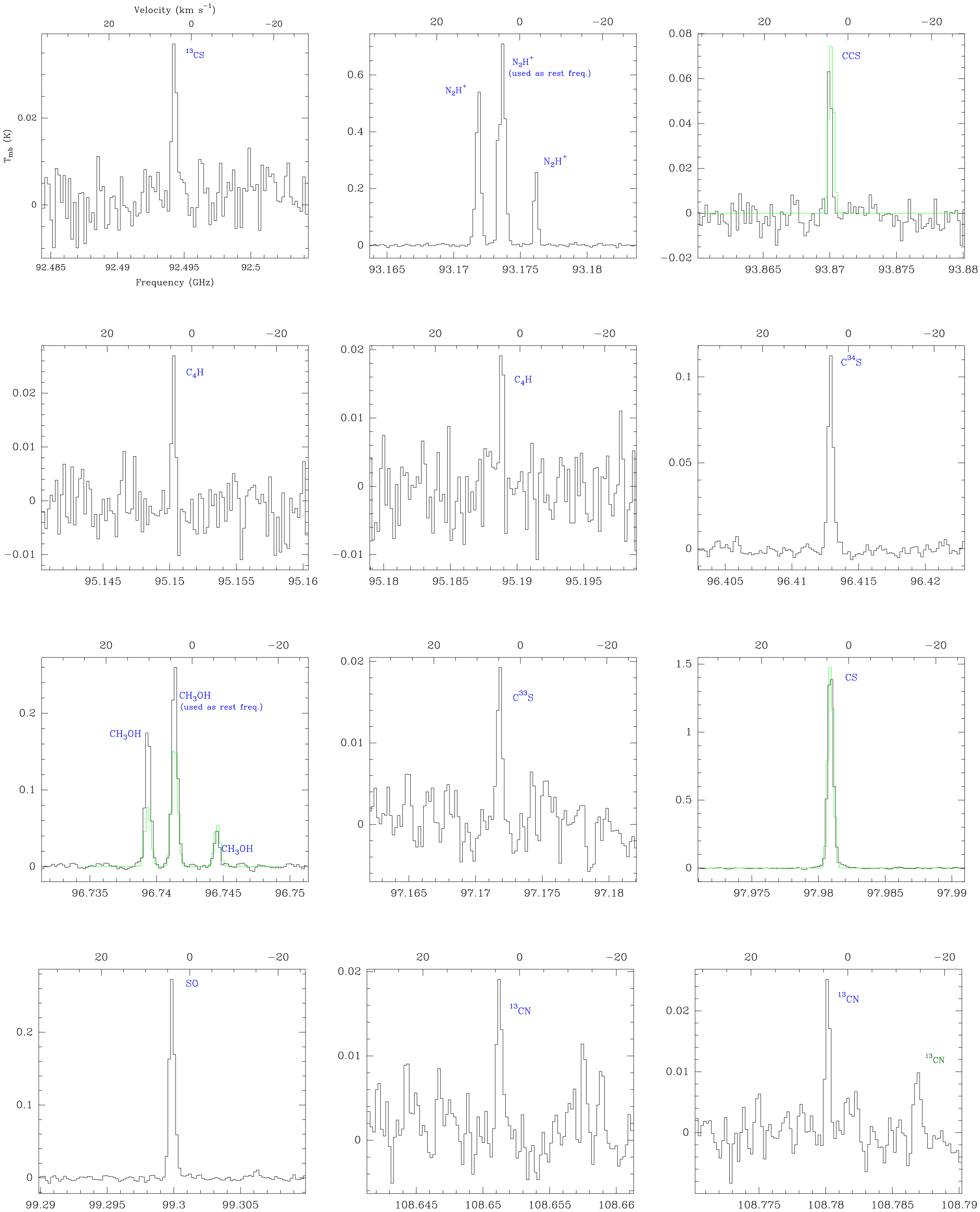

Figure B.4: Same as Figure B.1 but for the tuning at 94 GHz. Possible contamination from the image band (indicating rest frequency and peak temperature in K in the image band) are labelled in red.

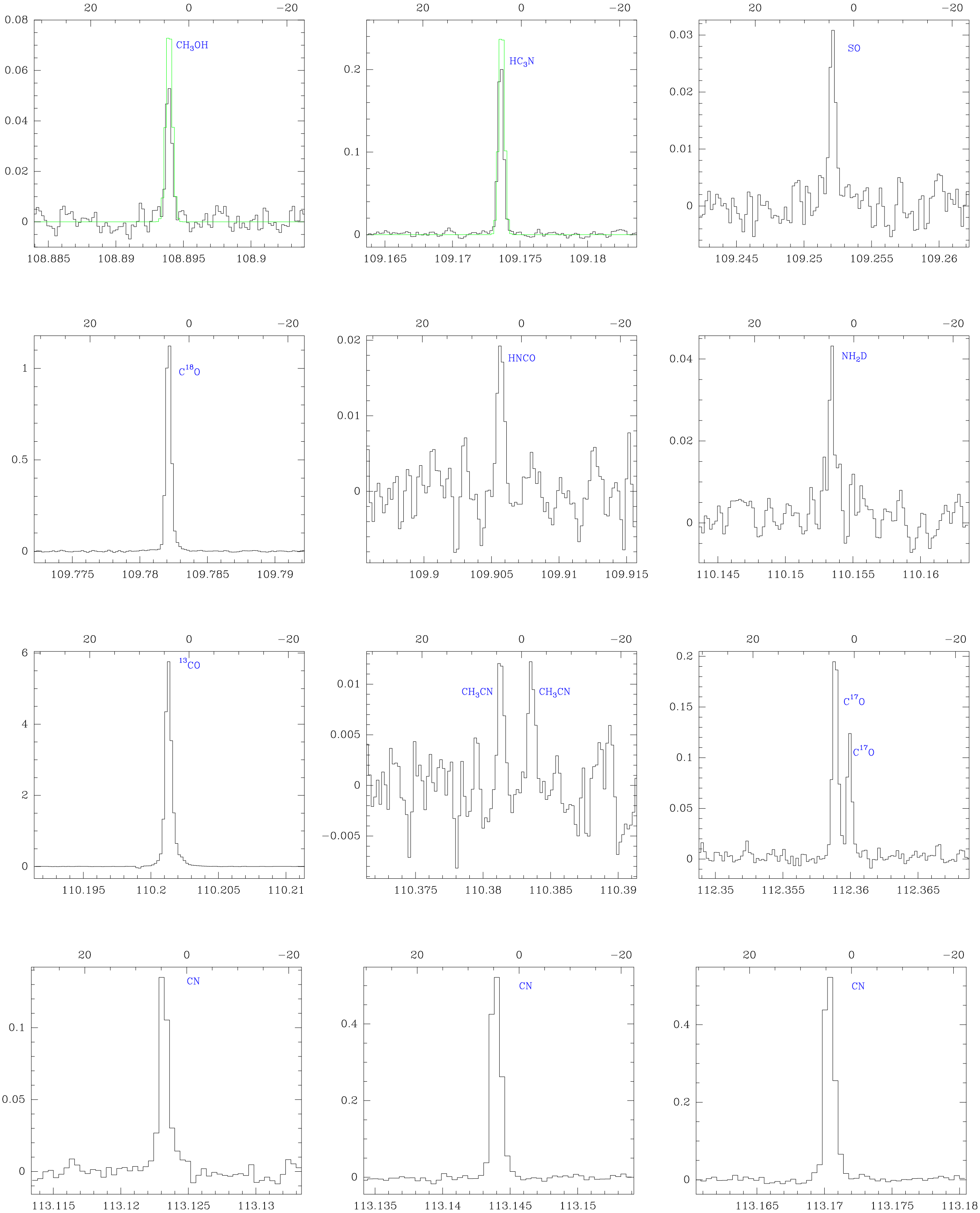

Figure B.4: Continued.

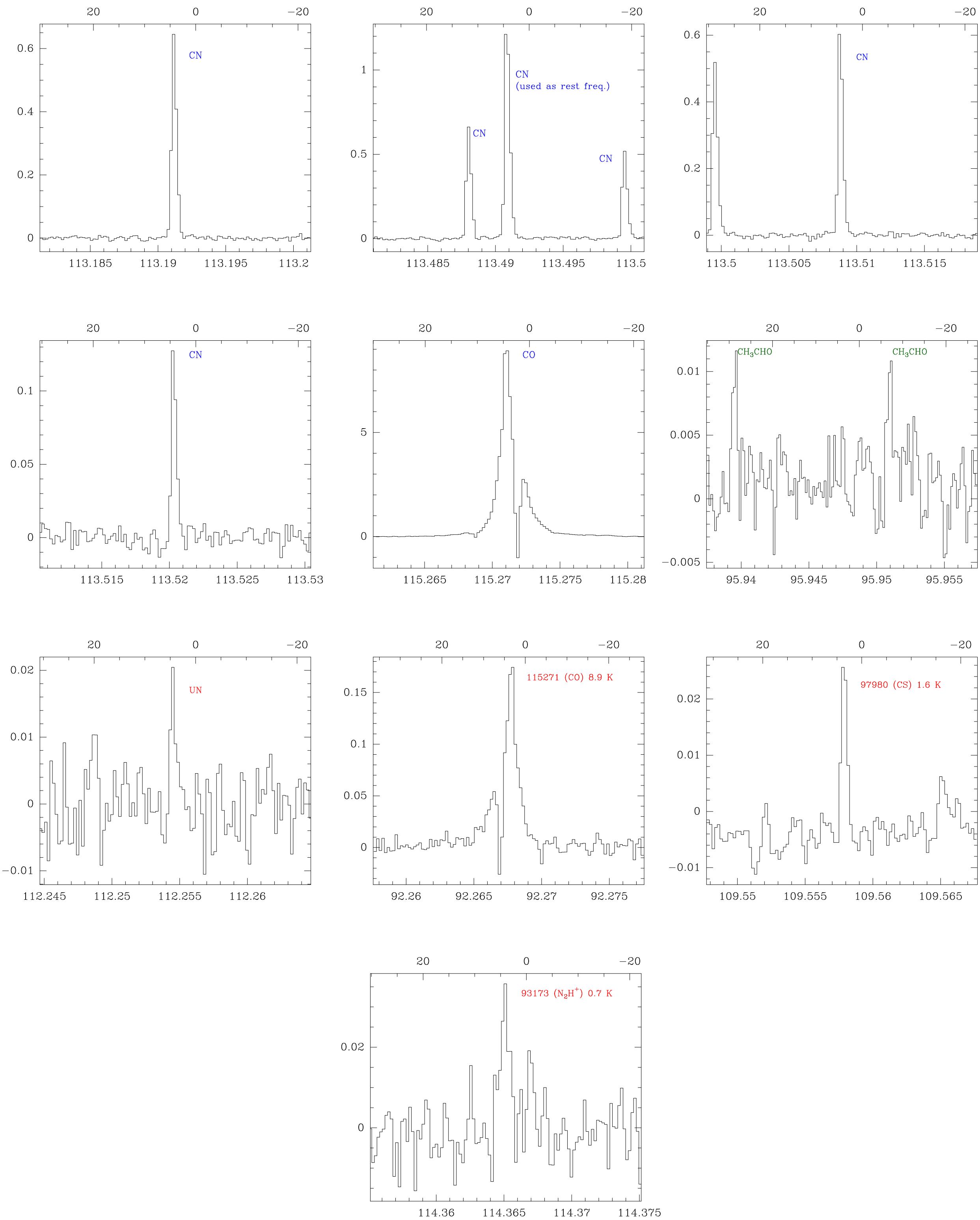

Figure B.4: Continued.

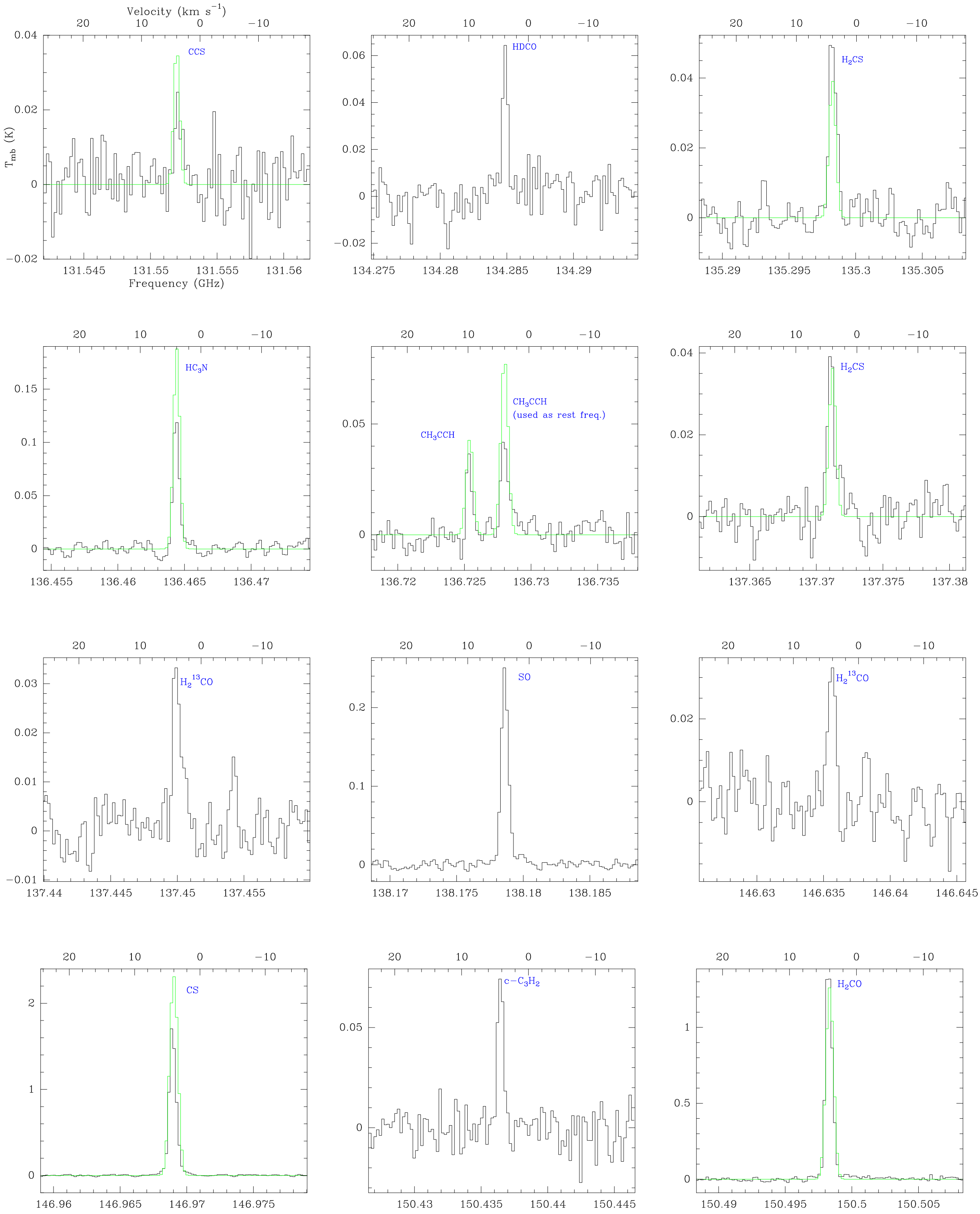

Figure B.5: Same as Figure B.1 but for the tuning at 133 GHz.

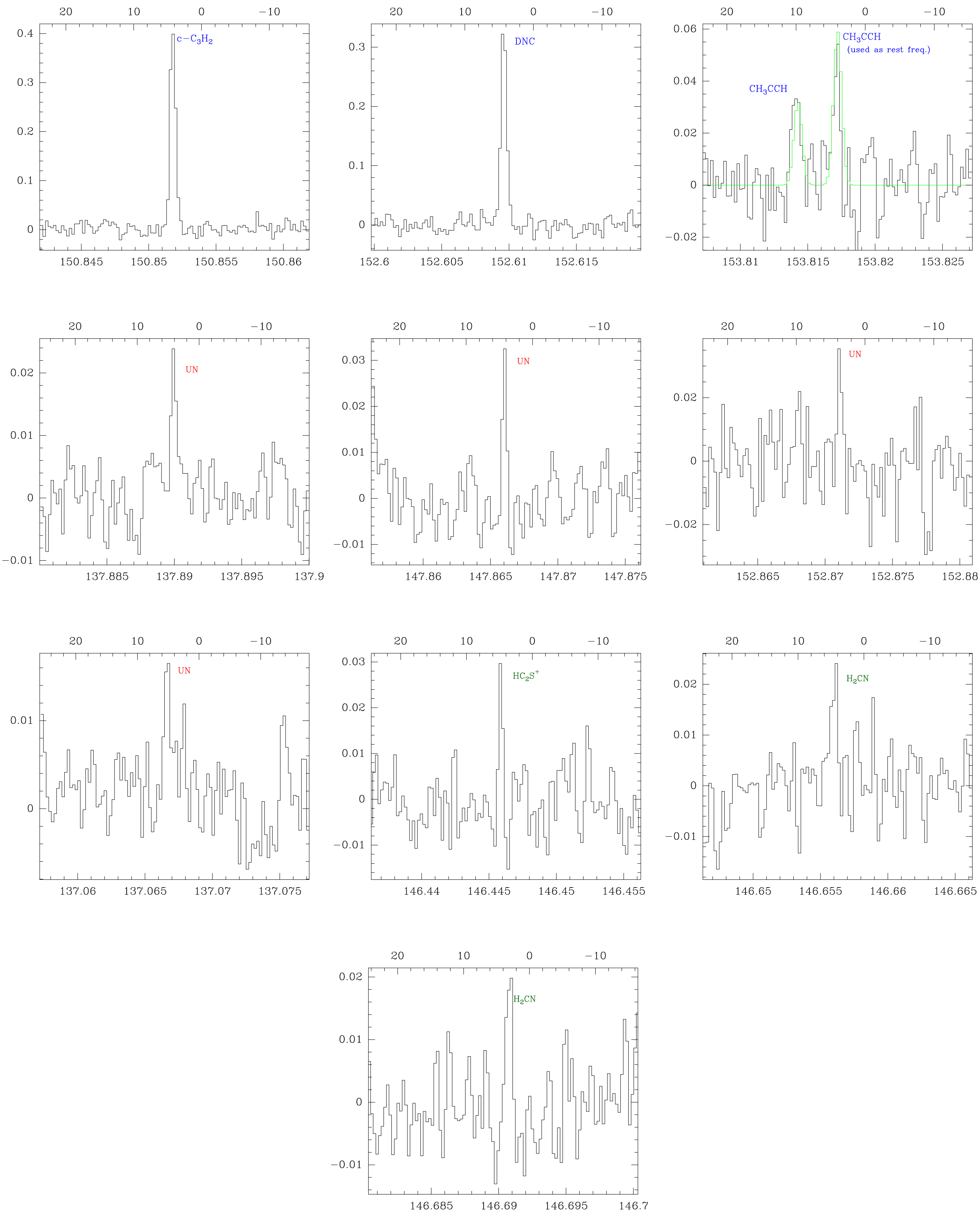

Figure B.5: Continued.

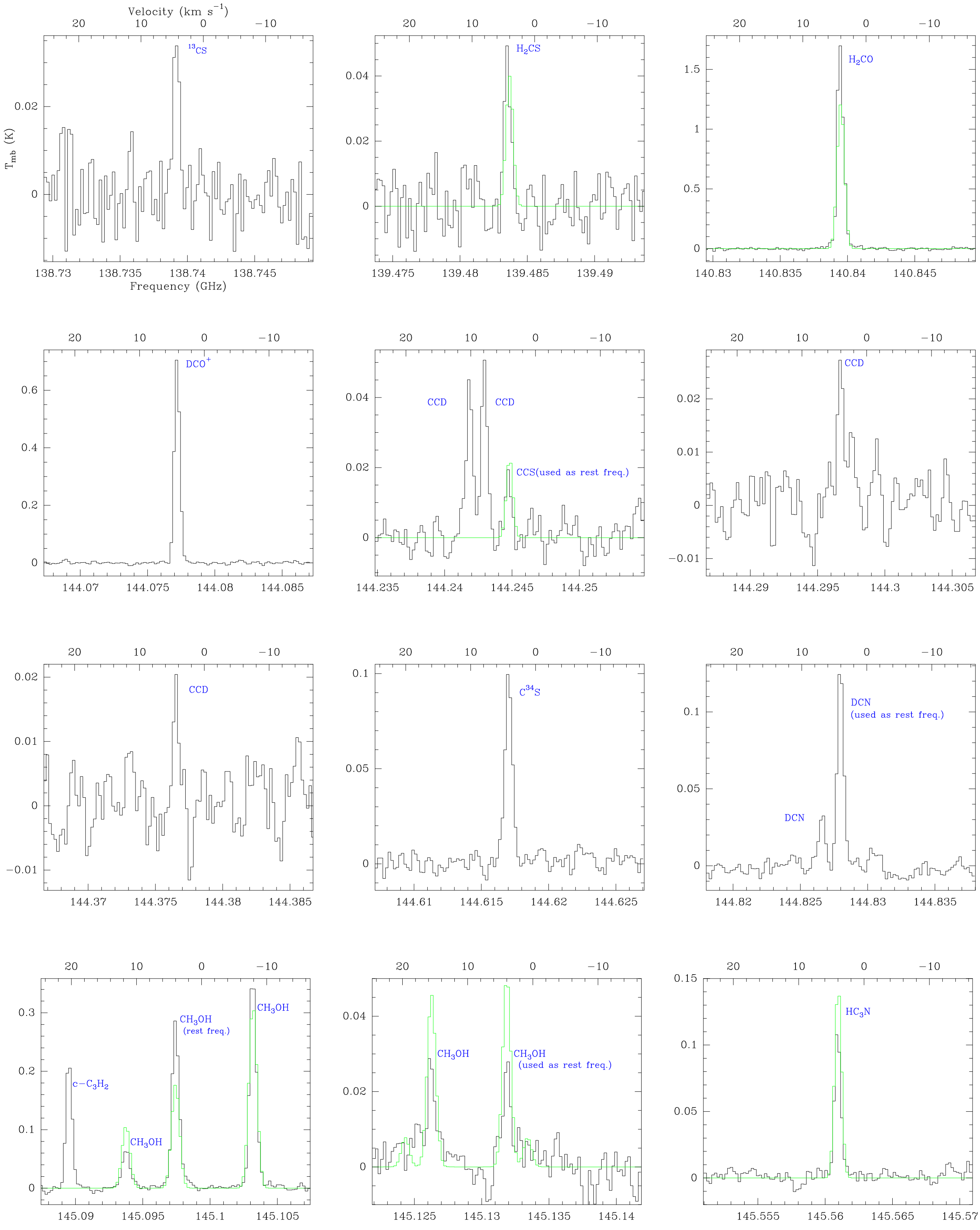

Figure B.6: Same as Figure B.1 but for the tuning at 141 GHz.

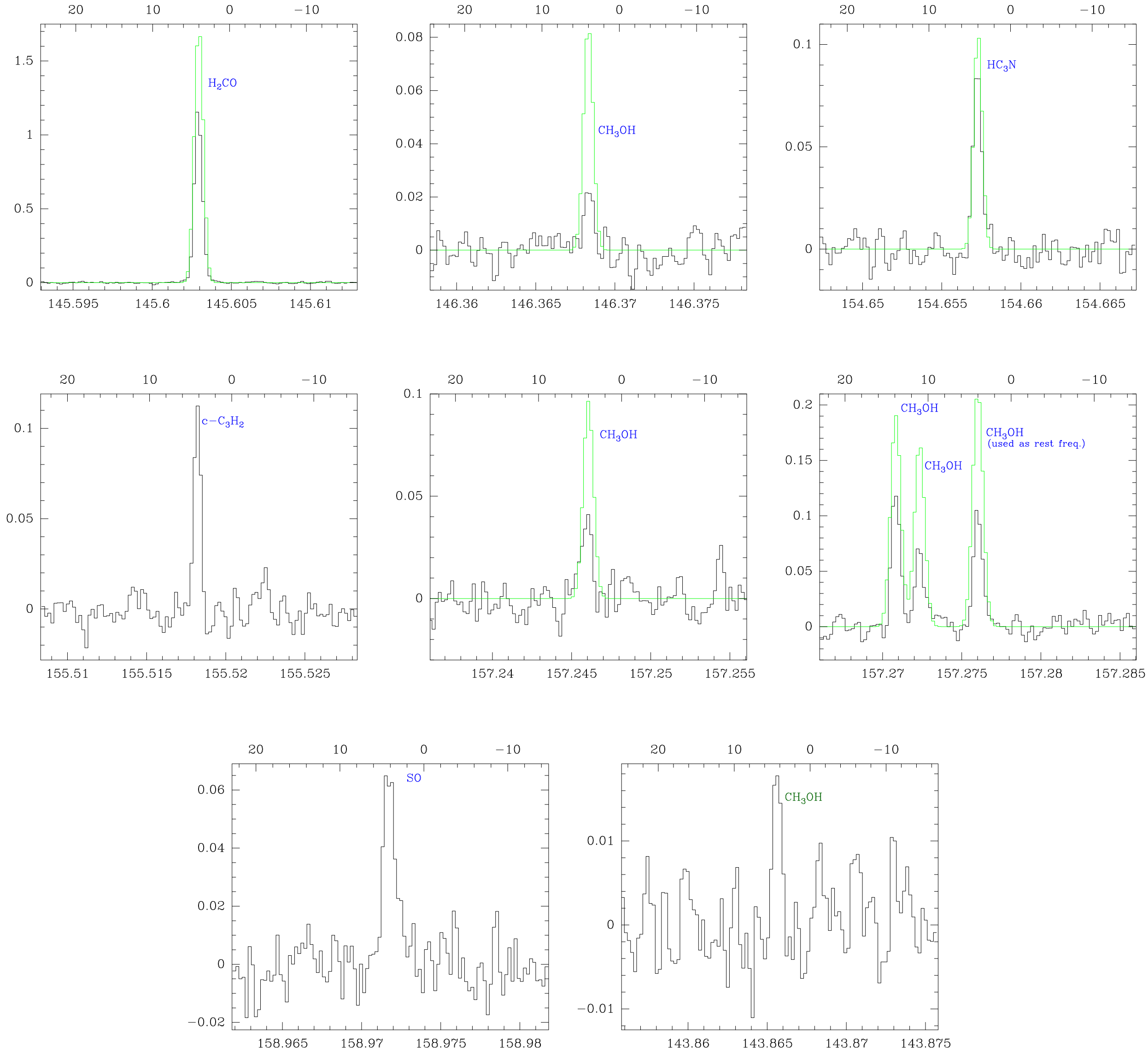

Figure B.6: Continued.

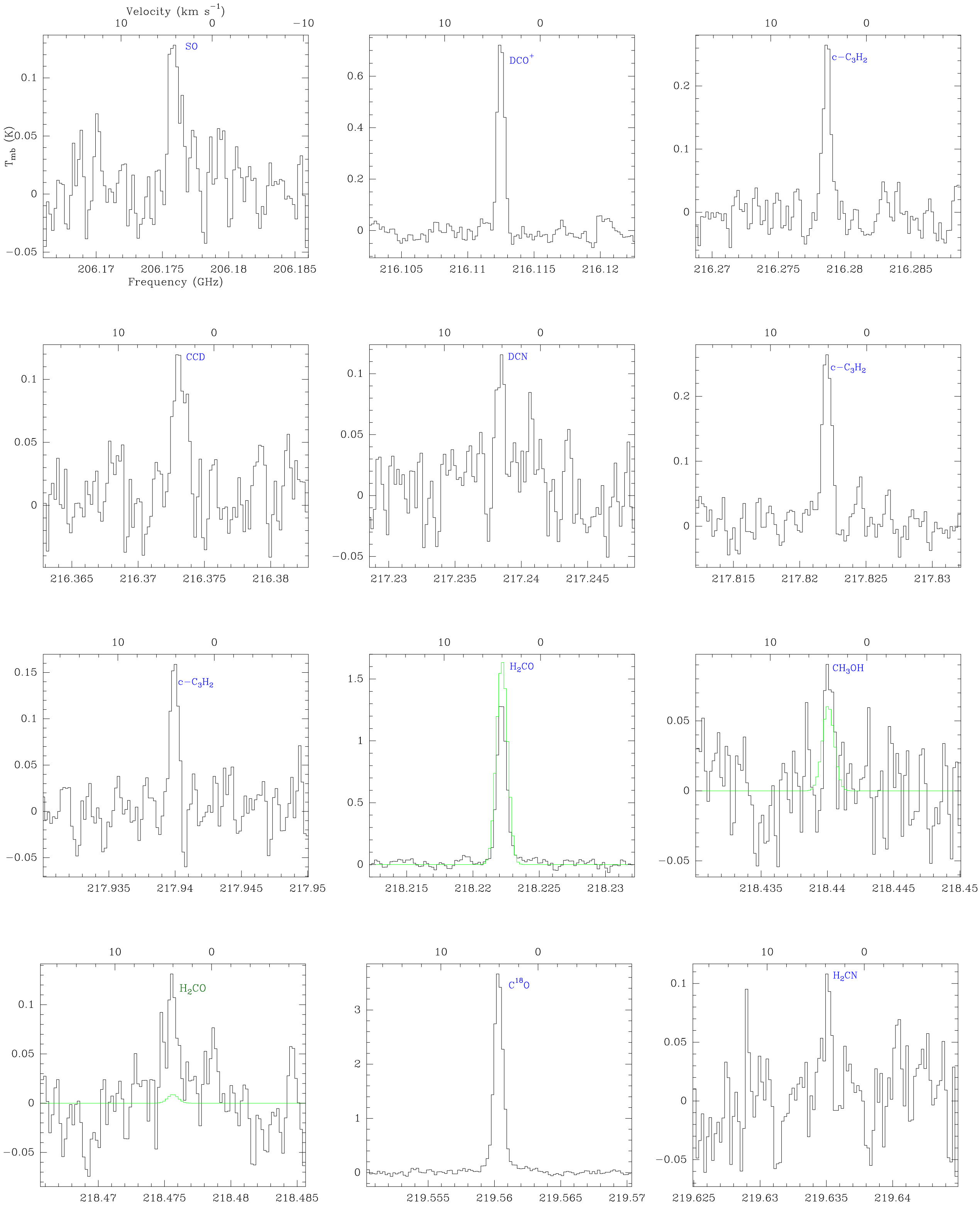

Figure B.7: Same as Figure B.1 but for the tuning at 202 GHz.

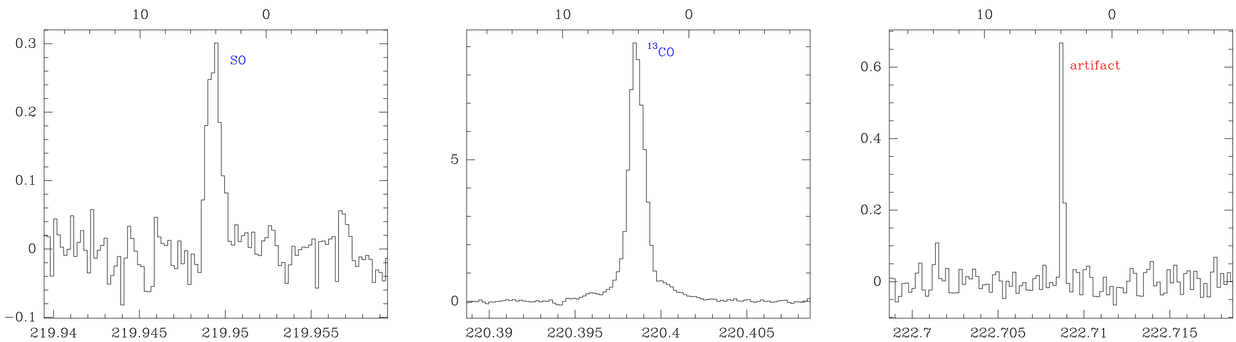

Figure B.7: Continued.

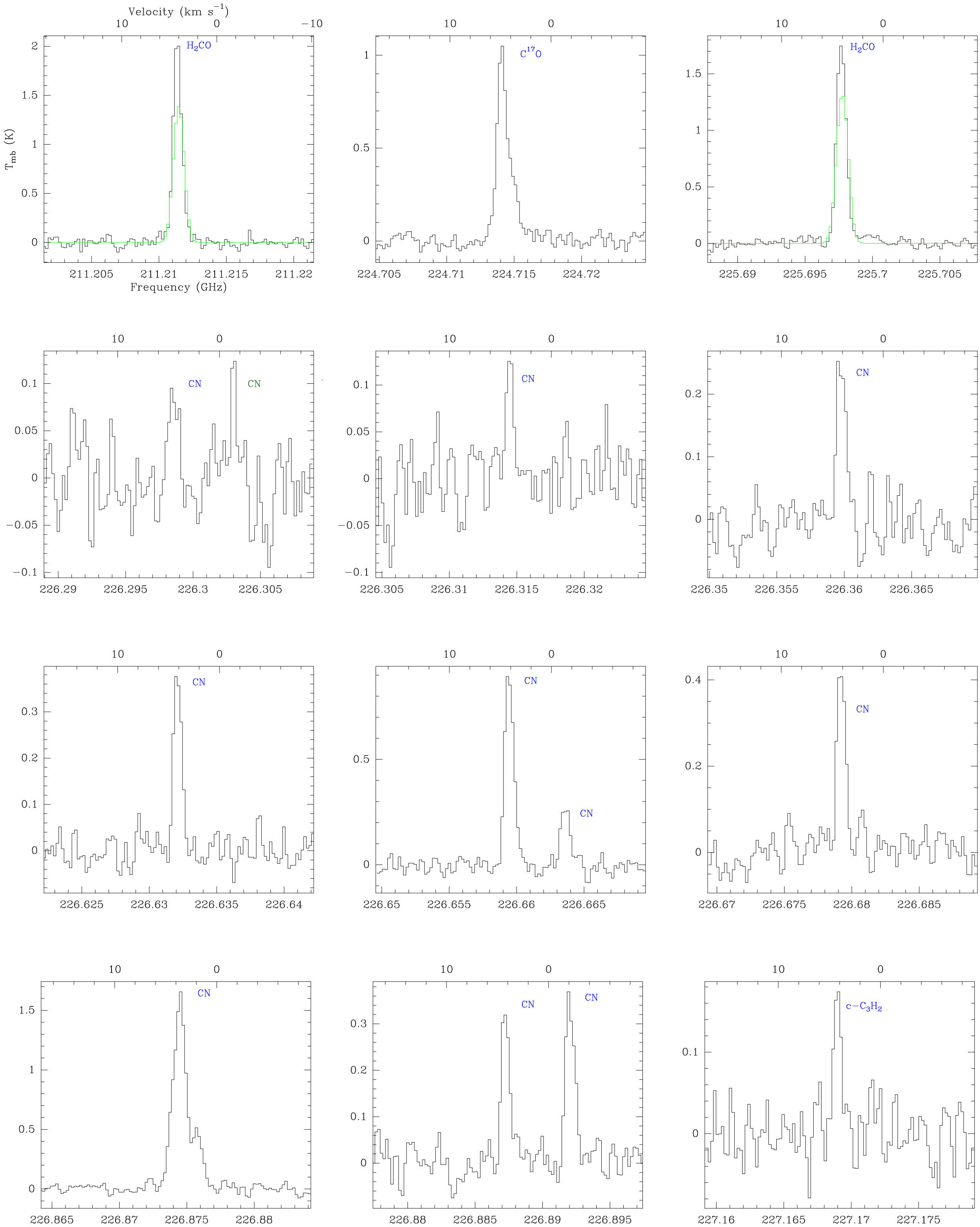

Figure B.8: Same as Figure B.1 but for the tuning at 210 GHz. Possible contamination from the image band (indicating rest frequency and peak temperature in K in the image band) are labelled in red.

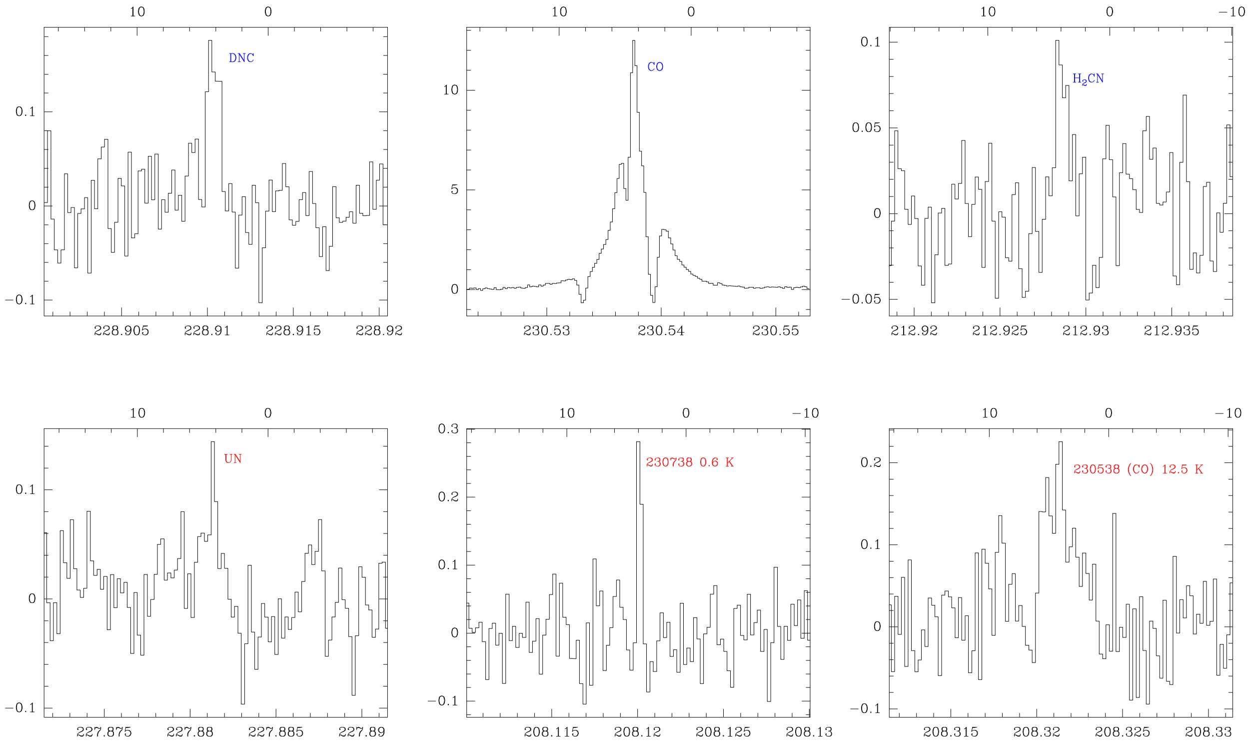

Figure B.8: Continued.

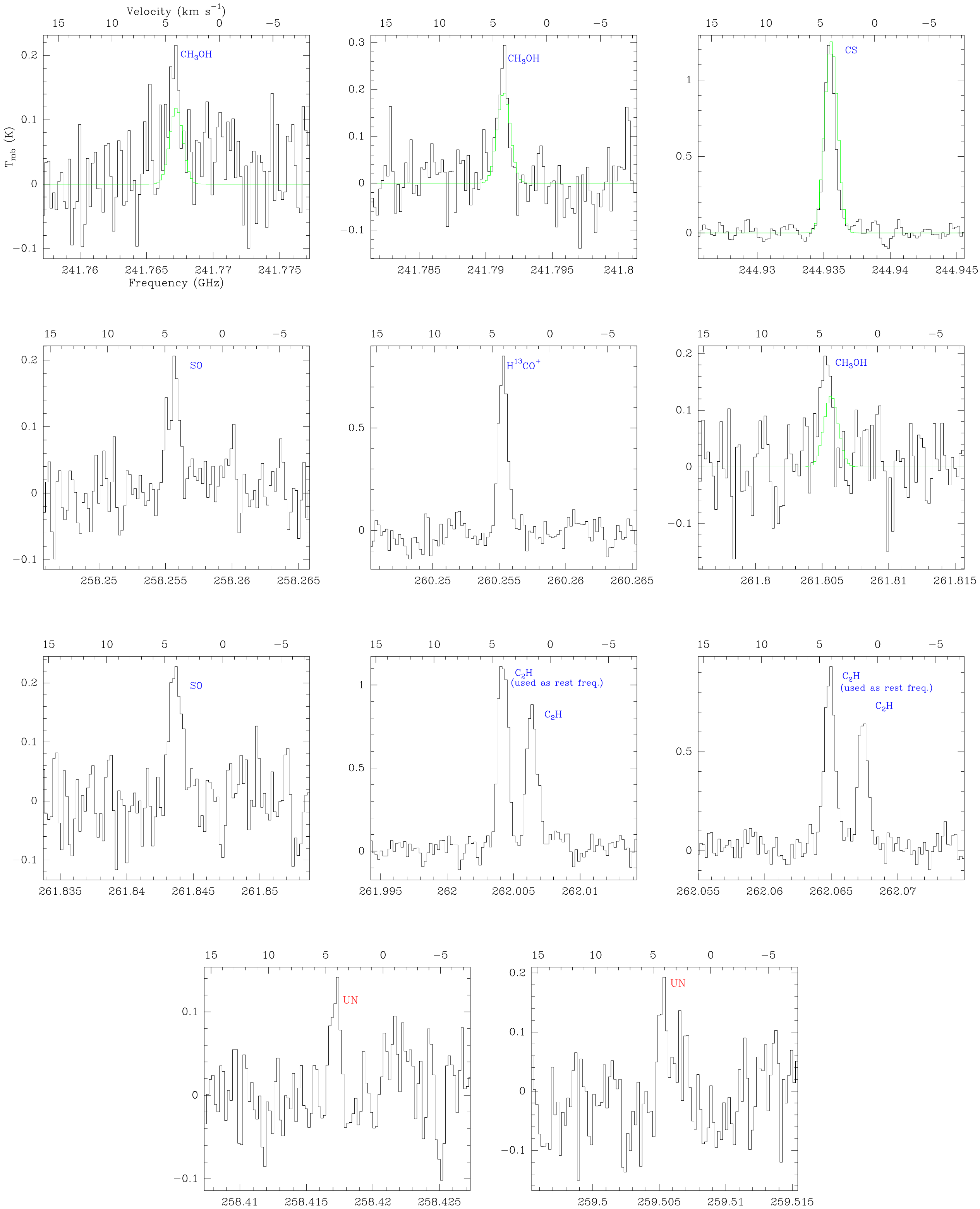

Figure B.9: Same as Figure B.1 but for the tuning at 242 GHz.

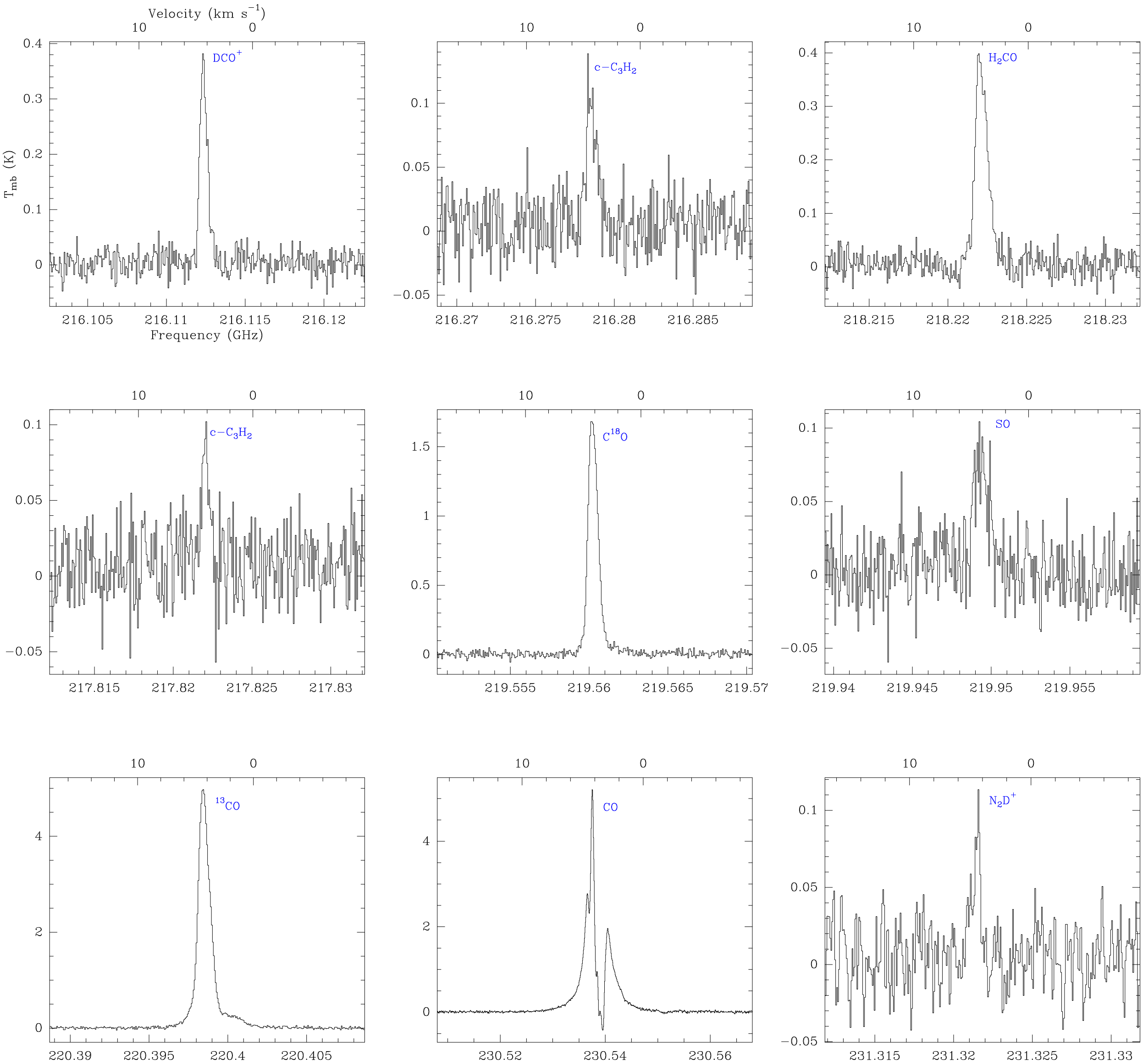

Figure B.10: Spectra of lines detected towards V1057 Cyg with the APEX 12-m telescope with nFLASH, displayed in main-beam temperature scale. Molecule names for identified lines are labelled in blue.

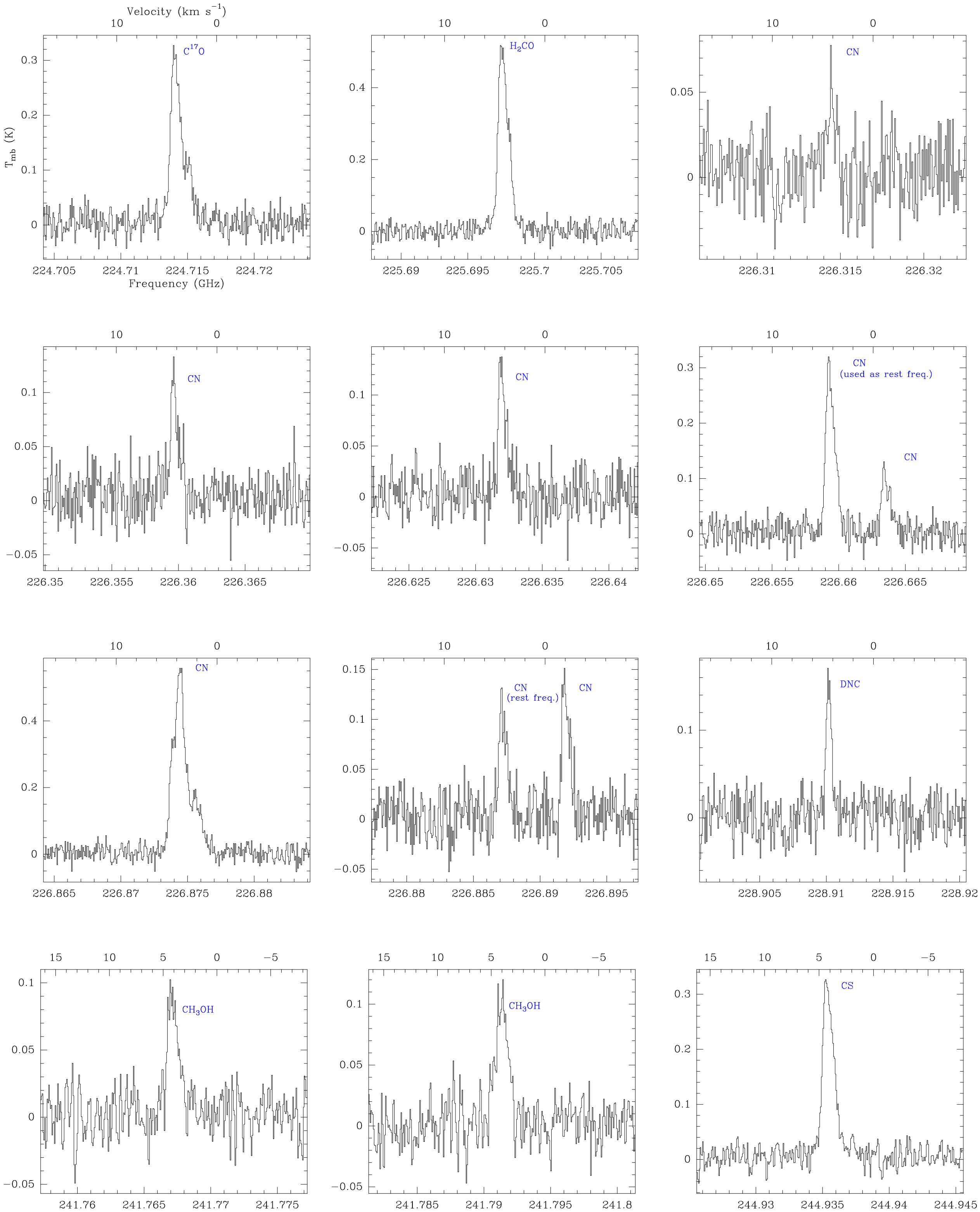

Figure B.11: Same as Figure B.10 but for the 227 GHz tuning.

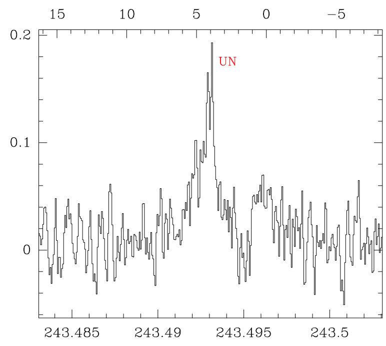

Figure B.11: Continued.

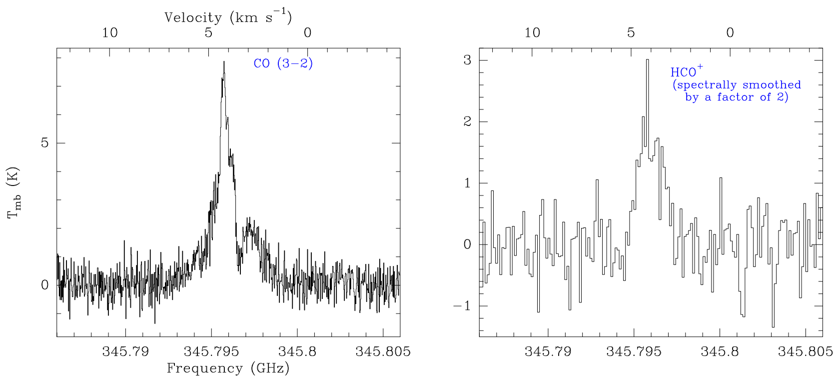

Figure B.12: Spectra obtained at the position of V1057 Cyg (i.e., 0″,0″) using the APEX 12-m telescope with LAsMA in the otf mode, displayed in main-beam temperature scale. The names of identified lines are labelled in blue.

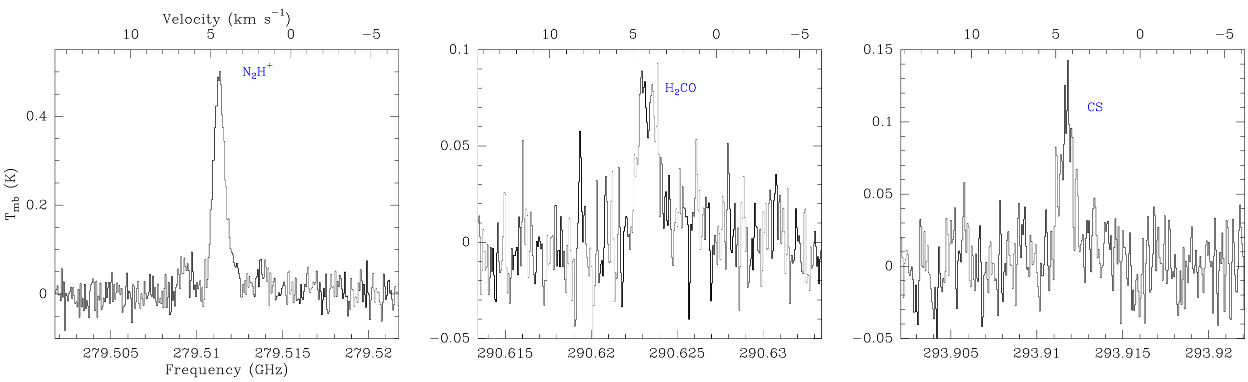

Figure B.13: Spectra obtained towards V1057 Cyg with the APEX 12-m telescope with SEPIA, displayed in main-beam temperature scale. The names of identified lines are labelled in blue.

Bibliography

Ábrahám, P. et al. 2009, Nature, 459, 224, 0906.3161

Ábrahám, P., Kóspál, Á., Csizmadia, S., Kun, M., Moór, A., & Prusti, T. 2004, A&A, 428, 89, astro-ph/0408048

Ábrahám, P. et al. 2018, ApJ, 853, 28, 1712.04968

Abraham, Z., Cohen, N. L., Opher, R., Raffaelli, J. C., & Zisk, S. H. 1981, A&A, 100, L10

Adams, F. C., Lada, C. J., & Shu, F. H. 1987, ApJ, 312, 788

Akimkin, V., Zhukovska, S., Wiebe, D., Semenov, D., Pavlyuchenkov, Y., Vasyunin, A., Birnstiel, T., & Henning, T. 2013, ApJ, 766, 8, 1302.1403

ALMA Partnership et al. 2015, ApJ, 808, L3, 1503.02649

Alves, J. et al. 2020, Nature, 578, 237, 2001.08748

André, P. et al. 2010, A&A, 518, L102, 1005.2618

Andre, P., Ward-Thompson, D., & Barsony, M. 1993, ApJ, 406, 122

Andreu, A., Coutens, A., Cruz-Sáenz de Miera, F., Houry, N., Jørgensen, J. K., Kóspál, A., & Harsono, D. 2023, A&A, 677, L17, 2309.01688

Anglada, G., Estalella, R., Pastor, J., Rodriguez, L. F., & Haschick, A. D. 1996, ApJ, 463, 205

Anglada, G., Rodriguez, L. F., Girart, J. M., Estalella, R., & Torrelles, J. M. 1994, ApJ, 420, L91

Anglada, G., Rodríguez, L. F., & Torrelles, J. M. 2000, ApJ, 542, L123

Antoniucci, S. et al. 2016, A&A, 593, L13, 1608.07974

Arce, H. G., & Goodman, A. A. 2001, ApJ, 551, L171, astro-ph/0103483

Armitage, P. J., Livio, M., & Pringle, J. E. 2001, MNRAS, 324, 705, astro-ph/0101253

Arzoumanian, D. et al. 2011, A&A, 529, L6, 1103.0201

Aspin, C., & Reipurth, B. 2009, AJ, 138, 1137, 0907.4402

Aspin, C., Reipurth, B., Herczeg, G. J., & Capak, P. 2010, ApJ, 719, L50, 1007.4178

Audard, M. et al. 2014, in Protostars and Planets VI, ed. H. Beuther, R. S. Klessen, C. P. Dullemond, & T. Henning, 387, 1401.3368

Audard, M. et al. 2010, A&A, 511, A63, 0912.3224

Bachiller, R., Gueth, F., Guilloteau, S., Tafalla, M., & Dutrey, A. 2000, A&A, 362, L33, astro-ph/0009439

Bae, J.-H., Kim, K.-T., Youn, S.-Y., Kim, W.-J., Byun, D.-Y., Kang, H., & Oh, C. S. 2011, ApJS, 196, 21, 1108.3878

Baek, G. et al. 2020, ApJ, 895, 27, 2004.05600

Bai, X.-N. 2011, ApJ, 739, 50, 1107.2935

Bailer-Jones, C. A. L., Rybizki, J., Fouesneau, M., Demleitner, M., & Andrae, R. 2021, AJ, 161, 147, 2012.05220

Bailer-Jones, C. A. L., Rybizki, J., Fouesneau, M., Mantelet, G., & Andrae, R. 2018a, AJ, 156, 58, 1804.10121

——. 2018b, VizieR Online Data Catalog, I/347

Banzatti, A., Meyer, M. R., Manara, C. F., Pontoppidan, K. M., & Testi, L. 2014, ApJ, 780, 26, 1310.8299

Batrla, W., & Menten, K. M. 1988, ApJ, 329, L117

Bayandina, O. S. et al. 2022, A&A, 664, A44, 2206.12119

Bechis, K. P., & Lo, K. Y. 1975, ApJ, 201, 118

Bell, K. R., Lin, D. N. C., Hartmann, L. W., & Kenyon, S. J. 1995, ApJ, 444, 376

Belloche, A., Garrod, R. T., Müller, H. S. P., Menten, K. M., Comito, C., & Schilke, P. 2009, A&A, 499, 215, 0902.4694

Belloche, A., Menten, K. M., Comito, C., Müller, H. S. P., Schilke, P., Ott, J., Thorwirth, S., & Hieret, C. 2008, A&A, 482, 179, 0801.3219

Belloche, A., Müller, H. S. P., Garrod, R. T., & Menten, K. M. 2016, A&A, 587, A91, 1511.05721

Belloche, A., Müller, H. S. P., Menten, K. M., Schilke, P., & Comito, C. 2013, A&A, 559, A47, 1308.5062

Benson, P. J., & Myers, P. C. 1989, ApJS, 71, 89

Beuther, H., Schilke, P., Sridharan, T. K., Menten, K. M., Walmsley, C. M., & Wyrowski, F. 2002, A&A, 383, 892, astro-ph/0110372

Bianchi, E. et al. 2020, MNRAS, 498, L87, 2007.10275

Blitz, L., & Lada, C. J. 1979, ApJ, 227, 152

Boboltz, D. A., Simonetti, J. H., Dennison, B., Diamond, P. J., & Uphoff, J. A. 1998, ApJ, 509, 256

Bonnefoy, M. et al. 2017, A&A, 597, A91, 1608.08035

Borchert, E. M. A., Price, D. J., Pinte, C., & Cuello, N. 2021, MNRAS, 2111.12723

Breen, S. L., Contreras, Y., Dawson, J. R., Ellingsen, S. P., Voronkov, M. A., & McCarthy, T. P. 2019, MNRAS, 484, 5072, 1812.08290

Brogan, C. L. et al. 2018, ApJ, 866, 87, 1809.04178

Bronfman, L., Nyman, L. A., & May, J. 1996, A&AS, 115, 81

Burns, R. A., Handa, T., Nagayama, T., Sunada, K., & Omodaka, T. 2016, MNRAS, 460, 283, 1604.05682

Busch, L. A., Belloche, A., Garrod, R. T., Müller, H. S. P., & Menten, K. M. 2024, A&A, 681, A104, 2310.11339

Butner, H. M., Evans, Neal J., I., Lester, D. F., Levreault, R. M., & Strom, S. E. 1991, ApJ, 376, 636

Calahan, J. K., Bergin, E. A., van't Hoff, M., Zhang, K., Calvet, N., & Hartmann, L. 2024, ApJ, 967, 158, 2409.04527

Canto, J., Rodriguez, L. F., Calvet, N., & Levreault, R. M. 1984, ApJ, 282, 631

Cao, Y., Qiu, K., Zhang, Q., Wang, Y., Hu, B., & Liu, J. 2019, ApJS, 241, 1, 1901.06475

Carter, M. et al. 2012a, A&A, 538, A89

——. 2012b, A&A, 538, A89

Ceccarelli, C. et al. 2017, ApJ, 850, 176, 1710.10437

——. 2022, arXiv e-prints, arXiv:2206.13270, 2206.13270

Cesaroni, R., Palagi, F., Felli, M., Catarzi, M., Comoretto, G., Di Franco, S., Giovanardi, C., & Palla, F. 1988, A&AS, 76, 445

Chen, X. et al. 2013, ApJ, 768, 110, 1304.0436

Chen, X., Ellingsen, S. P., Shen, Z.-Q., Titmarsh, A., & Gan, C.-G. 2011, ApJS, 196, 9, 1107.2914

Chen, X., Launhardt, R., & Henning, T. 2007, ApJ, 669, 1058, 0707.4419

Chen, Z., Sun, W., Chini, R., Haas, M., Jiang, Z., & Chen, X. 2021, ApJ, 922, 90, 2108.12554

Cheung, A. C., Rank, D. M., Townes, C. H., Thornton, D. D., & Welch, W. J. 1968, Phys. Rev. Lett., 21, 1701

Cieza, L. A. et al. 2016, Nature, 535, 258, 1607.03757

——. 2018, MNRAS, 474, 4347, 1711.08693

Clarke, C. J., Lodato, G., Melnikov, S. Y., & Ibrahimov, M. A. 2005, MNRAS, 361, 942, 0505515

Claussen, M. J., Wilking, B. A., Benson, P. J., Wootten, A., Myers, P. C., & Terebey, S. 1996, ApJS, 106, 111

Codella, C., Palumbo, G. G. C., Pareschi, G., Scappini, F., Caselli, P., & Attolini, M. R. 1995, MNRAS, 276, 57

Coffey, D., Downes, T. P., & Ray, T. P. 2004, A&A, 419, 593, astro-ph/0402635

Condon, J. J., & Ransom, S. M. 2016, Essential Radio Astronomy (Princeton University Press)

Connelley, M. S., & Greene, T. P. 2010, AJ, 140, 1214, 1009.0547

Connelley, M. S., & Reipurth, B. 2018, ApJ, 861, 145, 1806.08880

Costigan, G., Vink, J. S., Scholz, A., Ray, T., & Testi, L. 2014, MNRAS, 440, 3444, 1403.4088

Cruz-Sáenz de Miera, F. et al. 2023a, A&A, 678, A88, 2308.02849

Cruz-Sáenz de Miera, F., Kóspál, Á., Ábrahám, P., Csengeri, T., Fehér, O., Güsten, R., & Henning, T. 2023b, ApJ, 945, 80, 2301.03387

Cruz-Sáenz de Miera, F. et al. 2022a, ApJ, 927, 125, 2112.04140

——. 2022b, ApJ, 927, 125, 2112.04140

Cyganowski, C. J., Koda, J., Rosolowsky, E., Towers, S., Donovan Meyer, J., Egusa, F., Momose, R., & Robitaille, T. P. 2013, ApJ, 764, 61, 1210.5528

Dalba, P. A., & Stahler, S. W. 2012, MNRAS, 425, 1591, 1207.1453

Dame, T. M., Hartmann, D., & Thaddeus, P. 2001, ApJ, 547, 792, astro-ph/0009217

Deguchi, S., Nakada, Y., & Forster, J. R. 1989, MNRAS, 239, 825

Devine, K. E., Chandler, C. J., Brogan, C., Churchwell, E., Indebetouw, R., Shirley, Y., & Borg, K. J. 2011, ApJ, 733, 44, 1103.0328

Di Francesco, J. et al. 2020, ApJ, 904, 172, 2010.09894

Diaz-Rodriguez, A. K. et al. 2022, ApJ, 930, 91, 2111.11787

Dong, R. et al. 2022, Nature Astronomy, 6, 331, 2201.05617

Dullemond, C. P., & Monnier, J. D. 2010, ARA&A, 48, 205, 1006.3485

Dunham, M. K., Rosolowsky, E., Evans, Neal J., I., Cyganowski, C., & Urquhart, J. S. 2011, ApJ, 741, 110, 1108.1812

Dunham, M. M. et al. 2015, ApJS, 220, 11, 1508.03199

——. 2013, AJ, 145, 94, 1301.4416

Dunham, M. M., & Vorobyov, E. I. 2012, ApJ, 747, 52, 1112.4789

Dutrey, A. et al. 2014, in Protostars and Planets VI, ed. H. Beuther, R. S. Klessen, C. P. Dullemond, & T. Henning, 317–338, 1402.3503

Eisloeffel, J., Guenther, E., Hessman, F. V., Mundt, R., Poetzel, R., Carr, J. S., Beckwith, S., & Ray, T. P. 1991, ApJ, 383, L19

Elia, D. et al. 2017, MNRAS, 471, 100, 1706.01046

Elias, J. H. 1978, ApJ, 223, 859

Elitzur, M. 1992, ARA&A, 30, 75

Elitzur, M., & Fuqua, J. B. 1989, ApJ, 347, L35

Elitzur, M., Hollenbach, D. J., & McKee, C. F. 1989a, ApJ, 346, 983

——. 1989b, ApJ, 346, 983

Endres, C. P., Schlemmer, S., Schilke, P., Stutzki, J., & Müller, H. S. P. 2016, Journal of Molecular Spectroscopy, 327, 95, 1603.03264

Evans, Neal J., I., Balkum, S., Levreault, R. M., Hartmann, L., & Kenyon, S. 1994, ApJ, 424, 793

Evans, Neal J., I. et al. 2009, ApJS, 181, 321, 0811.1059

Event Horizon Telescope Collaboration et al. 2019, ApJ, 875, L1, 1906.11238

Fazio, G. G. et al. 2004, ApJS, 154, 10, astro-ph/0405616

Fehér, O., Kóspál, Á., Ábrahám, P., Hogerheijde, M. R., & Brinch, C. 2017, A&A, 607, A39, 1709.07458

Feng, S., Liu, H. B., Caselli, P., Burkhardt, A., Du, F., Bachiller, R., Codella, C., & Ceccarelli, C. 2022, ApJ, 933, L35, 2206.06585

Fiebig, D. 1995, A&A, 298, 207

Fiebig, D., Duschl, W. J., Menten, K. M., & Tscharnuter, W. M. 1996, A&A, 310, 199

Fiorellino, E. et al. 2021, MNRAS, 500, 4257, 2010.15241

Fischer, W. J., Hillenbrand, L. A., Herczeg, G. J., Johnstone, D., Kospal, A., & Dunham, M. M. 2023, in Astronomical Society of the Pacific Conference Series, Vol. 534, Protostars and Planets VII, ed. S. Inutsuka, Y. Aikawa, T. Muto, K. Tomida, & M. Tamura, 355, 2203.11257

Fischer, W. J. et al. 2012, ApJ, 756, 99, 1207.2466

Fridlund, C. V. M., Bergman, P., White, G. J., Pilbratt, G. L., & Tauber, J. A. 2002, A&A, 382, 573

Fuente, A., Martin-Pintado, J., Cernicharo, J., & Bachiller, R. 1990, A&A, 237, 471

Fujiyoshi, T., Wright, C. M., & Moore, T. J. T. 2015, MNRAS, 451, 3371, 1505.05563

Fuller, G. A., Ladd, E. F., Padman, R., Myers, P. C., & Adams, F. C. 1995, ApJ, 454, 862

Furlan, E. et al. 2016, ApJS, 224, 5, 1602.07314

Furuya, R. S., Kitamura, Y., Wootten, A., Claussen, M. J., & Kawabe, R. 2003, ApJS, 144, 71

Furuya, R. S., Kitamura, Y., Wootten, H. A., Claussen, M. J., & Kawabe, R. 2001, ApJ, 559, L143

Gaia Collaboration et al. 2016, A&A, 595, A1, 1609.04153

Galloway, E. T., & Herbst, E. 1989, A&A, 211, 413

Giannini, T., Lorenzetti, D., Antoniucci, S., Arkharov, A. A., Larionov, V. M., Di Paola, A., Bisogni, S., & Marchetti, A. 2016, ApJ, 819, L5, 1602.01688

Gildas Team. 2013, GILDAS: Grenoble Image and Line Data Analysis Software, 1305.010

Goldsmith, P. F. 2001, ApJ, 557, 736

Goldsmith, P. F., & Langer, W. D. 1999, ApJ, 517, 209

Goodrich, R. W. 1986, AJ, 92, 885

Gould, B. A. 1879, Resultados del Observatorio Nacional Argentino, 1, I

Gramajo, L. V., Rodón, J. A., & Gómez, M. 2014, AJ, 147, 140, 1402.3240

Gray, M. 2012, Maser Sources in Astrophysics, book published by the Cambridge University Press (Cambridge University Press)

Gray, M. D., Etoka, S., Richards, A. M. S., & Pimpanuwat, B. 2022, MNRAS, 513, 1354

Green, J. D. et al. 2013, ApJ, 772, 117, 1306.0666

Green, J. D., Hartmann, L., Calvet, N., Watson, D. M., Ibrahimov, M., Furlan, E., Sargent, B., & Forrest, W. J. 2006, ApJ, 648, 1099, astro-ph/0605365

Greene, T. P., Wilking, B. A., Andre, P., Young, E. T., & Lada, C. J. 1994, ApJ, 434, 614

Greenhill, L. J., Jiang, D. R., Moran, J. M., Reid, M. J., Lo, K. Y., & Claussen, M. J. 1995, ApJ, 440, 619

Guesten, R., & Fiebig, D. 1988, A&A, 204, 253

Hacar, A., Alves, J., Burkert, A., & Goldsmith, P. 2016, A&A, 591, A104, 1603.08521

Hacar, A., Clark, S. E., Heitsch, F., Kainulainen, J., Panopoulou, G. V., Seifried, D., & Smith, R. 2023, in Astronomical Society of the Pacific Conference Series, Vol. 534, Protostars and Planets VII, ed. S. Inutsuka, Y. Aikawa, T. Muto, K. Tomida, & M. Tamura, 153, 2203.09562

Hacar, A., Tafalla, M., & Alves, J. 2017, A&A, 606, A123, 1703.07029

Hales, A. S., Corder, S. A., Dent, W. R. D., Andrews, S. M., Eisner, J. A., & Cieza, L. A. 2015, ApJ, 812, 134, 1509.02543

Hales, A. S. et al. 2020, ApJ, 900, 7, 2007.04348

Hartmann, L. 2001, Accretion Processes in Star Formation (Cambridge University Press)

Hartmann, L., & Kenyon, S. J. 1985, ApJ, 299, 462

——. 1996, ARA&A, 34, 207

Harvey, P. M. et al. 2008, ApJ, 680, 495

Haschick, A. D., Moran, J. M., Rodriguez, L. F., Burke, B. F., Greenfield, P., & Garcia-Barreto, J. A. 1980, ApJ, 237, 26

Henning, T., Cesaroni, R., Walmsley, M., & Pfau, W. 1992, A&AS, 93, 525

Herbig, G. H. 1960, ApJS, 4, 337

——. 1966, Vistas in Astronomy, 8, 109

——. 1977, ApJ, 217, 693

Herbig, G. H. 1989, in European Southern Observatory Conference and Workshop Proceedings, Vol. 33, European Southern Observatory Conference and Workshop Proceedings, ed. B. Reipurth, 233–246

——. 1990, ApJ, 360, 639

——. 2008, AJ, 135, 637

——. 2009, AJ, 138, 448

Herbig, G. H., Petrov, P. P., & Duemmler, R. 2003, ApJ, 595, 384, astro-ph/0306559

Herbst, E., & Klemperer, W. 1973, ApJ, 185, 505

Herbst, E., & van Dishoeck, E. F. 2009, ARA&A, 47, 427

Herbst, W., Eislöffel, J., Mundt, R., & Scholz, A. 2007, in Protostars and Planets V, ed. B. Reipurth, D. Jewitt, & K. Keil, 297, astro-ph/0603673

Herschel, Sir, J. F. W. 1847, Results of astronomical observations made during the years 1834, 5, 6, 7, 8, at the Cape of Good Hope; being the completion of a telescopic survey of the whole surface of the visible heavens, commenced in 1825

HI4PI Collaboration et al. 2016, A&A, 594, A116, 1610.06175

Hildebrand, R. H. 1983, QJRAS, 24, 267

Hillenbrand, L. A. et al. 2018, ApJ, 869, 146, 1812.06640

——. 2013, AJ, 145, 59, 1208.2066

Hillenbrand, L. A., Reipurth, B., Connelley, M., Cutri, R. M., & Isaacson, H. 2019, AJ, 158, 240, 1910.05790

Hillenbrand, L. A., & Rodriguez, A. C. 2022, Research Notes of the American Astronomical Society, 6, 6, 2201.01012

Hirahara, Y. et al. 1992, ApJ, 394, 539

Hirota, T. et al. 2011, ApJ, 739, L59, 1108.3889

Ho, P. T. P., & Townes, C. H. 1983, ARA&A, 21, 239

Hodapp, K. W., Chini, R., Watermann, R., & Lemke, R. 2012, ApJ, 744, 56, 1109.3728

Hodapp, K.-W., Hora, J. L., Rayner, J. T., Pickles, A. J., & Ladd, E. F. 1996, ApJ, 468, 861

Hodapp, K. W. et al. 2019, AJ, 158, 241, 1909.10636

Hodgkin, S. T. et al. 2021, A&A, 652, A76, 2106.01394

Hogerheijde, M. R., van Dishoeck, E. F., Salverda, J. M., & Blake, G. A. 1999, ApJ, 513, 350, astro-ph/9810047

Holdship, J., Viti, S., Jiménez-Serra, I., Makrymallis, A., & Priestley, F. 2017, AJ, 154, 38, 1705.10677

Hollenbach, D., & McKee, C. F. 1989, ApJ, 342, 306

Hunter, T. R., Taylor, G. B., Felli, M., & Tofani, G. 1994, A&A, 284, 215

Inutsuka, S., Aikawa, Y., Muto, T., Tomida, K., & Tamura, M., eds. 2023, Astronomical Society of the Pacific Conference Series, Vol. 534, Protostars and Planets VII

Ioannidis, G., & Froebrich, D. 2012, MNRAS, 425, 1380, 1206.5095

Jhan, K.-S., & Lee, C.-F. 2021, ApJ, 909, 11, 2012.15057

Jijina, J., Myers, P. C., & Adams, F. C. 1999, ApJS, 125, 161

Jørgensen, J. K., Belloche, A., & Garrod, R. T. 2020, ARA&A, 58, 727, 2006.07071

Juhász, A. et al. 2012, ApJ, 744, 118, 1110.3754

Kadam, K., Vorobyov, E., Regály, Z., Kóspál, Á., & Ábrahám, P. 2020, ApJ, 895, 41, 2005.03578

Kang, M., Lee, J.-E., Choi, M., Choi, Y., Kim, K.-T., Di Francesco, J., & Park, Y.-S. 2013, ApJS, 209, 25, 1310.8030

Kauffmann, J., Bertoldi, F., Bourke, T. L., Evans, N. J., I., & Lee, C. W. 2008, A&A, 487, 993, 0805.4205

Kazarovets, E. V., Samus, N. N., & Goranskij, V. P. 1993, Information Bulletin on Variable Stars, 3840, 1

Kenyon, S. J., & Hartmann, L. 1995, ApJS, 101, 117

Kenyon, S. J., Hartmann, L., Gomez, M., Carr, J. S., & Tokunaga, A. 1993, AJ, 105, 1505

Kenyon, S. J., Hartmann, L., & Hewett, R. 1988, ApJ, 325, 231

Kenyon, S. J., & Hartmann, L. W. 1991, ApJ, 383, 664

Kenyon, S. J., Hartmann, L. W., Strom, K. M., & Strom, S. E. 1990, AJ, 99, 869

Kim, C.-H., Kim, K.-T., & Park, Y.-S. 2018, ApJS, 236, 31, 1805.06257

Kim, J.-S. et al. 2013, ApJ, 767, 86, 1303.1686

Klein, B., Hochgürtel, S., Krämer, I., Bell, A., Meyer, K., & Güsten, R. 2012a, A&A, 542, L3, 1203.3972

——. 2012b, A&A, 542, L3, 1203.3972

Klein, B., Philipp, S. D., Krämer, I., Kasemann, C., Güsten, R., & Menten, K. M. 2006, A&A, 454, L29

Könyves, V. et al. 2020, A&A, 635, A34, 1910.04053

Koresko, C. D., Beckwith, S. V. W., Ghez, A. M., Matthews, K., & Neugebauer, G. 1991, AJ, 102, 2073

Kóspál, Á. 2011, A&A, 535, A125, 1109.3622

Kóspál, Á. et al. 2011, A&A, 527, A133, 1011.4009

——. 2016, A&A, 596, A52, 1607.05925

——. 2008, MNRAS, 383, 1015, 0710.1431

Kóspál, Á., Ábrahám, P., Csengeri, T., Henning, T., Moór, A., & Güsten, R. 2017a, ApJ, 836, 226, 1701.05018

Kóspál, Á., Ábrahám, P., Moór, A., Haas, M., Chini, R., & Hackstein, M. 2015, ApJ, 801, L5, 1501.07735

Kóspál, Á., Ábrahám, P., Prusti, T., Siebenmorgen, R., Acosta-Pulido, J., & Moór, A. 2006, in Astronomical Society of the Pacific Conference Series, Vol. 349, Astrophysics of Variable Stars, ed. C. Aerts & C. Sterken, 269

Kóspál, Á., Ábrahám, P., Westhues, C., & Haas, M. 2017b, A&A, 597, L10, 1701.00250

Kóspál, Á. et al. 2021, ApJS, 256, 30, 2106.14409

Kóspál, Á., Szabó, Z. M., Ábrahám, P., Kraus, S., Takami, M., Lucas, P. W., Peña, C. C., & Udalski, A. 2020, The Astrophysical Journal, 889, 148

Kramer, B. H., Menten, K. M., & Kraus, A. 2018, in Astrophysical Masers: Unlocking the Mysteries of the Universe, ed. A. Tarchi, M. J. Reid, & P. Castangia, Vol. 336, 279–280

Kraus, S., Caratti o Garatti, A., Garcia-Lopez, R., Kreplin, A., Aarnio, A., Monnier, J. D., Naylor, T., & Weigelt, G. 2016, MNRAS, 462, L61, 1607.03114

Kravtsova, A. S., Lamzin, S. A., Errico, L., & Vittone, A. 2007, Astronomy Letters, 33, 755

Kóspál, , Nemeth, P., Abraham, P., Kun, M., Henden, A., & Jones, A. F. 2008, Information Bulletin on Variable Stars, 5819, 1

Labdon, A. et al. 2021, A&A, 646, A102, 2011.07865

Lada, C. J. 1987, in Star Forming Regions, ed. M. Peimbert & J. Jugaku, Vol. 115, 1

Ladeyschikov, D. A., Sobolev, A. M., Bayandina, O. S., & Shakhvorostova, N. N. 2022, AJ, 163, 124

Lang, K. R., & Willson, R. F. 1979, ApJ, 227, 163

Langer, W. D., Velusamy, T., Kuiper, T. B. H., Levin, S., Olsen, E., & Migenes, V. 1995, ApJ, 453, 293

Lee, J.-E. et al. 2024, ApJ, 966, 119, 2403.03436

——. 2019, Nature Astronomy, 3, 314, 1809.00353

Lee, S., Lee, J.-E., Aikawa, Y., Herczeg, G., & Johnstone, D. 2020, ApJ, 889, 20, 1911.10318

Leemker, M., van't Hoff, M. L. R., Trapman, L., van Gelder, M. L., Hogerheijde, M. R., Ruíz-Rodríguez, D., & van Dishoeck, E. F. 2021, A&A, 646, A3, 2011.12319

Lekht, E. E., & Sorochenko, R. L. 1984, Soviet Astronomy Letters, 10, 307

Levreault, R. M. 1988, ApJS, 67, 283

Lin, D. N. C., & Papaloizou, J. 1985, in Protostars and Planets II, ed. D. C. Black & M. S. Matthews, 981–1072

Liu, H. B. et al. 2018, A&A, 612, A54, 1710.08686

——. 2021, ApJ, 923, 270, 2110.09684

Lo, K. Y., & Bechis, K. P. 1973, ApJ, 185, L71

——. 1974a, ApJ, 190, L125

Lo, K. Y., & Bechis, K. P. 1974b, in Bulletin of the American Astronomical Society, Vol. 6, 221

Looney, L. W., Mundy, L. G., & Welch, W. J. 1997, ApJ, 484, L157

Lorenzetti, D. et al. 2006, A&A, 453, 579, astro-ph/0603388

Lorenzetti, D., Larionov, V. M., Giannini, T., Arkharov, A. A., Antoniucci, S., Nisini, B., & Di Paola, A. 2009, ApJ, 693, 1056, 0811.1164

Lykou, F. et al. 2022, A&A, 663, A86, 2205.10173

Lyo, A. R., Kim, J., Byun, D.-Y., & Lee, H.-G. 2014, AJ, 148, 80, 1407.6776

MacLeod, G. C. et al. 2018, MNRAS, 478, 1077, 1804.05308

Magakian, T. Y. et al. 2013, MNRAS, 432, 2685, 1304.5033

Marchand, P., Coutens, A., Scigliuto, J., de Miera, F. C.-S., Andreu, A., Loison, J. C., Kóspál, Á., & Ábráham, P. 2024, A&A, 687, A195, 2405.08517

Maret, S., Hily-Blant, P., Pety, J., Bardeau, S., & Reynier, E. 2011, A&A, 526, A47, 1012.1747

Mathieu, R. D., Martin, E. L., & Magazzu, A. 1996, in American Astronomical Society Meeting Abstracts, Vol. 188, American Astronomical Society Meeting Abstracts #188, 60.05

Mauron, N., & Thouvenot, E. 1991, SVS 13, http://www.cbat.eps.harvard.edu/iauc/05200/05261.html

Maury, A. J. et al. 2019, A&A, 621, A76, 1810.11221

McMuldroch, S., Blake, G. A., & Sargent, A. I. 1995, AJ, 110, 354

Mercimek, S. et al. 2022, A&A, 659, A67, 2111.07573

Miller, A. A. et al. 2015, The Astronomer's Telegram, 7428, 1

——. 2011, ApJ, 730, 80, 1011.2063

Molyarova, T., Akimkin, V., Semenov, D., Ábrahám, P., Henning, T., Kóspál, Á., Vorobyov, E., & Wiebe, D. 2018, ApJ, 866, 46, 1809.01925

Mookerjea, B., Ghosh, S. K., Karnik, A. D., Rengarajan, T. N., Tandon, S. N., & Verma, R. P. 1999, Bulletin of the Astronomical Society of India, 27, 155

Moriarty-Schieven, G. H., Aspin, C., & Davis, G. R. 2008, AJ, 136, 1658, 0807.5133

Moscadelli, L., Sanna, A., Goddi, C., Krishnan, V., Massi, F., & Bacciotti, F. 2019, A&A, 631, A74, 1909.08374

Moscadelli, L., Testi, L., Furuya, R. S., Goddi, C., Claussen, M., Kitamura, Y., & Wootten, A. 2006, A&A, 446, 985, astro-ph/0509663

Müller, H. S. P., Schlöder, F., Stutzki, J., & Winnewisser, G. 2005, Journal of Molecular Structure, 742, 215

Müller, H. S. P., Thorwirth, S., Roth, D. A., & Winnewisser, G. 2001, A&A, 370, L49

Nagy, Z. et al. 2022, MNRAS, 515, 1774, 2207.02341

——. 2023, MNRAS, 524, 3344, 2307.01629

——. 2021, MNRAS, 504, 185, 2103.10313

Natta, A., Testi, L., & Randich, S. 2006, A&A, 452, 245, astro-ph/0602618

Neufeld, D. A., & Melnick, G. J. 1991, ApJ, 368, 215

Newville, M., Stensitzki, T., Allen, D. B., & Ingargiola, A. 2014, LMFIT: Non-Linear Least-Square Minimization and Curve-Fitting for Python

Nogueira, P. H. et al. 2023, MNRAS, 523, 4970, 2305.15647

Offner, S. S. R., & McKee, C. F. 2011, ApJ, 736, 53, 1105.0671

Ohishi, M., Irvine, W. M., & Kaifu, N. 1992, in Astrochemistry of Cosmic Phenomena, ed. P. D. Singh, Vol. 150, 171

Olmi, L., Araya, E. D., Chapin, E. L., Gibb, A., Hofner, P., Martin, P. G., & Poventud, C. M. 2010, ApJ, 715, 1132, 1001.4910

Omodaka, T. et al. 1999, PASJ, 51, 333

Ortiz-León, G. N., Plunkett, A. L., Loinard, L., Dzib, S. A., Rodríguez-Garza, C. B., Pillai, T., Gong, Y., & Brunthaler, A. 2021, AJ, 162, 68, 2105.11747

Ott, M., Witzel, A., Quirrenbach, A., Krichbaum, T. P., Standke, K. J., Schalinski, C. J., & Hummel, C. A. 1994, A&A, 284, 331

Paczynski, B. 1976, in IAU Symposium, Vol. 73, Structure and Evolution of Close Binary Systems, ed. P. Eggleton, S. Mitton, & J. Whelan, 75

Palla, F., & Prusti, T. 1993, A&A, 272, 249

Park, S. et al. 2022, ApJ, 941, 165, 2211.02137

——. 2021, ApJ, 923, 171, 2109.11283

——. 2020, ApJ, 900, 36, 2007.03197

Parsamian, E. S., & Mujica, R. 2004, Astrophysics, 47, 433

Peck, A. B., & Taylor, G. B. 2001, ApJ, 554, L147, astro-ph/0105310

Perault, M. et al. 1996, A&A, 315, L165

Pérez, S. et al. 2020, ApJ, 889, 59, 1911.11282

Persi, P., Palagi, F., & Felli, M. 1994, A&A, 291, 577

Pety, J. 2005a, in SF2A-2005: Semaine de l'Astrophysique Francaise, ed. F. Casoli, T. Contini, J. M. Hameury, & L. Pagani, 721

Pety, J. 2005b, in SF2A-2005: Semaine de l'Astrophysique Francaise, ed. F. Casoli, T. Contini, J. M. Hameury, & L. Pagani, 721

Pety, J. 2005c, in SF2A-2005: Semaine de l'Astrophysique Francaise, ed. F. Casoli, T. Contini, J. M. Hameury, & L. Pagani, 721

Pezzuto, S. et al. 2021, A&A, 645, A55, 2010.00006

Pezzuto, S., Strafella, F., & Lorenzetti, D. 1997, ApJ, 485, 290

Pickett, H. M., Poynter, R. L., Cohen, E. A., Delitsky, M. L., Pearson, J. C., & Müller, H. S. P. 1998a, J. Quant. Spec. Radiat. Transf., 60, 883

——. 1998b, J. Quant. Spec. Radiat. Transf., 60, 883

Pillai, T., Wyrowski, F., Carey, S. J., & Menten, K. M. 2006, A&A, 450, 569, astro-ph/0601078

Pineda, J. E. et al. 2023, in Astronomical Society of the Pacific Conference Series, Vol. 534, Protostars and Planets VII, ed. S. Inutsuka, Y. Aikawa, T. Muto, K. Tomida, & M. Tamura, 233, 2205.03935

Plambeck, R. L., & Menten, K. M. 1990, ApJ, 364, 555

Plunkett, A. L., Arce, H. G., Corder, S. A., Mardones, D., Sargent, A. I., & Schnee, S. L. 2013, ApJ, 774, 22, 1307.3558

Plunkett, A. L., Arce, H. G., Mardones, D., van Dokkum, P., Dunham, M. M., Fernández-López, M., Gallardo, J., & Corder, S. A. 2015, Nature, 527, 70, 1511.01100

Podio, L. et al. 2021, A&A, 648, A45, 2012.15379

Principe, D. A. et al. 2018, MNRAS, 473, 879, 1709.01924

Quanz, S. P., Henning, T., Bouwman, J., Linz, H., & Lahuis, F. 2007a, ApJ, 658, 487, astro-ph/0612096

Quanz, S. P., Henning, T., Bouwman, J., van Boekel, R., Juhász, A., Linz, H., Pontoppidan, K. M., & Lahuis, F. 2007b, ApJ, 668, 359, 0706.3593

Rab, C. et al. 2017, A&A, 604, A15, 1705.03946

Ragan, S. E., Bergin, E. A., & Wilner, D. 2011, ApJ, 736, 163, 1105.4182

Redaelli, E., Bovino, S., Sanhueza, P., Morii, K., Sabatini, G., Caselli, P., Giannetti, A., & Li, S. 2022, ApJ, 936, 169

Reid, M. J., & Honma, M. 2014, ARA&A, 52, 339, 1312.2871

Reid, M. J. et al. 2009, ApJ, 700, 137, 0902.3913

Reipurth, B., & Aspin, C. 1997, AJ, 114, 2700

Reipurth, B., Aspin, C., & Herbig, G. H. 2012, ApJ, 748, L5

Reipurth, B., Bally, J., & Devine, D. 1997, AJ, 114, 2708

Rodríguez, L. F., Anglada, G., & Curiel, S. 1997, ApJ, 480, L125

Rodríguez, L. F., Anglada, G., Torrelles, J. M., Mendoza-Torres, J. E., Haschick, A. D., & Ho, P. T. P. 2002, A&A, 389, 572

Roy, A. et al. 2013, ApJ, 763, 55, 1211.6475

Ruíz-Rodríguez, D., Cieza, L. A., Williams, J. P., Principe, D., Tobin, J. J., Zhu, Z., & Zurlo, A. 2017a, MNRAS, 468, 3266, 1703.07006

Ruíz-Rodríguez, D. et al. 2017b, MNRAS, 466, 3519, 1612.08799

——. 2017c, MNRAS, 466, 3519, 1612.08799

Ruíz-Rodríguez, D. A., Williams, J. P., Kastner, J. H., Cieza, L., Leemker, M., & Principe, D. A. 2022, MNRAS, 515, 2646, 2207.02252

Sandell, G., & Aspin, C. 1998, A&A, 333, 1016

Sandell, G., & Weintraub, D. A. 2001, ApJS, 134, 115

Scappini, F., Caselli, P., & Palumbo, G. G. C. 1991, MNRAS, 249, 763

Schmalzl, M. et al. 2010, ApJ, 725, 1327, 1010.2755

Schneider, N. et al. 2013, ApJ, 766, L17, 1304.0327

Schöier, F. L., van der Tak, F. F. S., van Dishoeck, E. F., & Black, J. H. 2005, A&A, 432, 369, astro-ph/0411110

Schulz, N. S. 2005, From Dust To Stars Studies of the Formation and Early Evolution of Stars (Springer)

Segura-Cox, D. M. et al. 2018, ApJ, 866, 161, 1808.10438

Semkov, E. H., Ibryamov, S. I., & Peneva, S. P. 2019, Serbian Astronomical Journal, 199, 39, 1911.06622

Sepúlveda, I. et al. 2020, A&A, 644, A128, 2011.01651

Shirley, Y. L. 2015, PASP, 127, 299, 1501.01629

Shu, F. H., Adams, F. C., & Lizano, S. 1987, ARA&A, 25, 23

Sipos, N., Ábrahám, P., Acosta-Pulido, J., Juhász, A., Kóspál, Á., Kun, M., Moór, A., & Setiawan, J. 2009, A&A, 507, 881, 0906.3168

Snell, R. L., Dickman, R. L., & Huang, Y. L. 1990, ApJ, 352, 139

Stahler, S. W., & Palla, F. 2004, The Formation of Stars (WILEY-VCH Verlag GmbH & Co. KGaA, Weinheim)

Stäuber, P., Benz, A. O., Jørgensen, J. K., van Dishoeck, E. F., Doty, S. D., & van der Tak, F. F. S. 2007, A&A, 466, 977, astro-ph/0608393

Staude, H. J., & Neckel, T. 1991, A&A, 244, L13

Stecklum, B., Melnikov, S. Y., & Meusinger, H. 2007, A&A, 463, 621, astro-ph/0611314

Stojimirović, I., Snell, R. L., & Narayanan, G. 2008, ApJ, 679, 557

Strom, S. E., Strom, K. M., Yost, J., Carrasco, L., & Grasdalen, G. 1972, ApJ, 173, 353

Strom, S. E., Vrba, F. J., & Strom, K. M. 1976, AJ, 81, 314

Sunada, K., Nakazato, T., Ikeda, N., Hongo, S., Kitamura, Y., & Yang, J. 2007, PASJ, 59, 1185

Szabó, Z. M. et al. 2025, A&A, 694, A329, 2501.14553

——. 2023a, A&A, 672, A158, 2302.03371

——. 2023b, A&A, 674, A202, 2305.00736

——. 2021, ApJ, 917, 80, 2105.10405

——. 2022, ApJ, 936, 64, 2206.12446

Szegedi-Elek, E. et al. 2020, ApJ, 899, 130, 2005.11537

Szymczak, M., Olech, M., Wolak, P., Bartkiewicz, A., & Gawroński, M. 2016, MNRAS, 459, L56, 1604.00796

Tafalla, M., & Bachiller, R. 1995, ApJ, 443, L37

Tafalla, M., Myers, P. C., Caselli, P., & Walmsley, C. M. 2004, A&A, 416, 191

Takagi, Y., Honda, S., Arai, A., Morihana, K., Takahashi, J., Oasa, Y., & Itoh, Y. 2018, AJ, 155, 101, 1801.00883

Takami, M. et al. 2019, ApJ, 884, 146, 1909.05520

——. 2018, ApJ, 864, 20, 1807.03499

Tambovtseva, L., & Grinin, V. 2016, in Accretion Processes in Cosmic Sources, 56

Tanner, J. D., & Arce, H. G. 2011, ApJ, 726, 40, 1011.4197

Thum, C., Bertout, C., & Downes, D. 1981, A&A, 94, 80

Tobin, J. J. et al. 2023, Nature, 615, 227

Torrelles, J. M., Ho, P. T. P., Moran, J. M., Rodriguez, L. F., & Canto, J. 1986, ApJ, 307, 787

Turner, N. J. J., Bodenheimer, P., & Bell, K. R. 1997, ApJ, 480, 754

Umemoto, T., Mikami, H., Yamamoto, S., & Hirano, N. 1999, ApJ, 525, L105, astro-ph/9909328

Ungerechts, H., & Guesten, R. 1984, A&A, 131, 177

Urquhart, J. S. et al. 2009, A&A, 507, 795, 0909.1720

——. 2011, MNRAS, 418, 1689, 1107.3913

van Haarlem, M. P. et al. 2013, A&A, 556, A2, 1305.3550

van 't Hoff, M. L. R., Tobin, J. J., Trapman, L., Harsono, D., Sheehan, P. D., Fischer, W. J., Megeath, S. T., & van Dishoeck, E. F. 2018, ApJ, 864, L23, 1808.08258

Velilla Prieto, L. et al. 2017, A&A, 597, A25, 1609.01904

Visser, A. E., Richer, J. S., & Chandler, C. J. 2002, AJ, 124, 2756

Visser, R., Bergin, E. A., & Jørgensen, J. K. 2015, A&A, 577, A102, 1503.04951

Vorobyov, E. I., & Basu, S. 2005, ApJ, 633, L137, astro-ph/0510014

——. 2006, ApJ, 650, 956, astro-ph/0607118

——. 2010, ApJ, 719, 1896, 1007.2993

Wachmann, A. 1954, ZAp, 35, 74

Walmsley, C. M., & Ungerechts, H. 1983, A&A, 122, 164

Wang, M.-T. et al. 2023, ApJ, 957, 113, 2308.11895

Waters, L. B. F. M., & Waelkens, C. 1998, ARA&A, 36, 233

Watson, W. D. 1976, Reviews of Modern Physics, 48, 513

Weber, P. et al. 2025, arXiv e-prints, arXiv:2504.05439, 2504.05439

Weintraub, D. A., Sandell, G., & Duncan, W. D. 1991, ApJ, 382, 270

Welin, G. 1971a, A&A, 12, 312

——. 1971b, Information Bulletin on Variable Stars, 581, 1

Wendeborn, J. et al. 2020, ApJ, 897, 54, 2005.10371

White, G. J., Fridlund, C. W. M., Bergman, P., Beardsmore, A., Liseau, R., Price, M., & Phillips, R. R. 2006, ApJ, 651, L41, astro-ph/0609661

White, J. A. et al. 2019, ApJ, 877, 21, 1904.07269

Wielebinski, R., Junkes, N., & Grahl, B. H. 2011, Journal of Astronomical History and Heritage, 14, 3

Wienen, M., Wyrowski, F., Schuller, F., Menten, K. M., Walmsley, C. M., Bronfman, L., & Motte, F. 2012, A&A, 544, A146, 1208.4848

Wilson, T. L., Rohlfs, K., & Hüttemeister, S. 2009, Tools of Radio Astronomy (Springer)

Winkel, B., Kraus, A., & Bach, U. 2012a, A&A, 540, A140, 1203.0741

——. 2012b, A&A, 540, A140, 1203.0741

Winnberg, A., Graham, D., Walmsley, C. M., & Booth, R. S. 1981, A&A, 93, 79

Woitke, P., Kamp, I., & Thi, W. F. 2009, A&A, 501, 383, 0904.0334

Woitke, P. et al. 2016, A&A, 586, A103, 1511.03431

Wouterloot, J. G. A., & Brand, J. 1989, A&AS, 80, 149

Wouterloot, J. G. A., Brand, J., & Fiegle, K. 1993, A&AS, 98, 589

Yamamoto, S. 2017, Introduction to Astrochemistry: Chemical Evolution from Interstellar Clouds to Star and Planet Formation

Yamato, Y., Notsu, S., Aikawa, Y., Okoda, Y., Nomura, H., & Sakai, N. 2024, AJ, 167, 66, 2312.01300

Yan, Q.-Z., Yang, J., Yang, S., Sun, Y., & Wang, C. 2021, ApJ, 910, 109, 2102.06917

Yang, J., Umemoto, T., Iwata, T., & Fukui, Y. 1991, ApJ, 373, 137

Yang, W. et al. 2023, A&A, 675, A112, 2305.04264

Zapata, L. A. et al. 2015, ApJ, 811, L4, 1509.00316

Zhang, S. B., Yang, J., Xu, Y., Pandian, J. D., Menten, K. M., & Henkel, C. 2011, ApJS, 193, 10, 1101.4072

Zhou, W., Chen, Z., Jiang, Z., Feng, H., & Jiang, Y. 2024, ApJ, 969, L6, 2406.04980

Zhu, Z., Hartmann, L., & Gammie, C. 2009, ApJ, 694, 1045, 0811.1762

Zucker, C., Speagle, J. S., Schlafly, E. F., Green, G. M., Finkbeiner, D. P., Goodman, A. A., & Alves, J. 2019, ApJ, 879, 125, 1902.01425

Zurlo, A. et al. 2017, MNRAS, 465, 834, 1611.00765

Zwicky, L., Molyarova, T., Akimkin, V., Smirnov-Pinchukov, G. V., Semenov, D., Kóspál, Á., & Ábrahám, P. 2024, MNRAS, 527, 7652, 2311.17499